

Part I: The Equations of Plasma Physics and The
Richtmyer-Meshkov Instability in
Magnetohydrodynamics

Part II: Evolution of Perturbed Planar Shockwaves

Thesis by
Naijian Shen

In Partial Fulfillment of the Requirements for the
Degree of
Doctor of Philosophy

The logo for the California Institute of Technology (Caltech), featuring the word "Caltech" in a bold, orange, sans-serif font.

CALIFORNIA INSTITUTE OF TECHNOLOGY
Pasadena, California

2021
Defended 24 September 2020

© 2021

Naijian Shen

ORCID: 0000-0002-0533-8081

All rights reserved.

ACKNOWLEDGEMENTS

This work is partially supported by the KAUST Office of Sponsored Research under Award No. URF/1/3418-01.

I wish to express my deepest gratitude to my advisor, Professor Dale Pullin, who guided me through every step towards the completion and recognition of this work. His passionate, audacious and persistent pursuit of science has been an inspiration. It is my great fortune and honor to be his student.

With great appreciation I would like to acknowledge our collaborators, Yuan Li and Prof. Ravi Samtaney at King Abdullah University of Science and Technology, and Prof. Vincent Wheatley at University of Queensland. Their resources, experience, and wisdom contributed indispensably to the present investigation.

For lending their time, interest, and insight I wish to thank the members of my Examination Committee: Prof. Paul Bellan, Prof. Dan Meiron, and Prof. Beverly McKeon. Sincere thanks also to Prof. Hans Hornung for many thought-provoking discussions.

I extend my thanks to the Caltech nonacademic community, in particular, the International Students Programs, the Student Wellness Services, the Graduate Office and the Caltech Children Center for helping my family tremendously. I thank the GALCIT options manager Christine Ramirez and administrative assistant Barbara Slater for being incredibly resourceful and nice to me both professionally and personally.

It is highly appreciated that the warmth of my friends has made this adventure wonderfully fun and memorable. My thanks to Conor Martin and Keree McGuire for their warmheartedness and generosity, always looking after my family even during our darkest period. I thank Benjamin Riviere for our deep rapport sharing highs and lows, and Kai Matsuka for encouraging me with his enthusiasm and optimism.

I am forever grateful for my parents who show me unconditional love. For too long, they have been selflessly sacrificing to support my overseas education. I am also much indebted to my wife Grace, who left everything behind to follow my dreams. The finishing of this work would not have been possible without her commitment, care, and love. And I am thankful for our son Liam, a celestial blessing gifted to us in this journey. This thesis is dedicated to Grace and Liam, to whom I will always give all I can.

ABSTRACT

Part I: Mitigating the Richtmyer-Meshkov instability (RMI) is critical for energy production in inertial confinement fusion. Suitable plasma models are required to study the hydrodynamic and electromagnetic interactions associated with the RMI in a conducting medium. First, a sequence of asymptotic expansions in several small parameters, as formal limits of the non-dissipative and non-resistive two-fluid plasma equations, leads to five simplified plasma/magnetohydrodynamics (MHD) systems. Each system is characterized by its own physical range of validity and dispersion relations, and includes the widely used magnetohydrodynamic (MHD) and Hall-MHD equations. Next we focus on the RMI in MHD. Using ideal MHD, it has been shown that the RMI is suppressed by the presence of an external magnetic field. We utilize the incompressible, Hall-MHD model to investigate the stabilization mechanism when the plasma ion skin depth and Larmor radius are nonzero. The evolution of an impulsively accelerated, sinusoidally perturbed density interface between two conducting fluids is solved as a linearized initial-value problem. An initially uniform background magnetic field of arbitrary orientation is applied. The incipient RMI is found suppressed through oscillatory motions of the interface due to the ion cyclotron effect. This suppression is most effective for near tangential magnetic fields but becomes less effective with increasing plasma length scales. The vorticity dynamics that facilitates the stabilization is discussed.

Part II: We consider the evolution of a planar gas-dynamic shock wave subject to smooth initial perturbations in both Mach number and shock shape profile. A complex variable formulation for the general shock motion is developed based on an expansion of the Euler equations proposed by Best [*Shock Waves*, 1: 251-273, (1991)]. The zeroth-order truncation of Best's system is related to the well-known geometrical shock dynamics (GSD) equations while higher-order corrections provide a hierarchy of closed systems, as detailed initial flow conditions immediately behind the shock are prescribed. Solutions to Best's generalized GSD system for the evolution of two-dimensional perturbations are explored numerically up to second order in the weak and strong shock limits. Two specific problems are investigated: a shock generated by an impulsively accelerated piston with a corrugated surface, and a shock traversing a density gradient. For the piston-driven flow, it is shown that this approach allows full determination of derivative jump conditions across the shock required to specify initial conditions for the retained, higher-order correction

equations. In both cases, spontaneous development of curvature singularity in the shock shape is detected. The critical time at which a singularity occurs follows a scaling inversely proportional to the initial perturbation size. This result agrees with the weakly nonlinear GSD analysis of Mostert *et al.* [*J. Fluid Mech.*, 846: 536-562, (2018)].

PUBLISHED CONTENT AND CONTRIBUTIONS

- [1] N. Shen, D. I. Pullin, R. Samtaney, and V. Wheatley. Evolution of a shock generated by an impulsively accelerated, sinusoidal piston. *Journal of Fluid Mechanics*, 2020. doi: 10.1017/jfm.2020.775. (in print).

N. S. proposed the project, developed the models, analyzed and solved the equations, drafted a manuscript and helped editing the article.

- [2] Naijian Shen, Yuan Li, D. I. Pullin, Ravi Samtaney, and Vincent Wheatley. On the magnetohydrodynamic limits of the ideal two-fluid plasma equations. *Physics of Plasmas*, 25(12):122113, 2018. doi: 10.1063/1.5067387.

N. S. derived the plasma equations, solved the corresponding wave systems, drafted a manuscript and helped editing the article.

- [3] Naijian Shen, D. I. Pullin, Vincent Wheatley, and Ravi Samtaney. Impulse-driven richtmyer-meshkov instability in hall-magnetohydrodynamics. *Physical Review Fluids*, 4(10):103902, 2019. doi: 10.1103/PhysRevFluids.4.103902.

N. S. participated in the conception of the project, developed the models, analyzed and solved the equations, drafted a manuscript and helped editing the article.

- [4] Naijian Shen, Vincent Wheatley, D. I. Pullin, and Ravi Samtaney. Magneto-hydrodynamic richtmyer-meshkov instability under an arbitrarily oriented magnetic field. *Physics of Plasmas*, 27(6):062101, 2020. doi: 10.1063/1.5142042.

N. S. proposed the project, derived and solved the incompressible flow, drafted a manuscript and helped editing the article.

TABLE OF CONTENTS

Acknowledgements	iii
Abstract	iv
Published Content and Contributions	vi
Bibliography	vi
Table of Contents	vi
List of Illustrations	x
List of Tables	xviii

I The Equations of Plasma Physics and The Richtmyer-Meshkov Instability in Magnetohydrodynamics	1
Chapter I: Introduction	2
1.1 Plasma kinetic theory and ideal fluid equations	5
1.1.1 Vlasov-Boltzmann equation	5
1.1.2 Ideal two-fluid equations	7
1.1.3 Ideal magnetohydrodynamics	8
1.2 Hydrodynamic RMI	9
1.3 Magnetohydrodynamic RMI	10
1.4 Two-fluid plasma RMI	12
1.5 Part I outline	13
Chapter II: Magnetohydrodynamic limits of the ideal two-fluid plasma equations	16
2.1 Introduction	16
2.2 Non-dimensional ideal two-fluid plasma equations	19
2.2.1 Equations of motion	19
2.2.2 Center-of-mass representation	21
2.2.3 Dispersion relation for 2FP	23
2.3 Infinite speed-of-light limit	29
2.3.1 Leading order equations: $c \rightarrow \infty$	29
2.3.2 Dispersion relation for 2FMHD	32
2.4 Small electron Inertia limit	36
2.4.1 Leading-order equations: $M \rightarrow \infty$	36
2.4.2 Dispersion relation for 1FP	38
2.5 Zero skin depth limit	40
2.5.1 Leading order equations: $d_S \rightarrow 0$	41
2.5.2 Dispersion relation for QMHD	43
2.6 Magnetohydrodynamic reductions	44
2.6.1 Hall-MHD reduction	45
2.6.2 Ideal MHD reduction	47
2.7 Summary	51

Chapter III: Impulse-driven RMI in Hall-MHD	52
3.1 Introduction	52
3.2 Incompressible ion Compressible electron Hall-MHD (IICE)	54
3.2.1 Governing equations	54
3.2.2 Linearized system	56
3.2.3 General solution	59
3.2.4 Interface jump conditions	61
3.3 Analysis	63
3.3.1 Vorticity dynamics	64
3.3.2 Asymptotic analysis	65
3.4 Incompressible ion incompressible electron Hall-MHD (IIIE)	70
3.4.1 Governing equations and general solutions	70
3.4.2 Modified interface jump conditions	71
3.4.3 Asymptotic flow field	72
3.5 Numerical results	73
3.5.1 IICE results	74
3.5.2 IIIE results and model comparison	81
3.6 Summary	83
Chapter IV: Hall-MHD RMI under an arbitrarily oriented magnetic field	85
4.1 Introduction	85
4.2 Incompressible Hall-MHD model	86
4.2.1 Governing equations	86
4.2.2 Rankine-Hugoniot conditions	88
4.2.3 Linearized equations	89
4.3 Flow field calculation	91
4.3.1 Transverse magnetic field	91
4.3.2 Oblique magnetic field	94
4.3.3 Vorticity transport	98
4.4 Asymptotic analysis	99
4.4.1 The MHD limit	100
4.4.2 Large skin depth limit	103
4.4.3 Strong field limit	105
4.4.4 Large angle limit	106
4.5 Numerical results	108
4.5.1 Growth of the interface perturbation	110
4.5.2 Circulation deposition	113
4.5.3 Normal velocity profile	115
4.5.4 Vorticity dynamics	119
4.6 Summary	122
Chapter V: Conclusions	124
II Evolution of Perturbed Planar Shockwaves	127
Chapter VI: Introduction	129
6.1 Geometrical shock dynamics	131

6.1.1	The A – M relation	131
6.1.2	Two-dimension shock propagation	132
6.2	Part II outline	133
Chapter VII:	Generalized geometrical shock dynamics	135
7.1	Quasi-one-dimensional Euler equations	135
7.1.1	A – M relation revisited	136
7.2	Two-dimensional Euler equations	137
7.2.1	Tangential derivatives	138
7.2.2	Time and normal derivatives	140
7.3	Geometrical equivalence	140
7.4	A hierarchical expansion of the Euler equations	141
7.5	Evolution of a periodic, perturbed planar shock	144
7.5.1	A complex-variable formulation	144
7.5.2	Zeroth-order GGSD system: GGSD-0	145
7.5.3	First order GGSD system: GGSD-1	147
7.5.4	Second order GGSD system: GGSD-2	149
7.5.5	Unbounded linear growth	151
Chapter VIII:	Applications: formation of shock curvature singularity	154
8.1	Shock generated by a corrugated piston	154
8.1.1	Base motion	154
8.1.2	Initial values for Z and M	155
8.1.3	Initial values for Q_1 and Q_2	156
8.1.4	Numerical results	159
8.2	Shock traversing a density gradient	169
8.2.1	Compact perturbation field	169
8.2.2	Leading order IVP	170
8.2.3	Numerical results	171
Chapter IX:	Conclusions	175
Appendix A:	Zero plasma beta limit of 2FP	177
Appendix B:	Limiting linear equations for coefficients α	179
Appendix C:	Analytical Laplace transform inversion	181
Appendix D:	Linearized Rankine-Hugoniot conditions	183
Appendix E:	Tables of coefficients	185
Appendix F:	Partial derivatives of flow variables	188
F.1	General solutions	188
F.2	Asymptotic solutions	189
Appendix G:	An edge-detection algorithm	193
Bibliography	195

LIST OF ILLUSTRATIONS

<i>Number</i>	<i>Page</i>
1.1 A schematic cutaway view of a NIF target, showing the various layers of ablator, the frozen DT shell, and the gaseous DT interior. Image reproduced from Moses <i>et al.</i> [74]	3
1.2 (a) Simulation schematically showing the growth of a preimposed ripple in density from a capsule radius of 900–300 μm at the ablation front. Image reproduced from Smalyuk <i>et al.</i> [94]. (b) 3D implosion simulation of a NIF capsule at bang time. The outer surface shows the ablation front and is colored by the electron temperature with the color scale on the lower left. The left half shows the ion temperature with the color scale on the upper left, and the right half shows the density with the color scale on the right. Image reproduced from Clark <i>et al.</i> [20].	3
1.3 Illustration of shock-interface interaction and RMI. (a) Perturbed density interface and incident shock I . (b) Shock passage with reflected shock R and transmitted shock T . (c) Circulation deposition. (d) Instability rolling up into characteristic mushroom-shape.	10
1.4 Density field from the Richtmyer-Meshkov simulations of Samtaney [87], after the incident shock passage. The external magnetic field is turned off and on in the top and bottom images respectively. The transmitted shock is located near the right edge of each image.	11
1.5 Vorticity (top) and density (bottom) fields in each panel, from compressible MHD simulations using $M = 2$, $\gamma = 5/3$, $\rho_2/\rho_1 = 3$, $\eta_0 k = 0.2\pi$, and $B = 0$ in (i), $\beta = 2p_0/B^2 = 1$ in (ii), at three different times in (a)–(c). Image reproduced from Wheatley <i>et al.</i> [105].	11
1.6 Density fields from cylindrically converging MHD RMI simulations with $B_0 = 0$ and horizontal and saddle geometry initial magnetic fields. Magnetic field lines are overlaid where relevant. A portion of the initial density field is also shown. Image generated from the simulations of Mostert <i>et al.</i> [76].	12

1.7	Evolution of ion (left) and electron (right) number density fields with $d_L = d_D = 0.1$ (nondimensional). Hydrodynamic interface location is overlaid on ion plots. Image reproduced from Bond <i>et al.</i> [12].	14
1.8	Rotation of ion vorticity and torque due to the magnetic field sampled at a point fixed to the interface approximately midway between the bubble and spike. Image reproduced from Bond <i>et al.</i> [13].	15
2.1	Dispersion diagram for waves from an ideal two-fluid hydrogen plasma 2FP (solid lines) and its limit 2FMHD as $c \rightarrow \infty$ (dashed lines). $\lambda = 0.5, \alpha = 0.5, \beta = 0.15, d_S = 1, M = 1836$. In particular, $c = 170$ for the two-fluid system.	35
2.2	Dispersion diagram for waves from an ideal two-fluid hydrogen plasma 2FP (solid lines) and its limit 1FP as $M \rightarrow \infty$ (dashed lines). $\lambda = 0.5, \alpha = 0.5, \beta = 0.15, d_S = 1, c = 170$. In particular, $M = 1836$ for the two-fluid system.	40
2.3	Waves comparison of a hydrogen plasma described by the Hall-MHD equations against (a) the 2FMHD model where $M = 1836$, and (b) the 1FP model, where $c = 170$. In both cases $\lambda = 0.5, \beta = 0.15$, and $d_S = 1$	47
2.4	Dispersion diagram for waves of a hydrogen plasma described by the ideal MHD (solid lines), Hall-MHD (dashed line), and QMHD equations (circles). $\lambda = 0.5k, \beta = 0.15$; and $d_S = 1$ for Hall-MHD, $c = 10$ for QMHD.	50
3.1	(a) Geometry and initial condition for compressible RMI with an external magnetic field. (b) The incompressible flow model that mimics the shock with an impulsive acceleration.	54
3.2	Growth rate of the density interface perturbation, $d\eta/dt = \tilde{w}(0)$, as a function of the Larmor radius d_L : (a) convergence towards the MHD limit ($d_L = 0$, dashed) as d_L decreases, represented in original time t ; and (b) convergence towards the large d_L asymptote (dashed) as d_L increases, represented in the rescaled time $T = t/d_L$. In both cases, the energy ratio and the Atwood number are fixed at $\beta = 2$ and $\mathcal{A} = 0.5$, respectively.	75

- 3.3 Amplitude of the interface perturbation as a function of the Larmor radius d_L , in the incompressible ion compressible electron (IICE) Hall-MHD model. In (a), the original time unit t and length unit η_0 are used for decreasing values of $d_L = 0.4, 0.2, 0.1$ (solid lines), and $d_L = 0$ (the MHD limit, dashed line). In (b), rescaled time $T = t/d_L$ and length η/d_L are used with d_L varying from 0.1 to infinity (dashed). For all series, the energy ratio and the Atwood number are fixed at $\beta = 2$ and $\mathcal{A} = 0.5$, respectively. 76
- 3.4 Amplitude of the interface perturbation as a function of energy ratio β for (a) fixed Larmor radius $d_L = 1$, and (b) fixed ion skin depth $d_S = 1$. The IICE model with an Atwood number of $\mathcal{A} = 0.5$ is used throughout. Convergence towards the small β limit (dashed line) is shown with decreasing $\beta = 200, 20, 2$, (solid lines) in (a), whereas convergence towards zero interface growth is shown by further reducing $\beta = 2, 0.2, 0.02$, in (b). 77
- 3.5 Normal velocity profile from the IICE model, $\tilde{w}(z, t)$, for $t = 0^+, 0.5, 1, 2$, in (a)–(d), respectively. The Hall-MHD solutions, obtained for $\beta = 2$, $d_L = d_S = 0.1$ and $\mathcal{A} = 0.5$, given by the solid lines, are compared to the regular MHD solutions of the same energy ratio and Atwood number, shown as dashed lines. 78
- 3.6 Normal velocity profiles from the IICE model, $\tilde{w}(z, t = 0.5)$, for increasing strength of the applied magnetic field, with varying $\beta = 2, 0.2, 0.02$ and constant $d_S = 1$, $\mathcal{A} = 0.5$ 79
- 3.7 Effect of increasing applied magnetic field in the IICE model on the circulation deposition at the interface, γ_0 , as β is decreased using $\beta = 2, 0.2, 0.02$ with constant $d_S = 1$, $\mathcal{A} = 0.5$ over (a) the original time scale t , and (b) the cyclotron time scale $T = t/d_L$ 79
- 3.8 Effect of increasing ion skin depth in the IICE model on the circulation deposition at the interface, γ_0 , for constant $\mathcal{A} = 0.5$. (a) Increase d_S via decreasing energy ratio $\beta = 100, 2, 0$, while holding $d_L = 1$ fixed. (b) Increase d_S via increasing Larmor radius $d_L = 0.1, 0.5, \infty$, in rescaled time $T = t/d_L$, while holding $\beta = 2$ fixed. In both cases, the dashed line represents the same asymptotic limit of $d_S = \infty$ 80
- 3.9 Vorticity profile $\tilde{\omega}_y(z, t)$ at two time instants obtained using the IICE model: $t = 0.1$ (solid) and $t = 0.2$ (dashed). Both solutions are obtained for $d_L = 0.1, \beta = 2$ and $\mathcal{A} = 0.5$ 81

- 3.10 Amplitude growth of the interface perturbation, η/η_0 , predicted by the IICE model (solid lines), and the IIIE model (dashed lines). Comparisons are made for varying $d_S = 0.1, 1, 10$, with $\beta = 2$ fixed in (a), and for changing $\beta = 0.2, 2, 20$, with $d_S = 1$ fixed in (b). All series are obtained in the cyclotron time scale T for fluids with $\mathcal{A} = 0.5$ 81
- 3.11 Convergence of interface statistics obtained from the IICE model (solid lines), towards those of the IIIE model (dashed lines), as $\mathcal{A} \rightarrow 1$. The $d_S = \infty$ asymptotic behavior of (a) the renormalized interface growth $\hat{\eta}$, and (b) the renormalized circulation deposition $\hat{\gamma}_0$, are plotted as functions of increasing $\mathcal{A} = 0, 0.5, 0.8, 1$. Similar comparisons are made for finite $d_S = 1$ corresponding solutions for η and γ_0 in (c) and (d), respectively. $\beta = 2$ is used throughout. 82
- 3.12 Comparison of normal velocity profile between the IICE (solid line) and IIIE (dashed line) flow models for high density ratio, $\mathcal{A} = 0.98$, at time $t = 0.5$ in (a) and $t = 1.5$ in (b). $d_S = 0.1$ and $\beta = 2$ are held fixed in all cases. The vertical lines indicate the position of Alfvén wavefronts associated with the MHD model traveling at speed v_{A_i} in the fluid region $i = 1, 2$, left or right to the interface. 83
- 4.1 (a) Geometry and initial condition for incompressible RMI with an external magnetic field \mathbf{B}_0 of arbitrary orientation. The perturbed density interface with wavelength Λ and amplitude η_0 experiences impulsive acceleration $V_0\delta(t)$. (b) Two-dimensional incompressible RM flow representation. ϕ is the angle made by the in-plane background magnetic field with the z -axis. The hat symbol is used to denote dimensionless variables. (c) Initial conditions for the shock-driven compressible MHD RMI simulation. The asterisk symbol denotes a different non-dimensionalization scheme. 86
- 4.2 MHD interface perturbation amplitude histories. (a) Comparison of the incompressible model and the simulated η histories corresponding to the shock driven case with $\phi = 4\pi/9$. (b) Incompressible model η histories for the same parameters with varying ϕ 110
- 4.3 MHD normalized limiting interface perturbation amplitude for varying ϕ and Atwood number. 111

- 4.4 The growth of the interfacial perturbation amplitude obtained at an oblique magnetic field angle $\phi = 70^\circ$. Convergence towards (a) the MHD solution via decreasing d_L , (b) the large skin depth limit via increasing $d_L = d_S$ at a constant $\beta = 2$, and (c) the strong magnetic field limit via decreasing β at a constant $d_S = 1$ are shown. The Atwood number $\mathcal{A} = 0.5$ is held constant. 112
- 4.5 Interfacial perturbation growth as a function of the magnetic field angle ϕ . Explicit comparison between $0 \leq \phi < 90^\circ$ and $\phi = 90^\circ$ are made for $d_L = d_S = 1$ in (a) and $d_L = d_S = 0.1$ in (b). $\mathcal{A} = 0.5$ is fixed in both cases. 113
- 4.6 Normalized circulation deposition $\hat{\gamma}_0$ at the interface in response to (a) decreasing $\beta = 2, 0.2, 0.02$, and (b) increasing $d_S = 0.1, 0.5, \infty$. The magnetic field is imposed at an angle of $\phi = 45^\circ$ and the cyclotron time T is used for all series. 114
- 4.7 Effect of the magnetic field angle ϕ on the circulation deposition $\hat{\gamma}_0$. In (a), ϕ is increased from 0 to the left limit of 90° for finite $d_S = d_L = 0.1$. In (b), the non-uniform convergence of $\hat{\gamma}_0$ as $\phi \rightarrow 90^\circ$ is highlighted for $d_S = \infty$. $\mathcal{A} = 0.5$ is used throughout. 115
- 4.8 Normal velocity profile $w(x = 0, z, T)$ in the large d_S limit. Six time instances from $T = 0^+$, the initial impulse, to $T = 8$ are taken for a range of magnetic field angle: $\phi = 0$ (solid), $\phi = 30^\circ$ (dashed), $\phi = 60^\circ$ (dot-dashed) and $\phi \rightarrow 90^\circ$ (dotted). $\mathcal{A} = 0.5$ in all cases. . . 116
- 4.9 Two-dimensional contours of the normal velocity field $w(x, z, T)$ in the large d_S limit for an oblique magnetic field with $\phi = 45^\circ$, and a plasma Atwood number $\mathcal{A} = 0.5$. Two different color scales are assigned for $T = 1, 2, 4$ and $T = 6, 8, 12$, respectively. 117
- 4.10 Three-dimensional surfaces of the normal velocity field $w(x, z, t)$, as a function of time t , resulted from the MHD model [(b)–(c)] where $d_L = d_S = 0$ and the Hall-MHD model [(d)–(f)] where $d_L = d_S = 0.1$. Both systems share a common initial impulse given in (a), as well as an Atwood number of $\mathcal{A} = 0.5$. Results are shown over two wavelength, $x \in [-1, 1]$, to highlight the wave propagation along the magnetic field with $\phi = 45^\circ$ 118
- 4.11 Short term evolution of the post-shock vorticity field near the interface from the compressible simulation with $\phi = 4\pi/9$. Frame timestamps are non-dimensionalized by $\Lambda\sqrt{\rho_1^*/p_0^*}$ 119

- 4.12 Two-dimensional contours of the out-of-plane vorticity $\omega_y(x, z, T)$ in the $d_S = \infty$ limit for an oblique magnetic field with $\phi = 45^\circ$, and a plasma Atwood number $\mathcal{A} = 0.5$. The color scale is reset for each time instant ($T = 2, 4, 6, 8$) to show vorticity production as the flow evolves. 121
- 4.13 Evolution of the interface vortex strength ζ in (a) components and (b) vector form. Its time derivative ι is similarly given in in (c)-(d). Results are obtained at $x = \pi/4$ using a magnetic field angle $\phi = 0$ and plasma parameters $\mathcal{A} = 0.5, d_S = d_L = 1$ 122
- 6.1 (α, β) -curvilinear orthogonal coordinates system for geometrical shock dynamics. 132
- 7.1 (a) Local Cartesian coordinates fixed at a point on shock normal (x -direction) and tangential (y -direction) to the curve. Downstream velocity vectors and Mach numbers are shown at the origin and a differential nearby point at $(\delta x, \delta y)$, whose arclength is δs 138
- 8.1 Shock generated by a flat piston shown in (a), and a corrugated piston of perturbation amplitude ϵ shown in (b), at time $t = 0^+$. Both pistons share the same velocity U_p , giving a constant Mach number M_0 when the piston is flat. In (b) the Mach number profile is $M(\beta, 0^+)$. The flow between the piston and the shock is uniform in (a), but non-uniform with initial velocity u_0 , acceleration \dot{u}_0 , and jerk \ddot{u}_0 in (b). 156
- 8.2 Spontaneous development of curvature singularities illustrated using GGSD-0 with initial conditions $M_0 = 50$ and $\epsilon = 0.03$. The Mach number and shock shape perturbation profiles are given over four oscillation periods up to the critical time in (a) and (b), respectively. The shock slope and curvature distributions are shown as the critical time is approached with time increments of $\Delta\tau = 0.5$, in (c) and (d), respectively. 160
- 8.3 Shock trajectories with perturbation in the Y -direction amplified ten times for piston perturbation size $\epsilon = 0.05$. The initial piston Mach number is $M_0 = 1.1$ in (a)–(c) and $M_0 = 10$ in (d)–(f), corresponding to results obtained from the zeroth, first, and second order GGSD systems, respectively. In each panel, successive trajectories are shown in increments of $\Delta\tau = 2$, up to the final curve given at the critical time τ_c 162

- 8.4 History of Mach number perturbation profile m along the evolving shock, for $\epsilon = 0.05$ and $M_0 = 10$. Results obtained using three different orders of GGSD models are shown in (a)–(c). 163
- 8.5 Critical times in strong and weak shock limits given for (a) $M_0 = 10$, (b) $M_0 = 50$, (c) $M_0 = 1.1$ and (d) $M_0 = 1.02$. In all four cases, results obtained using GGSD-0 are shown as disks, GGSD-1 as squares and GGSD-2 as diamonds. In each panel, the dashed line without markers displays a reference function that has inverse power law of degree one. 164
- 8.6 Convergence of critical time as M_0 increases in the strong shock limit for $\epsilon = 0.02$ in (a), and as M_0 decreases in the weak shock limit for $\epsilon = 0.01$ in (b). Disks, squares, and diamonds correspond to GGSD-0, GGSD-1, and GGSD-2 data. 165
- 8.7 Temporal shock profile statistics comparison between the flat (hollow circles) and perturbed shock due to three GGSD systems (lines of different dashing), made for $M_0 = 50$ and $\epsilon = 0.02$. (a,b) Mean and standard deviation of the Mach number perturbation profile. (c) Average shock advancement in the unperturbed shock normal direction. (d) Standard deviation of the shock shape perturbation. . . 166
- 8.8 History of the non-uniformity measure Q_1 behind the evolving shock as a function of shock positions in two-dimensions. (a) and (b) compare results obtained for $M_0 = 50$ and $\epsilon = 0.02$, using GGSD-1 and GGSD-2, respectively. 168
- 8.9 (a) Percentage maximum distance lead of average shock position given by GGSD-1 (disks) and GGSD-2 (squares) over the reference flat shock. (b) Distance lead of average shock position at a fixed time that is the critical time for the second order method. In both cases, $M_0 = 50$, $\epsilon = 0.03$, and the dashed line represents the first order, while the solid line gives the second order method. The dashed line without markers in (b) shows an explicit function of quadratic power law. 169
- 8.10 Plane shock of constant Mach number M_0 traversing a density gradient of compact domain. (a) The peak perturbation line Y_p of amplitude ϵ_A is given by the solid line; and width of the perturbation field, 10σ , is bounded by the dashed lines. (b) 3D visualisation of the shock initial conditions drawn for $\epsilon_\rho = 0.1$, $\sigma = 1$ and $\epsilon_A = 0.5$. Here $\Delta\rho = \rho_0 - \bar{\rho}_0$ is colour coded. 170

- 8.11 Trajectories of an initially flat shock of $M_0 = 50$ traversing a color coded density gradient with $\epsilon_\rho = 0.1$, $\sigma = \epsilon_A = 0.5$. The shock shape perturbation z_1 is amplified 30 times in the Y -direction. A sequence of instances at $\tau = 0, 9, 10.5, 13, \dots, 48, 49.6$ is given. The dotted, dash-dotted, and solid lines correspond to GGSD-0, GGSD-1, and GGSD-2, respectively. 172
- 8.12 Critical time τ_c as a function of σ [in (a,b)], ϵ_ρ [in (c,d)] and ϵ_A [in (e,f)], for a strong shock of $M_0 = 50$. In each panel, the dashed line indicates a slope of negative one in log-log scale. 173
- 8.13 Critical time τ_c as a function of σ [in (a)], ϵ_ρ [in (b)] and ϵ_A [in (c)], for a weak shock of $M_0 = 1.1$. In each panel, the dashed line indicates a slope of negative one in log-log scale. 174

LIST OF TABLES

<i>Number</i>	<i>Page</i>
2.1 Non-zero coefficients of the dispersion equation (2.32) for an ideal two-fluid model.	27
2.2 Non-zero coefficients of the dispersion equation (2.66) for an 1FP model.	38
2.3 Various limits of the ideal two-fluid plasma equations.	51
4.1 Nonzero elements of matrix A_i specified for Eq. (4.25).	95
4.2 Components of the eigenvector \mathbf{v} corresponding to a given eigenvalue λ , as seen in Eq. (4.27). The matrix entries $a_{i,j}$ are specified in Table 4.1.	95
E.1 Constant coefficient functions in the GGSD systems, up to second order, in terms of the specific heat ratio γ	186
E.2 Constant coefficients for the second order partial derivatives of flow variables in the strong shock limit, found in Eqs. (F.15)–(F.18); and those for the initial value of Q_2 , found in Eq. (8.12), associated with shock driven by a corrugated piston. These coefficients are expressed in terms of other constant functions of γ listed in Table E.1.	187

Part I

The Equations of Plasma Physics and The Richtmyer-Meshkov Instability in Magnetohydrodynamics

Chapter 1

INTRODUCTION

The Richtmyer-Meshkov instability (RMI) refers to the growth of perturbations to an interface separating neutral fluids of different densities, typically due to a shock wave traversing through the interface. This shock-wave-density-interface interaction problem was first considered by Markstein [68], however the associated interface instability is named after the analytical and numerical analysis of Richtmyer [85], and the following shock tube experiments of Meshkov [71].

The RMI is pertinent to a wide range of science and engineering applications, including supernova explosion and stellar evolution models in astrophysics [4], shock-flame interactions in combustion systems [52], mixing phenomena in supersonic jet engines [110] and more as surveyed in the review of Brouillette [16]. Perhaps more importantly, a richer literature is motivated by the development of inertial confinement fusion (ICF), a technology with the potential to demonstrate highly efficient carbon-free energy production [37]. In ICF, a spherically converging shock is driven into a target capsule containing deuterium-tritium (DT) fuel, generating, in principle, a hot-spot at the center where fusion is initiated. Various indirect drive ICF ignition targets have been tested at the National Ignition Facility (NIF) [74], where the DT fuel target is placed inside a hohlraum, a hollow cylindrical chamber made of a gold alloy. A system of immensely powerful laser beams is focused on the hohlraum, causing intense X-ray radiation onto the target capsule, that is fabricated with a beryllium or plastic outer shell (ablator), and a cocktail of elements in the shell's interior. The ignition point design used in the NIF experiments is shown in Figure 1.1. However, the presence of hydrodynamic instabilities, including Rayleigh-Taylor instability (RTI) and RMI, disrupt the smooth, symmetric implosions essential to reach the ignition conditions, and give rise to mixing between the capsule material and the fuel within, compromising the chance of achieving energy break-even or production [59, 84, 94]. These instabilities, as illustrated in Figure 1.2, are identified as a key area of research to improve the performance of ignition in the review of the National Ignition Campaign, which ended in 2013 [58]. Converging shock-driven RMI in both gases [5, 46, 53, 62, 63, 72] and solids [64, 65] has therefore received attention. Moreover, the high temperatures associated with ICF implosion inevitably causes rapid ionization of the involved

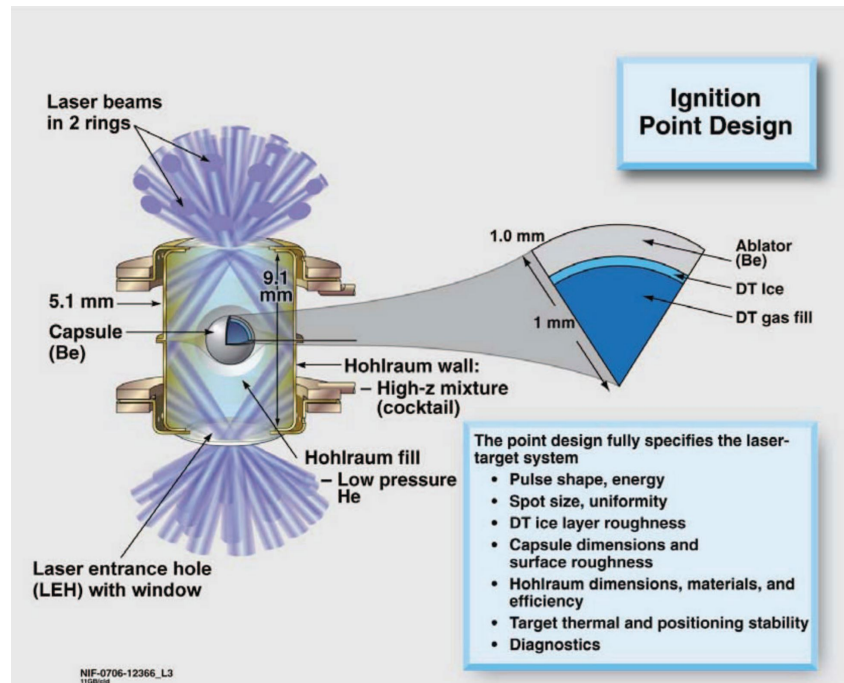


Figure 1.1: A schematic cutaway view of a NIF target, showing the various layers of ablator, the frozen DT shell, and the gaseous DT interior. Image reproduced from Moses *et al.* [74]

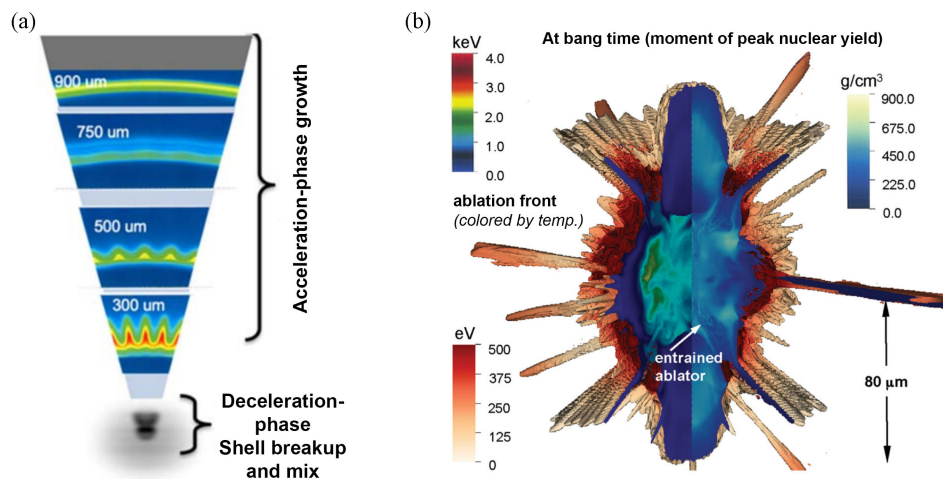


Figure 1.2: (a) Simulation schematically showing the growth of a preimposed ripple in density from a capsule radius of 900–300 μm at the ablation front. Image reproduced from Smalyuk *et al.* [94]. (b) 3D implosion simulation of a NIF capsule at bang time. The outer surface shows the ablation front and is colored by the electron temperature with the color scale on the lower left. The left half shows the ion temperature with the color scale on the upper left, and the right half shows the density with the color scale on the right. Image reproduced from Clark *et al.* [20].

materials, which then leads to interaction between the conducting fluids and magnetic fields that are imposed or self-generated [12, 49, 67, 90]. The OMEGA laser experiments by Hohenberger *et al.* [44] exploited this by immersing ICF targets in a near-uniform seed magnetic field before implosion, leading to enhanced compression and electron confinement. As a result, significant increase of ion temperature and neutron yield from the implosion was observed. In addition, two-dimensional radiation-hydrodynamics simulations by Perkins *et al.* [83] show that uniform seed magnetic fields increase the robustness of ICF implosions to the outer perturbation amplitude.

Several theoretical descriptions have been proposed in order to model the coupled evolution of plasmas and magnetic fields that naturally arise in astrophysical phenomena and ICF applications. One framework is the single-fluid ideal magnetohydrodynamic (MHD) system, where it is demonstrated that the growth of the RMI is suppressed in the presence of an initially uniform magnetic field either normal [5, 87, 104, 105] or tangential [17, 107] to the interface. The cylindrically and spherically converging MHD RMI is also suppressed under a range of seed magnetic field configurations, as investigated numerically by Mostert *et al.* [75, 76]. In the cylindrical geometry, it is shown that while the suppression occurs along the entire density interface, its extent and the behavior of the interface are highly dependent on the local orientation of the magnetic field. Away from the ideal MHD region, where the ion cyclotron effect is significant, Srinivasan & Tang [96] adopted the Hall-MHD model to examine the magnetic field generation and growth for the gravity induced RTI. Shen *et al.* [92, 93] employed incompressible Hall-MHD models to study the impulse-driven RMI under an arbitrarily oriented initial magnetic field. The suppression of the RMI is again established, although the vorticity transport mechanism responsible for such suppression differs markedly from that of the ideal MHD system. Using a more general two-fluid plasma model, Bond *et al.* [12] investigated computationally the planar shock-driven RMI for an initially unmagnetized plasma and observed self-generated magnetic fields. The following study for a magnetized plasma subject to a background magnetic field normal to the mean interface finds suppression of the interface perturbation growth with effectiveness determined by plasma length scale [13].

By truncating moments of the Vlasov-Boltzmann equation from classic kinetic theory, the various widely used plasma models surveyed above can be viewed as averaged continuum descriptions of ionized gases with different levels of re-

tained ion-electron species properties. Among these continuum models, in order of decreasing complexity, Shen *et al.* [91] showed that the ideal two-fluid plasma equations, the Hall-MHD and regular MHD models are connected via a series of limiting processes with respect to the appropriately scaled parameters including the speed-of-light, the ion skin depth, and ion-to-electron mass ratio.

In the remainder of this introductory chapter, Section 1.1 references the plasma kinetic theory from which the two-fluid equations are derived; Section 1.2 gives a hydrodynamic origin of the RMI; Section 1.3 summarizes the prerequisite results of the RMI suppression mechanism in MHD; and Section 1.4 presents the key numerical findings of RMI in a two-fluid plasma. These sections lay a theoretical foundation underpinning the first part of the present thesis. The outline of thesis Part I is given in Section 1.5.

1.1 Plasma kinetic theory and ideal fluid equations

In this section we introduce the ideal two-fluid plasma and MHD models from a kinetic perspective using the Vlasov-Boltzman equation. The derivations given by Goedbloed & Poetds [38] and Bellan [9] are summarized in the following.

1.1.1 Vlasov-Boltzmann equation

We consider a fully ionized plasma consisting of two species of charged particles, denoted using subscript $\alpha \in \{i, e\}$, for ion and electron of charge q_α . For each particle, its instantaneous position \mathbf{x} and velocity \mathbf{v} are prescribed as independent variable functions of time t , forming a six-dimensional phase space. We then hypothesize a probability distribution function, $f_\alpha(\mathbf{x}, \mathbf{v}, t)$, for each species, such that at time t , the number of particles of the same species found within the differential volume $d\mathbf{x}d\mathbf{v}$ centered around (\mathbf{x}, \mathbf{v}) in the phase space is given by

$$dN_\alpha(\mathbf{x}, \mathbf{v}, t) = f_\alpha(\mathbf{x}, \mathbf{v}, t)d\mathbf{x}d\mathbf{v}. \quad (1.1)$$

Therefore integrating f_α over all possible velocity vectors immediately gives the species number density n_α ,

$$n_\alpha(\mathbf{x}, t) = \int f_\alpha(\mathbf{x}, \mathbf{v}, t)d\mathbf{v}, \quad (1.2)$$

which is related to the mass density ρ_α simply via the particle mass m_α as

$$\rho_\alpha(\mathbf{x}, t) = m_\alpha n_\alpha(\mathbf{x}, t). \quad (1.3)$$

Equation (1.1) also provides a probabilistic meaning of species average velocity \mathbf{u}_α calculated as the expectation of the random variable \mathbf{v} , denoted as $\langle \mathbf{v} \rangle_\alpha$,

$$\mathbf{u}_\alpha(\mathbf{x}, t) = \langle \mathbf{v} \rangle_\alpha = \frac{1}{n_\alpha(\mathbf{x}, t)} \int \mathbf{v} f_\alpha(\mathbf{x}, \mathbf{v}, t) d\mathbf{v}. \quad (1.4)$$

The charge density τ and current density \mathbf{j} then follow by accounting for the particle charges,

$$\tau(\mathbf{x}, t) = \sum_\alpha q_\alpha n_\alpha(\mathbf{x}, t), \quad \mathbf{j}(\mathbf{x}, t) = \sum_\alpha q_\alpha n_\alpha(\mathbf{x}, t) \mathbf{u}_\alpha(\mathbf{x}, t). \quad (1.5)$$

Similarly, an average stress tensor \mathbf{P}_α can be defined by taking the second moment,

$$\mathbf{P}_\alpha(\mathbf{x}, t) = m_\alpha \int (\mathbf{v} - \mathbf{u}_\alpha) \otimes (\mathbf{v} - \mathbf{u}_\alpha) f_\alpha(\mathbf{x}, \mathbf{v}, t) d\mathbf{v}. \quad (1.6)$$

In the case of f_α being isotropic, a scalar pressure p_α can then be defined from the trace of \mathbf{P} , yielding

$$p_\alpha(\mathbf{x}, t) = \frac{\text{tr}(\mathbf{P}_\alpha)}{3} = \frac{m_\alpha}{3} \int |\mathbf{v} - \mathbf{u}_\alpha|^2 f_\alpha(\mathbf{x}, \mathbf{v}, t) d\mathbf{v} = \frac{1}{3} \rho_\alpha \langle |\mathbf{v} - \mathbf{u}_\alpha|^2 \rangle_\alpha. \quad (1.7)$$

It is noted that Eq. (1.7) also gives a measure of the mean kinetic energy of the particles in a moving frame of velocity \mathbf{u}_α , which defines the species temperature T_α ,

$$T_\alpha = \frac{m_\alpha}{3k} \langle |\mathbf{v} - \mathbf{u}_\alpha|^2 \rangle_\alpha, \quad (1.8)$$

where k is the Boltzmann constant. Therefore it follows that p_α and T_α are related through the ideal gas law,

$$p_\alpha = n_\alpha k T_\alpha. \quad (1.9)$$

The evolution of the distribution function f_α is governed by the Vlasov-Boltzmann equation, which can be understood as the total derivative of f_α following a particle trajectory, given by

$$\frac{d}{dt} f_\alpha(\mathbf{x}(t), \mathbf{v}(t), t) = \frac{\partial f_\alpha}{\partial t} + \mathbf{v} \cdot \frac{\partial f_\alpha}{\partial \mathbf{x}} + \mathbf{a} \cdot \frac{\partial f_\alpha}{\partial \mathbf{v}} = C_\alpha. \quad (1.10)$$

Here, $\mathbf{a} \equiv d\mathbf{v}/dt$ is the particle acceleration determined by the Lorentz force, $\mathbf{F} = q_\alpha(\mathbf{E} + \mathbf{v} \times \mathbf{B})$, that is the sum of electric and magnetic force experienced by a moving particle of velocity \mathbf{v} due to local electric field $\mathbf{E}(\mathbf{x}, t)$, and magnetic field $\mathbf{B}(\mathbf{x}, t)$. Therefore Newton's law gives

$$\mathbf{a} = \frac{q_\alpha}{m_\alpha} (\mathbf{E} + \mathbf{v} \times \mathbf{B}). \quad (1.11)$$

C_α is the rate of change of the distribution function due to short-range binary particle collisions. Closure for determining f_α , \mathbf{E} and \mathbf{B} is achieved by including the Maxwell equations,

$$\begin{aligned}\nabla \times \mathbf{E} &= -\frac{\partial \mathbf{B}}{\partial t}, & \nabla \times \mathbf{B} &= \mu_0 \mathbf{j} + \frac{1}{c^2} \frac{\partial \mathbf{E}}{\partial t}, \\ \nabla \cdot \mathbf{E} &= \frac{\tau}{\epsilon_0}, & \nabla \cdot \mathbf{B} &= 0,\end{aligned}\tag{1.12}$$

where μ_0 is the free space permeability, ϵ_0 is the vacuum permittivity, and $c = (\mu_0 \epsilon_0)^{-1/2}$ is the speed of light.

One important steady state solution to (1.10) is the Maxwell distribution given by

$$f_\alpha^0(\mathbf{x}, \mathbf{v}, t) = n_\alpha \left(\frac{m_\alpha}{2\pi k T_\alpha} \right)^{3/2} \exp\left(-\frac{m_\alpha |\mathbf{v} - \mathbf{u}_\alpha|^2}{2k T_\alpha}\right),\tag{1.13}$$

which represents species local thermal equilibrium. Indeed, substituting (1.13) into (1.7) verifies the ideal gas law.

1.1.2 Ideal two-fluid equations

To proceed, we concentrate on ideal plasma where the pressure tensor seen in (1.6) is isotropic, and the collision effects are further neglected by setting $C_\alpha = 0$ in the Vlasov-Boltzmann equation (1.10). Essentially, thermal equilibrium given by (1.13) is assumed for both species. The validity of these assumptions will be briefly discussed in Chapter 2. More details are found in Goedbloed & Poedts [38].

Dynamic equations for species macroscopic quantities n_α , \mathbf{u}_α and T_α are obtained by taking moments of (1.10). Specifically, the zeroth moment computed by integrating (1.10) over velocity space gives the continuity equation,

$$\frac{\partial n_\alpha}{\partial t} + \nabla \cdot (n_\alpha \mathbf{u}_\alpha) = 0.\tag{1.14}$$

The first moment, obtained by multiplying (1.10) with $m_\alpha \mathbf{v}$ and integrating over velocities produces the momentum equation,

$$\frac{\partial}{\partial t}(\rho_\alpha \mathbf{u}_\alpha) + \nabla \cdot (\rho_\alpha \langle \mathbf{v} \mathbf{v} \rangle_\alpha) - n_\alpha q_\alpha (\mathbf{E} + \mathbf{u}_\alpha \times \mathbf{B}) = 0,\tag{1.15}$$

which can be simplified using (1.6), (1.7) and (1.14) to give

$$\rho_\alpha \left(\frac{\partial \mathbf{u}_\alpha}{\partial t} + \mathbf{u}_\alpha \cdot \nabla \mathbf{u}_\alpha \right) + \nabla p_\alpha - n_\alpha q_\alpha (\mathbf{E} + \mathbf{u}_\alpha \times \mathbf{B}) = 0.\tag{1.16}$$

Similarly the scalar second moment that follows from multiplying (1.10) with $m_\alpha v^2/2$ before integrating over velocities yields the energy equation,

$$\frac{\partial}{\partial t} \left(\frac{\rho_\alpha \langle v^2 \rangle_\alpha}{2} \right) + \nabla \cdot \left(\frac{\rho_\alpha \langle v^2 \mathbf{v} \rangle_\alpha}{2} \right) - q_\alpha n_\alpha \mathbf{E} \cdot \mathbf{u}_\alpha = 0, \quad (1.17)$$

which simplifies using (1.7) and (1.9) as

$$\frac{3kn_\alpha}{2} \left(\frac{\partial T_\alpha}{\partial t} + \mathbf{u}_\alpha \cdot \nabla T_\alpha \right) + p \nabla \cdot \mathbf{u}_\alpha + \nabla \cdot \mathbf{h}_\alpha = 0, \quad (1.18)$$

where

$$\mathbf{h}_\alpha = \frac{\rho_\alpha}{2} \langle |\mathbf{v} - \mathbf{u}_\alpha|^2 (\mathbf{v} - \mathbf{u}_\alpha) \rangle_\alpha, \quad (1.19)$$

is the heat flux vector, often modeled by the Fourier law $\mathbf{h}_\alpha \sim \kappa_\alpha \nabla(kT_\alpha)$, where κ_α is the heat conductivity. Again, for ideal plasma whose heat conductivity is negligible, $\mathbf{h}_\alpha = 0$ is assumed. As a result, (1.18) can be rewritten in terms of pressure p_α by substituting the specific heat ratio γ into (1.9), giving

$$\frac{\partial p_\alpha}{\partial t} + \mathbf{u}_\alpha \cdot \nabla p_\alpha + \gamma p_\alpha \nabla \cdot \mathbf{u}_\alpha = 0. \quad (1.20)$$

Together with the Maxwell equations (1.12), Eqs. (1.14), (1.16) and (1.20) constitute the ideal two-fluid plasma equations.

1.1.3 Ideal magnetohydrodynamics

Unlike the two-fluid theory, the magnetohydrodynamic (MHD) equations were originally posed as reasonable postulates for a hypothetical medium that behaves like a perfectly conducting fluid interacting with a magnetic field [38]. However, for its relative simplicity and robustness, the MHD model is far more ubiquitous in the literature. The complete set of ideal MHD equations is as follows:

$$\begin{aligned} \frac{\partial \rho}{\partial t} + \nabla \cdot (\rho \mathbf{U}) &= 0, \\ \rho \left(\frac{\partial \mathbf{U}}{\partial t} + \mathbf{U} \cdot \nabla \mathbf{U} \right) &= -\nabla p + \mathbf{j} \times \mathbf{B}, \\ \frac{\partial p}{\partial t} + \mathbf{U} \cdot \nabla p + \gamma p \nabla \cdot \mathbf{U} &= 0, \\ \mathbf{E} + \mathbf{U} \times \mathbf{B} &= 0, \\ \frac{\partial \mathbf{B}}{\partial t} + \nabla \times \mathbf{E} &= 0, \quad \nabla \cdot \mathbf{B} = 0, \end{aligned} \quad (1.21)$$

where ρ , p , and \mathbf{U} are not associated different species, but rather describe the bulk flow. From a two-fluid perspective, they are

$$\rho = \sum_\alpha m_\alpha n_\alpha, \quad p = \sum_\alpha p_\alpha, \quad \mathbf{U} = \frac{1}{\rho} \sum_\alpha m_\alpha n_\alpha \mathbf{u}_\alpha. \quad (1.22)$$

A rigorous derivation of Eqs. (1.21) using the ideal two-fluid theory will be given in Chapter 2.

1.2 Hydrodynamic RMI

Here we discuss the mechanism that drives the Richtmyer-Meshkov instability in non-conducting hydrodynamics, where the shock-interface interaction is considered.

The shock traversing the perturbed density interface results in a misalignment between the pressure gradient ∇p across the shock and the density gradient $\nabla \rho$ across the material interface, generating baroclinic vorticity along the interface. In hydrodynamics, this can be seen from the inviscid vorticity equation,

$$\frac{\partial \boldsymbol{\omega}}{\partial t} + (\mathbf{u} \cdot \nabla) \boldsymbol{\omega} = (\boldsymbol{\omega} \cdot \nabla) \mathbf{u} - \boldsymbol{\omega} (\nabla \cdot \mathbf{u}) + \frac{\nabla \rho \times \nabla p}{\rho^2}, \quad (1.23)$$

where \mathbf{u} is the Eulerian flow velocity and $\boldsymbol{\omega} = \nabla \times \mathbf{u}$ is the vorticity. The last term in (1.23), known as the baroclinic torque, shows the production of vorticity when $\nabla \rho \times \nabla p \neq 0$. This may be intuited in general as fluids across different density contours being accelerated unequally by the local pressure gradient. Therefore, the passage of shock deposits circulation, $\Gamma = \oint \boldsymbol{\omega} \cdot d\mathbf{A}$, on the interface, leading to the interfacial perturbation growth. The process of shock-interface interaction is illustrated in Figure 1.3.

To model the interface perturbation growth, Richtmyer [85] proposed a linear incompressible inviscid flow theory for a single sinusoidal mode perturbation on a contact discontinuity (CD) between two incompressible fluids of densities ρ_1 and ρ_2 , subject to an impulsive acceleration. From the impulse model, the perturbation amplitude η grows at the rate,

$$\frac{d\eta}{dt} = kV\eta_0\mathcal{A}, \quad (1.24)$$

where k is the perturbation wavenumber, V is the velocity imparted to the interface with the incident shock, η_0 is the initial perturbation amplitude, and $\mathcal{A} = (\rho_2 - \rho_1)/(\rho_2 + \rho_1)$ is the Atwood number. The linear growth given by (1.24) is valid immediately after the shock passage, provided that $k\eta_0 \ll 1$. As the perturbation amplitude increases, the Kelvin-Helmholtz instability (KHI) appears as a secondary instability, and spikes of the heavy fluid penetrate into the lighter fluid, as shown in Figure 1.3(d). Smaller scale perturbations also develop at later times, eventually leading to a turbulent mixing zone between the two fluids.

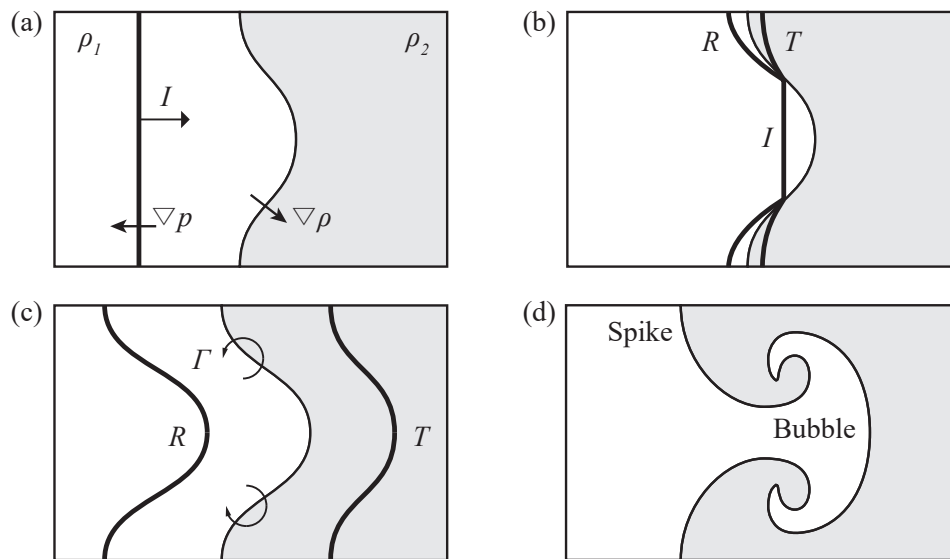


Figure 1.3: Illustration of shock-interface interaction and RMI. (a) Perturbed density interface and incident shock I . (b) Shock passage with reflected shock R and transmitted shock T . (c) Circulation deposition. (d) Instability rolling up into characteristic mushroom-shape.

1.3 Magnetohydrodynamic RMI

Numerically simulating the the RM type shock-interface interaction problem using the ideal MHD equations, Samtaney [87] first demonstrated that the presence of an external magnetic field suppresses the instability. In this study, the incident shock and the CD, both planar, form an oblique angle, while if present, the background magnetic field aligns with the shock normal direction. The effect of the applied magnetic field is shown in the comparison of Figure 1.4 against the case without the background field. While the baroclinic vorticity generation remains the same regardless of whether an external field is applied, the presence of a magnetic field enables vorticity transport away from the contact surface by MHD shocks, preventing the local formation of KHI along the interface.

Wheatley *et al.* [104] theoretically investigated the vorticity transport mechanism in ideal MHD using the impulse model, for an external magnetic field normal to the mean interface. It was identified that once baroclinically generated, vorticity propagates away from the interface at the speeds of local Alfvén waves. As a result, the amplitude of the interface perturbation plateaus asymptotically in time, giving

$$\eta_{\infty} = \lim_{t \rightarrow \infty} \eta(t) = \eta_0 \left[1 + V \left(\frac{1}{C_{A2}} - \frac{1}{C_{A1}} \right) \right], \quad (1.25)$$

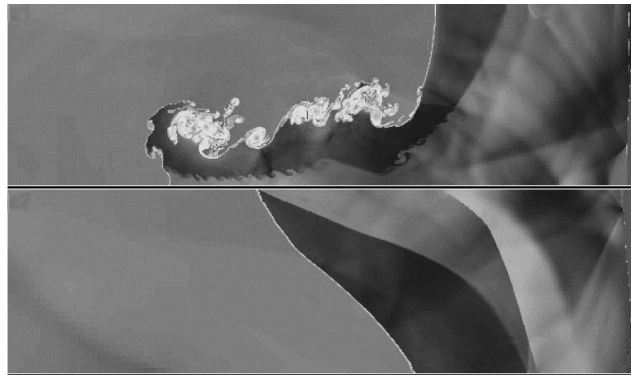


Figure 1.4: Density field from the Richtmyer-Meshkov simulations of Samtaney [87], after the incident shock passage. The external magnetic field is turned off and on in the top and bottom images respectively. The transmitted shock is located near the right edge of each image.

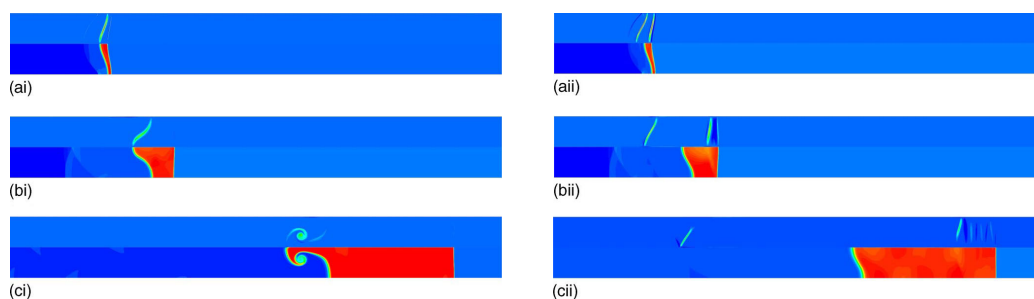


Figure 1.5: Vorticity (top) and density (bottom) fields in each panel, from compressible MHD simulations using $M = 2$, $\gamma = 5/3$, $\rho_2/\rho_1 = 3$, $\eta_0 k = 0.2\pi$, and $B = 0$ in (i), $\beta = 2p_0/B^2 = 1$ in (ii), at three different times in (a)–(c). Image reproduced from Wheatley *et al.* [105].

where C_{A_2} and C_{A_1} are Alfvén speeds given by

$$C_{A_i} = \frac{B}{\sqrt{\mu_0 \rho_i}}, \quad i = 1, 2. \quad (1.26)$$

And thus increasing the magnetic field strength with $B \in [0, \infty)$ inversely reduces the final interface amplitude from $\eta_\infty = \infty$, as in the hydrodynamic case, to $\eta_\infty = \eta_0$, where the RMI is completely suppressed.

Later, the corresponding compressible MHD flow simulations by Wheatley *et al.* [105] confirm the instability suppression mechanism predicted by the incompressible theory, by visualizing the evolution of vorticity and density fields in Figure 1.5, where results obtained with and without a magnetic field are compared.

Analysis was also extended to the case where the background magnetic field is parallel to the perturbed interface by Cao *et al.* [17] and the mean interface by

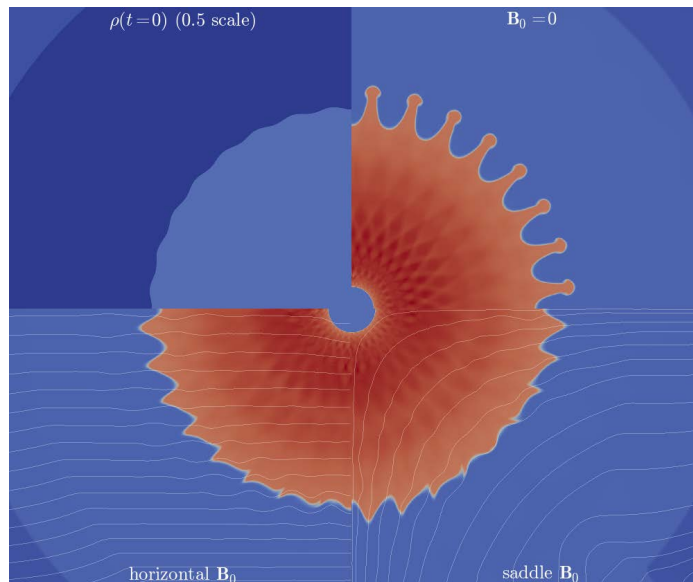


Figure 1.6: Density fields from cylindrically converging MHD RMI simulations with $B_0 = 0$ and horizontal and saddle geometry initial magnetic fields. Magnetic field lines are overlaid where relevant. A portion of the initial density field is also shown. Image generated from the simulations of Mostert *et al.* [76].

Wheatley *et al.* [107]. The RMI suppression was again observed in these cases, however undertaking a different vorticity transport process: circulation distribution present on the interface immediately after the shock acceleration breaks up into waves traveling parallel and anti-parallel to the magnetic field. The effect of magnetic fields of varying orientation in MHD with cylindrical and spherical geometries is particularly important to ICF implosions, and this was numerically investigated by Mostert *et al.* [75, 76]. Figure 1.6 shows the suppression of the cylindrically converging MHD RMI in the presence of magnetic fields of strength B_0 of with two different configurations, at a time after the perturbed cylindrical density interface has interacted with an imploding shock, just prior to the transmitted shock converging on the origin. It can be seen that while the RMI is suppressed along the entire density interface, the extent of that suppression and the behaviour of the interface is highly dependent on the local orientation of the magnetic field.

1.4 Two-fluid plasma RMI

More recently, the two-fluid plasma model has been adopted by Bond *et al.* [12] to account for plasma length scales that are not accessible in ideal MHD. These include the Debye length d_D which measures the distance across the ion's electrostatic field shielded by the electrons, and the Larmor radius d_L which is the orbiting radius of

charged particles around a magnetic line. Significant charge separation was observed in an initially unmagnetized plasma with a perturbed thermal density discontinuity, driven by a precursor electron shock that impacts the density interface ahead of the ion shock. The resulting self-generated electromagnetic fields causes the electron shock to degenerate and periodically accelerate the electron and ion interfaces, substantially increasing the interfacial growth over the hydrodynamic case. The distinct ion and electron evolution is illustrated in Figure 1.7, showcasing the small scale secondary instabilities particularly prominent along the electron interface.

In their numerical study for a magnetized two-fluid plasma, Bond *et al.* [13] found suppression of the RMI increases effectiveness as plasma length scale is decreased. Stabilization is attributed to the magnetic field's contribution to the Lorentz force. This acts to rotate the vorticity vector in each fluid about the local magnetic field vector leading to cyclic inversion and transport of the out-of-plane vorticity that drives perturbation growth, as shown in Figure 1.8.

1.5 Part I outline

The rest of thesis Part I is organized in the form of a series of publications that further the topics introduced in Chapter 1. The outline is given as follows.

In Chapter 2—*Magnetohydrodynamic limits of the ideal two-fluid plasma equations*, we derive five simplified plasma models, including the widely used Hall-MHD and regular MHD systems, as formal limits of the nondimensional ideal two-fluid plasma equations. This is achieved through a sequence of asymptotic expansions, in terms of small parameters related to the speed-of-light, the ion-to-electron mass ratio, and the ion skin depth. The dispersion relation of the linear wave systems that each of the reduced plasma model admits are computed to demonstrate the different model properties.

In Chapter 3—*Impulse-driven RMI in Hall-MHD*, we utilize the incompressible, Hall-MHD model to investigate the effect of Hall current on the stability of an impulsively accelerated, perturbed density interface, separating two fluids in the presence of a background magnetic field normal to the mean interface. This is used as a simple model, in a conducting fluid, of a RM type flow. The solution to the corresponding linearized initial-value problem shows that the presence of the magnetic field suppresses the incipient RMI, through oscillatory motions of the interface due to the ion cyclotron effect. The vorticity dynamics that facilitates the instability suppression are discussed.

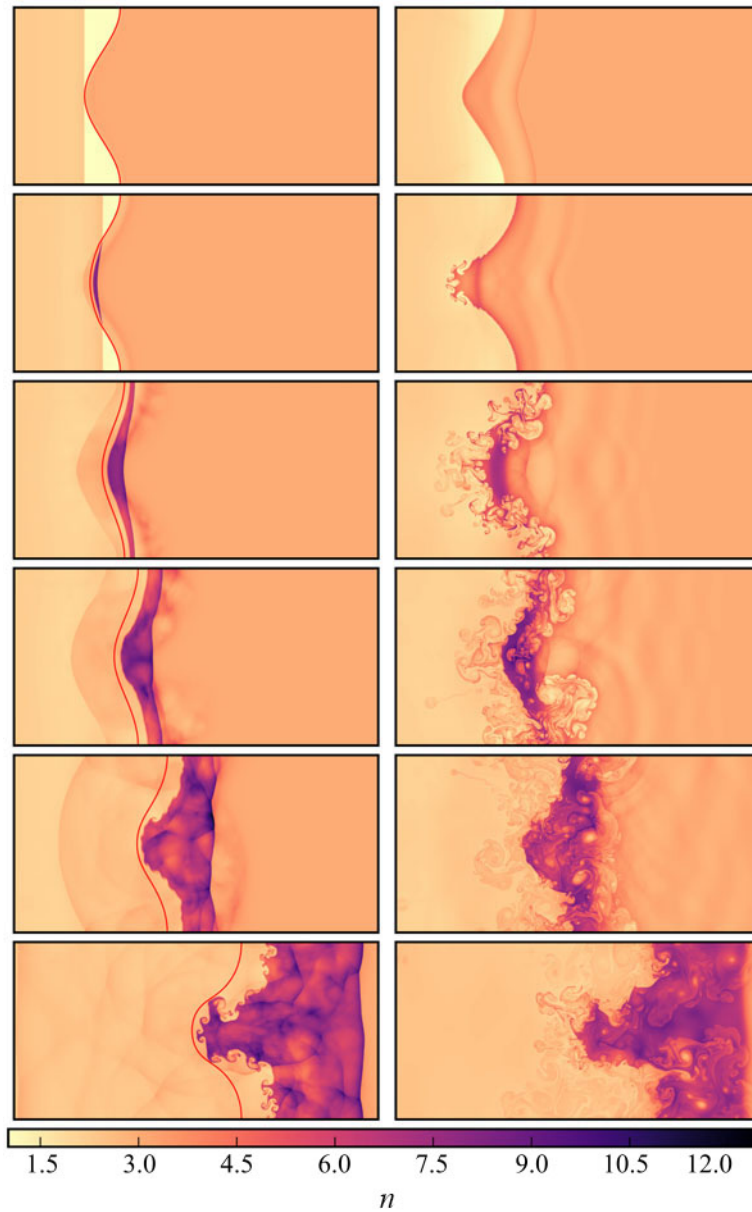


Figure 1.7: Evolution of ion (left) and electron (right) number density fields with $d_L = d_D = 0.1$ (nondimensional). Hydrodynamic interface location is overlaid on ion plots. Image reproduced from Bond *et al.* [12].

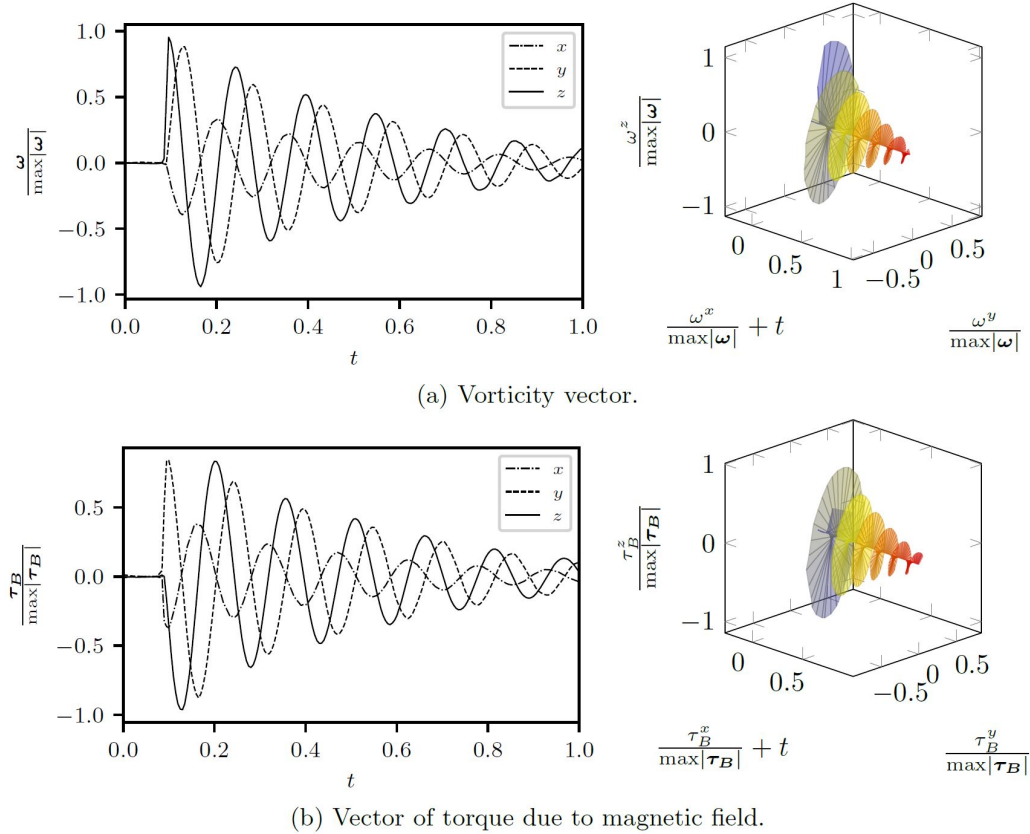


Figure 1.8: Rotation of ion vorticity and torque due to the magnetic field sampled at a point fixed to the interface approximately midway between the bubble and spike. Image reproduced from Bond *et al.* [13].

In Chapter 4—*Hall-MHD RMI under an arbitrarily oriented magnetic field*, we study the effect of an initially uniform magnetic field of arbitrary orientation on the RMI in Hall-MHD and ideal MHD. Attention is restricted to the case where the initial density interface has a single-mode sinusoidal perturbation in amplitude and is accelerated by a shock traveling perpendicular to the interface. The incompressible impulsive Hall-MHD flow is determined by extending the formulation of Chapter 3. The ideal MHD theory naturally follows by taking the limit of vanishing ion skin depth. It is found that the RMI suppression is most effective for near tangential fields but becomes less effective with increasing plasma length scales. The linear model is validated using the corresponding shock-driven nonlinear compressible simulations in ideal MHD.

In Chapter 5—*Conclusions*, the main findings of thesis Part I are summarized.

MAGNETOHYDRODYNAMIC LIMITS OF THE IDEAL TWO-FLUID PLASMA EQUATIONS

This chapter is based on the following journal article:

Naijian Shen, Yuan Li, D. I. Pullin, Ravi Samtaney, and Vincent Wheatley. On the magnetohydrodynamic limits of the ideal two-fluid plasma equations. *Physics of Plasmas*, 25(12):122113, 2018. doi: 10.1063/1.5067387.

Here, we derive five simplified plasma models, including the widely used Hall-MHD and regular MHD systems, as formal limits of the nondimensional ideal two-fluid plasma equations. This is achieved through a sequence of asymptotic expansions, in terms of small parameters related to the speed-of-light, the ion-to-electron mass ratio, and the ion skin depth. The dispersion relation of the linear wave systems that each of the reduced plasma model admits are computed to demonstrate the different model properties.

2.1 Introduction

Starting with the Vlasov-Boltzmann equation in classic kinetic theory where a Maxwellian velocity distribution function is assumed, the two-fluid equations for a plasma emerge from truncating the moment series [6, 14, 19]. Closure for such a five moment system is obtained provided that the hydrodynamic time scale of interest, τ_H , is much slower than the thermal relaxation time scales, $\tau_{e,i}$, for both electrons and ions in a two-fluid plasma. That is, $\tau_{e,i} \ll \tau_H$, for a fluidic description for the plasma to be applicable. For a plasma with singly charged ion and equal species temperatures, explicit estimates for these relaxation times are found as [38],

$$\tau_e = 6\pi\sqrt{2\pi}\epsilon_0^2 \frac{m_e^{1/2}(k_B T)^{3/2}}{\ln \Lambda e^4 n_e}, \quad \tau_i = 6\pi\sqrt{2\pi}\epsilon_0^2 \frac{m_i^{1/2}(k_B T)^{3/2}}{\ln \Lambda e^4 n_i}, \quad (2.1)$$

where $m_{e,i}$ is the electron, ion mass; e the electron charge, n_i the ion number density, T the temperature, k_B the Boltzmann constant, ϵ_0 the vacuum permittivity and $\ln \Lambda$ the Coulomb logarithm which evaluates to be of order $O(10)$ in most of plasmas. The two-fluid plasma model, henceforth denoted as 2FP, is particularly relevant when the characteristic length scale is comparable to the ion skin depth and the characteristic time scale is comparable to the ion cyclotron period [95].

Under mild restrictions, a wide range of plasma applications can be suitably described by the ideal 2FP equations, where dissipative effects are neglected. The validity of such a simplification requires expressions for the transport coefficients derived from the Chapman-Enskog expansion [6] where distribution functions deviating from local thermal equilibrium, are expanded in powers of small parameters $\epsilon_{e,i} = \tau_{e,i}/\tau_H \ll 1$. Goedbloed & Poedts [38] summarizes that viscosity and thermal conductivity can be neglected if the dissipative diffusion occurs at time scales sufficiently large compared to τ_H , which is generally satisfied over macroscopic geometries. The ideal 2FP model is valid for τ_H smaller than the diffusion or dissipation time scale τ_D , *i.e.*, $\tau_H \ll \tau_D$. Ion diffusion processes appear in two flavors: one is parallel to the magnetic field lines $\tau_{D,\parallel,i} \propto (v_{th,i}^2 \tau_i)^{-1}$, where $v_{th,i}$ is the ion thermal speed, and the other is perpendicular to field lines is $\tau_{D,\perp,i} \propto \tau_{D,\parallel,i} (\Omega_i \tau_i)^2$, where Ω_i is the ion cyclotron frequency. For most systems of interest, both parallel and perpendicular diffusion time scales are generally much larger than τ_H [38].

Resistivity, due to ion-electron momentum transfer, gives a time scale, τ_R , which can be estimated as

$$\tau_R = \left(\frac{a}{\delta_e} \right)^2 \tau_e, \quad (2.2)$$

where a is a scale associated with the plasma system size and δ_e is the electron skin depth. Generally, resistivity is negligible if $\tau_H \ll \tau_R$ [38].

Lastly, heat flux due to interspecies collisions is considered small so long as τ_H differs significantly from the overall, longest thermal equilibration time, τ_{eq} , which scales as $\tau_{eq} \sim \sqrt{M} \tau_i \sim M \tau_e$, with $M \equiv m_i/m_e \gg 1$, assuming Eq. (2.1) holds. It is also noted that the large M assumption is essential in obtaining these time scale estimates from the Landau collision integral. Thus the ideal 2FP model considers each species to be in its own kinetic-collisional equilibrium, but not necessarily with the same temperatures, with the ion and electron temperatures equilibrating over the time scale τ_{eq} . Later on, we will show that the large $M \gg 1$ assumption is not essential in obtaining the single fluid MHD equations. Considering that above we stated that the ideal 2FP model is derived under $M \gg 1$ we may have an apparent contradiction. However, this is resolved easily because the heat flux due to interspecies collision can also be neglected for the hydrodynamic time scale exceeding τ_{eq} , and here we have an equilibration of ion and electron temperatures and the ideal 2FP system of equations is still valid. Hence, for such cases of interest $\tau_H \gg \tau_{eq}$, the requirement of $M \gg 1$ may be relaxed.

Although less general, reduced plasma models such as the Hall-MHD and ideal MHD equations are more popular than the 2FP description for modeling low frequency processes owing to their relative simplicity. When approached from the kinetic theory or the 2FP equations the foundation basis underlying these reduced systems often relies on tailored physical approximations. For example, it is commonly believed that in order to obtain the MHD equations one needs a series of independent assumptions including large speed-of-light, charge neutrality, large ion-to-electron mass ratio, and small Larmor radius [39]. Similarly the Hall-MHD model is obtained by relaxing specific constraints on the generalized Ohm's law posed in MHD [9]. An analytically consistent treatment bridging the two-fluid system with the various MHD formulations appears to have received little attention.

This chapter is intended to provide a mathematically firm derivation of various limiting forms of the ideal 2FP equations, including both the Hall-MHD and MHD equations, by taking a sequence of formal asymptotic limits with respect to suitably defined dimensionless parameters, namely, large speed-of-light, c , large ion-electron mass ratio M , small plasma skin depth, d_S and finite plasma parameter β . The associated homogeneous dispersion relation for each derived limiting system is also calculated analytically and compared with existing results where applicable [38, 42, 80, 95]. Asymptotic analysis for extreme values of the frequency and wave number is performed in order to provide physical insight into the appropriate wave-propagation physics. Conveniently, none of the aforementioned conditions for the ideal fluids assumption is violated in the limiting processes because a large relative speed-of-light would drive a slow hydrodynamic process to ensure $\epsilon_{e,i} \ll 1$. Further, it can be shown from Eq. (2.2) that if d_S is defined using mass m_i , then $\tau_R \sim M/d_S^2 \tau_e$, so that both large mass ratio and small skin depth would imply a long resistance delay time to guarantee $\tau_H \ll \tau_R$.

The remainder of the chapter is structured as follows. Section 2.2 introduces the non-dimensional ideal two-fluid plasma equations written in the center-of-mass frame and studies its dispersion relation. Sections 2.3, 2.4 and 2.5 individually examine the infinite c , large M and the small plasma skin depth d_S limits of the two-fluid system, leading to three corresponding closed set of equations in the limit. In Section 2.6 two out of the three limits are applied consecutively to obtain the well-known Hall-MHD and ideal MHD equations. Dispersion relations derived for all limiting forms of the two-fluids equations are analytically determined and asymptotically compared.

2.2 Non-dimensional ideal two-fluid plasma equations

2.2.1 Equations of motion

We begin with the two-fluid equations of an ideal plasma (2FP) given by [12]

$$\begin{aligned}
\frac{\partial \rho_\alpha}{\partial t} + \nabla \cdot (\rho_\alpha \mathbf{u}_\alpha) &= 0, \\
\frac{\partial \rho_\alpha \mathbf{u}_\alpha}{\partial t} + \nabla \cdot (\rho_\alpha \mathbf{u}_\alpha \mathbf{u}_\alpha + p_\alpha \mathbf{I}) &= n_\alpha q_\alpha (\mathbf{E} + \mathbf{u}_\alpha \times \mathbf{B}), \\
\frac{\partial \varepsilon_\alpha}{\partial t} + \nabla \cdot ((\varepsilon_\alpha + p_\alpha) \mathbf{u}_\alpha) &= n_\alpha q_\alpha \mathbf{E} \cdot \mathbf{u}_\alpha, \\
\frac{\partial \mathbf{B}}{\partial t} + \nabla \times \mathbf{E} &= \mathbf{0}, \\
\frac{\partial \mathbf{E}}{\partial t} - c^2 \nabla \times \mathbf{B} &= -\frac{1}{\epsilon_0} \sum_\alpha n_\alpha q_\alpha \mathbf{u}_\alpha, \\
\nabla \cdot \mathbf{E} &= \frac{1}{\epsilon_0} \sum_\alpha n_\alpha q_\alpha, \\
\nabla \cdot \mathbf{B} &= 0,
\end{aligned} \tag{2.3}$$

where

$$\rho_\alpha = n_\alpha m_\alpha, \quad p_\alpha = n_\alpha k_B T_\alpha, \quad \varepsilon_\alpha = \frac{p_\alpha}{\gamma - 1} + \frac{\rho_\alpha |\mathbf{u}_\alpha|^2}{2}. \tag{2.4}$$

Here, \mathbf{x} is the position vector, t is the time. The subscript α denotes ion or electron species, with ρ_α being the mass density, m_α the particle mass, n_α the species number density, \mathbf{u}_α the species velocity, q_α the particle charge, T_α the species temperature, p_α the pressure and ε the thermal energy. Separate equations-of-state, with k_B being the Boltzmann constant and γ the specific heat ratio, are applied for both ions and electrons, meaning that each species is in its own kinetic-collisional equilibrium, but not necessarily with the same temperatures. In Maxwell's equations, \mathbf{B} and \mathbf{E} are the magnetic and electric fields respectively and the speed-of-light is given by $c = (\mu_0 \epsilon_0)^{-1/2}$ with permeability of free space μ_0 and vacuum permittivity ϵ_0 .

In order to obtain self-consistent limits we introduce a non-dimensionalization scheme where reference scales are chosen for length as L_{ref} , mass as m_{ref} , number density as n_{ref} , velocity as u_{ref} , charge as q_{ref} , and magnetic field as B_{ref} . Dimensionless variables are defined accordingly:

$$\begin{aligned}
\hat{\mathbf{x}} &= \frac{\mathbf{x}}{L_{\text{ref}}}, \quad \hat{t} = \frac{t}{L_{\text{ref}}/u_{\text{ref}}}, \quad \hat{\rho}_\alpha = \frac{\rho_\alpha}{n_{\text{ref}} m_{\text{ref}}}, \quad \hat{m}_\alpha = \frac{m_\alpha}{m_{\text{ref}}}, \quad \hat{n}_\alpha = \frac{n_\alpha}{n_{\text{ref}}}, \quad \hat{\mathbf{u}}_\alpha = \frac{\mathbf{u}_\alpha}{u_{\text{ref}}}, \\
\hat{q}_\alpha &= \frac{q_\alpha}{q_{\text{ref}}}, \quad \hat{p}_\alpha = \frac{p_\alpha}{n_{\text{ref}} m_{\text{ref}} u_{\text{ref}}^2}, \quad \hat{\varepsilon}_\alpha = \frac{\varepsilon_\alpha}{n_{\text{ref}} m_{\text{ref}} u_{\text{ref}}^2}, \quad \hat{\mathbf{B}} = \frac{\mathbf{B}}{B_{\text{ref}}}, \quad \hat{\mathbf{E}} = \frac{\mathbf{E}}{u_{\text{ref}} B_{\text{ref}}}.
\end{aligned} \tag{2.5}$$

It is noted that assuming plasma is initially magnetized, an independent scale for magnetic field B_{ref} is introduced. Additionally, instead of defaulting the speed-of-light, c , as reference velocity, an independent characteristic speed, u_{ref} , is allowed to scale c and give \hat{c} .

Therefore expressed in terms of the dimensionless variables with the hat symbol dropped henceforth for brevity, the non-dimensional ideal two-fluid equations are given by

$$\frac{\partial \rho_\alpha}{\partial t} + \nabla \cdot (\rho_\alpha \mathbf{u}_\alpha) = 0, \quad (2.6a)$$

$$\frac{\partial \rho_\alpha \mathbf{u}_\alpha}{\partial t} + \nabla \cdot (\rho_\alpha \mathbf{u}_\alpha \mathbf{u}_\alpha + p_\alpha \mathbf{I}) = \frac{n_\alpha q_\alpha}{d_L} (\mathbf{E} + \mathbf{u}_\alpha \times \mathbf{B}), \quad (2.6b)$$

$$\frac{\partial \varepsilon_\alpha}{\partial t} + \nabla \cdot ((\varepsilon_\alpha + p_\alpha) \mathbf{u}_\alpha) = \frac{n_\alpha q_\alpha}{d_L} \mathbf{E} \cdot \mathbf{u}_\alpha, \quad (2.6c)$$

$$\frac{\partial \mathbf{B}}{\partial t} + \nabla \times \mathbf{E} = \mathbf{0}, \quad (2.6d)$$

$$\frac{\partial \mathbf{E}}{\partial t} - c^2 \nabla \times \mathbf{B} = -\frac{d_L}{d_D^2} \sum_\alpha n_\alpha q_\alpha \mathbf{u}_\alpha, \quad (2.6e)$$

$$\nabla \cdot \mathbf{E} = \frac{d_L}{d_D^2} \sum_\alpha n_\alpha q_\alpha, \quad (2.6f)$$

$$\nabla \cdot \mathbf{B} = 0, \quad (2.6g)$$

where

$$\rho_\alpha = n_\alpha m_\alpha, \quad \varepsilon_\alpha = \frac{p_\alpha}{\gamma - 1} + \frac{\rho_\alpha |\mathbf{u}_\alpha|^2}{2}, \quad (2.7)$$

and

$$d_D \equiv \sqrt{\frac{u_{\text{ref}}^2 \epsilon_0 m_{\text{ref}}}{n_{\text{ref}} q_{\text{ref}}^2 L_{\text{ref}}^2}} = \frac{1}{q_{\text{ref}} c L_{\text{ref}}} \sqrt{\frac{m_{\text{ref}}}{n_{\text{ref}} \mu_0}}, \quad d_L \equiv \frac{u_{\text{ref}} m_{\text{ref}}}{q_{\text{ref}} B_{\text{ref}} L_{\text{ref}}}, \quad (2.8)$$

are the dimensionless Debye length and Larmor radius, respectively.

Since the Debye length d_D varies with c , it is more convenient to introduce the plasma skin depth, d_S ,

$$d_S \equiv \frac{1}{q_{\text{ref}} L_{\text{ref}}} \sqrt{\frac{m_{\text{ref}}}{\mu_0 n_{\text{ref}}}}, \quad (2.9)$$

which measures the distance of which electromagnetic waves can penetrate, and the plasma parameter β ,

$$\beta \equiv \frac{2\mu_0 n_{\text{ref}} m_{\text{ref}} u_{\text{ref}}^2}{B_{\text{ref}}^2}, \quad (2.10)$$

which measures the relative size of thermal energy over magnetic energy. Using the following mapping between the two parameter sets,

$$d_D = \frac{d_S}{c}, \quad d_L = \sqrt{\frac{\beta}{2}} d_S, \quad (2.11)$$

the behavior of the ideal two-fluid system can be fully characterized by the four independent non-dimensional parameters, namely, c , M , d_S , and β .

2.2.2 Center-of-mass representation

We proceed with the singly charged ion case where $q_i = e$ is the dimensionless proton charge. For the purpose of enabling a clear and physically insightful asymptotic analysis, it is convenient to transform the primitive variables for each species, $(\rho_{i,e}, p_{i,e}, \mathbf{u}_{i,e})^T$, into their corresponding counterparts viewed from the center-of-mass frame, by defining the total mass density ρ , charge density ρ_c , net pressure p , center-of-mass velocity \mathbf{u} , and current \mathbf{j} . The change of variables is then

$$\begin{aligned} \rho &= \rho_i + \rho_e, \\ \rho_c &= e(n_i - n_e), \\ p &= p_i + p_e, \\ \mathbf{u} &= \frac{\rho_i \mathbf{u}_i + \rho_e \mathbf{u}_e}{\rho_i + \rho_e}, \\ \mathbf{j} &= e(n_i \mathbf{u}_i - n_e \mathbf{u}_e). \end{aligned} \quad (2.12)$$

The original species variables can be recovered by

$$\begin{aligned} \rho_i &= \frac{M\rho + \rho_c m_i/e}{1 + M}, & \rho_e &= \frac{\rho - \rho_c m_i/e}{1 + M}, \\ \mathbf{u}_i &= \frac{M\rho \mathbf{u} + \mathbf{j} m_i/e}{M\rho + \rho_c m_i/e}, & \mathbf{u}_e &= \frac{\rho \mathbf{u} - \mathbf{j} m_i/e}{\rho - \rho_c m_i/e}, \end{aligned} \quad (2.13)$$

where

$$M = \frac{m_i}{m_e} \quad (2.14)$$

is the particle mass ratio. It might be tempting at this point to set m_{ref} to be the ion mass and q_{ref} to be the proton charge, giving $m_i = e = 1$. In general a specific choice for reference scales is not necessarily made until a specific flow is considered, so that we here reserve the capability to easily convert the dimensionless equations back to their dimensional form.

Substituting (2.13) into the 2FP equations, one obtains the following conservation laws,

- mass and charge density continuity,

$$\frac{\partial \rho}{\partial t} + \nabla \cdot (\rho \mathbf{u}) = 0, \quad (2.15)$$

$$\frac{\partial \rho_c}{\partial t} + \nabla \cdot \mathbf{j} = 0, \quad (2.16)$$

- momentum and current conservation,

$$\frac{\partial \rho \mathbf{u}}{\partial t} + \nabla \cdot (\rho \mathbf{u} \mathbf{u} + p \mathbf{I}) + \nabla \cdot \mathbf{f}_{mom} = \frac{\sqrt{2}}{\sqrt{\beta} d_S} (\mathbf{j} \times \mathbf{B} + \rho_c \mathbf{E}), \quad (2.17)$$

$$\frac{\partial \mathbf{j}}{\partial t} + \nabla \cdot \left(\mathbf{u} \mathbf{j} + \mathbf{j} \mathbf{u} - \frac{m_i}{e \rho} \mathbf{j} \mathbf{j} \right) + \nabla \cdot \mathbf{f}_{cur} = \frac{\sqrt{2} e^2 M \rho (\mathbf{E} + \mathbf{u} \times \mathbf{B})}{\sqrt{\beta} d_S m_i^2} + \mathbf{s}_{cur}, \quad (2.18)$$

where

$$\begin{aligned} \mathbf{f}_{mom} &= \rho \frac{m_i^2}{e^2} \frac{\rho_c^2 \mathbf{u} \mathbf{u} - \rho_c \mathbf{u} \mathbf{j} - \rho_c \mathbf{j} \mathbf{u} + \mathbf{j} \mathbf{j}}{(M \rho + \rho_c m_i / e)(\rho - \rho_c m_i / e)}, \\ \mathbf{f}_{cur} &= \frac{m_i \left[\mathbf{j} \mathbf{j} (e^2 \rho^2 - \rho_c m_i (\rho_c m_i + e M \rho)) + e \rho \rho_c (\mathbf{j} \mathbf{u} + \mathbf{u} \mathbf{j}) (\rho_c m_i + e(M-1)\rho) \right]}{e \rho (e \rho - \rho_c m_i) (\rho_c m_i + e M \rho)} \\ &\quad - \frac{e^3 M \rho^3 \rho_c \mathbf{u} \mathbf{u}}{e \rho (e \rho - \rho_c m_i) (\rho_c m_i + e M \rho)} + \frac{e (p - (M+1)p_e)}{m_i} \mathbf{I}, \\ \mathbf{s}_{cur} &= \frac{\sqrt{2}(1-M)e}{\sqrt{\beta} d_S m_i} (\rho_c \mathbf{E} + \mathbf{j} \times \mathbf{B}), \end{aligned} \quad (2.19)$$

- total energy conservation,

$$\frac{\partial \mathcal{E}}{\partial t} + \frac{\partial \mathcal{E}_{erg}}{\partial t} + \nabla \cdot \left((\mathcal{E}_h + p) \mathbf{u} + \frac{2}{\beta} \mathbf{E} \times \mathbf{B} \right) + \nabla \cdot \mathbf{f}_{erg} = 0, \quad (2.20)$$

where

$$\begin{aligned} \mathcal{E} &= \mathcal{E}_h + \frac{|\mathbf{B}|^2}{\beta}, \quad \mathcal{E}_h = \frac{p}{\gamma-1} + \frac{1}{2} \rho |\mathbf{u}|^2, \quad \mathcal{E}_{erg} = \rho \frac{m_i^2}{e^2} \frac{(|\mathbf{u}| \rho_c - |\mathbf{j}|)^2}{2(1+M)^2 \rho_i \rho_e} + \frac{|\mathbf{E}|^2}{\beta c^2}, \\ \mathbf{f}_{erg} &= \frac{\rho m_i^2 (|\mathbf{j}| - |\mathbf{u}| \rho_c) \left[\rho_c (\rho_c m_i (m_i (|\mathbf{u}| \rho_c + |\mathbf{j}|) + 2e(M-1)\rho |\mathbf{u}|) - 3e^2 M \rho^2 |\mathbf{u}|) + e^2 |\mathbf{j}| M \rho^2 \right]}{2(e \rho - \rho_c m_i)^2 (\rho_c m_i + e M \rho)^2} \mathbf{u} \\ &\quad - \frac{\rho m_i^2 (|\mathbf{j}| - |\mathbf{u}| \rho_c) (e(M-1)\rho m_i (|\mathbf{u}| \rho_c + |\mathbf{j}|) + 2|\mathbf{j}| \rho_c m_i^2 - 2e^2 M \rho^2 |\mathbf{u}|)}{2(e \rho - \rho_c m_i)^2 (\rho_c m_i + e M \rho)^2} \mathbf{j} \\ &\quad - \frac{\gamma}{\gamma-1} \frac{m_i (\mathbf{j} - \mathbf{u} \rho_c) (p \rho_c m_i + e(M+1)\rho p_e - e p \rho)}{(e \rho - \rho_c m_i) (\rho_c m_i + e M \rho)}, \end{aligned} \quad (2.21)$$

- electron pressure equation

$$\frac{\partial p_e}{\partial t} + \left(\mathbf{u} - \frac{m_i}{e \rho} \mathbf{j} \right) \cdot \nabla p_e + \gamma p_e \nabla \cdot \left(\mathbf{u} - \frac{m_i}{e \rho} \mathbf{j} \right) + S_{p_e} = 0, \quad (2.22)$$

where

$$S_{p_e} = \frac{\rho_c m_i}{e \rho - \rho_c m_i} \left[\left(\mathbf{u} - \frac{m_i}{e \rho} \mathbf{j} \right) \cdot \nabla p_e + \gamma p_e \nabla \cdot \left(\mathbf{u} - \frac{m_i}{e \rho} \mathbf{j} \right) \right]; \quad (2.23)$$

and the Maxwell's equations

$$\frac{\partial \mathbf{B}}{\partial t} + \nabla \times \mathbf{E} = \mathbf{0}, \quad (2.24a)$$

$$\frac{1}{c^2} \frac{\partial \mathbf{E}}{\partial t} - \nabla \times \mathbf{B} = -\frac{\sqrt{\beta}}{\sqrt{2}d_S} \mathbf{j}, \quad (2.24b)$$

$$\frac{1}{c^2} \nabla \cdot \mathbf{E} = \frac{\sqrt{\beta}}{\sqrt{2}d_S} \rho_c, \quad (2.24c)$$

$$\nabla \cdot \mathbf{B} = 0. \quad (2.24d)$$

Hence Eq. (2.15-2.24d) give the center-of-mass representation of the ideal 2FP equations. Symmetry breaks down in this form when the equations of motion are written for macroscopic quantities, for instance the current, resulting in algebraically formidable expressions. Nonetheless, such preparation is necessary to enable a discussion of various limits of 2FP system with respect to c , M , d_S , and β , as well as the physical implications of these limits.

Among the various 2FP contractions discussed in the sequel, it is useful to define a distinction between what we refer to as a ‘‘plasma’’ (P) model, which supports non vanishing charge separation and a wide spectrum of waves including electromagnetic waves, and a ‘‘magnetohydrodynamic’’ (MHD) model which we will define, as is conventional, to satisfy charge quasi-neutrality [39].

2.2.3 Dispersion relation for 2FP

Linearization around a homogeneous equilibrium

It is insightful to analyze the waves permitted by the 2FP system, as an example of the general procedure that will be repeatedly used. We consider perturbation away from a homogeneous stationary background equilibrium (subscripted by zero), where $\tilde{\mathbf{u}}_0 = \tilde{\mathbf{j}}_0 = \tilde{\mathbf{E}}_0 = \mathbf{0}$, $\tilde{\rho}_{c0} = 0$, and $\tilde{\mathbf{B}}_0$, \tilde{p}_0 , \tilde{p}_{e0} , $\tilde{\rho}_0$ define the unperturbed constant state. Here the tilde symbol refers variables to their dimensional form. This leads to the following natural choice for reference scales:

$$B_{\text{ref}} = |\tilde{\mathbf{B}}_0|, \quad u_{\text{ref}} = \sqrt{\frac{\gamma \tilde{p}_0}{n_{\text{ref}} m_{\text{ref}}}}, \quad m_{\text{ref}} = \tilde{m}_i + \tilde{m}_e, \quad n_{\text{ref}} = \tilde{n}_{i0} = \tilde{n}_{e0}, \quad q_{\text{ref}} = \tilde{e}. \quad (2.25)$$

It immediately follows that $m_i = M/(M + 1)$ and $e = 1$. Since the background equilibrium is stationary, a velocity scale is conveniently found through the initial pressure in the form of speed-of-sound. The benefit of this choice is that the background pressure can be normalized in the linearized equations. Additionally

the length scale, L_{ref} , in this case has to be inferred from a known value of d_S , according to Eq. (2.9).

The non-dimensional field variables can now be expanded as a regular perturbation around the background solution, giving

$$\begin{aligned} \rho &= 1 + \rho', & \rho_c &= \rho'_c, & \mathbf{u} &= \mathbf{u}', & \mathbf{j} &= \mathbf{j}', \\ p &= \frac{1}{\gamma} + p', & p_e &= \frac{\alpha}{\gamma} + p'_e, & \mathbf{B} &= \mathbf{b} + \mathbf{B}', & \mathbf{E} &= \mathbf{E}', \end{aligned} \quad (2.26)$$

where $\alpha \equiv \tilde{p}_{e0}/\tilde{p}_0 \in (0, 1)$ is the initial electron temperature fraction, and \mathbf{b} is the unit vector in the direction of background magnetic field, $\tilde{\mathbf{B}}_0$. Substituting (2.26) into (2.15-2.24d), using the Faraday law to expose pressure from the energy equation, and retaining terms linear in perturbation quantities gives the linearized 2FP equations

$$\begin{aligned} \frac{\partial \rho'}{\partial t} + \nabla \cdot \mathbf{u}' &= 0, \\ \frac{\partial \rho'_c}{\partial t} + \nabla \cdot \mathbf{j}' &= 0, \\ \frac{\partial \mathbf{u}'}{\partial t} + \nabla p' &= \frac{1}{d_S} \sqrt{\frac{2}{\beta}} \mathbf{j}' \times \mathbf{b}, \\ \frac{\partial \mathbf{j}'}{\partial t} + \frac{1+M}{M} \nabla p' - \frac{(1+M)^2}{M} \nabla p'_e &= \sqrt{\frac{2}{\beta}} \frac{(1+M)^2 (\mathbf{E}' + \mathbf{u}' \times \mathbf{b}) + (1-M^2) \mathbf{j}' \times \mathbf{b}}{M d_S}, \\ \frac{\partial p'}{\partial t} + \nabla \cdot \mathbf{u}' - \frac{\alpha(1+M) - 1}{1+M} \nabla \cdot \mathbf{j}' &= 0, \\ \frac{\partial p'_e}{\partial t} + \alpha \nabla \cdot \mathbf{u}' - \frac{\alpha M}{1+M} \nabla \cdot \mathbf{j}' &= 0, \\ \frac{\partial \mathbf{B}'}{\partial t} + \nabla \times \mathbf{E}' &= 0, \\ \frac{1}{c^2} \frac{\partial \mathbf{E}'}{\partial t} - \nabla \times \mathbf{B}' &= -\frac{1}{d_S} \sqrt{\frac{\beta}{2}} \mathbf{j}'. \end{aligned} \quad (2.27)$$

Both of the divergence constrains on \mathbf{E} and \mathbf{B} have been omitted with the consequence that spurious stationary waves could be introduced together with the genuine entropy waves that are also stationary [38]. However, neither of these null solutions are of interest, and so only positive wave frequencies are considered throughout the analysis.

Plane wave solutions

We seek plane wave solutions of the form

$$\xi(\mathbf{x}, t) = |\xi| \exp(i\mathbf{k} \cdot \mathbf{x} - i\omega t), \quad (2.28)$$

where ξ represents a general function of space and time. Both the wave-number vector \mathbf{k} and the angular frequency ω are dimensionless, scaled by $1/L_{\text{ref}}$ and $u_{\text{ref}}/L_{\text{ref}}$ respectively. The Cartesian coordinates are oriented such that \mathbf{b} is along the z -direction, and \mathbf{k} lies in the x, z -plane

$$\mathbf{b} = (0, 0, 1), \quad \mathbf{k} = (k_{\perp}, 0, k_{\parallel}), \quad \lambda \equiv \frac{k_{\parallel}}{|\mathbf{k}|} = \frac{k_{\parallel}}{k}, \quad (2.29)$$

where k_{\perp} and k_{\parallel} are respectively the wave number components perpendicular and parallel to the background magnetic field, and λ gives the cosine of the angle between \mathbf{b} and \mathbf{k} .

Now that ρ_1 and ρ_{c1} decouple from the system, they can be consistently dropped together with the two divergence constraints on \mathbf{E}' and \mathbf{B}' . Using the ansatz Eq. (2.28), the remaining equations lead to an algebraic system for p' , p'_e , \mathbf{u}' , \mathbf{j}' , \mathbf{B}' and \mathbf{E}' . Here we note that there are two wave families that are considered "marginal", *i.e.*, corresponding to $\omega = 0$ [38]. These waves correspond to spatial distributions of ion and electron density, and pressure balanced by the longitudinal electric field. By excluding marginal waves for which $\omega = 0$, after some algebra, all the other unknowns can be expressed in terms of \mathbf{u}' and \mathbf{E}' only, giving a reduced eigenvalue problem,

$$\begin{bmatrix} i(k_{\perp}^2 - \omega^2) & 0 & ik_{\perp}k_{\parallel} & a_1 l_1 k_{\perp}^2 \omega & \frac{2i(c^2 k_{\perp}^2 - \omega^2)}{c^2 \beta} & a_1 l_1 k_{\perp} k_{\parallel} \omega \\ 0 & -i\omega^2 & 0 & \frac{2i(\omega^2 - c^2 k_{\parallel}^2)}{c^2 \beta} & 0 & \frac{2ik_{\perp}k_{\parallel}}{\beta} \\ ik_{\perp}k_{\parallel} & 0 & i(k_{\parallel}^2 - \omega^2) & a_1 l_1 k_{\perp} k_{\parallel} \omega & 0 & a_1 l_1 k_{\parallel}^2 \omega \\ -ia_2 k_{\perp}^2 & -l_2 \omega & -ia_2 k_{\perp} k_{\parallel} & l_1 \omega (\omega^2 - a_3 k_{\perp}^2 - c^2 k_{\parallel}^2) & il_3 (\omega^2 - c^2 k^2) & a_4 l_1 k_{\perp} k_{\parallel} \omega \\ l_2 \omega & 0 & 0 & -l_2 \omega & l_1 \omega (\omega^2 - c^2 k^2) - l_2 \omega & -il_3 c^2 k_{\perp} k_{\parallel} \\ -ia_2 k_{\perp} k_{\parallel} & 0 & -ia_2 k_{\parallel}^2 & a_4 l_1 k_{\perp} k_{\parallel} \omega & 0 & l_1 \omega (\omega^2 - a_3 k_{\parallel}^2 - c^2 k_{\perp}^2) \\ & & & & & -l_2 \omega \end{bmatrix} \cdot [\mathbf{u}', \mathbf{E}']^T = 0, \quad (2.30)$$

where

$$a_1 = \frac{\alpha + \alpha M - 1}{M + 1}, \quad a_2 = \frac{(M + 1)(\alpha + \alpha M - 1)}{M}, \quad a_3 = \frac{-\alpha + \alpha M^2 + 1}{M}, \quad a_4 = \frac{\alpha + M(c^2 - \alpha M) - 1}{M}, \\ l_1 = \sqrt{\frac{2}{\beta}} \frac{d_S}{c^2}, \quad l_2 = \sqrt{\frac{2}{\beta}} \frac{(1 + M)^2}{d_S M}, \quad l_3 = \frac{2(M^2 - 1)}{\beta c^2 M}. \quad (2.31)$$

The dispersion relation for the 2FP system is obtained by requiring the matrix determinant to be zero. This gives a normalized polynomial equation of order six in ω^2 ,

$$\sum_{m=1}^7 \sum_{n=1}^5 A_{mn} k^{2(n-1)} \omega^{2(m-1)} = 0, \quad (2.32)$$

where the coefficients, $A_{mn} = A_{mn}(c, M, d_S, \alpha, \beta, \lambda)$, are given in Table 2.1. For each k^2 there corresponds six two-fold degenerate waves. The degeneracy corresponds to the fact that we have six solutions for ω^2 such that for each solution of ω^2 we have two waves propagating in opposite direction (one for $\omega > 0$ and the other corresponding to $\omega < 0$). The 2FP system is not a strictly hyperbolic system of PDEs: in such a system we only encounter waves such that $\omega \propto k$, and there are no degenerate eigen values. The 2FP system of wave equations includes dispersive waves where the dispersive waves stem from the electromagnetic source terms in the ion and electron momentum and energy equations.

An equivalent polynomial, although derived using different scaling, is given by Goedbloed & Poedts [38], where the 6-wave structure associated with the two-fluid model and its asymptotic limits for extreme values of ω and k are discussed in terms of the background physical variables. We are particularly interested in three regions of these asymptotes under the current non-dimensionalization scheme, in order to facilitate a comparison against those of the other limiting forms of the two-fluid equations derived in the following sections. Readers are referred to Goedbloed & Poedts [38] for more details.

Asymptotic waves

First, the resonance limit, where $k \rightarrow \infty$ while keeping ω finite, are computed by solving the corresponding limit of Eq. (2.32), given by

$$\left(A_{51} + A_{52}\omega^2 + A_{53}\omega^4 \right) k^8 = 0, \quad (2.33)$$

whose two positive roots lead to the ion and electron cyclotron resonant frequencies, ω_{ic} and ω_{ie} , respectively,

$$\omega_{ic} = \sqrt{\frac{2}{\beta}} \frac{\lambda}{d_S} \left(1 + \frac{1}{M} \right), \quad \omega_{ec} = \sqrt{\frac{2}{\beta}} \frac{\lambda}{d_S} (1 + M). \quad (2.34)$$

These frequencies correspond to spatially localized cyclotron waves.

$$\begin{aligned}
A_{14} &= -\frac{c^2(M+1)^6(\beta c^2+2)^2}{\beta^2 d_S^6 M^3} \\
A_{15} &= \frac{(M+1)^4(2\beta c^2+2\beta c^2 M^2+M(3\beta^2 c^4+4\beta c^2+4))}{\beta^2 d_S^4 M^3} \\
A_{16} &= -\frac{(M+1)^2(3\beta c^2 M+2M^2+2)}{\beta d_S^2 M^2} \\
A_{17} &= 1 \\
A_{23} &= \frac{c^6\left(\frac{1}{M}+1\right)^6 M^3\left(\beta+\frac{2}{c^2}\right)\left(\beta+2\left(\frac{1}{c^2}+1\right)\lambda^2+2\right)}{\beta^2 d_S^6} \\
A_{24} &= -\frac{(1+M)^4}{\beta^2 d_S^4 M^3} \left[2\beta^2 c^6 M + 4\lambda^2(-\alpha + \alpha M^2 + M + 1) \right. \\
&\quad \left. + \beta c^4(-\alpha\beta + \beta + 2\lambda^2 + M^2(\alpha\beta + 2\lambda^2 + 2)) + M(3\beta - 2\lambda^2 + 6) + 2 \right. \\
&\quad \left. + 2c^2\left(\beta(-3\alpha\lambda^2 + \alpha + 3\lambda^2) + \beta M^2(3\alpha\lambda^2 - \alpha + 1) + 2(\beta + 2)M\right) \right] \\
A_{25} &= \frac{(M+1)^2(4\beta c^4 M^2 + c^2 M(-2\alpha\beta + 2\beta + 2M^2(\alpha\beta + 2) + 3\beta M + 4)) + 2(M+1)(\alpha M^3 \lambda^2 - (\alpha - 1)M^2 + \alpha M - (\alpha - 1)\lambda^2)}{\beta d_S^2 M^3} \\
A_{26} &= -2c^2 + \frac{\alpha - 1}{M} - \alpha M - 1 \\
A_{32} &= -\frac{4c^4(M+1)^6 \lambda^2 (\beta + 1)c^2 + \lambda^2 + 1}{\beta^2 d_S^6 M^3} \\
A_{33} &= \frac{(1+M)^4}{\beta^2 d_S^4 M^3} \left[-4c^2 \lambda^2 (M+1) \left(\alpha^2 \beta (M+1) - \alpha(\beta + (\beta + 2)M - 2) - 2 \right) \right. \\
&\quad \left. - 4(\alpha - 1)\alpha \lambda^4 (M+1)^2 + 2\beta c^6 (\lambda^2 + \lambda^2 M^2 + M(\beta - \lambda^2 + 1)) \right. \\
&\quad \left. + c^4 M(-2(\alpha - 1)\alpha \beta^2 + 4\beta + 4) + c^4 \beta(-\alpha^2 \beta + \alpha(\beta - 6\lambda^2 + 2) + 8\lambda^2) \right. \\
&\quad \left. + c^4 \beta + M^2(-\alpha^2 \beta + \alpha(\beta + 6\lambda^2 - 2) + 2(\lambda^2 + 1)) \right] \\
A_{34} &= -\frac{(1+M)^2}{\beta d_S^2 M^3} \left[\beta c^6 M^2 + 2c^4 M(-\alpha\beta + \beta + M^2(\alpha\beta + 1) + 2\beta M + 1) \right. \\
&\quad \left. - 2(\alpha - 1)\alpha \lambda^2 (M+1)^2 (M^2 + 1) \right. \\
&\quad \left. + 2c^2 (M+1) \left(-2(\alpha - 1)\lambda^2 + 2\alpha \lambda^2 M^3 - (\alpha - 1)M^2(\alpha\beta + 2) + \alpha M(-\alpha\beta + \beta + 2) \right) \right] \\
A_{35} &= \frac{c^4 M + 2c^2(-\alpha + \alpha M^2 + M + 1) - (\alpha - 1)\alpha (M+1)^2}{M} \\
A_{41} &= \frac{4c^6(M+1)^6 \lambda^4}{\beta^2 d_S^6 M^3} \\
A_{42} &= -\frac{2c^2 \lambda^2 (M+1)^4 (\beta c^4 (M^2 + 1) - 2c^2 (M+1) (\alpha^2 \beta (M+1) - \alpha(\beta + \beta M + M - 1) - 1) - 4(\alpha - 1)\alpha \lambda^2 (M+1)^2)}{\beta^2 d_S^4 M^3} \\
A_{43} &= \frac{c^2 (M+1)^2 (\beta c^4 M^2 + 2c^2 (M+1) (-(\alpha - 1)\lambda^2 + \alpha \lambda^2 M^3 - (\alpha - 1)M^2 (\alpha\beta + 1) + \alpha M(-\alpha\beta + \beta + 1)) - 4(\alpha - 1)\alpha \lambda^2 (M+1)^2 (M^2 + 1))}{\beta d_S^2 M^3} \\
A_{44} &= -\frac{c^2 (M+1) (c^2 (\alpha (M - 1) + 1) - 2(\alpha - 1)\alpha (M+1))}{M} \\
A_{51} &= -\frac{4(\alpha - 1)\alpha c^4 \lambda^4 (M+1)^6}{\beta^2 d_S^4 M^3} \\
A_{52} &= \frac{2(\alpha - 1)\alpha c^4 \lambda^2 (M+1)^4 (M^2 + 1)}{\beta d_S^2 M^3} \\
A_{53} &= -\frac{(\alpha - 1)\alpha c^4 (M+1)^2}{M}
\end{aligned}$$

Table 2.1: Non-zero coefficients of the dispersion equation (2.32) for an ideal two-fluid model.

Second, the local high-frequency distinguished limit $k \rightarrow \infty$, $\omega \rightarrow \infty$, with ω/k finite, follows from the asymptotic dispersion equation as

$$A_{17}\omega^{12} + A_{26}k^2\omega^{10} + A_{35}k^4\omega^8 + A_{44}k^6\omega^6 + A_{53}k^8\omega^4 = 0, \quad (2.35)$$

which factorizes to give two repeated speed-of-light and the ion, electron sound speeds,

$$\omega_{EM} = kc, \quad \omega_{is} = k\sqrt{(1-\alpha)\left(1+\frac{1}{M}\right)}, \quad \omega_{es} = k\sqrt{\alpha(1+M)}. \quad (2.36)$$

The two EM waves are light waves of with different polarization states. Under the present choice of u_{ref} in their dimensional form these are

$$\tilde{\omega}_{EM} = \tilde{k}\tilde{c}, \quad \tilde{\omega}_{is} = \tilde{k}\sqrt{\frac{\gamma\tilde{P}_{i0}}{\tilde{n}_{i0}\tilde{m}_i}}, \quad \tilde{\omega}_{es} = \tilde{k}\sqrt{\frac{\gamma\tilde{P}_{e0}}{\tilde{n}_{e0}\tilde{m}_e}}. \quad (2.37)$$

In the limit $k \rightarrow 0$ the high frequency waves, viz., the two EM light waves branch off and along with the electron acoustic wave asymptote to three plasma waves corresponding to the plasma frequency, and the upper and lower cutoff plasma frequencies [38]. These high frequency waves, as will be seen later, are removed from the dispersion relation in the limit $c \rightarrow \infty$.

Finally, the global low-frequency limit $k \rightarrow 0$, $\omega \rightarrow 0$, with ω/k finite, is obtained from

$$A_{14}\omega^6 + A_{23}k^2\omega^4 + A_{32}k^4\omega^2 + A_{41}k^6 = 0, \quad (2.38)$$

which contains the perturbed MHD Alfvén wave and two acoustic waves due to finite speed-of-light, given by

$$\omega_A = k_{\parallel}\sqrt{\frac{2}{\beta + 2/c^2}},$$

$$\omega_{f,s} = \left(\frac{k^2(2+\beta) + 2k_{\parallel}^2/c^2}{2(\beta + 2/c^2)} \pm \sqrt{\frac{\left(1 + \frac{\beta}{2}\right)^2 k^4 - \left[\beta\left(2 - \frac{1}{c^2}\right) + \frac{2}{c^2}\right] k_{\parallel}^2 k^2 + \frac{k_{\parallel}^4}{c^4}}{(\beta + 2/c^2)^2}} \right)^{1/2}. \quad (2.39)$$

One might immediately identify that these solutions converge exactly to the single-fluid MHD three waves (Alfvén, fast and slow magnetosonic waves) in the limit as $c \rightarrow \infty$, which is discussed in more detail in Section 2.6.2.

2.3 Infinite speed-of-light limit

We first examine the $c \rightarrow \infty$ limit of the 2FP equations. This corresponds to the formal asymptotic limit where the small parameter $\delta_c \equiv 1/c^2 = u_{\text{ref}}^2 \mu_0 \epsilon_0 \rightarrow 0$ while keeping M , d_S , and β fixed. This is realized by requiring $(u_{\text{ref}}^2 \epsilon_0) \rightarrow 0$ with μ_0 fixed.

2.3.1 Leading order equations: $c \rightarrow \infty$

Perturbation analysis

Since the $\delta_c \rightarrow 0$ limit is singular for the Ampère's law (2.24b) and for Gauss's divergence constraint on \mathbf{E} , (2.24c), it is constructive to perform a perturbation expansion in powers of δ_c for all field variables of the form

$$\zeta = \zeta_0 + \zeta_1 \delta_c + O(\delta_c^2), \quad (2.40)$$

where ζ is generically used to represent ρ , ρ_c , p , p_e , \mathbf{u} , \mathbf{j} , \mathbf{B} and \mathbf{E} ; the subscript zero now refers to the leading order solution and the subscript one indicates first order correction. In particular, substituting the ρ_c and \mathbf{E} expansions into (2.24c) yields

$$O(1) : \quad \frac{\rho_{c0}}{d_S} \sqrt{\frac{\beta}{2}} = \frac{e}{d_S} \sqrt{\frac{\beta}{2}} (n_{i0} - n_{e0}) = 0, \quad (2.41)$$

$$O(\delta_c) : \quad \frac{\rho_{c1}}{d_S} \sqrt{\frac{\beta}{2}} = \frac{e}{d_S} \sqrt{\frac{\beta}{2}} (n_{i1} - n_{e1}) = \nabla \cdot \mathbf{E}_0, \quad (2.42)$$

where the definition for charge density is used. This implies, in the limit of infinite speed-of-light ($c \rightarrow \infty$) while keeping β , $d_S > 0$, the plasma is exactly charge neutral, by $\rho_{c0} = 0$, as the Gauss's law for electric field requires. However for any large but finite speed-of-light ($\delta_c \ll 1$), the charge density needs not vanish identically, and its value, being asymptotically small [$\sim O(\delta_c)$], is explicitly related to the leading order electric field solution \mathbf{E}_0 , *i.e.*,

$$\rho_c = d_S \sqrt{\frac{2}{\beta}} (\nabla \cdot \mathbf{E}_0) \delta_c + O(\delta_c^2). \quad (2.43)$$

Consistency between the constraint (2.43) and (2.16), (3.2d), which respectively govern the time evolution of ρ_c and \mathbf{E} , must be ensured. Therefore these two equations are also expanded, giving at order $O(1)$,

$$\frac{\partial \rho_{c0}}{\partial t} + \nabla \cdot \mathbf{j}_0 = 0, \quad (2.44)$$

$$\nabla \times \mathbf{B}_0 = \frac{\sqrt{\beta}}{\sqrt{2} d_S} \mathbf{j}_0, \quad (2.45)$$

and at order $O(\delta_c)$,

$$\frac{\partial \rho_{c_1}}{\partial t} + \nabla \cdot \mathbf{j}_1 = 0, \quad (2.46)$$

$$\frac{\partial \mathbf{E}_0}{\partial t} - \nabla \times \mathbf{B}_1 = -\frac{\sqrt{\beta}}{\sqrt{2}d_S} \mathbf{j}_1. \quad (2.47)$$

Substituting the divergences of Eqs. (2.45) and (2.47) into (2.44) and (2.46) respectively produces

$$\frac{\partial \rho_{c_0}}{\partial t} = 0, \quad \frac{\partial}{\partial t} \left(\rho_{c_1} - d_S \sqrt{\frac{2}{\beta}} (\nabla \cdot \mathbf{E}_0) \right) = 0. \quad (2.48)$$

It is clear that the divergence condition, (2.43), automatically satisfies the evolution equations for ρ_c to first order, and \mathbf{E} to zeroth order, in δ_c .

Zeroth-order equations

To close the system, the remaining equations of motion must be included. Various flux and source terms involved in (2.15-2.24d) simplify significantly owing to $\rho_{c_0} = 0$, giving

$$\mathbf{f}_{mon} = \frac{m_i^2}{e^2} \frac{\mathbf{j}_0 \mathbf{j}_0}{M \rho_0} + O(\delta_c), \quad (2.49a)$$

$$\mathbf{f}_{cur} = \frac{m_i}{e \rho_0 M} \mathbf{j}_0 \mathbf{j}_0 + \frac{e(p_0 - (M+1)p_{e_0})}{m_i} \mathbf{I} + O(\delta_c), \quad (2.49b)$$

$$\mathbf{s}_{cur} = \frac{\sqrt{2}(1-M)e}{\sqrt{\beta} d_S m_i} \mathbf{j}_0 \times \mathbf{B}_0 + O(\delta_c), \quad (2.49c)$$

$$\mathcal{E}_{erg} = \frac{m_i^2}{e^2} \frac{|\mathbf{j}_0|^2}{2M \rho_0} + O(\delta_c), \quad (2.49d)$$

$$\begin{aligned} \mathbf{f}_{erg} = & \frac{|\mathbf{j}_0|^2 m_i^2}{2e^2 M \rho_0} \mathbf{u}_0 - \frac{\gamma m_i ((M+1)p_{e_0} - p_0)}{(\gamma-1)e M \rho_0} \mathbf{j}_0 \\ & - \frac{|\mathbf{j}_0| m_i^2 (|\mathbf{j}_0| (M-1)m_i - 2e M \rho_0 |\mathbf{u}_0|)}{2e^3 M^2 \rho_0^2} \mathbf{j}_0 + O(\delta_c), \end{aligned} \quad (2.49e)$$

$$S_{p_e} = O(\delta_c). \quad (2.49f)$$

It is straightforward to collect the non-trivial leading order equations from the 2FP [see (2.15-2.24d)] to obtain a closed set of equations for all of the zeroth order variables as $c \rightarrow \infty$, except for ρ_c , which is shown to be identically zero at leading

order. With the subscript zero dropped, this limiting set follows as

$$\frac{\partial \rho}{\partial t} + \nabla \cdot (\rho \mathbf{u}) = 0, \quad (2.50a)$$

$$\frac{\partial \rho \mathbf{u}}{\partial t} + \nabla \cdot (\rho \mathbf{u} \mathbf{u} + p \mathbf{I}) = -\nabla \cdot \left(\frac{m_i^2}{e^2} \frac{\mathbf{j} \mathbf{j}}{M \rho} \right) + \frac{\sqrt{2}}{\sqrt{\beta} d_S} \mathbf{j} \times \mathbf{B}, \quad (2.50b)$$

$$\begin{aligned} \frac{\partial \mathbf{j}}{\partial t} + \nabla \cdot \left(\mathbf{u} \mathbf{j} + \mathbf{j} \mathbf{u} - \frac{m_i(1-M)}{e \rho M} \mathbf{j} \mathbf{j} + \frac{e(p - (M+1)p_e)}{m_i} \mathbf{I} \right) \\ = \frac{\sqrt{2}e}{\sqrt{\beta} d_S m_i} \left(\frac{e M \rho}{m_i} (\mathbf{E} + \mathbf{u} \times \mathbf{B}) + (1-M) \mathbf{j} \times \mathbf{B} \right), \end{aligned} \quad (2.50c)$$

$$\frac{\partial}{\partial t} \left(\mathcal{E} + \frac{m_i^2}{e^2} \frac{|\mathbf{j}|^2}{2M\rho} \right) + \nabla \cdot \left((\mathcal{E}_h + p) \mathbf{u} + \frac{2}{\beta} \mathbf{E} \times \mathbf{B} \right) + \nabla \cdot \mathbf{f}_{erg} = 0, \quad (2.50d)$$

$$\frac{\partial p_e}{\partial t} + \left(\mathbf{u} - \frac{m_i}{e \rho} \mathbf{j} \right) \cdot \nabla p_e + \gamma p_e \nabla \cdot \left(\mathbf{u} - \frac{m_i}{e \rho} \mathbf{j} \right) = 0, \quad (2.50e)$$

$$\frac{\partial \mathbf{B}}{\partial t} + \nabla \times \mathbf{E} = \mathbf{0}, \quad (2.50f)$$

$$\nabla \times \mathbf{B} = \frac{\sqrt{\beta}}{\sqrt{2} d_S} \mathbf{j}, \quad (2.50g)$$

$$\nabla \cdot \mathbf{B} = 0, \quad (2.50h)$$

where

$$\begin{aligned} \mathcal{E} = \mathcal{E}_h + \frac{|\mathbf{B}|^2}{\beta}, \quad \mathcal{E}_h = \frac{p}{\gamma - 1} + \frac{1}{2} \rho |\mathbf{u}|^2, \\ \mathbf{f}_{erg} = \frac{|\mathbf{j}|^2 m_i^2}{2e^2 M \rho} \mathbf{u} - \frac{\gamma m_i ((M+1)p_e \rho - p \rho)}{(\gamma - 1) e M \rho^2} \mathbf{j} - \frac{|\mathbf{j}| m_i^2 (|\mathbf{j}| (M-1) m_i - 2e M \rho |\mathbf{u}|)}{2e^3 M^2 \rho^2} \mathbf{j}. \end{aligned} \quad (2.51)$$

We denote this system the two-fluid MHD equations, denoted henceforth as 2FMHD henceforth, for the strict charge neutrality imposed at zeroth order.

Discussion

The preceding perturbation analysis provides a clear interpretation of the ‘‘quasi-neutrality assumption’’ often discussed in magnetohydrodynamics [9, 39, 89, 95]. Because $\rho_c \rightarrow 0$ as $c \rightarrow \infty$ charge separation does not occur in the limit. But for finite but large c , charge separation exists at a magnitude that can be consistently determined using (2.43), *i.e.*, the divergence constrain on the electric field (Gauss’s law). Some authors [39, 89] discuss this using scaling arguments in the form of a ‘‘quasi-neutrality approximation’’ for the single-fluid MHD equations. We show that in the $c \rightarrow \infty$ limit, strict charge neutrality holds in the limiting 2FMHD system

because the divergence constraint only applies to first and higher order perturbations of ρ_c that do not contribute in any other zeroth order equations.

It follows from zeroth-order charge neutrality that the evolution of the electric field, \mathbf{E} , is locked with that of the magnetic field, \mathbf{B} in the 2FMHD equations. To obtain \mathbf{B} , one uses Faraday's law (2.50f) and eliminates both \mathbf{j} and \mathbf{E} by taking the curl of the current equation (2.50c) after utilizing (2.50g). \mathbf{E} is then retrieved after \mathbf{B} , \mathbf{u} and p_e are known, again using the current equation. It is also clear that the electron pressure decouples from the system, owing to the identity $\nabla \times (\nabla p_e) = 0$.

We remark that the plasma parameter β can be absorbed into \mathbf{B} and \mathbf{E} by defining

$$\bar{\mathbf{B}} = \frac{\mathbf{B}}{\sqrt{\beta}}, \quad \bar{\mathbf{E}} = \frac{\mathbf{E}}{\sqrt{\beta}}. \quad (2.52)$$

This also applies to the original non-dimensional 2FP equations (2.15-2.24d). This is equivalent to removing the independent scale B_{ref} in Eq. (2.5) and replacing it by $(2\mu_0 n_{\text{ref}} m_{\text{ref}} u_{\text{ref}}^2)^{1/2}$. As a result, Eqs. (2.50a-2.50h) expressed in terms of these rescaled magnetic and electric fields become independent of β , effectively by substituting $\beta = 1$ and writing $\bar{\mathbf{B}}$ and $\bar{\mathbf{E}}$ in places of \mathbf{B} and \mathbf{E} respectively in the original equations. The β -independent equation set is computationally convenient, since any strength of the external magnetic field can still be accommodated by suitable choice of initial/boundary conditions. The benefit of using the 2FMHD equations over the two-fluid model for numerical solutions is that the infinite speed-of-light limit eliminates fast transients that require stringently small time steps to resolve. However, as discussed above, the disadvantage of the 2FMHD equations is that the \mathbf{E} field has to be solved implicitly through other variables, whose solutions depend on nested differential operators that are expensive to compute.

2.3.2 Dispersion relation for 2FMHD

Plane wave solutions

Next we examine the behavior of waves admitted by the asymptotic two-fluid system as $c \rightarrow \infty$, considering again a homogeneous background. Using the same

perturbations given in Eqs. (2.26), the two-fluid system in this limit linearizes to

$$\begin{aligned}
\frac{\partial \rho'}{\partial t} + \nabla \cdot \mathbf{u}' &= 0, \\
\frac{\partial \mathbf{u}'}{\partial t} + \nabla p' &= \frac{1}{d_S} \sqrt{\frac{2}{\beta}} \mathbf{j}' \times \mathbf{b}, \\
\frac{\partial \mathbf{j}_1}{\partial t} + \frac{1+M}{M} \nabla p' - \frac{(1+M)^2}{M} \nabla p'_e &= \sqrt{\frac{2}{\beta}} \frac{(1+M)^2 (\mathbf{E}' + \mathbf{u}' \times \mathbf{b}) + (1-M^2) \mathbf{j}' \times \mathbf{b}}{M d_S}, \\
\frac{\partial p'}{\partial t} + \nabla \cdot \mathbf{u}' &= 0, \\
\frac{\partial p'_e}{\partial t} + \alpha \nabla \cdot \mathbf{u}' &= 0, \\
\frac{\partial \mathbf{B}'}{\partial t} + \nabla \times \mathbf{E}' &= 0, \\
\nabla \times \mathbf{B}' &= \frac{1}{d_S} \sqrt{\frac{\beta}{2}} \mathbf{j}'.
\end{aligned} \tag{2.53}$$

In this case, it is convenient to eliminate \mathbf{j}_1 and \mathbf{E}_1 since p_{e1} does not enter the equations after the curl of \mathbf{E}_1 is taken. An application of the plane wave ansatz Eq. (2.28), together with Eq. (2.29), yields the following linear system in terms of \mathbf{u}_1 and \mathbf{B}_1 ,

$$\begin{bmatrix}
k_\perp^2 - \omega^2 & 0 & k_\perp k_\parallel & -\frac{2k_\parallel \omega}{\beta} & 0 & \frac{2k_\perp \omega}{\beta} \\
0 & \omega & 0 & 0 & \frac{2k_\parallel}{\beta} & 0 \\
k_\perp k_\parallel & 0 & k_\parallel^2 - \omega^2 & 0 & 0 & 0 \\
-k_\parallel & 0 & 0 & -\left(\frac{d_S^2 M k_\parallel^2}{(M+1)^2} + 1\right) \omega & i\sqrt{\frac{2}{\beta}} \frac{d_S (1-M) k_\parallel^2}{M+1} & \frac{d_S^2 M k_\perp k_\parallel \omega}{(M+1)^2} \\
0 & -k_\parallel & 0 & i\sqrt{\frac{2}{\beta}} \frac{d_S (M-1) k_\parallel^2}{M+1} & -\frac{(M(k^2 d_S^2 + M+2) + 1) \omega}{(M+1)^2} & i\sqrt{\frac{2}{\beta}} \frac{d_S (1-M) k_\perp k_\parallel}{M+1} \\
k_\perp & 0 & 0 & \frac{d_S^2 M k_\perp k_\parallel \omega}{(M+1)^2} & i\sqrt{\frac{2}{\beta}} \frac{d_S (M-1) k_\perp k_\parallel}{M+1} & -\left(\frac{d_S^2 M k_\perp^2}{(M+1)^2} + 1\right) \omega
\end{bmatrix}
\begin{bmatrix}
\mathbf{u}' \\
\mathbf{B}'
\end{bmatrix} = 0. \tag{2.54}$$

The corresponding wave dispersion relation follows from the matrix determinant, giving a polynomial equation

$$\sum_{m=1}^4 \sum_{n=1}^4 C_{mn} k^{2(m-1)} \omega^{2(n-1)} = 0, \tag{2.55}$$

where the coefficients C_{mn} form the following matrix,

$$C = \begin{bmatrix}
0 & 0 & 0 & 1 \\
0 & 0 & -\frac{2\lambda^2 + \beta + 2}{\beta} & \frac{2d_S^2 M}{(M+1)^2} \\
0 & \frac{4\lambda^2(\beta+1)}{\beta^2} & -\frac{2d_S^2 (M^2 \lambda^2 + \lambda^2 + M(-\lambda^2 + \beta + 1))}{(M+1)^2 \beta} & \frac{d_S^4 M^2}{(M+1)^4} \\
-\frac{4\lambda^4}{\beta^2} & \frac{2d_S^2 (M^2 + 1) \lambda^2}{(M+1)^2 \beta} & -\frac{d_S^4 M^2}{(M+1)^4} & 0
\end{bmatrix}. \tag{2.56}$$

It is straightforward to verify that one could arrive at the same result by directly taking the limit, $c \rightarrow \infty$, of the two-fluid dispersion relation derived in Eqs. (2.32), after the renormalization where the coefficient A_{14} is made unity, *i.e.*, $C_{mn} = \lim_{c \rightarrow \infty} (A_{mn}/A_{14})$. This provides a shortcut to obtain dispersion relations for other closed limiting systems to be derived in the following sections.

Comparison with two-fluid plasma (2FP) waves

Evidently, compared to the original 2FP dispersion relation, Eq. (2.55) is now only of order three in both of ω^2 and k^2 , suggesting that the cutoff and plasma frequencies occurring for $k \rightarrow 0$, $\omega > 0$ are eliminated together with the double electromagnetic waves traveling at the speed-of-light, due to charge neutrality. More is revealed by examining the high-frequency asymptote as $k \rightarrow \infty$, $\omega \rightarrow \infty$, that is, solving

$$C_{34}k^4\omega^6 + C_{43}k^6\omega^4 = 0, \quad (2.57)$$

showing that there is now only one positive root given by

$$\omega_{os} = k. \quad (2.58)$$

Therefore compared to Eqs. (2.35) and (2.36), the electron and ion sound waves in the two-fluid system now coalesce into one overall sound wave, traveling at the speed of $u_{\text{ref}} = \sqrt{\gamma\tilde{p}_0/\tilde{\rho}_0}$ in real units. This is caused by the linearization given in Eqs. (2.53), where the electron pressure always remains a constant fraction, α , of the total pressure. Since ion and electron also share the same number density in the $c \rightarrow \infty$ limit, their temperature ratio must stay the same at all time. Therefore in the linear region, the two species described by the 2FMHD equations behave like a mixture, permitting only one sonic speed. And the difference between ω_{os} and $\omega_{is,es}$ will not decay when c is increased, due to the limit being singular in the dispersion polynomial which decreases its order.

The low-frequency limit in this case follows from

$$C_{14}\omega^6 + C_{23}k^2\omega^4 + C_{32}k^4\omega^2 + C_{41}k^6 = 0, \quad (2.59)$$

and coincides with the continuous limit of Eqs.(2.38) and (2.39) as $c \rightarrow \infty$, giving exactly the well-known MHD 3-wave,

$$\omega_A = k_{\parallel}\sqrt{\frac{2}{\beta}}, \quad \omega_{f,s} = \left(\frac{k^2}{2} \left(\frac{\beta}{2} + 1 \right) \pm k \sqrt{\left[\frac{k}{2} \left(\frac{\beta}{2} + 1 \right) \right]^2 - \frac{2k_{\parallel}^2}{\beta}} \right)^{1/2}. \quad (2.60)$$

More interestingly, the cyclotron resonance obtained from

$$\left(C_{41} + A_{42}\omega^2 + A_{43}\omega^4\right) k^6 = 0 \quad (2.61)$$

is unaffected in the infinite speed-of-light limit, giving exactly the same ion and electron resonant frequencies as before in Eq. (2.34).

Figure 2.1 shows a direct comparison between the oblique waves of the 2FP system and the infinite speed-of-light 2FMHD system, where all positive roots of Eqs. (2.32) and (2.55) are plotted. The parameters (λ , α , β , d_S , and M) are chosen in accordance with the numerical example for a hydrogen plasma shown in Fig. 3.1 of Ref. [38].

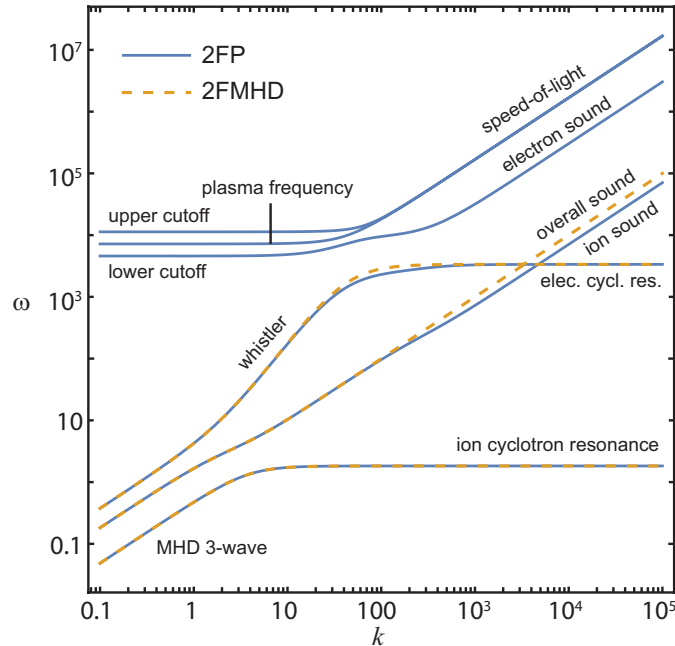


Figure 2.1: Dispersion diagram for waves from an ideal two-fluid hydrogen plasma 2FP (solid lines) and its limit 2FMHD as $c \rightarrow \infty$ (dashed lines). $\lambda = 0.5$, $\alpha = 0.5$, $\beta = 0.15$, $d_S = 1$, $M = 1836$. In particular, $c = 170$ for the two-fluid system.

It is seen that indeed the infinite speed-of-light assumption leads to a loss of information about the high-frequency waves and a systematic departure from the ion or electron sound wave at high wave numbers, where sonic speeds for individual species merge into a combined value. Apart from this, the cyclotron resonance is retained exactly for both ion and electron, and there is no noticeable deviation introduced by the $c \rightarrow \infty$ limit at low frequencies. We also note that the branch corresponding to the fast magnetosonic wave smoothly changes into the Whistler

branch [99] (with twice the slope on a $\log \omega$ vs $\log k$ plot) before it asymptotes to the electron cyclotron wave.

2.4 Small electron Inertia limit

Conventionally, a single-fluid plasma model refers to the approximation that electron inertia is negligible compared to the ion's. This limit is investigated in this section by applying $\delta_M \equiv 1/M \rightarrow 0$ to the two-fluid equations in the center-of-mass frame given in Eqs. (2.15-2.24d), while keeping c , d_S and β fixed.

2.4.1 Leading-order equations: $M \rightarrow \infty$

Similar to (2.40), a perturbation series here in powers of δ_M is used

$$\zeta = \zeta_0 + \zeta_1 \delta_M + O(\delta_M^2). \quad (2.62)$$

Conveniently, this limit only applies to the momentum (2.17), current (2.18) and energy equation (2.20), where the miscellaneous terms in Eqs. (2.19) and (2.21) simplify, giving

$$\begin{aligned} \mathbf{f}_{mom} &= O(\delta_M), \quad \mathbf{f}_{cur} = \frac{-e p_{e0}}{m_i \delta_M} \mathbf{I} + O(\delta_M^0), \\ \mathbf{s}_{cur} &= \frac{-\sqrt{2} e (\rho_{c0} \mathbf{E}_0 + \mathbf{j}_0 \times \mathbf{B}_0)}{\sqrt{\beta} d_S m_i \delta_M} + O(\delta_M^0), \quad \mathcal{E}_{erg} = \frac{|\mathbf{E}_0|^2}{\beta c^2} + O(\delta_M^2), \\ \mathbf{f}_{erg} &= -\frac{\gamma}{\gamma - 1} \frac{m_i p_{e0} (\mathbf{j}_0 - \rho_{c0} \mathbf{u}_0)}{e \rho_0 - \rho_{c0} m_i} + O(\delta_M). \end{aligned} \quad (2.63)$$

Therefore under the expansion (2.62), collecting all of the leading order equations from (2.15-2.24d) gives another closed limiting system corresponding to the zero electron inertia limit at zeroth order. With the subscript zero removed, this system

reads,

$$\frac{\partial \rho}{\partial t} + \nabla \cdot (\rho \mathbf{u}) = 0, \quad (2.64a)$$

$$\frac{\partial \rho_c}{\partial t} + \nabla \cdot \mathbf{j} = 0, \quad (2.64b)$$

$$\frac{\partial \rho \mathbf{u}}{\partial t} + \nabla \cdot (\rho \mathbf{u} \mathbf{u} + p \mathbf{I}) = \frac{\sqrt{2}}{\sqrt{\beta} d_S} (\mathbf{j} \times \mathbf{B} + \rho_c \mathbf{E}), \quad (2.64c)$$

$$\nabla p_e = \frac{\sqrt{2}}{\sqrt{\beta} d_S} \left[-\frac{e\rho}{m_i} (\mathbf{E} + \mathbf{u} \times \mathbf{B}) + \rho_c \mathbf{E} + \mathbf{j} \times \mathbf{B} \right], \quad (2.64d)$$

$$\frac{\partial}{\partial t} \left(\mathcal{E} + \frac{|\mathbf{E}_0|^2}{\beta c^2} \right) + \nabla \cdot \left((\mathcal{E}_h + p) \mathbf{u} + \frac{2}{\beta} \mathbf{E} \times \mathbf{B} \right) + \nabla \cdot \mathbf{f}_{erg} = 0, \quad (2.64e)$$

$$\frac{\partial p_e}{\partial t} + \left(\mathbf{u} - \frac{m_i}{e\rho} \mathbf{j} \right) \cdot \nabla p_e + \gamma p_e \nabla \cdot \left(\mathbf{u} - \frac{m_i}{e\rho} \mathbf{j} \right) + S_{p_e} = 0, \quad (2.64f)$$

$$\frac{\partial \mathbf{B}}{\partial t} + \nabla \times \mathbf{E} = \mathbf{0}, \quad (2.64g)$$

$$\frac{1}{c^2} \frac{\partial \mathbf{E}}{\partial t} - \nabla \times \mathbf{B} = -\frac{\sqrt{\beta}}{\sqrt{2} d_S} \mathbf{j}, \quad (2.64h)$$

$$\frac{1}{c^2} \nabla \cdot \mathbf{E} = \frac{\sqrt{\beta}}{\sqrt{2} d_S} \rho_c, \quad (2.64i)$$

$$\nabla \cdot \mathbf{B} = 0, \quad (2.64j)$$

where

$$\begin{aligned} \mathcal{E} &= \mathcal{E}_h + \frac{|\mathbf{B}|^2}{\beta}, \quad \mathcal{E}_h = \frac{p}{\gamma - 1} + \frac{1}{2} \rho |\mathbf{u}|^2, \quad \mathbf{f}_{erg} = -\frac{\gamma}{\gamma - 1} \frac{m_i p_{e0} (\mathbf{j}_0 - \rho_{c0} \mathbf{u}_0)}{e \rho_0 - \rho_{c0} m_i}, \\ S_{p_e} &= \frac{\rho_c m_i}{e \rho - \rho_c m_i} \left[\left(\mathbf{u} - \frac{m_i}{e \rho} \mathbf{j} \right) \cdot \nabla p_e + \gamma p_e \nabla \cdot \left(\mathbf{u} - \frac{m_i}{e \rho} \mathbf{j} \right) \right]. \end{aligned} \quad (2.65)$$

Unlike the 2FMHD system [Eq. (2.50a-2.50h)], here none of the variables vanishes or decouples at zeroth order and all of the corresponding equations from the 2FP model are retained in the $M \rightarrow \infty$ limit. In particular is charge separation and the presence of electromagnetic waves persist. For this reason, we refer to Eqs. (2.64a-2.64j) as the single- or one- fluid plasma model, henceforth denoted as 1FP.

One notable difference compared to 2FP system is that the current equation (2.64d) now loses its time derivative, resembling some key features of the generalized Ohm's law used in the Hall-MHD model (to be derived in Section 2.6.1). In fact the system formed by (2.64a-2.64j) extends the Hall-MHD model by incorporating the electrostatic component of the Lorentz force, $\rho_c \mathbf{E}$, in addition to the magnetic component, $\mathbf{j} \times \mathbf{B}$, into the momentum, current, and energy conservations. Owing

$$\begin{aligned}
D_{14} &= -\frac{(\beta c^2 + 2)^2}{2\beta d_S^2} \\
D_{15} &= 1 \\
D_{23} &= \frac{(\beta c^2 + 2)(c^2(\beta + 2\lambda^2 + 2) + 2\lambda^2)}{2\beta d_S^2} \\
D_{24} &= -3\alpha\lambda^2 + \alpha - \frac{1}{2}c^2(\alpha\beta + 2\lambda^2 + 2) - \frac{2\alpha\lambda^2}{\beta c^2} - 1 \\
D_{25} &= \frac{\alpha d_S^2 \lambda^2}{c^2} \\
D_{32} &= -\frac{2c^2\lambda^2((\beta+1)c^2 + \lambda^2 + 1)}{\beta d_S^2} \\
D_{33} &= \frac{2\alpha\lambda^2(-\alpha\beta + \beta + 2)}{\beta} + c^4\lambda^2 + c^2\left(-\frac{\alpha^2\beta}{2} + \frac{1}{2}\alpha(\beta + 6\lambda^2 - 2) + \lambda^2 + 1\right) - \frac{2(\alpha-1)\alpha\lambda^4}{\beta c^2} \\
D_{34} &= \alpha d_S^2 \lambda^2 \left(\frac{\alpha-1}{c^2} - 2\right) \\
D_{41} &= \frac{2c^4\lambda^4}{\beta d_S^2} \\
D_{42} &= -\frac{\lambda^2(-4(\alpha-1)\alpha\lambda^2 + \beta c^4 + 2\alpha c^2(-\alpha\beta + \beta + 1))}{\beta} \\
D_{43} &= \alpha d_S^2 \lambda^2 (-2\alpha + c^2 + 2) \\
D_{51} &= -\frac{2(\alpha-1)\alpha c^2 \lambda^4}{\beta} \\
D_{52} &= (\alpha - 1)\alpha c^2 d_S^2 \lambda^2
\end{aligned}$$

Table 2.2: Non-zero coefficients of the dispersion equation (2.66) for an 1FP model.

to finite c these two forces could be comparable in magnitude. Therefore the 1FP description may also be viewed as an extension to the Hall-MHD model.

2.4.2 Dispersion relation for 1FP

Plane wave solutions

Since the structure of the 1FP system is that of the 2FP equations, plane waves subject to the zero electron inertia limit can be found following the same procedure described in Section 2.2.3, effectively turning each step into the corresponding $M \rightarrow \infty$ limit. The mass reference in this case is required to be \tilde{m}_i , such that $m_i = 1$, and (2.26) still holds. Without repeating details, the final expression for the dispersion relation of the 1FP model is given by

$$\sum_{m=1}^5 \sum_{n=1}^5 D_{mn} k^{2(n-1)} \omega^{2(m-1)} = 0, \quad (2.66)$$

where D_{mn} are listed in Table 2.2. As mentioned in Section 2.3.2, these coefficients can also be accessed as $D_{mn} = \lim_{M \rightarrow \infty} (A_{mn}/A_{15})$ [see Eq.(2.32)].

Comparison with 2FP waves

By retaining finite c , it is expected that electromagnetic waves should be present. Indeed, solving the high-frequency asymptotic relation,

$$D_{25}k^2\omega^8 + D_{34}k^4\omega^6 + D_{43}k^6\omega^4 + D_{52}k^8\omega^2 = 0, \quad (2.67)$$

produces two positive wave speeds,

$$\omega_{EM} = kc, \quad \omega_{is} = k\sqrt{1 - \alpha}, \quad (2.68)$$

for light and ion sound respectively. Compared to (2.36), although the M dependence is eliminated, the ion sound is still exact for our adjusted mass reference ($m_i = 1$). Because the electron is massless, its sonic speed escapes to infinity. Similarly the cyclotron resonance now occurs only for ions now, obtained from

$$D_{51}k^8 + D_{52}k^6\omega^2 = 0, \quad (2.69)$$

as

$$\omega_{ic} = \sqrt{\frac{2}{\beta}} \frac{\lambda}{d_S}. \quad (2.70)$$

A further consequence of the $M \rightarrow \infty$, $c < \infty$ limit lies in a reduced set of cut-off frequencies. Solving

$$D_{14}\omega^6 + D_{15}\omega^8 = 0 \quad (2.71)$$

gives a single cut-off frequency

$$\omega_{cut} = \frac{2 + \beta c^2}{\sqrt{2\beta} d_S} = \frac{\omega_{ic}}{\lambda} + \frac{\lambda \omega_{pi}^2}{\omega_{ic}}. \quad (2.72)$$

This is neither the large M limit of the plasma frequency nor upper/lower cutoffs observed in the original 2FP model, but is related to the ion plasma frequency ω_{pi} [95]. At the low-frequency end, the 1FP model exhibits identical behavior as the waves given in (2.39), where finite c corrects the MHD 3-wave, independent of M .

A numerical comparison between the 2FP and the 1FP systems is shown in Figure 2.2, where the same plasma considered in Figure 2.1 is used.

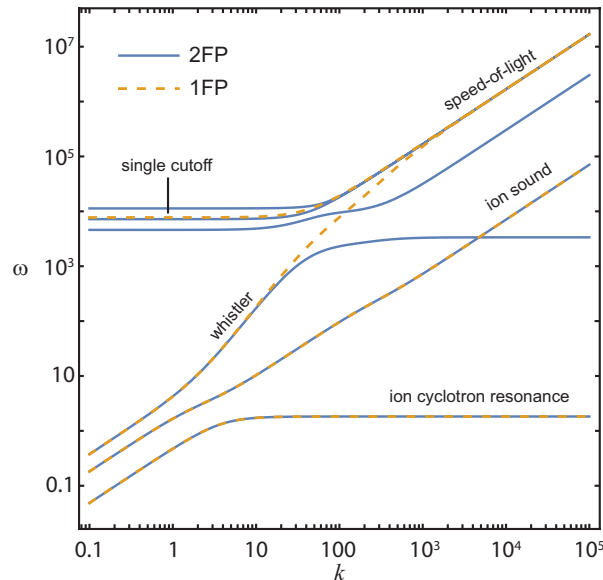


Figure 2.2: Dispersion diagram for waves from an ideal two-fluid hydrogen plasma 2FP (solid lines) and its limit 1FP as $M \rightarrow \infty$ (dashed lines). $\lambda = 0.5$, $\alpha = 0.5$, $\beta = 0.15$, $d_S = 1$, $c = 170$. In particular, $M = 1836$ for the two-fluid system.

It is seen that since the electron wave is lost, the whistler wave is forced to merge with the light wave at high frequencies, whereas the ion acoustic and resonant waves are preserved exactly. The single cutoff associated with the 1FP model should not be confused with the plasma frequency of the 2FP system, because these two do not communicate through a continuous limit.

2.5 Zero skin depth limit

There are three commonly used assumptions in magnetohydrodynamics, often described by the celebrated single-fluid ideal MHD equations [39]: (a) charge quasi-neutrality, (b) negligible electron inertia, and (c) small Larmor radius. Presently approximations (a) and (b) have been studied individually, first by applying formal limit of $c \rightarrow \infty$ in Section 2.3, and independently, $M \rightarrow \infty$ in Section 2.4, to the ideal 2FP equations. In this section, we isolate assumption (c), $d_L \rightarrow 0$, and revisit the concept of “quasi-neutrality” discussed in Section 2.3.1. Under the present non-dimensionalization scheme, the zero Larmor radius limit could be achieved by two means due to Eq. (2.11): either letting the plasma beta $\beta \rightarrow 0$ while keeping the d_S , fixed or requiring $d_S \rightarrow 0$, while keeping β fixed. We use the latter limit applied directly to the 2FP equations (2.15-2.24d), while keeping c , M , and β fixed. A brief discussion on the former route ($\beta \rightarrow 0$) is found in Appendix A.

2.5.1 Leading order equations: $d_S \rightarrow 0$

Perturbation analysis

In the 2FP model [Eqs. (2.15-2.24d)], field variables $\rho, \rho_c, p, p_e, \mathbf{u}, \mathbf{j}, \mathbf{B}$, and \mathbf{E} are expanded in powers of d_S this time in the form of

$$\zeta = \zeta_0 + \zeta_1 d_S + O(d_S^2), \quad (2.73)$$

where the subscripts indicate zeroth- and first- order quantities. The convergence properties of such expansion is not clear for the present study. It is most revealing to expand (2.24b) and (2.24c) first, showing that at order $O(d_S^{-1})$,

$$\mathbf{j}_0 = \mathbf{0}, \quad (2.74)$$

$$\rho_{c_0} = 0, \quad (2.75)$$

and at order $O(d_S^0)$,

$$\frac{1}{c^2} \frac{\partial \mathbf{E}_0}{\partial t} - \nabla \times \mathbf{B}_0 = -\frac{\sqrt{\beta}}{\sqrt{2}} \mathbf{j}_1, \quad (2.76)$$

$$\frac{1}{c^2} \nabla \cdot \mathbf{E}_0 = \frac{\sqrt{\beta}}{\sqrt{2}} \rho_{c_1}. \quad (2.77)$$

It follows immediately that the quasi-neutrality equation previously derived in (2.43) is here written alternatively with $d_S \rightarrow 0$ as,

$$\rho_c = \frac{d_S}{c^2} \sqrt{\frac{2}{\beta}} (\nabla \cdot \mathbf{E}_0) + O(d_S^2). \quad (2.78)$$

Also, compatibility with the evolution equation at first order [expanded using (2.73)] is established by substituting explicit expressions for \mathbf{j}_1 and ρ_{c_1} , given in (2.76) and (2.77), into the charge density continuity equation (2.16). As a result (2.16) can be safely removed from the $d_S \rightarrow 0$ limit.

Using Eqs. (2.73)-(2.75), the continuity (2.15) and momentum (2.17) equations jointly give at $O(d_S^0)$,

$$\rho_0 \left(\frac{\partial \mathbf{u}_0}{\partial t} + \mathbf{u}_0 \cdot \nabla \mathbf{u}_0 \right) = -\nabla p_0 + \sqrt{\frac{2}{\beta}} (\mathbf{j}_1 \times \mathbf{B}_0 + \rho_{c_1} \mathbf{E}_0), \quad (2.79)$$

which now involves first order perturbations \mathbf{j}_1 and ρ_{c_1} . Fortunately, these two unknowns can be consistently eliminated using (2.76) and (2.77) respectively. Further, the current equation (2.18) at $O(d_S^{-1})$ leads to

$$\mathbf{E}_0 + \mathbf{u}_0 \times \mathbf{B}_0 = 0, \quad (2.80)$$

which is precisely the Ohm's law used in the single-fluid ideal MHD equations. It is stressed that we arrive at this result without invoking the $c \rightarrow \infty$ limit.

Similarly, the energy equation (2.20) at $O(d_S^0)$ gives

$$\frac{\partial}{\partial t} \left(\mathcal{E}_{h_0} + \frac{|\mathbf{B}_0|^2}{\beta} + \frac{|\mathbf{E}_0|^2}{\beta c^2} \right) + \nabla \cdot \left((\mathcal{E}_{h_0} + p_0) \mathbf{u}_0 + \frac{2}{\beta} \mathbf{E}_0 \times \mathbf{B}_0 \right) = 0, \quad (2.81)$$

where

$$\mathcal{E}_{h_0} = \frac{p_0}{\gamma - 1} + \frac{1}{2} \rho_0 |\mathbf{u}_0|^2. \quad (2.82)$$

Subtracting the kinetic, magnetic and electric energies away from this total energy conservation leads to an equivalent equation for total pressure,

$$\frac{\partial p_0}{\partial t} + \mathbf{u}_0 \cdot \nabla p_0 + \gamma p_0 \nabla \cdot \mathbf{u}_0 = 0. \quad (2.83)$$

The leading order equation for electron pressure obtained from expanding (2.22) shares the same operator on total pressure, that is

$$\frac{\partial p_{e_0}}{\partial t} + \mathbf{u}_0 \cdot \nabla p_{e_0} + \gamma p_{e_0} \nabla \cdot \mathbf{u}_0 = 0. \quad (2.84)$$

Since p_{e_0} decouples from the general system, it can be omitted in the $d_S \rightarrow 0$ limiting set.

Combing these results, including those for (2.15) and (2.24a), with (2.84) as an auxiliary relation, a significantly simplified system is obtained by only applying the $d_S \rightarrow 0$ limit to the 2FP model,

$$\frac{\partial \rho_0}{\partial t} + \nabla \cdot (\rho_0 \mathbf{u}_0) = 0, \quad (2.85a)$$

$$\rho_0 \left(\frac{\partial \mathbf{u}_0}{\partial t} + \mathbf{u}_0 \cdot \nabla \mathbf{u}_0 \right) = -\nabla p_0 + \sqrt{\frac{2}{\beta}} (\mathbf{j}_1 \times \mathbf{B}_0 + \rho_{c_1} \mathbf{E}_0), \quad (2.85b)$$

$$\frac{\partial p_0}{\partial t} + \mathbf{u}_0 \cdot \nabla p_0 + \gamma p_0 \nabla \cdot \mathbf{u}_0 = 0, \quad (2.85c)$$

$$\mathbf{E}_0 + \mathbf{u}_0 \times \mathbf{B}_0 = \mathbf{0}, \quad (2.85d)$$

$$\frac{\partial \mathbf{B}_0}{\partial t} + \nabla \times \mathbf{E}_0 = \mathbf{0}, \quad (2.85e)$$

$$\frac{1}{c^2} \frac{\partial \mathbf{E}_0}{\partial t} - \nabla \times \mathbf{B}_0 = -\sqrt{\frac{\beta}{2}} \mathbf{j}_1, \quad (2.85f)$$

$$\frac{1}{c^2} \nabla \cdot \mathbf{E}_0 = \sqrt{\frac{\beta}{2}} \rho_{c_1}, \quad (2.85g)$$

$$\nabla \cdot \mathbf{B}_0 = 0. \quad (2.85h)$$

We call this system the Quasi-neutral MHD equations (QMHD) for reasons discussed in the following.

Discussion

Owing to simplifications made by (2.74) and (2.75), all of the leading order equations are independent of M in the $d_S \rightarrow 0$ limit. This does not imply that the QMHD is a single-fluid model. In fact for any $M > 0$, by solving the augmented system which includes (2.84) for the electron pressure, all field variables for individual species can be recovered via the transformation given in (2.13). Since ion and electron pressures are governed by the same equation, they behave thermally like a mixture.

That first order perturbations, namely ρ_{c_1} and \mathbf{j}_1 , appear in the leading order system is very different from the 2FMHD and 1FP models. An important consequence is that the quasi-neutral effect originating from the $\nabla \cdot \mathbf{E}_0$ constraint contributes explicitly in the QMHD model, while being neglected as a next order correction in the 2FMHD system, where strict neutrality applies (see derivation for (2.50a-2.50h) in Section 2.3.1). Here, because of finite c , charge separation at first order in d_S gives rise to an electrostatic force that is not negligible, and the displacement current is important in determining the first order current \mathbf{j}_1 .

Lastly, without invoking either $c \rightarrow \infty$ or $m \rightarrow \infty$, we arrive at a closed system that is remarkably similar to the single-fluid ideal MHD model. In fact further applying the $\delta_c = 1/c^2 \rightarrow 0$ limit to the QMHD system apparently leads to,

$$\begin{aligned} \rho_{c_1} &= O(\delta_c), \\ \nabla \times \mathbf{B}_0 - \sqrt{\frac{2}{\beta}} \mathbf{j}_1 &= O(\delta_c). \end{aligned} \tag{2.86}$$

Thus ρ_{c_1} exits the system together with the $\nabla \cdot \mathbf{E}$ constraint, eliminating the displacement current and electrostatic force. The ideal MHD equations are hence obtained exactly at order unity. This argument can be made rigorous by a perturbation analysis on the QMHD system, following a similar procedure given in Section 2.3.1.

2.5.2 Dispersion relation for QMHD

Plane waves associated with the QMHD system, (2.85a-2.85h), are found for the same homogeneous background considered in Section 2.2.3. Applying the ansatz given in (2.26), (2.28), and (2.29) again to the linearized QMHD system leads to

the following eigenvalue problem in terms of \mathbf{u}' and \mathbf{B}' ,

$$\begin{bmatrix} k_{\perp}^2 - \left(1 + \frac{2}{c^2\beta}\right)\omega^2 & 0 & k_{\perp}k_{\parallel} & -\frac{2}{\beta}k_{\parallel}\omega & 0 & \frac{2}{\beta}k_{\perp}\omega \\ 0 & -\left(1 + \frac{2}{c^2\beta}\right)\omega & 0 & 0 & -\frac{2k_{\parallel}}{\beta} & 0 \\ k_{\perp}k_{\parallel} & 0 & k_{\parallel}^2 - \omega^2 & 0 & 0 & 0 \\ -k_{\parallel} & 0 & 0 & -\omega & 0 & 0 \\ 0 & -k_{\parallel} & 0 & 0 & -\omega & 0 \\ k_{\perp} & 0 & 0 & 0 & 0 & -\omega \end{bmatrix} \begin{bmatrix} \mathbf{u}' \\ \mathbf{B}' \end{bmatrix} = 0. \quad (2.87)$$

The dispersion relation follows from the determinant, giving

$$\left[\left(1 + \frac{2}{\beta c^2}\right)\omega^2 - \frac{2k_{\parallel}^2}{\beta} \right] \left[\left(1 + \frac{2}{\beta c^2}\right)\omega^4 - \left(\frac{2+\beta}{\beta} + \frac{2\lambda^2}{\beta c^2}\right)k^2\omega^2 + \frac{2k_{\parallel}^2k^2}{\beta} \right] = 0. \quad (2.88)$$

Once again it is verified that this relation is also directly obtained from Eq. (2.32) as

$$\lim_{d_S \rightarrow 0} \sum_{m,n} \frac{A_{mn}}{A_{14}} k^{2n-2} \omega^{2m-2} = 0. \quad (2.89)$$

It can be safely concluded that all three limits of the 2FP model considered so far admit corresponding limiting dispersion relations, after the coefficient of a unique term in (2.32) is appropriately renormalized to unity for the limits to exist. Interestingly, (2.88) is also identical to the 2FP low-frequency asymptote given in (2.38), whose solutions are already shown in Eq. (2.39). It is not surprising that the QMHD waves provide finite speed-of-light corrections to the ideal MHD three waves. Curiously, despite finite c , electromagnetic waves traveling at the speed-of-light are lost in the QMHD system. This is because the electric field \mathbf{E}_0 is no longer an independent variable due to the ideal Ohm' law (2.85d) with the result that the Ampère's law (2.85f) serves as an explicit expression for the current perturbation \mathbf{j}_1 in terms of the magnetic field \mathbf{B}_0 .

2.6 Magnetohydrodynamic reductions

Having independently investigated the $c \rightarrow \infty$, $M \rightarrow \infty$ and $d_S \rightarrow 0$ limits in Sections 2.3, 2.4 and 2.5, respectively, we now investigate limiting forms of the 2FP model subject to multiple limits. This is achieved under the present framework by applying consecutive limits in terms of c , M , and d_S , while exhausting all permutations, should any two of the limits do not commute. Fortunately, it is not difficult to verify that all three limits do commute, resulting in two more sets

of equations that are widely used in magnetohydrodynamics, namely, the single-fluid Hall-MHD and ideal MHD equations. In this section, we demonstrate the derivation following one path for each of these two models without a full proof of the commutative property.

2.6.1 Hall-MHD reduction

First we utilize the $c \rightarrow \infty$ of the 2FP model (2FMHD) and apply additionally the zero electron mass limit $\delta_M = 1/M \rightarrow 0$. The plasma skin depth, d_S , and hence Larmor radius, d_L [see (2.8)], are held finite.

Leading order equations: $c \rightarrow \infty, M \rightarrow \infty$

Using perturbation expansions in the form given by Eq. (2.62), at order $O(\delta_M^0)$ the 2FMHD continuity (2.50a) and momentum (2.50b) equations jointly give

$$\rho \left(\frac{\partial \mathbf{u}}{\partial t} + \mathbf{u} \cdot \nabla \mathbf{u} \right) = -\nabla p + \frac{\sqrt{2}}{\sqrt{\beta} d_S} \mathbf{j} \times \mathbf{B} + O(\delta_M); \quad (2.90)$$

while the energy equation (2.50d) leads to

$$\frac{\partial \mathcal{E}}{\partial t} + \nabla \cdot \left((\mathcal{E}_h + p) \mathbf{u} + \frac{2}{\beta} \mathbf{E} \times \mathbf{B} - \frac{\gamma}{\gamma - 1} \frac{m_i p_e}{e \rho} \mathbf{j} \right) = O(\delta_M), \quad (2.91)$$

where

$$\mathcal{E}_h = \frac{p}{\gamma - 1} + \frac{1}{2} \rho |\mathbf{u}|^2, \quad \mathcal{E} = \mathcal{E}_h + \frac{|\mathbf{B}|^2}{\beta}. \quad (2.92)$$

The current equation (2.50c) at order $O(\delta_M^{-1})$ reduces to,

$$\frac{\sqrt{2}}{\sqrt{\beta} d_S} \left(\frac{e \rho}{m_i} (\mathbf{E} + \mathbf{u} \times \mathbf{B}) - \mathbf{j} \times \mathbf{B} \right) + \nabla p_e = O(\delta_M). \quad (2.93)$$

Recalling $n_i - n_e = O(\delta_c)$ from (2.43) and $m_e/m_i = \delta_M$ by definition, (2.93) can be shown to be asymptotically equivalent to the generalized Ohm's law [89] with zero resistivity, namely,

$$\frac{\sqrt{2}}{\sqrt{\beta} d_S} \left(\mathbf{E} + \mathbf{u} \times \mathbf{B} - \frac{1}{e n_e} \mathbf{j} \times \mathbf{B} \right) + \frac{1}{e n_e} \nabla p_e = O(\delta_c) + O(\delta_M). \quad (2.94)$$

Combined with the leading-order equations in the 2FMHD system, a complete set

of single-fluid equations, in the $\delta_c \rightarrow 0$, $\delta_M \rightarrow 0$ limit is given by

$$\frac{\partial \rho}{\partial t} + \nabla \cdot (\rho \mathbf{u}) = 0, \quad (2.95a)$$

$$\rho \left(\frac{\partial \mathbf{u}}{\partial t} + \mathbf{u} \cdot \nabla \mathbf{u} \right) = -\nabla p + \frac{\sqrt{2}}{\sqrt{\beta} d_S} \mathbf{j} \times \mathbf{B}, \quad (2.95b)$$

$$\frac{\partial \mathcal{E}}{\partial t} + \nabla \cdot \left((\mathcal{E}_h + p) \mathbf{u} + \frac{2}{\beta} \mathbf{E} \times \mathbf{B} - \frac{\gamma}{\gamma - 1} \frac{m_i p_e}{e \rho} \mathbf{j} \right) = 0, \quad (2.95c)$$

$$\frac{\partial p_e}{\partial t} + \left(\mathbf{u} - \frac{m_i}{e \rho} \mathbf{j} \right) \cdot \nabla p_e + \gamma p_e \nabla \cdot \left(\mathbf{u} - \frac{m_i}{e \rho} \mathbf{j} \right) = 0, \quad (2.95d)$$

$$\frac{\sqrt{2}}{\sqrt{\beta} d_S} \left(\mathbf{E} + \mathbf{u} \times \mathbf{B} - \frac{1}{e n_e} \mathbf{j} \times \mathbf{B} \right) + \frac{1}{e n_e} \nabla p_e = 0, \quad (2.95e)$$

$$\frac{\partial \mathbf{B}}{\partial t} + \nabla \times \mathbf{E} = \mathbf{0}, \quad (2.95f)$$

$$\nabla \times \mathbf{B} = \frac{\sqrt{\beta}}{\sqrt{2} d_S} \mathbf{j}, \quad (2.95g)$$

$$\nabla \cdot \mathbf{B} = 0. \quad (2.95h)$$

After converting to dimensional quantities, this equation set can be identified precisely as a more complete version of the Hall-MHD model (see Srinivasan & Shumlak [95], Hameiri [41] and Hagstrom & Hameiri [40]), obtained by both the $c \rightarrow \infty$, $M \rightarrow \infty$ limits. The electron thermal term, ∇p_e , in (2.94) is sometimes dropped in the Hall-MHD model [9, 42, 80], which is a choice made for simplicity typically based on physical arguments [89].

Dispersion relation for Hall-MHD

Waves admitted by the Hall-MHD system given in (2.95a-2.95h) can be routinely determined in the linear region using the Fourier ansatz (2.28). Here we take the established shortcut, by letting $M \rightarrow \infty$ in (2.55) [or $c \rightarrow \infty$ in (2.66)] to yield

$$\left(\omega^2 - \frac{2k_{\parallel}^2}{\beta} \right) \left(\omega^4 - \left(\frac{2}{\beta} + 1 \right) k^2 \omega^2 + \frac{2k_{\parallel}^2 k^2}{\beta} \right) - \frac{2d_S^2}{\beta} k_{\parallel}^2 k^2 \omega^2 (\omega^2 - k^2) = 0. \quad (2.96)$$

In its dimensional form, this relation is well-known [42, 80]. Asymptotic solutions to (2.96) feature the same overall sound and low-frequency waves as those observed in the 2FMHD system [see (2.58) and (2.60)]. But these differ from the 1FP model where the sonic speed of ions is retained and the MHD 3-wave depends on finite

c. A unique property of the Hall-MHD dispersion relation is that its Whistler wave frequency is now unbounded and grows quadratically with $k \rightarrow \infty$ as

$$\omega = \sqrt{\frac{2}{\beta}} d_S k_{\parallel} k. \quad (2.97)$$

This is different from the 2FMHD system where the Whistler wave levels off at the electron cyclotron resonance and the 1FP model where it merges with the speed-of-light.

These results are illustrated in Figure 2.3, where the entire Hall-MHD dispersion diagram is compared against that of the 2FMHD system in (a) and the 1FP model in (b). Clearly, the unbounded growth of the Whistler wave speed with k , also observed by Srinivasan & Shumlak [95], makes the Hall-MHD model distinct, as a double limit ($c \rightarrow \infty, M \rightarrow \infty$).

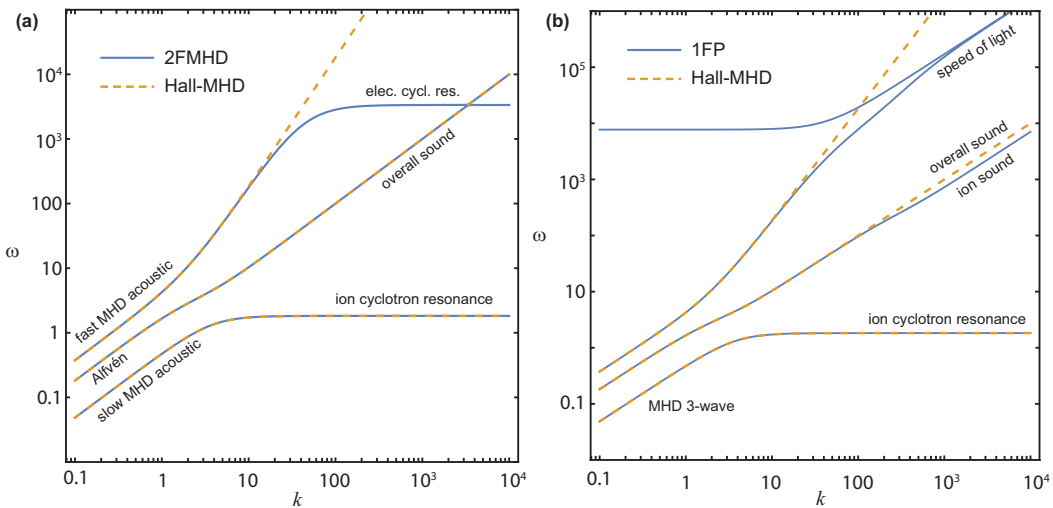


Figure 2.3: Waves comparison of a hydrogen plasma described by the Hall-MHD equations against (a) the 2FMHD model where $M = 1836$, and (b) the 1FP model, where $c = 170$. In both cases $\lambda = 0.5$, $\beta = 0.15$, and $d_S = 1$.

2.6.2 Ideal MHD reduction

It was noted in Section 2.5.1 that the celebrated single-fluid ideal MHD equations can be derived from the $c \rightarrow \infty$ limit in addition to the $d_S \rightarrow 0$ condition to the 2FP model, without restrictions on the ion or electron masses (finite M). Here, as an example of the limits being commutative, we interchange the limiting order and formally arrive at the ideal MHD system via taking the $d_S \rightarrow 0$ limit of the 2FMHD equations.

Leading-order equations: $c \rightarrow \infty, d_S \rightarrow 0$

The d_S perturbation expansions used in (2.73) are employed. For completeness, the expanded 2FMHD equations (2.50a-2.50h) are the following: continuity equation,

$$O(1) : \quad \frac{\partial \rho_0}{\partial t} + \nabla \cdot (\rho_0 \mathbf{u}_0) = 0; \quad (2.98)$$

momentum equation,

$$O(d_S^{-1}) : \quad \mathbf{j}_0 \times \mathbf{B}_0 = 0, \quad (2.99)$$

$$O(d_S^0) : \quad \rho_0 \left(\frac{\partial \mathbf{u}_0}{\partial t} + \mathbf{u}_0 \cdot \nabla \mathbf{u}_0 \right) + \nabla p_0 = -\nabla \cdot \left(\frac{m_i^2}{e^2} \frac{\mathbf{j}_0 \mathbf{j}_0}{M \rho_0} \right) + \sqrt{\frac{2}{\beta}} (\mathbf{j}_0 \times \mathbf{B}_1 + \mathbf{j}_1 \times \mathbf{B}_0); \quad (2.100)$$

current equation,

$$O(d_S^{-1}) : \quad \frac{eM\rho_0}{m_i} (\mathbf{E}_0 + \mathbf{u}_0 \times \mathbf{B}_0) + (1 - M) \mathbf{j}_0 \times \mathbf{B}_0 = \mathbf{0}; \quad (2.101)$$

energy equation,

$$O(d_S^0) : \quad \frac{\partial}{\partial t} \left(\mathcal{E}_0 + \frac{m_i^2}{e^2} \frac{|\mathbf{j}_0|^2}{2M\rho_0} \right) + \nabla \cdot \left((\mathcal{E}_{h_0} + p_0) \mathbf{u} + \frac{2}{\beta} \mathbf{E}_0 \times \mathbf{B}_0 \right) + \nabla \cdot \mathbf{f}_{erg_0} = 0, \quad (2.102)$$

where

$$\begin{aligned} \mathcal{E}_{h_0} &= \frac{p_0}{\gamma - 1} + \frac{1}{2} \rho_0 |\mathbf{u}_0|^2, \quad \mathcal{E}_0 = \mathcal{E}_{h_0} + \frac{|\mathbf{B}_0|^2}{\beta}, \\ \mathbf{f}_{erg_0} &= \frac{|\mathbf{j}_0|^2 m_i^2}{2e^2 M \rho_0} \mathbf{u}_0 - \frac{\gamma m_i ((M + 1)p_{e0} - p_0)}{(\gamma - 1)eM\rho_0} \mathbf{j}_0 \\ &\quad - \frac{|\mathbf{j}_0| m_i^2 (|\mathbf{j}_0| (M - 1)m_i - 2eM\rho_0 |\mathbf{u}_0|)}{2e^3 M^2 \rho_0^2} \mathbf{j}_0; \end{aligned} \quad (2.103)$$

electron pressure equation,

$$O(d_S^0) : \quad \frac{\partial p_{e0}}{\partial t} + \left(\mathbf{u}_0 - \frac{m_i}{e\rho_0} \mathbf{j}_0 \right) \cdot \nabla p_{e0} + \gamma p_{e0} \nabla \cdot \left(\mathbf{u}_0 - \frac{m_i}{e\rho_0} \mathbf{j}_0 \right) = 0; \quad (2.104)$$

and the reduced Maxwell equations,

$$\begin{aligned} O(d_S^{-1}) : \quad & \mathbf{j}_0 = \mathbf{0}, \\ O(d_S^0) : \quad & \nabla \times \mathbf{B}_0 = \sqrt{\frac{\beta}{2}} \mathbf{j}_1, \\ O(d_S^0) : \quad & \frac{\partial \mathbf{B}_0}{\partial t} + \nabla \times \mathbf{E}_0 = \mathbf{0}, \\ O(d_S^0) : \quad & \nabla \cdot \mathbf{B}_0 = 0. \end{aligned} \quad (2.105)$$

Since the lowest order Ampere's law again forces $\mathbf{j}_0 = \mathbf{0}$, the M dependence is eliminated in all of leading order equations, yielding the closed system given by,

$$\frac{\partial \rho_0}{\partial t} + \nabla \cdot (\rho_0 \mathbf{u}_0) = 0, \quad (2.106a)$$

$$\rho_0 \left(\frac{\partial \mathbf{u}_0}{\partial t} + \mathbf{u}_0 \cdot \nabla \mathbf{u}_0 \right) = -\nabla p_0 + \sqrt{\frac{2}{\beta}} \mathbf{j}_1 \times \mathbf{B}_0, \quad (2.106b)$$

$$\frac{\partial}{\partial t} \left(\mathcal{E}_{h_0} + \frac{|\mathbf{B}_0|^2}{\beta} \right) + \nabla \cdot \left((\mathcal{E}_{h_0} + p_0) \mathbf{u}_0 + \frac{2}{\beta} \mathbf{E}_0 \times \mathbf{B}_0 \right) = 0, \quad (2.106c)$$

$$\mathbf{E}_0 + \mathbf{u}_0 \times \mathbf{B}_0 = \mathbf{0}, \quad (2.106d)$$

$$\frac{\partial \mathbf{B}_0}{\partial t} + \nabla \times \mathbf{E}_0 = \mathbf{0}, \quad (2.106e)$$

$$\nabla \times \mathbf{B}_0 = \sqrt{\frac{\beta}{2}} \mathbf{j}_1, \quad (2.106f)$$

$$\nabla \cdot \mathbf{B}_0 = 0, \quad (2.106g)$$

where

$$\mathcal{E}_{h_0} = \frac{p_0}{\gamma - 1} + \frac{1}{2} \rho_0 |\mathbf{u}_0|^2. \quad (2.107)$$

As in the QMHD system [see (2.85a-2.85h)], the electron pressure, although decoupled, is governed by the same equation for total pressure, obtained from the energy conservation and given by

$$\left(\frac{\partial}{\partial t} + \mathbf{u}_0 \cdot \nabla + \gamma \nabla \cdot \mathbf{u}_0 \right) p_0 = 0. \quad (2.108)$$

That is, by utilizing $c \rightarrow \infty$ and $d_S \rightarrow 0$ alone, one arrives at the ideal MHD equations (2.106a-2.106g), where the single-fluid assumption made by $M \rightarrow \infty$ is not necessary. This finding suggests that a plasma with comparable ion and electron masses can still be well described by the ideal MHD equations in the center-of-mass frame, assuming c is large and d_S is small.

The behavior of the MHD system is now controlled by a single parameter β , which measures the relative magnitude of the thermal energy to the magnetic energy. The $\beta \rightarrow 0$ limit, outlined briefly in Appendix A, corresponds to a description of the overwhelming background magnetic field, whereas the $\beta \rightarrow \infty$ limit is the Euler equation for a fluid subject to no body force.

Dispersion Relation for Ideal MHD Equations

The MHD three-waves are classic results in plasma physics. Their dispersion relation is found by taking the $d_S \rightarrow 0$ limit of (2.55), or equivalently the $c \rightarrow \infty$

limit of (2.88), giving

$$\left(\omega^2 - \frac{2k_{\parallel}^2}{\beta}\right)\left(\omega^4 - \left(\frac{2}{\beta} + 1\right)k^2\omega^2 + \frac{2k_{\parallel}^2k^2}{\beta}\right) = 0, \quad (2.109)$$

whose solutions are already shown in Eq. (2.60). This clarifies that the MHD equations are a reasonably accurate model for low frequency, macroscopic ideal plasma processes. Compared to the QMHD model, where the global three waves are exact, the ideal MHD model introduces deviations from the 2FP system in this region that decay rapidly at a rate of $O(1/c^2)$ [see (2.39)].

Both of the QMHD and ideal MHD systems forget all information at high frequencies and thus fail to capture the ion cyclotron resonance and the overall sound wave occurring at large wave numbers that the Hall-MHD model is able to maintain, as shown in Figure 2.4.

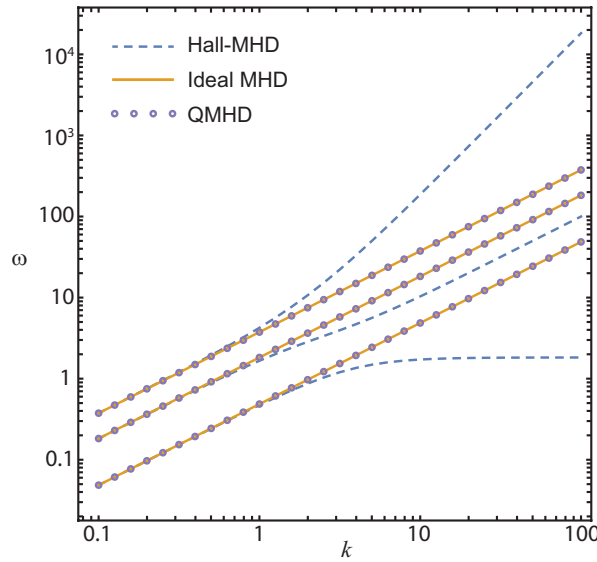


Figure 2.4: Dispersion diagram for waves of a hydrogen plasma described by the ideal MHD (solid lines), Hall-MHD (dashed line), and QMHD equations (circles). $\lambda = 0.5k$, $\beta = 0.15$; and $d_S = 1$ for Hall-MHD, $c = 10$ for QMHD.

Both incorporating the infinite speed-of-light assumption, the Hall-MHD and ideal MHD equations inherit the property of strict neutrality from the 2FMHD model in the limit, where first order charge separation does not affect the models at leading order. In particular, for the ideal MHD system where the skin depth is also made small, the magnitude of quasi-neutral effect is of order $O(d_S/c^s)$, asymptotically smaller than any other limiting models that are derived in the chapter.

2.7 Summary

By exploring various limits with respect to the speed-of-light, c , mass ratio, M , and plasma skin depth, d_S , five different limiting forms of the two-fluids plasma (2FP) equations are derived. Namely, (a) the 2FMHD equations, (b) the 1FP equations, (c) the QMHD equations, (d) the Hall-MHD equations, and (e) the ideal MHD equations. For all of the derived systems, their corresponding dispersion relations are also analytically determined and compared. Table 2.3 summarizes the key results.

c	M	d_S	β	d_L	d_D	Limiting equations	Dispersion relation	Label
$< \infty$	$< \infty$	> 0	> 0	> 0	> 0	Eqs.(2.6)	Eq. (2.32)	2FP
∞	$< \infty$	> 0	> 0	> 0	0	Eqs.(2.50)	Eq. (2.55)	2FMHD
$< \infty$	∞	> 0	> 0	> 0	> 0	Eqs.(2.64)	Eq. (2.66)	1FP
$< \infty$	≥ 0	0	> 0	0	0	Eqs.(2.85)	Eq. (2.88)	QMHD
∞	∞	> 0	> 0	> 0	0	Eqs.(2.95)	Eq. (2.96)	Hall-MHD
∞	≥ 0	0	> 0	0	0	Eqs.(2.106)	Eq. (2.109)	Ideal MHD

Table 2.3: Various limits of the ideal two-fluid plasma equations.

The hierarchy of closed systems listed in Table 2.3 document how plasmas can be appropriately modeled in situations where any combination of the limits investigated are appropriate. This may be particularly valuable for problems where only one of the limits applies, which lie in the parameter space in-between where the two-fluid plasma and Hall-MHD models are appropriate. The first of these systems, the 2FMHD equations, are the zeroth-order description in the $c \rightarrow \infty$ limit. Strict charge neutrality holds in the limiting 2FMHD equations, but it nonetheless uniquely determines the perturbation charge non-neutrality at first order for large but finite c . The electron pressure decouples from the system, and information on high frequency waves is lost. The second system, the 1FP equations, corresponds to the $M \rightarrow \infty$ limit. In this system, no variables decouple from the system, and the presence of charge separation and electromagnetic waves persists. The evolution equation for the current does lose its time derivative, however, resulting in a system of equations that might be viewed as an extension to the Hall-MHD model. Finally, the QMHD system corresponds the $d_S \rightarrow 0$ limit. In this system, first order perturbations in the charge density and current explicitly contribute to the leading order system, unlike in the previous two. Aside from the presence of these perturbations and the displacement current, the QMHD system is remarkably similar to the single-fluid MHD model.

IMPULSE-DRIVEN RMI IN HALL-MHD

This chapter is based on the following journal article:

Naijian Shen, D. I. Pullin, Vincent Wheatley and Ravi Samtaney. Impulse-driven Richtmyer-Meshkov instability in Hall-magnetohydrodynamics. *Physical Review Fluids*, 4(10):103902, 2019. doi: 10.1103/PhysRevFluids.4.103902.

We adopt the incompressible, Hall-MHD model in this chapter to study the evolution of an impulsively accelerated, perturbed density interface, separating two fluids in the presence of a background magnetic field normal to the mean interface. The solution to the corresponding linearized initial-value problem shows that the presence of the magnetic field suppresses the incipient RMI, and the interface undertaking oscillatory motion associated with the ion cyclotron effect. Markedly distinct from the ideal MHD model, the Hall-MHD vortex dynamics that facilitates the RMI suppression is emphasized.

3.1 Introduction

First introduced by Markstein [68], before it was studied theoretically by Richtmyer [85] and experimentally by Meshkov [71], the Richtmyer–Meshkov instability (RMI) refers to the growth of perturbations to an interface separating neutral fluids of different densities, typically due to a shock wave traversing the interface. The RMI is pertinent to a wide range of applications, including stellar evolution models in astrophysics [4], shock–flame interactions in combustion systems [52], mixing phenomena in supersonic jet engines [110] and more as surveyed in the review of Brouillette [16]. A richer literature is motivated by inertial confinement fusion (ICF), where a spherically converging shock is driven into a target capsule containing fuel, generating, in principle, conditions at the center sufficient to initiate fusion. The RMI however produces mixing between the capsule material and the fuel within, limiting final compression and hot-spot production, and thus the ability to achieve energy output [59].

The extreme temperatures required for ICF implosion inevitably cause rapid ionization of the involved materials, which then leads to interaction between the conducting fluids and magnetic fields that are imposed or self-generated [12, 49, 67, 90]. In

order to model the coupled evolution of plasmas and magnetic fields, several theoretical descriptions have been considered. Samtaney [87] and Wheatley, Samtaney & Pullin [104, 105] employed the single-fluid ideal magnetohydrodynamic (MHD) system to show that the growth of the RMI is suppressed in the presence of a magnetic field normal to the interface. Cao *et al.* [17] and Wheatley *et al.* [107] demonstrated that the suppression also occurs for a tangentially applied magnetic field, under the MHD scheme. Srinivasan & Tang [96] adopted the Hall-MHD model to examine the magnetic field generation and growth for the gravity induced Rayleigh-Taylor instabilities (RTI). More recently, Bond *et al.* [12] investigated computationally the RMI without initial magnetic field using the ideal two-fluid plasma equations. In order of decreasing complexity, Shen *et al.* [91] showed that the ideal two-fluid plasma equations, the Hall-MHD and regular MHD models are connected via a series of limiting processes with respect to the appropriately scaled parameters including the speed-of-light, the ion skin depth, and ion-to-electron mass ratio.

The present study concentrates on the Hall-MHD system, which is a reduced single-fluid model applicable in the regime where the speed-of-light is large compared to particle thermal speeds, and the electron mass is negligible compared to the ion mass. Such system is categorized as a magnetohydrodynamic model for its property of charge neutrality due to effectively infinite speed of light [91]. Nevertheless, the Hall-MHD model captures some features of the more general two-fluid plasma equations over small length scales such as the Larmor radius and skin depth for ions, that are missing in the ideal MHD equations. Under the Hall-MHD framework, we are interested in the effect of a magnetic field on the RMI flow resulting from a shock wave accelerating a density interface with a single-mode sinusoidal perturbation in amplitude. As an idealization, the thickness of the interface is assumed to be zero, unaffected by diamagnetic effects associated with finite Larmor radius [9]. This is illustrated in Fig. 3.1(a), where the 2D interface defines a contact discontinuity (CD) between fluids of densities ρ_1 and ρ_2 , that is to be processed by an incident normal shock of Mach number M , traversing in the same direction of an external uniform magnetic field of strength B . Cartesian coordinates are assigned so that the unperturbed interface lies in the x, y -plane and the single-mode perturbation of wavelength Λ and amplitude η_0 varies its magnitude along the x -direction.

A more convenient approach, enabling analytic solutions, is to consider an incompressible model for the mass and momentum transport, that mimics the shock driven

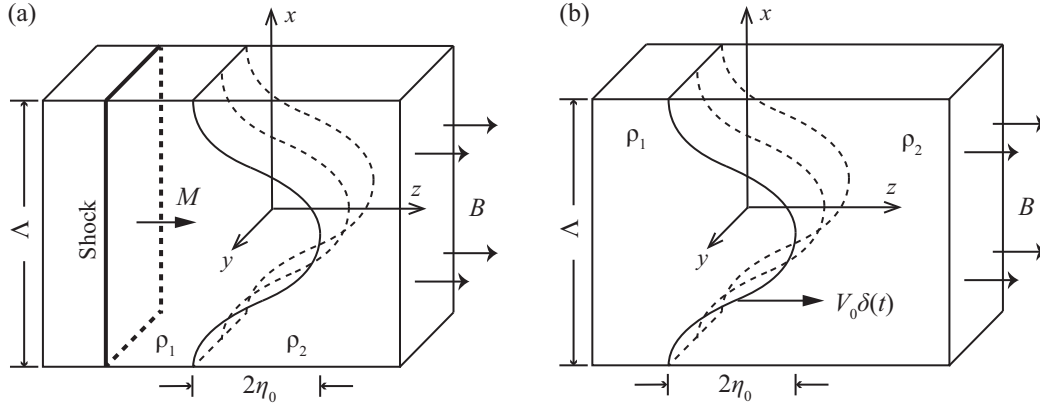


Figure 3.1: (a) Geometry and initial condition for compressible RMI with an external magnetic field. (b) The incompressible flow model that mimics the shock with an impulsive acceleration.

acceleration by an impulse [81, 104]. Since the electrons are not responsible for the mass transport in Hall-MHD, we consider incompressible flow for the ions throughout this paper. The impulse is depicted in Fig. 3.1(b), where the leading-order effect of the shock is approached by the acceleration, $V_0\delta(t)$, where V_0 matches the post-shock interface velocity that would result in a full RM flow, and $\delta(t)$ is the Dirac delta function of time t . The dynamic response to such an impulse is investigated using two models: first the incompressible ion, compressible electron (IICE) Hall-MHD, and second the incompressible ion, incompressible electron (IIIE) Hall-MHD.

This chapter is structured as follows: Section 3.2 first derives the general solutions to the linearized IICE Hall-MHD equations, using weak formulation. The Rankine-Hugoniot conditions for a contact discontinuity specific to the Hall-MHD system are then discussed in order to uniquely close the problem. Section 3.3 explores the suppression mechanism for the RMI due to the presence of the magnetic field by examining the vorticity dynamics and performing asymptotic analysis for the IICE system. The alternative IIIE Hall-MHD model is introduced and analysed in Sec. 3.4. Illustrative results for the interface behavior and flow profiles are given for both models in Sec. 3.5, before conclusions are drawn in Sec. 3.6.

3.2 Incompressible ion Compressible electron Hall-MHD (IICE)

3.2.1 Governing equations

We begin with the flow model where the density interface perturbed by a single sinusoidal mode is impulsively accelerated to speed V_0 in the z -direction, due to the

forcing given by

$$\mathbf{f} = [\rho_1 + H(z) (\rho_2 - \rho_1)] V_0 \delta(t) \hat{\mathbf{z}}, \quad (3.1)$$

where $H(z)$ is the Heaviside function and $\hat{\mathbf{z}}$ is the unit vector in z -direction. This leads to a convenient noninertial reference frame that has acceleration $V_0 \delta(t) \hat{\mathbf{z}}$. A connection with a shock-generated Richtmyer-Meshkov flow can be made by identifying the present impulsive velocity V_0 with the velocity imparted to the CD by a shock-CD impact. This can be analysed by the solution to a suitable Riemann-type problem.

Unless otherwise specified, all variables are henceforth made dimensionless by choosing length scale Λ , velocity scale V_0 , magnetic field scale B , charge scale the proton charge e , mass scale the ion mass m_i , and mass density scale ρ_1 . These also lead to the derived reference quantities including the time scale Λ/V_0 , the particle number density scale ρ_1/m_i , the pressure scale $\rho_1 V_0^2$, the electric field scale $V_0 B$, and the electric current scale $e \rho_1 V_0 / m_i$. This normalization scheme arises naturally from the geometry and initial conditions of the present problem, but it differs the two-fluid plasma RMI study by Bond *et al.* [12], where the physical Larmor radius and Debye length are used to deduce reference scales for the magnetic field and fluid density.

As a result, one obtains the following non-dimensional ideal Hall-MHD equations [91] that govern the evolution of the initial impulse for incompressible ions and compressible electrons,

$$\nabla \cdot \mathbf{u} = 0, \quad (3.2a)$$

$$\rho \left(\frac{\partial \mathbf{u}}{\partial t} + \mathbf{u} \cdot \nabla \mathbf{u} \right) = -\nabla p + \frac{1}{d_L} \mathbf{j} \times \mathbf{B} + \mathbf{f} - \rho \delta(t) \hat{\mathbf{z}}, \quad (3.2b)$$

$$\frac{\partial p_e}{\partial t} + \left(\mathbf{u} - \frac{\mathbf{j}}{\rho} \right) \cdot \nabla p_e + \gamma p_e \nabla \cdot \left(\mathbf{u} - \frac{\mathbf{j}}{\rho} \right) = 0, \quad (3.2c)$$

$$\frac{\partial \mathbf{B}}{\partial t} + \nabla \times \mathbf{E} = \mathbf{0}, \quad (3.2d)$$

$$\mathbf{E} + \mathbf{u} \times \mathbf{B} = \frac{\mathbf{j} \times \mathbf{B}}{\rho} - \frac{d_L}{\rho} \nabla p_e, \quad (3.2e)$$

$$\nabla \times \mathbf{B} = \frac{\beta}{2d_L} \mathbf{j}, \quad (3.2f)$$

$$\nabla \cdot \mathbf{B} = 0, \quad (3.2g)$$

where $\mathbf{u} = (u, v, w)$ is the flow velocity, ρ is the mass density, \mathbf{j} is the electric current density, p is the total ion and electron pressure, p_e is the electron pressure,

γ is the specific heat ratio, \mathbf{E} is the electric field and \mathbf{B} is the magnetic field. Two dimensionless parameters are introduced, namely the normalized Larmor radius d_L , and the energy ratio β , defined as

$$d_L = \frac{V_0 m_i}{e B \Lambda}, \quad \beta = \frac{2 \mu_0 \rho_1 V_0^2}{B^2}. \quad (3.3)$$

The Larmor radius d_L is the normal radius of the helix along which an ion moves about background magnetic field lines while β measures the ratio of kinetic to magnetic energy. Following Shen [91], it is useful to define one more related parameter, the normalized ion skin depth d_S , given by

$$d_S = d_L \sqrt{\frac{2}{\beta}}, \quad (3.4)$$

which is independent of the applied magnetic field strength. Moreover, the regular MHD equations are retrieved by taking the limit of $d_S \rightarrow 0$ of the Hall-MHD system [91]. Clearly for any fixed β , the MHD limit is equivalently achieved by taking $d_L \rightarrow 0$. The limit $\beta \rightarrow \infty$ recovers strictly hydrodynamic flow.

3.2.2 Linearized system

We first obtain a base flow solution to (3.2) that corresponds to the impulsive acceleration of an unperturbed interface. This base flow has no x, y dependence and, owing to the choice of reference frame, the only nonzero vector is the external constant magnetic field. Denoted by the bar symbol, the base flow is thus given by

$$\begin{aligned} \bar{\mathbf{u}} = \bar{\mathbf{j}} = \bar{\mathbf{E}} = \mathbf{0}, \quad \bar{\mathbf{B}} = \hat{\mathbf{z}}, \\ \bar{\rho}(z) = \rho_1 + H(z)(\rho_2 - \rho_1), \\ \bar{p}(z, t) = p_0, \quad \bar{p}_e(z) = p_{e_0}, \end{aligned} \quad (3.5)$$

where p_0 and p_{e_0} are the constant background total pressure and electron pressure, respectively.

For the perturbed interface, the density profile is expressed as

$$\rho = \bar{\rho}(z - h), \quad (3.6)$$

where $h(x, t)$ is the position of the contact discontinuity and $h \ll 1$ is required to ensure a small perturbation for which linear theory applies. As a result, Eqs. (3.2) can be linearized around the base flow by perturbing all flow fields using the form

$$\xi(x, z, t) = \bar{\xi}(z) + \xi'(x, z, t), \quad (3.7)$$

where ξ generically represents the scalar pressures p and p_e , or the vector components of \mathbf{u} and \mathbf{B} ; ξ' is the corresponding perturbation of small magnitude (*i.e.*, $|\xi'| \ll |\bar{\xi}|$). In this formulation we assume no y -dependence since the density interface is only perturbed in the x -direction without loss of generality.

Using (3.2f), \mathbf{j} is immediately eliminated in terms of \mathbf{B} . Likewise, taking the curl of (3.2e) and substituting into (3.2d) eliminates both \mathbf{E} and p_e , since ρ is constant in each fluid ($z \neq h$). We note that these reductions are independent of linearization. Therefore, \bar{p}_e can be viewed as a decoupled quantity that does not directly affect the magneto-fluid dynamics in either fluid. However, its behavior in the vicinity of the interface does play a role in the CD jump conditions, which will be discussed subsequently in Sec. 3.2.4. For this consideration, the perturbed electron pressure, p'_e , is explicitly allowed to be discontinuous across the interface by writing

$$p'_e(x, z, t) = p'_{e1} + H(z - h)(p'_{e2} - p'_{e1}). \quad (3.8)$$

As a result, the Hall-MHD system (3.2) linearizes to give

$$\frac{\partial u'}{\partial x} + \frac{\partial w'}{\partial z} = 0, \quad (3.9a)$$

$$\rho \frac{\partial u'}{\partial t} + \frac{\partial p'}{\partial x} = \frac{2}{\beta} \left(\frac{\partial B'_x}{\partial z} - \frac{\partial B'_z}{\partial x} \right), \quad (3.9b)$$

$$\rho \frac{\partial v'}{\partial t} = \frac{2}{\beta} \frac{\partial B'_y}{\partial z}, \quad (3.9c)$$

$$\rho \frac{\partial w'}{\partial t} + \frac{\partial p'}{\partial z} = (\rho_2 - \rho_1)[H(z) - H(z - h)]\delta(t), \quad (3.9d)$$

$$\frac{\partial B'_x}{\partial t} = \frac{\partial u'}{\partial z} + \frac{2d_L}{\beta\rho} \frac{\partial^2 B'_y}{\partial z^2}, \quad (3.9e)$$

$$\frac{\partial B'_y}{\partial t} = \frac{\partial v'}{\partial z} - \frac{2d_L}{\beta\rho} \frac{\partial}{\partial z} \left(\frac{\partial B'_x}{\partial z} - \frac{\partial B'_z}{\partial x} \right), \quad (3.9f)$$

$$\frac{\partial B'_z}{\partial t} = \frac{\partial w'}{\partial z} - \frac{2d_L}{\beta\rho} \frac{\partial}{\partial z} \left(\frac{\partial B'_y}{\partial x} \right), \quad (3.9g)$$

$$\frac{\partial B'_x}{\partial x} + \frac{\partial B'_z}{\partial z} = 0, \quad (3.9h)$$

where $B'_{x,y,z}$ are the three components of \mathbf{B}' . In particular, a simple auxiliary equation for p'_e follows from (3.2a) and (3.2f),

$$\frac{\partial p'_e}{\partial t} = 0. \quad (3.10)$$

Contrasting the strictly two-dimensional MHD case studied by Wheatley *et al.* [104], here the velocity and magnetic fields must allow nonzero components in

the y -direction, namely v' and B'_y , respectively, for Eqs. (3.9) to admit nontrivial solutions. Nonetheless, both v' and B'_y in (3.9) decouple from the system as $d_L \rightarrow 0$, and hence the linearized equations converge to those of the MHD case in the limit, as expected [see Eqs. (1)–(5) of Ref. [104]].

To proceed, we make the ansatz that the solutions we are seeking have the following single Fourier-mode form,

$$\xi'(x, z, t) = \tilde{\xi}(z, t)e^{ikx}, \quad (3.11)$$

where i is the imaginary unit and k is the non-dimensional wavenumber, which takes the value $k = 2\pi$ since a fixed wavelength of Λ (dimensional) is used for reference length. The contact is located at $z = h(x, t)$, where

$$h(x, t) = \eta(t)e^{ikx}, \quad (3.12)$$

and $\eta(t)$ is the perturbation amplitude.

After substituting (3.11) into (3.9), the temporal Laplace transform,

$$\mathcal{L}[\tilde{\xi}(t)] = \int_0^\infty \tilde{\xi}(t)e^{-st} dt, \quad \text{Re}(s) > 0, \quad (3.13)$$

is further applied in the region $z < 0$ and $z > h$, where the impulsive forcing vanishes in (3.9d). The initial conditions are taken at $t = 0^-$, just prior to the impulse, when the velocity and magnetic field perturbations are zero. As a result, we obtain for each fluid in the region subscripted by $i = 1$ or 2 , a system of ordinary differential equations (ODEs) in the Laplace space given by

$$ikU_i + \frac{dW_i}{dz} = 0, \quad (3.14a)$$

$$s\rho_i U_i + ikP_i = \frac{2}{\beta} \left(\frac{dH_{xi}}{dz} - ikH_{zi} \right), \quad (3.14b)$$

$$s\rho_i V_i = \frac{2}{\beta} \frac{dH_{yi}}{dz}, \quad (3.14c)$$

$$s\rho_i W_i + \frac{dP_i}{dz} = 0, \quad (3.14d)$$

$$s\rho_i H_{xi} = \rho_i \frac{dU_i}{dz} + \frac{2d_L}{\beta} \frac{d^2 H_{yi}}{dz^2}, \quad (3.14e)$$

$$s\rho_i H_{yi} = \rho_i \frac{dV_i}{dz} - \frac{2d_L}{\beta} \left(\frac{d^2 H_{xi}}{dz^2} - ik \frac{dH_{zi}}{dz} \right), \quad (3.14f)$$

$$s\rho_i H_{zi} = \rho_i \frac{dW_i}{dz} - \frac{2d_L}{\beta} ik \frac{dH_{yi}}{dz}, \quad (3.14g)$$

$$ikH_{xi} + \frac{dH_{zi}}{dz} = 0, \quad (3.14h)$$

where U, V, W, H_x, H_y, H_z and P are the Laplace transforms for $\tilde{u}, \tilde{v}, \tilde{w}, \tilde{B}_x, \tilde{B}_y, \tilde{B}_z$ and \tilde{p} , respectively.

Importantly, substituting the Fourier ansatz (3.11) of p'_e into (3.10) implies that for all $z \neq h$ and $t > 0$,

$$\tilde{p}_e(z, t) = \tilde{p}_e(z, 0^-) = 0, \quad (3.15)$$

Therefore the electron pressure field remains constant, *i.e.*,

$$p_e = p_{e0}. \quad (3.16)$$

3.2.3 General solution

Equations (3.14) can be reduced to a single sixth order ODE for W_i , given by

$$\mathcal{F}_i \left[\left(\frac{d^2}{dz^2} - k^2 \right) W_i(z) \right] = 0, \quad (3.17)$$

where $\mathcal{F}_i, i = 1, 2$, is the operator defined for an arbitrary function of z as follows:

$$\mathcal{F}_i = 4 \left(1 + d_L^2 s^2 \right) \frac{d^4}{dz^4} - 4s^2 \left(k^2 d_L^2 + \beta \rho_i \right) \frac{d^2}{dz^2} + s^4 \beta^2 \rho_i^2. \quad (3.18)$$

The fact that (3.17), derived for the present Hall-MHD model, is of order six is fundamentally different from the regular MHD case where its corresponding ODE for W_i is fourth order [see Eq. (12) in Ref. [104]]. Importantly, an order reduction cannot be realized by taking the limit $d_L \rightarrow 0$ of (3.17), where the highest derivative in \mathcal{F} persists. However, $\lim_{d_L \rightarrow 0} \mathcal{F}$ does factorize to produce a repeated root, rendering the ODE for W_i associated with the regular MHD model a subset of (3.17) and therefore sufficiently satisfied. This increased order of the present Hall-MHD model is a direct consequence of the velocity and magnetic fields having a self-generated y -component, whose significance is discussed also in Sec. 3.2.4, where the physical interface boundary conditions required for the Hall-MHD equations are addressed.

The general solution to (3.17) is composed of six linearly independent exponentials with coefficients to be determined from appropriate boundary conditions. To proceed, the definition of \mathcal{F} and Eqs. (3.14) imply the following relations:

$$\mathcal{F}_i \left[sH_{zi} - \frac{dW_i}{dz} \right] = 0, \quad (3.19)$$

$$\mathcal{F}_i [sH_{xi} - ikW_i] = 0, \quad (3.20)$$

$$\mathcal{F}_i [H_{yi}] = 0, \quad (3.21)$$

$$\mathcal{F}_i \left[s\rho_i \frac{dW_i}{dz} + k^2 P_i \right] = 0. \quad (3.22)$$

Equation (3.22), as a consequence of (3.20) and (3.21), immediately gives

$$Q_i \equiv s\rho_i \frac{dW_i}{dz} + k^2 P_i = A_i e^{-\mu_i z} + B_i e^{\mu_i z} + C_i e^{-\lambda_i z} + D_i e^{\lambda_i z}, \quad (3.23)$$

where A_i, B_i, C_i, D_i are coefficients to be determined, and

$$\lambda_i = \sqrt{\frac{s^2 (\beta\rho_i + k^2 d_L^2) + d_L \sqrt{s^4 (2\beta k^2 \rho_i - \beta^2 s^2 \rho_i^2 + k^4 d_L^2)}}{2d_L^2 s^2 + 2}}, \quad (3.24)$$

$$\mu_i = \sqrt{\frac{s^2 (\beta\rho_i + k^2 d_L^2) - d_L \sqrt{s^4 (2\beta k^2 \rho_i - \beta^2 s^2 \rho_i^2 + k^4 d_L^2)}}{2d_L^2 s^2 + 2}},$$

are the eigenvalues of the ODE system. Here we choose the branch of the square root that returns positive real part. The boundedness of Q_i at $z = \pm\infty$ immediately requires that $A_1 = B_2 = C_1 = D_2 = 0$.

Next, we observe that substituting (3.14d) into (3.23) yields

$$\frac{d^2 P_i}{dz^2} - k^2 P_i = -Q_i, \quad (3.25)$$

while using (3.14a)–(3.14c) and (3.14h), together with (3.23), leads to

$$\frac{d^2 H_{zi}}{dz^2} - k^2 H_{zi} = \frac{\beta}{2} Q_i. \quad (3.26)$$

Therefore taking the general expression for Q_i found in (3.23), P_i and H_{zi} can be solved exactly to give

$$P_i(z) = E_i e^{-k|z|} + I_i, \quad H_{zi}(z) = F_i e^{-k|z|} - \frac{\beta}{2} I_i, \quad (3.27)$$

where E_i and F_i are new coefficients to be determined and I_i are the following particular integrals:

$$I_1 = \frac{B_1 e^{\mu_1 z}}{k^2 - \mu_1^2} + \frac{D_1 e^{\lambda_1 z}}{k^2 - \lambda_1^2}, \quad I_2 = \frac{A_2 e^{-\mu_2 z}}{k^2 - \mu_2^2} + \frac{C_2 e^{-\lambda_2 z}}{k^2 - \lambda_2^2}. \quad (3.28)$$

Substituting (3.23) and (3.27) into (3.19) suggests that the coefficients E_i and F_i are necessarily related,

$$k^2 E_i + s^2 \rho_i F_i = 0. \quad (3.29)$$

With exact solutions for P_i and H_{zi} now found, all other variables follow directly from (3.14), giving

$$W_i(z) = -\frac{1}{s\rho_i} \frac{dP_i}{dz}, \quad U_i(z) = \frac{i}{k} \frac{dW_i}{dz}, \quad V_i(z) = \frac{i(sH_{zi} - dW_i/dz)}{k s d_L}, \quad (3.30)$$

$$H_{xi}(z) = \frac{i}{k} \frac{dH_{zi}}{dz}, \quad H_{yi}(z) = \frac{1}{s} \frac{dV_i}{dz} - \frac{2d_L}{s\beta\rho_i} \left(\frac{d^2 H_{xi}}{dz^2} - ik \frac{dH_{xi}}{dz} \right).$$

3.2.4 Interface jump conditions

With general solutions to Eqs. (3.14) to hand, the task remains to determine the six unknown coefficients A_2 , B_1 , C_2 , D_1 , F_1 , F_2 . This requires a dedicated discussion of the appropriate jump conditions across the contact discontinuity. For an adiabatically compressible Hall-MHD flow, Hameiri [41] derived in detail the general solvability conditions to support both shocks and CDs. Unlike the regular MHD model, the Hall-MHD shock jump conditions could be nonlocal, depending on the topology of the discontinuity surface and magnetic field. However, for the present investigation with planar density interface and a uniform magnetic field applied normal to the interface, Hameiri's global solvability constraints reduce to the usual Rankine-Hugoniot conditions, obtained by Rosenau *et al.* [86], from a set of local conservation laws. We adapt the derivation in the following.

The Hall-MHD evolution equations (3.2) can be formulated weakly in integral form as a system of conservation laws. In addition to (3.2a) and (3.2g) which are already in the divergence form, (3.2b) in the laboratory frame is equivalent to

$$\frac{\partial(\rho\mathbf{u})}{\partial t} + \nabla \cdot \left[\rho\mathbf{u}\mathbf{u} + \left(p + \frac{1}{\beta}B^2 \right) \mathbf{I} - \frac{2}{\beta}\mathbf{B}\mathbf{B} \right] = 0. \quad (3.31)$$

It was remarked earlier that the electron pressure cannot affect the flow dynamics in each fluid [9, 41, 86]. However, taking the curl of (3.2e) formally turns (3.2d) into

$$\frac{\partial\mathbf{B}}{\partial t} + \nabla \cdot \left[\mathbf{u}\mathbf{B} - \mathbf{B}\mathbf{u} + \frac{\mathbf{B}\mathbf{j} - \mathbf{j}\mathbf{B}}{\rho} \right] = d_L \nabla \times \left(\frac{\nabla p_e}{\rho} \right), \quad (3.32)$$

where the body force term is generally nonzero. However, under the present IICE model where the electron pressure is constant [see Eq. (3.16)], the body force vanishes across the entire flow domain. This holds particularly at the interface $z = h$, where $\nabla\rho$ diverges. The general consequences of both ρ and p_e being discontinuous will be further discussed in Sec. 3.4.2.

To proceed, for an incompressible CD, where the normal flow velocity across the surface vanishes in the interface-stationary reference frame, one must have, across the surface, conservation of mass, momentum and magnetic fluxes resulting from integrating (3.2a), (3.31), (3.32), and (3.2g) over a shrinking volume that encloses

the surface of discontinuity. This yields the following Rankine-Hugoniot conditions,

$$\llbracket u_n \rrbracket = 0, \quad (3.33a)$$

$$\llbracket \left(p + \frac{1}{\beta} B^2 \right) \hat{\mathbf{n}} - \frac{2}{\beta} B_n \mathbf{B} \rrbracket = 0, \quad (3.33b)$$

$$\llbracket \hat{\mathbf{n}} \times \frac{\mathbf{j} \times \mathbf{B}}{\rho} - B_n \mathbf{u}_t \rrbracket = 0, \quad (3.33c)$$

$$\llbracket B_n \rrbracket = 0, \quad (3.33d)$$

where the square brackets denote the difference in quantity between two sides of the interface, *i.e.*, $\llbracket \xi \rrbracket = \xi_2 - \xi_1$. The subscript “*n*” indicates the vector component normal to the surface and the subscript “*t*” indicates the two components tangential to the surface.

It immediately follows from (3.33) that, provided the magnetic field is not parallel to the interface, *i.e.* $B_n \neq 0$, both the pressure, p , and magnetic field, \mathbf{B} , must be continuous across the CD, whereas the tangential components of current \mathbf{j}_t , and velocity \mathbf{u}_t , can both jump discontinuously, forming a current sheet and shear layer at the interface. This result contrasts the properties of a regular MHD model where \mathbf{u}_t must also be continuous if $B_n \neq 0$. It is also noted that the continuity of \mathbf{B} validates the use of volume integration of Eq. (3.32) in order to obtain the correct jump condition, because the magnetic flux to be conserved remain uniformly bounded within the integral domain [41].

For our impulsively accelerated flow, the as yet unknown coefficients in Eqs. (3.27) can now be determined using (3.33). This is achieved by first linearising (3.33) around the base flow given in Eqs. (3.5) and (3.6), before the temporal Laplace transform is applied. As a result, the complete set of jump conditions across the interface [at $z = h(x, t) = \eta(t)e^{ikx}$] follows

$$\llbracket W \rrbracket_{z=0} = 0, \quad (3.34a)$$

$$\llbracket H_z \rrbracket_{z=0} = 0, \quad (3.34b)$$

$$\llbracket H_x \rrbracket_{z=0} = \llbracket H_y \rrbracket_{z=0} = 0, \quad (3.34c)$$

$$\llbracket U + \frac{2d_L}{\beta\rho} \frac{dH_y}{dz} \rrbracket_{z=0} = 0, \quad (3.34d)$$

$$\llbracket V - \frac{2d_L}{\beta\rho} \left(\frac{dH_x}{dz} - ikH_z \right) \rrbracket_{z=0} = 0, \quad (3.34e)$$

$$\llbracket P \rrbracket_{z=0} = \eta_0(\rho_2 - \rho_1). \quad (3.34f)$$

In particular, the pressure jump condition is obtained by integrating Eq. (3.9d) over the forcing region, $0 < z < h(x, t)$, and retaining terms of leading order in h to yield

$$\tilde{p}_2(0, t) - \tilde{p}_1(0, t) = (\rho_2 - \rho_1)\delta(t)\eta(t), \quad (3.35)$$

whose Laplace transform then leads to (4.32e).

Although equations (3.34) appear to be over-specified for only six unknown coefficients, (3.34b) and (3.34d) can be shown as linearly dependent. Therefore, by substituting (3.27), (3.30), and (3.29) into (3.34), one finds the unique solution to the vector $[A_2, B_1, C_2, D_1, F_1, F_2]$ as functions of s , hence Eqs. (3.14) is fully solved. The exact expressions for these coefficients are tedious, and are therefore omitted for brevity.

In the limit $d_L \rightarrow 0$, Eqs. (3.34) recovers all the jump boundary conditions for the regular MHD system, except that two new constraints are imposed on H_y and V , which are the two components in the y -direction that decouple in the MHD equations. This is precisely the reason that Eq. (3.17) is a sixth-order ODE, as opposed to its fourth-order MHD counterpart.

3.3 Analysis

The interface response to the impulsive acceleration is the present model for the Richtmyer-Meshkov instability in a Hall-MHD flow. For the present incompressible ion model, because the density interface is a material surface, the time derivative of its perturbation amplitude must equal the normal flow velocity at the interface [see Eq. (3.12)], that is,

$$\frac{d\eta}{dt} = \mathcal{L}^{-1} [W(z = 0; s)], \quad (3.36)$$

where \mathcal{L}^{-1} denotes the inverse Laplace transform, formally given by the Bromwich integral,

$$\mathcal{L}^{-1} [G(s)] = \frac{1}{2\pi i} \int_{r-i\infty}^{r+i\infty} G(s) e^{ts} ds, \quad (3.37)$$

where $r \in \mathbb{R}$ is greater than any real part of the singularities of the function $G(s)$. Consequently, the interface amplitude is calculated as

$$\eta(t) = \eta_0 + \mathcal{L}^{-1} \left[\frac{W(0; s)}{s} \right]. \quad (3.38)$$

Using the exact solution for either W_1 or W_2 , it can be verified that the initial interface growth rate is

$$\left. \frac{d\eta}{dt} \right|_{t=0^+} = \eta_0 k \mathcal{A}, \quad (3.39)$$

where $\mathcal{A} \equiv (\rho_2 - \rho_1)/(\rho_2 + \rho_1)$ is the Atwood number. This initial growth rate is the same as in both the MHD [104], and the hydrodynamic [85] cases, a result which is expected since the initial generation of baroclinic vorticity cannot be affected by the presence of the magnetic field. This is better understood in terms of circulation and vorticity dynamics discussed in the next section.

3.3.1 Vorticity dynamics

Owing to the boundary conditions (3.34d) and (3.34e), the tangential velocity obtained from the Hall-MHD description is allowed to slip through the interface, which implies circulation generation, particularly in the x, z -plane. To leading order, the circulation over a half wavelength (recalling $\Lambda = 1$, $k = 2\pi$) deposited at the interface is given by

$$\Gamma_0 = [U_2(0) - U_1(0)] \int_0^{\Lambda/2} e^{ikx} dx = \frac{2i\Delta U}{k}, \quad (3.40)$$

where $\Delta U \equiv U_2(0) - U_1(0)$. Analogous to (3.39), the initial circulation evaluates as

$$\gamma_0(t = 0^+) = \mathcal{L}^{-1} [\Gamma_0(s)] (t = 0^+) = 4\eta_0 \mathcal{A}, \quad (3.41)$$

as in the MHD case [105]. However, since $\Gamma_0(s) \neq 0$ for arbitrary s in general, the circulation deposit does not instantly leave the interface for the Hall-MHD model, as it does in the MHD case. This property strongly affects the suppression mechanism due to the magnetic field for the Richtmyer-Meshkov instability, as will be seen later.

By taking the curl of the momentum equation (3.2b), the evolution of vorticity, $\boldsymbol{\omega} = \nabla \times \mathbf{u}$, after the initial impulse, is governed by

$$\frac{\partial \boldsymbol{\omega}}{\partial t} + (\mathbf{u} \cdot \nabla) \boldsymbol{\omega} = (\boldsymbol{\omega} \cdot \nabla) \mathbf{u} + \frac{\nabla \rho \times \nabla p}{\rho^2} + \frac{2}{\beta \rho} [\nabla \times (\nabla \times \mathbf{B} \times \mathbf{B})], \quad (3.42)$$

where the baroclinic term explains the initial circulation generated during the impulsive acceleration. Away from the interface, we impose the same linearization (3.7) and perturbation (3.11), to rewrite the vorticity amplitude in the form

$$\tilde{\boldsymbol{\omega}} = \left(-\frac{\partial \tilde{v}}{\partial z}, -ik \tilde{w} + \frac{\partial \tilde{u}}{\partial z}, ik \tilde{v} \right). \quad (3.43)$$

Equation (3.42) then becomes

$$\frac{\partial \tilde{\boldsymbol{\omega}}}{\partial t} = \frac{2}{\beta \rho} \left(-\frac{\partial^2 \tilde{B}_y}{\partial z^2}, -ik \frac{\partial \tilde{B}_z}{\partial z} + \frac{\partial^2 \tilde{B}_x}{\partial z^2}, ik \frac{\partial \tilde{B}_y}{\partial z} \right). \quad (3.44)$$

Using (3.9e)–(3.9g), together with (3.43), and differentiating (3.44) with respect to t gives a forced wave equation for the vorticity vector in the smooth regions of the flow,

$$\frac{\partial^2 \tilde{\omega}}{\partial t^2} = \frac{2}{\beta \rho_i} \frac{\partial^2 \tilde{\omega}}{\partial z^2} + \frac{4d_L}{\beta^2 \rho_i^2} \left(\frac{\partial^4 \tilde{\mathbf{B}}}{\partial z^4} - k^2 \frac{\partial^2 \tilde{\mathbf{B}}}{\partial z^2} \right). \quad (3.45)$$

In the MHD limit, where $d_L \rightarrow 0$, the forcing term vanishes and the vorticity propagates in each side of the interface according to the wave equation, with normalized Alfvén speeds $v_A = \sqrt{2/(\beta \rho_i)}$ [91], for $i = 1, 2$, respectively. It may seem surprising that explicit d_L dependency is present in Eq. (3.45) but not in (3.44). This is because the Hall current affects the time derivative of (3.44) through the dynamics of the magnetic field [96]. Indeed, Eqs. (3.9e)–(3.9g) in Hall-MHD can be written compactly as

$$\frac{\partial \mathbf{B}'}{\partial t} = \frac{\partial \mathbf{u}'}{\partial z} - \frac{2d_L}{\beta \rho} \nabla \times (\nabla \times \mathbf{B}' \times \hat{z}), \quad (3.46)$$

giving origin to the wave production in (3.45). The MHD limit of Eq. (3.46) is equivalent to $\partial \mathbf{B}' / \partial t = \nabla \times (\mathbf{u}' \times \hat{z})$, which is also known as the induction equation and implies that the magnetic field is frozen into the fluid. A similar property was established for the canonical circulation, $\mathbf{Q} \equiv \nabla^2 \mathbf{B} - \mathbf{B}$, for an ion-stationary Hall-MHD flow by Yoon & Bellan [111].

Since circulation is only generated at the interface at $t = 0^+$ for the MHD flow before it is instantly carried away by the Alfvén waves, it is implied that the total circulation, integrated over the z -axis, must be conserved over time, as found by Wheatley *et al.* [105]. In contrast, for the present Hall-MHD flow, where $d_L > 0$, the forcing term in Eq. (3.45) is generally nonzero. Additionally, we have shown previously that there is always circulation accumulated on the interface. Therefore, the conservation of total circulation is not expected, which resembles a feature observed numerically for the two-fluid RMI flow [12].

3.3.2 Asymptotic analysis

In this section we explore analytically the behavior of the IICE Hall-MHD flow solution found in Sec. 3.2.3 for limiting values of the Larmor radius d_L and the energy ratio β .

Small Larmor radius: the MHD limit

It was previously shown in Sec. 3.2.3 that the $d_L \rightarrow 0$ limit of the linearized incompressible Hall-MHD system (3.14) contains the governing equations for the

MHD flow [104], and in Sec. 3.2.4 that the Hall-MHD jump conditions include all those of the MHD equations in this limit. Therefore, the Hall-MHD solutions obtained in Eq. (3.30) must converge to those in the MHD case. Indeed it is verified that for any fixed $\beta > 0$, the substitution of $d_L = 0$ into the exact expressions for coefficients $[A_2, B_1, \dots, F_2]$ produces a removable singularity. The limiting expression for W at the interface is given by

$$\lim_{d_L \rightarrow 0} W(0; s) = \frac{\eta_0 k \left[4k^2 (r - \sqrt{r}) v_{A_2} + 2k (\sqrt{r} - 1)^2 s - \sqrt{2\beta} (r - 1) s^2 \right]}{4k^3 r v_{A_2}^2 + 4k^2 r v_{A_2} s + 2k (r - 2\sqrt{r} - 1) s^2 - \sqrt{2\beta} (r + 1) s^3}, \quad (3.47)$$

where the normalization $r \equiv \rho_2/\rho_1 = \rho_2$ is used, and $v_{A_2} = \sqrt{2/\beta\rho_2}$ is the Alfvén speed in the region $i = 2$. This result agrees with the MHD solutions found by Wheatley *et al.* [104]. More interestingly, the y -components of the velocity and magnetic fields which are missing in the MHD description, decay identically in the limit:

$$\lim_{d_L \rightarrow 0} V_i(z; s) = \lim_{d_L \rightarrow 0} H_{y_i}(z; s) = 0. \quad (3.48)$$

This result validates the strictly two-dimensional flow assumption made by the MHD model [104, 105].

The success of recovering the MHD solution at leading order as $d_L \rightarrow 0$ usually suggests a first order Hall-MHD correction to the regular MHD theory for small values of d_L . Nonetheless, the existence of a uniformly-valid correction is contradicted by the exponential exponents associated with the general solutions, given in Eqs. (3.24). Specifically, these exponents (λ_i and μ_i) have singular points located at $s = \pm i/d_L$, therefore when expanded as power series around $d_L = 0$, the radius of convergence of the series decreases to zero as $\text{Im}(s)$ becomes large. Consequently, a uniformly-valid approximation of the exponents that is linear in d_L cannot exist along the entire Bromwich contour as would be required for accurate calculation of the inverse Laplace transform.

Small plasma beta limit

Here, we turn attention to a different flow region where the hydrodynamic forces are dominated by the electromagnetic forces, which corresponds to the asymptotic limit of $\beta \rightarrow 0$. Such limit may be approached while keeping either d_S or d_L fixed. In the former route where $\beta \rightarrow 0$ with d_S fixed, all field variables in (3.30) decay

asymptotically as

$$W_i, V_i \sim O(\beta^{1/2}), \quad U_i, H_{x_i}, H_{y_i}, H_{z_i} \sim O(\beta), \quad (3.49)$$

suggesting that increasing the external magnetic field eventually inhibits all dynamical motions in both flow regions separated by the density interface. In particular, the interface amplitude decays inversely proportional to the applied magnetic field strength for strong field, in agreement with the MHD theory [104].

However, the second route of taking $\beta \rightarrow 0$ while keeping d_L fixed produces a nontrivial solution. In this case, the eigenvalues, λ_i , μ_i , and consequently all the coefficients, $[A_2, B_1, \dots, F_2]$, can be Taylor expanded about $\beta = 0$ to give the leading order expressions:

$$\begin{aligned} A_2 &= \frac{\eta_0 k^2 (\rho_1 - \rho_2)^2 \rho_2}{\rho_1^2 (\alpha + 1) + 2\rho_2 \rho_1 (\alpha - 1) + \rho_2^2 (\alpha + 1)}, \\ B_1 &= \frac{\eta_0 k^2 \rho_1 (\rho_1 - \rho_2)^2}{\rho_1^2 - 2\rho_2 \rho_1 + \rho_2^2 + \alpha^2 (\rho_1 + \rho_2)^2}, \\ C_2 &= \frac{\eta_0 k^2 \rho_2 (\rho_2^2 - \rho_1^2)}{\rho_1^2 (\alpha^2 + \alpha) + 2\rho_2 \rho_1 (\alpha^2 - \alpha) + \rho_2^2 (\alpha^2 + \alpha)}, \\ D_1 &= \frac{\eta_0 k^2 \rho_1 (\rho_1^2 - \rho_2^2)}{\rho_1^2 (\alpha^2 + \alpha) + 2\rho_2 \rho_1 (\alpha^2 - \alpha) + \rho_2^2 (\alpha^2 + \alpha)}, \\ E_1 &= E_2 = F_1 = F_2 = 0, \end{aligned} \quad (3.50)$$

where $\alpha \equiv \sqrt{d_L^2 s^2 + 1}$.

It then follows from Eq. (3.30) that in the Laplace space, the limiting magnetic field perturbations are identically zero, *i.e.*, $H_x = H_y = H_z = 0$, while the flow velocities, U and W , are given by

$$U_{1,2}(z) = \pm \frac{i\eta_0 \mathcal{A} k d_L^2 s}{\alpha (\mathcal{A}^2 + \alpha)} \exp\left(-\frac{k d_L s}{\alpha} |z|\right), \quad (3.51)$$

$$W_{1,2}(z) = \frac{\eta_0 \mathcal{A} k d_L}{\mathcal{A}^2 + \alpha} \exp\left(-\frac{k d_L s}{\alpha} |z|\right). \quad (3.52)$$

Thus, using the Laplace final-value theorem, both velocities in the time domain converge to zero. More specifically, at $z = 0$, these expressions can be inverse transformed to give the x, z -plane circulation and the interface growth rate, using

Eqs. (3.41) and (3.36), respectively,

$$\hat{\gamma}_0 = \cos(\phi T) + \frac{1}{\mathcal{A}^2} \left[\phi \sin(\phi T) - \sin(T) + [\cos(T) - \cos(\phi T)] * \frac{J_1(T)}{T} \right], \quad (3.53)$$

$$\frac{d\hat{\eta}}{dt} = \cos(\phi T) - \frac{\mathcal{A}^2 \sin(\phi T)}{\phi} + \frac{\sin(\phi T)}{\phi} * \frac{J_1(T)}{T}, \quad (3.54)$$

where $\hat{\gamma}_0 \equiv \gamma_0/(4\eta_0\mathcal{A})$, $\phi \equiv \sqrt{1 - \mathcal{A}^4}$, $T \equiv t/d_L$, $\hat{\eta} \equiv \eta(\mathcal{A}\eta_0 k)^{-1}$, J_1 is the first order Bessel function of the first kind, and $*$ denotes the convolution integral defined as

$$f(T) * g(T) = \int_0^T f(\tau)g(T - \tau)d\tau. \quad (3.55)$$

Similarly, using Eq. (3.38), the limiting interface amplitude in the time domain is given by,

$$\frac{\hat{\eta}(t) - \hat{\eta}_0}{d_L} = \frac{\phi \sin(\phi T) - \mathcal{A}^2 [1 - \cos(\phi T)]}{\phi^2} + \frac{1 - \cos(\phi T)}{\phi^2} * \frac{J_1(T)}{T}, \quad (3.56)$$

whose long time behavior follows directly from (3.52),

$$\lim_{t \rightarrow \infty} \eta(t) = \eta_0 \left(1 + \frac{\mathcal{A} k d_L}{\mathcal{A}^2 + 1} \right). \quad (3.57)$$

In the zero β limit with d_L fixed, (3.53)–(3.56) clearly show oscillatory behavior of the flow occurring on a time scale T , that is completely specified by the non-dimensional Larmor radius d_L . This phenomenon differs significantly from the regular MHD case. For instance, unlike the MHD theory where the growth-rate of the interface amplitude decays monotonically towards zero, the limiting Hall-MHD model exhibits sinusoidal fluctuations with a decaying envelope, which eventually converges as $t \rightarrow \infty$, as seen in Eq. (3.54). We will see in Sec. 3.5 that such behavior can be extrapolated to solutions obtained for nonzero β .

To explain these periodic motions, the dispersive nature of the Hall-MHD equations is considered. In particular, the Hall-MHD system captures what is missing in the regular MHD description, the ion cyclotron resonance, whose frequency is inversely proportional to d_L [42, 91], naturally reflecting the new time scale T . Therefore, when the dimensional Larmor radius of the ions is comparable to the geometric length scale, namely, $d_L \sim O(1)$, the ion gyro motion around the overwhelming magnetic field lines becomes significant, as clearly manifested in the time domain solutions derived in this section, where time is more appropriately scaled by the cyclotron frequency and length is more suitably normalized by the Larmor radius.

Large Larmor radius limit

Inspired by the cyclotron frequency dependency discovered above, we here look for the asymptotic solution opposite to the MHD description, that is, the $d_L \rightarrow \infty$ limit for any constant time, $T = t/d_L$, which is rescaled according to the cyclotron frequency. Specifically, this limit is calculated by first applying the change of Laplace variable, $s \mapsto \sigma/d_L$. Exact expressions of the eigenvalues, λ_i and μ_i , hence all coefficients, $[A_2, B_2, \dots, F_2]$, derived from Eq. (3.34) as functions of σ , are then expanded in power series of $\epsilon \equiv 1/d_L$ around $\epsilon = 0$. Here, an effective distinguished limit is implied with $t \rightarrow \infty$ while holding T constant. Otherwise, convergent solutions cannot be found for the original time t , as $d_L \rightarrow \infty$.

Surprisingly, in the infinite Larmor radius limit with appropriate time rescaling, we obtain exactly the same expressions for all coefficients as those given in Eq. (3.50), except for F_1 and F_2 , whose asymptotic forms are found in the following,

$$F_1(\sigma) = \frac{\mathcal{A} \beta \eta_0 \rho_1 (\alpha + \mathcal{A}^2 - \mathcal{A} \sigma)}{2(\mathcal{A} - 1) (\alpha + \mathcal{A}^2)}, \quad F_2(\sigma) = \frac{\mathcal{A} \beta \eta_0 \rho_1 (\alpha + \mathcal{A}^2 + \mathcal{A} \sigma)}{2(1 - \mathcal{A}) (\alpha + \mathcal{A}^2)}, \quad (3.58)$$

where $\alpha = \sqrt{\sigma^2 + 1}$, as before. Therefore, the interface circulation deposit γ_0 , and the rescaled perturbation growth η/d_L (as a function of T), in this case are the same as those of the zero plasma beta limit, derived in Eqs. (3.53) and (3.56), respectively. Furthermore, nontrivial solutions in the Laplace space to the magnetic field perturbations $H_{x,y,z}$ appear in the $d_L \rightarrow \infty$ limit; for example, at the interface, one has

$$H_z(z = 0; \sigma) = \frac{\mathcal{A}^2 \beta \eta_0 \rho_1 (\alpha - \sigma + 1)}{2(\mathcal{A} - 1) (\alpha + \mathcal{A}^2)}. \quad (3.59)$$

However, the corresponding inverse transform of (3.59) in the cyclotron time scale ($\mathcal{L}^{-1} : \sigma \mapsto T$) again yields a vanishing physical field $\tilde{B}_z(T) = O(1/d_L)$, due to the change of variable $s = \sigma/d_L$.

Finally we remark on the commonalities between the zero beta limit and the infinite Larmor radius limit of the Hall-MHD theory. In both cases, the ion skin depth, d_S , defined in Eq. (3.4), approaches infinity, giving the same interface growth and circulation behavior that differs the MHD prediction, which corresponds to the zero ion skin depth limit of the Hall-MHD model. Graphical illustrations for this limit will be given in Sec. 3.5.1. Moreover, the magnetic field perturbations vanish in both cases, at a rate of $O(\beta)$ as $\beta \rightarrow 0$, or at a rate of $O(1/d_L)$ in the cyclotron time scale as $d_L \rightarrow \infty$.

3.4 Incompressible ion incompressible electron Hall-MHD (IIIE)

In this section, we propose a different Hall-MHD model which further assumes that the electrons also behave like an incompressible fluid, consistent with the ions. This leads to a subtle change in the CD jump conditions which then results in interface behavior different to that analysed previously for the IICE model.

3.4.1 Governing equations and general solutions

Although the Hall-MHD system is effectively a one-fluid model, it nevertheless allows a reconstruction of separate ion and electron velocity field, $\mathbf{u}_{i,e}$, respectively. Recalling $m_i = 1$ and $e = 1$ under the present non-dimensionlisation scheme, the species flow fields are given by [41, 91],

$$\mathbf{u}_i = \mathbf{u}, \quad \mathbf{u}_e = \mathbf{u} - \frac{\mathbf{j}}{\rho}. \quad (3.60)$$

Therefore the additional incompressible electrons assumption immediately gives the continuity condition in terms of the current \mathbf{j} ,

$$\nabla \cdot \left(\frac{\mathbf{j}}{\rho} \right) = 0, \quad (3.61)$$

at the cost of losing the dynamic equation for electron pressure, as (3.2c) in the IICE model. For completeness, the full set of governing equations in the impulsively accelerated frame is now given by

$$\begin{aligned} \nabla \cdot \mathbf{u} &= 0, & \nabla \cdot \left(\frac{\mathbf{j}}{\rho} \right) &= 0, \\ \rho \left(\frac{\partial \mathbf{u}}{\partial t} + \mathbf{u} \cdot \nabla \mathbf{u} \right) &= -\nabla p + \frac{1}{d_L} \mathbf{j} \times \mathbf{B} - \rho \delta(t) \hat{\mathbf{z}} + [\rho_1 + H(z) (\rho_2 - \rho_1)] \delta(t) \hat{\mathbf{z}}, \\ \frac{\partial \mathbf{B}}{\partial t} + \nabla \times \mathbf{E} &= \mathbf{0}, & \mathbf{E} + \mathbf{u} \times \mathbf{B} &= \frac{\mathbf{j} \times \mathbf{B}}{\rho} - \frac{d_L}{\rho} \nabla p_e, \\ \nabla \times \mathbf{B} &= \frac{\beta}{2d_L} \mathbf{j}, & \nabla \cdot \mathbf{B} &= 0. \end{aligned} \quad (3.62)$$

Importantly, it is noted that using system (3.62) in the smooth flow regions with constant density, the electron pressure p_e is indeterminate and the electric field \mathbf{E} is found up to a gauge. Indeed, we can define modified variables,

$$\mathbf{E}^* = \mathbf{E} - \nabla f, \quad p_e^* = p_e + \frac{\rho f}{d_L}, \quad (3.63)$$

using an arbitrary scalar function $f \in C^1(\mathbb{R}^3)$ to verify that Eqs. (3.62) are identically satisfied by the modified variables \mathbf{E}^* and p_e^* . For \mathbf{E} to be uniquely invertible, both

of its curl and divergence are needed. However $\nabla \cdot \mathbf{E}$ is related to small degree of charge separation that is not prescribed in Hall-MHD [91].

Nonetheless, p_e , \mathbf{E} and \mathbf{j} here can be conveniently eliminated as for the IICE model, leaving Eq. (3.61) automatically satisfied. The resulting simplified system thus becomes identical to Eqs. (3.9), subject to the same linearization around the base flow given in Sec. 3.2.2. Therefore, on each side of the perturbed interface, the general solutions to the flow velocity and magnetic fields derived in Sec. 3.2.3 are not affected by the additional treatment of incompressible electrons here. Similarly, the vorticity transport mechanism described in Sec. 3.3.1 applies the same for both of the IICE and IIIIE models.

3.4.2 Modified interface jump conditions

Losing the determinacy of p_e in the IIIIE model has not yet played a part in the flow dynamics in each fluid away from the density interface. However, as shown in Eq. (3.32), its behavior near the interface was crucial for the conservation of magnetic flux. Without an independent evolution equation for p_e in the present model, one cannot reach the constant electron pressure solution found in (3.16) for the IICE model. In this case, the forcing term in (3.32) could be evaluated using (3.6) and (3.12) to yield,

$$\mathbf{b} \equiv \nabla \times \left(\frac{\nabla p_e}{\rho} \right) = \left[\frac{\rho_1 - \rho_2}{\rho^2} \delta(z - \eta e^{ikx}) \left(\frac{\partial p_e}{\partial x} + ik\eta e^{ikx} \frac{\partial p_e}{\partial z} \right) \right] \hat{\mathbf{y}}, \quad (3.64)$$

where $\hat{\mathbf{y}}$ is the unit vector in y -direction. Further applying (3.8), (3.11) and integrating across the interface then gives

$$\int_{h^-}^{h^+} \mathbf{b} \cdot \hat{\mathbf{y}} dz = \frac{2ik(\rho_1 - \rho_2)}{(\rho_1 + \rho_2)^2} [\tilde{p}_{e1}(0^-, t) + \tilde{p}_{e2}(0^+, t)] e^{ikx} + O(\eta), \quad (3.65)$$

where $H(0) = 1/2$ for the Heaviside function is chosen.

Consequently, the conservation of magnetic flux across the interface as given in (3.33c) must be modified to incorporate the finite contribution from the body force. To leading order, (3.34e) should change into

$$\left[\left[V - \frac{2d_L}{\beta\rho} \left(\frac{dH_x}{dz} - ikH_z \right) \right] \right]_{z=0} = \frac{2ikd_L(\rho_1 - \rho_2)}{(\rho_1 + \rho_2)^2} \mathcal{L} [\tilde{p}_{e1}(0^-, t) + \tilde{p}_{e2}(0^+, t)] e^{ikx}, \quad (3.66)$$

which now serves as a constraint on p_e , which is indeterminate in the present IIIIE model.

Since (3.66) cannot be used effectively as a boundary condition in order to determine the coefficients $[A_2, B_1, C_2, D_1, F_1, F_2]$, closure must be established from the continuity condition (3.61), which is exclusive to the IIIE model and is nontrivial only across the interface, giving

$$\left[\left[\frac{j_n}{\rho} \right] \right] = \left[\left[\frac{1}{\rho} \frac{\partial B_y}{\partial x} \right] \right] = 0. \quad (3.67)$$

Therefore as density jumps over CD, the normal component of current density has to vanish. In the Laplace space, this implies at leading order,

$$\left[[H_y] \right]_{z=0} = 0. \quad (3.68)$$

Equation (3.67) effectively states that penetration of current across a density interface is prohibited, a direct consequence of both the ions and electrons being incompressible. The reason is that all charged particles for the IIIE model must move at the same velocity as the CD for the latter to evolve as a material surface. In contrast, for the previous IICE model, the electrons are free to move across the CD without violating conservation of mass in Hall-MHD.

3.4.3 Asymptotic flow field

Combining Eqs. (3.34a)–(3.34c), (3.34f), and (3.68) gives a linear system that uniquely determines the coefficients $[A_2, B_1, C_2, D_1, F_1, F_2]$, for the IIIE model. The complete solution differs from that discussed in Sec. 3.2.4. We present its asymptotic form in the same limits as discussed in Sec. 3.3.2.

First, it is no surprise that for a fixed energy ratio β , taking the $d_S \rightarrow 0$ limit recovers the regular MHD solution [see Sec. 3.3.2] in the IIIE model as well. Indeed the distinguishing boundary condition (3.68) is already met in the regular MHD model, where the vector fields are genuinely two-dimensional in the x, z -plane.

Here we focus on the large skin depth limit ($d_S \rightarrow \infty$), opposite to the regular MHD description, achieved via (a) taking $\beta \rightarrow 0$ while holding d_L fixed, or (b) letting $d_L \rightarrow \infty$ while keeping β finite. Analogous results to those obtained in Sec. 3.3.2 and 3.3.2 follow as

$$\begin{aligned} A_2 &= \frac{\eta_0 k^2 \rho_2 (\rho_2 - \rho_1)}{(\rho_1 + \rho_2) (\alpha + 1)}, & B_1 &= \frac{\eta_0 k^2 \rho_1 (\rho_1 - \rho_2)}{(\rho_1 + \rho_2) (\alpha + 1)}, \\ C_2 &= \frac{\eta_0 k^2 \rho_2 (\rho_2 - \rho_1)}{(\rho_1 + \rho_2) (\alpha^2 + \alpha)}, & D_1 &= \frac{\eta_0 k^2 \rho_1 (\rho_1 - \rho_2)}{(\rho_1 + \rho_2) (\alpha^2 + \alpha)}, \end{aligned} \quad (3.69)$$

and

$$F_1 = \begin{cases} 0, & \beta \rightarrow 0 \\ \frac{\mathcal{A}\beta\eta_0\rho_1(\alpha+1-\mathcal{A}\sigma)}{2(\mathcal{A}-1)(\alpha+1)}, & d_L \rightarrow \infty \end{cases}, \quad F_2 = \begin{cases} 0, & \beta \rightarrow 0 \\ \frac{\mathcal{A}\beta\eta_0\rho_1(\mathcal{A}\sigma+\alpha+1)}{2(1-\mathcal{A})(\alpha+1)}, & d_L \rightarrow \infty \end{cases}, \quad (3.70)$$

where $\sigma = d_L s$, $\alpha = \sqrt{\sigma^2 + 1}$ and $\mathcal{A} = (\rho_2 - \rho_1)/(\rho_2 + \rho_1)$ is the Atwood number, as before. This leads to the limiting in-plane flow field as $d_S \rightarrow \infty$ in the Laplace space given by

$$U_{1,2}(z) = \pm \frac{i\eta_0\mathcal{A}k d_L^2 s}{\alpha(1+\alpha)} \exp\left(-\frac{k\sigma}{\alpha}|z|\right), \quad (3.71)$$

$$W_{1,2}(z) = \frac{\eta_0\mathcal{A}k d_L}{1+\alpha} \exp\left(-\frac{k\sigma}{\alpha}|z|\right). \quad (3.72)$$

Interestingly, these expressions share the same limits of Eqs. (3.51) and (3.52) as $\mathcal{A} \rightarrow 1$, suggesting that the IICE and IIIIE models converge when both of the skin depth and density ratio become large ($d_S \rightarrow \infty$, $\rho_2/\rho_1 \rightarrow \infty$). In this case, the inverse transform ($\mathcal{L}^{-1} : \sigma \rightarrow T$) at the interface can be calculated in closed form using binomial expansion, to yield

$$\hat{\gamma}_0 = \mathcal{L}^{-1} \left[\frac{\sigma}{\alpha + \alpha^2} \right] = 1 - T {}_1F_2 \left(\frac{1}{2}; 1, \frac{3}{2}; -\frac{T^2}{4} \right), \quad (3.73)$$

and

$$\frac{d\hat{\eta}}{dt} = \mathcal{L}^{-1} \left[\frac{1}{1+\alpha} \right] = {}_1F_2 \left(-\frac{1}{2}; \frac{1}{2}, 1; -\frac{T^2}{4} \right) - T, \quad (3.74)$$

$$\frac{\hat{\eta} - \hat{\eta}_0}{d_L} = \mathcal{L}^{-1} \left[\frac{1}{\sigma(1+\alpha)} \right] = T {}_1F_2 \left(-\frac{1}{2}; 1, \frac{3}{2}; -\frac{T^2}{4} \right) - \frac{T^2}{2}, \quad (3.75)$$

where ${}_1F_2$ is the generalized hypergeometric function [3]; and again, $T = t/d_L$, $\hat{\gamma}_0 = \gamma_0/(4\eta_0\mathcal{A})$, $\hat{\eta} = \eta(\mathcal{A}\eta_0k)^{-1}$.

3.5 Numerical results

The time-dependent behavior of the velocity, vorticity and magnetic fields, interface growth, and other quantities of interest is retrieved from the s -dependent expressions given in Eqs. (3.27) and (3.30), for both the IICE and IIIIE models, by applying the inverse Laplace transform. For general parameter values of the Larmor radius d_L and the energy ratio β , this is performed numerically for a given time, t , using the multi-precision Talbot method [1], originally proposed by Talbot [100]. The

algorithm involves deforming the Bromwich contour [see Eq. (3.37)] using the parametrisation

$$s(\theta) = \frac{2N}{5t} \theta (\cot \theta + i), \quad -\pi < \theta < \pi, \quad (3.76)$$

where N is the truncation number used in the trapezoidal rule to numerically evaluate the deformed integral. N also specifies the number of precision decimal digits in a symbolic environment, such as Mathematica[®], where the Talbot algorithm is implemented. Convergent results are obtained by gradually increasing N up to $N = 300$. Particularly, the numerical solutions for the limiting parameters match those given by the exact asymptotic expressions available in Sec. 3.3.2 and 3.4.3. This shows the advantage of using a Laplace method over direct integration of the equations of motion in time so that analytical solutions are accessible in certain limiting plasma regions.

It is noted that since η_0 appears as a common factor of all quantities of interest, unity is assumed for its value in all the subsequent numerical results without loss of generality. Further, representative results are shown for the case $\rho_2 > \rho_1$, or equivalently, $0 < \mathcal{A} < 1$, in the following.

3.5.1 IICE results

We first establish the characteristic properties of the incompressible ion, compressible electron (IICE) Hall-MHD description by presenting illustrative solution in comparison with its various limiting cases, including the regular MHD theory.

Growth of the interface perturbation

The interface perturbation growth is first shown to establish the suppression of RMI due to a perpendicularly applied magnetic field. Figure 3.2 illustrates the decaying growth rate of the density interface perturbation for all ranges of the Larmor radius d_L , from the MHD limit where $d_L = 0$ shown in (a), to the infinite d_L limit shown in (b), with a fixed energy ratio β . The damped oscillation, analysed in Sec. 3.3.2 for large d_L , whose period depends on the ion cyclotron frequency, is also observed when d_L is finite. This characteristic feature distinguishes the Hall-MHD equations from the regular MHD system, where fluctuations do not occur.

Integrating the growth rate \tilde{w} over time leads to the magnitude of the interface perturbation, demonstrated in Fig. 3.3. When measured over the original time scale t , the effect of finite d_L to the growth of the density interface perturbation is twofold, as shown in Fig 3.3(a). First, it causes oscillations of increasing frequencies as d_L

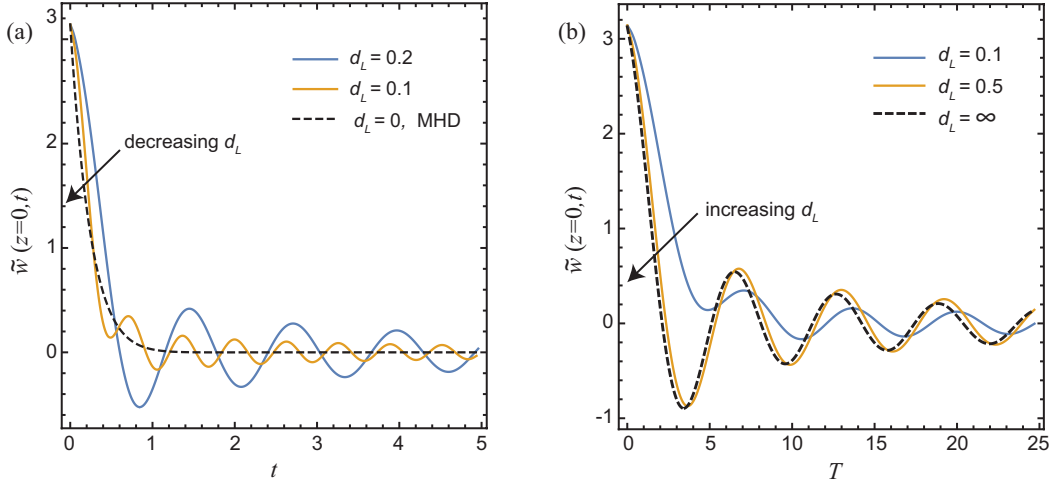


Figure 3.2: Growth rate of the density interface perturbation, $d\eta/dt = \tilde{w}(0)$, as a function of the Larmor radius d_L : (a) convergence towards the MHD limit ($d_L = 0$, dashed) as d_L decreases, represented in original time t ; and (b) convergence towards the large d_L asymptote (dashed) as d_L increases, represented in the rescaled time $T = t/d_L$. In both cases, the energy ratio and the Atwood number are fixed at $\beta = 2$ and $\mathcal{A} = 0.5$, respectively.

decreases, provided that $d_L > 0$, rendering the MHD description, which exhibits monotonic growth, a singular limit as $d_L \rightarrow 0$. Second, interface growth in the Hall-MHD model still saturates in the long term, as in the MHD case, but now to a level that increases without bound with increasing d_L .

More revealing observations are made when the rescaled units for time and length are used, as given in Fig. 3.3(b). It is evident that the oscillation frequencies collapse to a state dictated by the ion cyclotron, extrapolating the large d_L analysis as a convergent limit for increasing d_L [see Sec. 3.3.2].

Additionally, Fig. 3.2(b) and 3.3(b) both confirm that the Hall-MHD model is most sensitive to the Larmor radius only when the ion skin depth is small, *i.e.*, $0 < d_S \lesssim 1$. Therefore the large d_L asymptotes obtained in Eqs. (3.54) and (3.56) are very good approximations if the Larmor radius significantly exceeds the initial perturbation wavelength for a fixed energy ratio β .

Next, we illustrate in Fig. 3.4 the effect of changing energy ratio β on the interface growth. This is performed with d_L fixed in 3.4(a) and d_S fixed in 3.4(b). The former may be physically achieved by decreasing the upstream fluid density, and the latter by increasing the applied magnetic field strength. In both cases, as in the MHD study [104], increasing β in the Hall-MHD solution ultimately recovers the

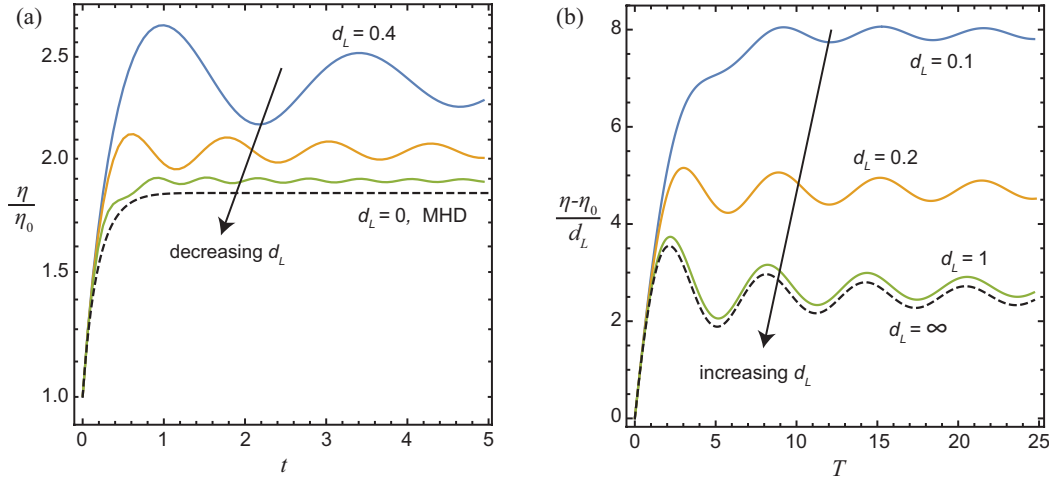


Figure 3.3: Amplitude of the interface perturbation as a function of the Larmor radius d_L , in the incompressible ion compressible electron (IICE) Hall-MHD model. In (a), the original time unit t and length unit η_0 are used for decreasing values of $d_L = 0.4, 0.2, 0.1$ (solid lines), and $d_L = 0$ (the MHD limit, dashed line). In (b), rescaled time $T = t/d_L$ and length η/d_L are used with d_L varying from 0.1 to infinity (dashed). For all series, the energy ratio and the Atwood number are fixed at $\beta = 2$ and $\mathcal{A} = 0.5$, respectively.

hydrodynamic RMI growth that is unbounded. However, the effect of decreasing β differs in the two cases shown. When the Larmor radius d_L is fixed, the interface growth is bounded below by the limiting $\beta = 0$, $d_S = \infty$ asymptote given in (3.56), where partial suppression of the RMI, predicted by Eq. (3.57) in the long term, is achieved at most; whereas when the ion skin depth d_S is fixed, complete suppression of the RMI occurs at a rate the same as in MHD, *i.e.*, $\eta(\infty)/\eta_0 \sim O(\beta^{1/2})$, while the oscillation frequency increases proportional to $d_L \propto \beta^{-1/2}$.

Velocity profile

Away from the interface, the normal flow velocity profile $\tilde{w}(z, t)$ is compared between the Hall-MHD and regular MHD models directly in Fig. 3.5, where the evolution of the velocity profile is shown at four sequential instants of time. At $t = 0^+$, the initial velocity distribution resulting from the impulsive acceleration is identical for the Hall-MHD and MHD systems, a purely hydrodynamic result, as shown in Fig. 3.5(a). Nonetheless, owing to its dispersive nature [91], the propagation of the initial impulse in the Hall-MHD system, demonstrated in Fig. 3.5(b)–(d) for $t > 0$, exhibits highly oscillatory patterns along the normal axis, which differs markedly from the MHD prediction where the Alfvén waves are responsible for carrying away

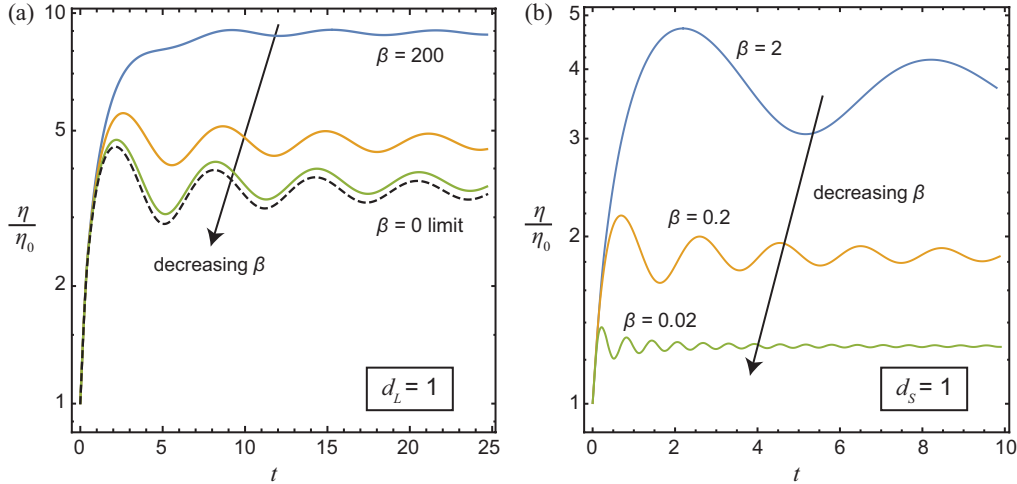


Figure 3.4: Amplitude of the interface perturbation as a function of energy ratio β for (a) fixed Larmor radius $d_L = 1$, and (b) fixed ion skin depth $d_S = 1$. The IICE model with an Atwood number of $\mathcal{A} = 0.5$ is used throughout. Convergence towards the small β limit (dashed line) is shown with decreasing $\beta = 200, 20, 2$, (solid lines) in (a), whereas convergence towards zero interface growth is shown by further reducing $\beta = 2, 0.2, 0.02$, in (b).

the velocity peak in each fluid region [104, 105]. Furthermore, it is clear that the fast waves associated with the Hall-MHD model is able to produce rotational flow ahead of the Alfvén wave fronts, which limits the propagation of information in the MHD description.

Increasing the applied magnetic field strength in this case has a twofold effect on stabilizing the interface growth, as shown in Fig. 3.6, where three velocity profiles are compared at one instance for different values of β . As β decreases, firstly, oscillations of the interface growth rate after the decay of the initially impulsively generated peak are suppressed; secondly, all of the induced disturbances are carried away at a faster speed by the Alfvén waves in both upstream and downstream flows [see Eq. (3.45)].

Circulation and vorticity

We now explore the IICE Hall-MHD model distribution of circulation and vorticity. First, as discussed in Sec. 3.3.1, the discontinuity of tangential velocity across the density interface gives rise to a vortex sheet where circulation is deposited, contrasting the regular MHD model that supports no-slip condition across the interface. The evolution of the accumulated circulation, γ_0 , derived from Eq. (3.40), is plotted

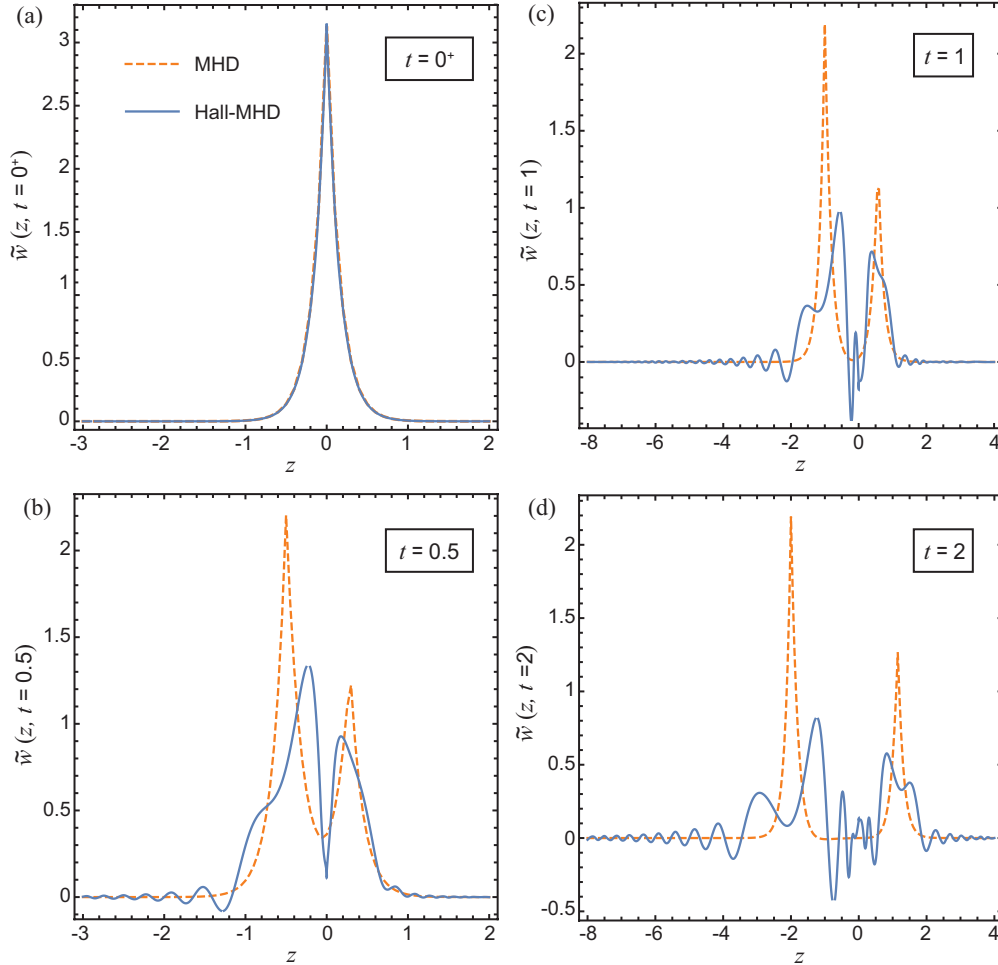


Figure 3.5: Normal velocity profile from the IICE model, $\tilde{w}(z, t)$, for $t = 0^+$, 0.5, 1, 2, in (a)–(d), respectively. The Hall-MHD solutions, obtained for $\beta = 2$, $d_L = d_S = 0.1$ and $\mathcal{A} = 0.5$, given by the solid lines, are compared to the regular MHD solutions of the same energy ratio and Atwood number, shown as dashed lines.

for decreasing β with d_S fixed using both time scales t , and T , in Fig. 3.7. Over the original time scale t , decreasing β captures more cycles of decaying oscillations over a finite initial window of time, so that in the $\beta \rightarrow 0$ limit, all fluctuations of finite amplitude are packed into an infinitesimally short period of time immediately after the initial impulse, leaving $\gamma_0 = 0$ for all $t > 0^+$. This is an example of nonuniform convergence at $t = 0$. More is revealed when the scaled time T is used in 3.7(b): curves obtained for different β all seem to collapse. This is indeed expected because substituting $\beta = 2d_L^2/d_S^2$ into (3.40) yields an expression of the form, $\Gamma_0/d_L = f(d_S; \sigma)$, where the known function f does not depend on β . Therefore this universal curve for all $\beta > 0$ encodes the entire decaying history of γ_0 over the

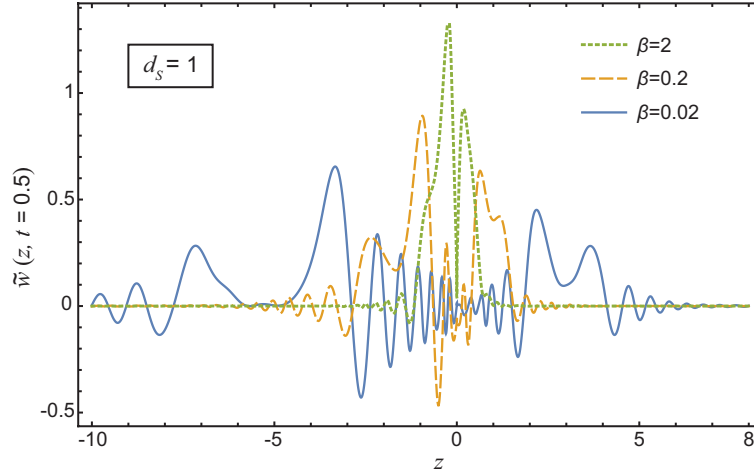


Figure 3.6: Normal velocity profiles from the IICE model, $\tilde{w}(z, t = 0.5)$, for increasing strength of the applied magnetic field, with varying $\beta = 2, 0.2, 0.02$ and constant $d_S = 1, \mathcal{A} = 0.5$.

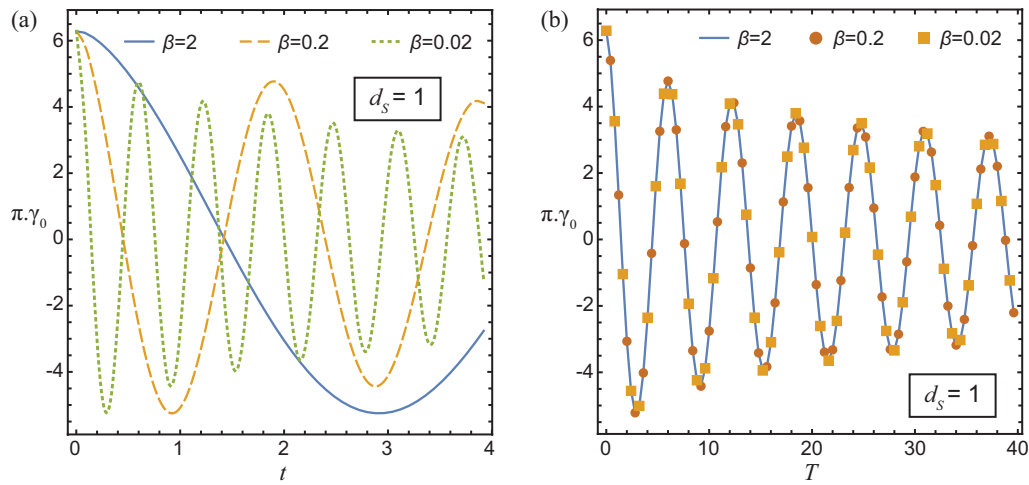


Figure 3.7: Effect of increasing applied magnetic field in the IICE model on the circulation deposition at the interface, γ_0 , as β is decreased using $\beta = 2, 0.2, 0.02$ with constant $d_S = 1, \mathcal{A} = 0.5$ over (a) the original time scale t , and (b) the cyclotron time scale $T = t/d_L$.

infinitesimal time window of t as $\beta \rightarrow 0$ shown in 3.7(a).

Having established that the shape of $\gamma_0(T)$ only depends on d_S (for a fixed \mathcal{A}), Fig. 3.8 plots its convergence to the $d_S \rightarrow \infty$ limit obtained in (3.53) through either decreasing β as presented in (a) or increasing d_L as depicted in (b). It is clear that the decaying rate of the oscillation envelope is maximized at the limiting solution. Nevertheless, as in the case for the interface growth presented earlier,

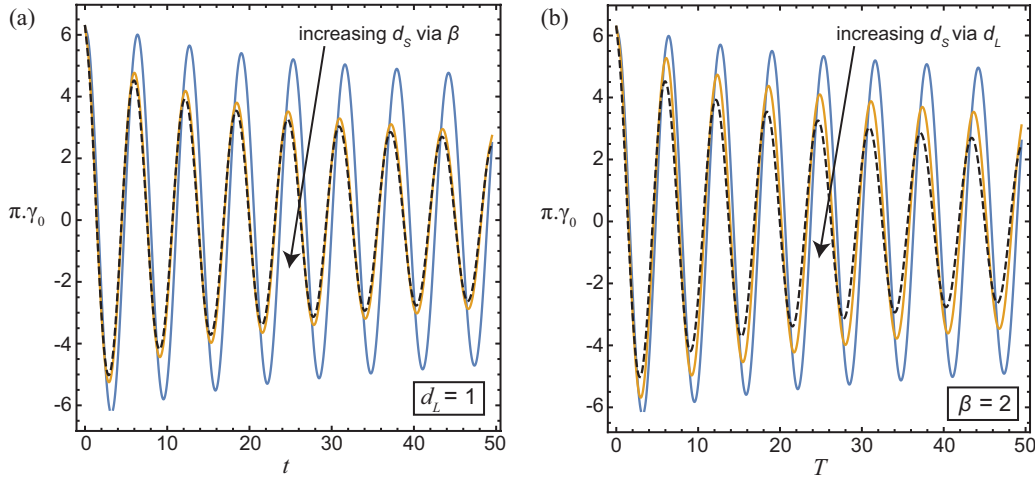


Figure 3.8: Effect of increasing ion skin depth in the IICE model on the circulation deposition at the interface, γ_0 , for constant $\mathcal{A} = 0.5$. (a) Increase d_S via decreasing energy ratio $\beta = 100, 2, 0$, while holding $d_L = 1$ fixed. (b) Increase d_S via increasing Larmor radius $d_L = 0.1, 0.5, \infty$, in rescaled time $T = t/d_L$, while holding $\beta = 2$ fixed. In both cases, the dashed line represents the same asymptotic limit of $d_S = \infty$.

the convergence of circulation deposition towards the large d_S limiting value is fast. For moderate values of β and d_L , the asymptotic limit provides reasonable approximation to the true solution.

Away from the interface, because the y -component of vorticity in the continuous flow domain is governed by the forced wave equation [see Eq. (3.45)], rotational flow is no longer confined to a region defined by the two Alfvén wave fronts in each fluid, as in the MHD system. This is demonstrated in Fig. 3.9, where the vorticity profile excluding $z = 0$ is plotted for two instants of time.

Therefore, the total circulation in the x, z -plane, calculated by integrating the vorticity component ω_y over the infinite band $\{(x, z) : z \in \mathbb{R}, x \in (0, \Lambda/2)\}$, given by

$$\gamma(t) = \gamma_0(t) + \frac{i}{\pi} \int_{\mathbb{R} \setminus \{0\}} \tilde{\omega}_y(z, t) dz, \quad (3.77)$$

is nonconservative over time. For example, as seen in Fig. 3.8(b) and 3.9, it is numerically verified that $\gamma(0.2) > \gamma(0.1)$, implying that circulation is generated by the magnetic forcing during that period of time. It is stressed that the total circulation collects a point mass contribution γ_0 at the interface $z = 0$, at any instant. In comparison, the regular MHD model cannot sustain circulation at the interface, nor does it inject additional vorticity into the flow after the initial baroclinic generation.

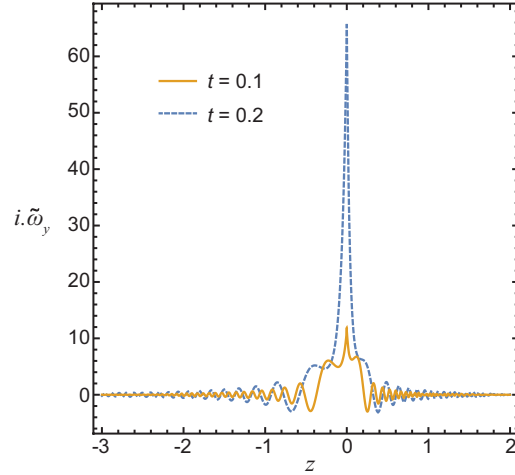


Figure 3.9: Vorticity profile $\tilde{\omega}_y(z, t)$ at two time instants obtained using the IICE model: $t = 0.1$ (solid) and $t = 0.2$ (dashed). Both solutions are obtained for $d_L = 0.1$, $\beta = 2$ and $\mathcal{A} = 0.5$.

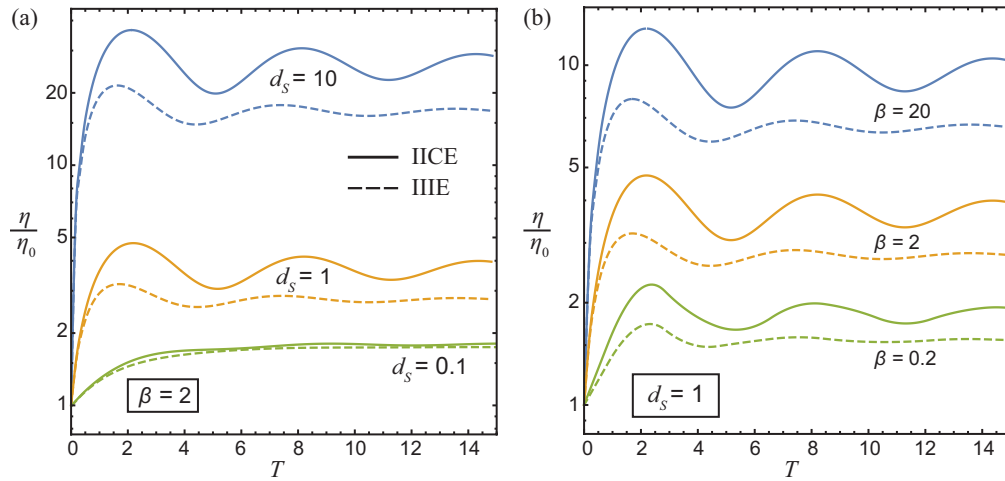


Figure 3.10: Amplitude growth of the interface perturbation, η/η_0 , predicted by the IICE model (solid lines), and the IIIE model (dashed lines). Comparisons are made for varying $d_S = 0.1, 1, 10$, with $\beta = 2$ fixed in (a), and for changing $\beta = 0.2, 2, 20$, with $d_S = 1$ fixed in (b). All series are obtained in the cyclotron time scale T for fluids with $\mathcal{A} = 0.5$.

3.5.2 IIIE results and model comparison

Finally, we show results obtained using the incompressible ion incompressible electron (IIIIE) Hall-MHD model and make a comparison against the IICE system to show that the key features are qualitatively similar in both models.

The growth of the interface amplitude predicated by the two models is first illustrated in Fig. 3.10 as a function of d_S and β , where the cyclotron frequency rescaling

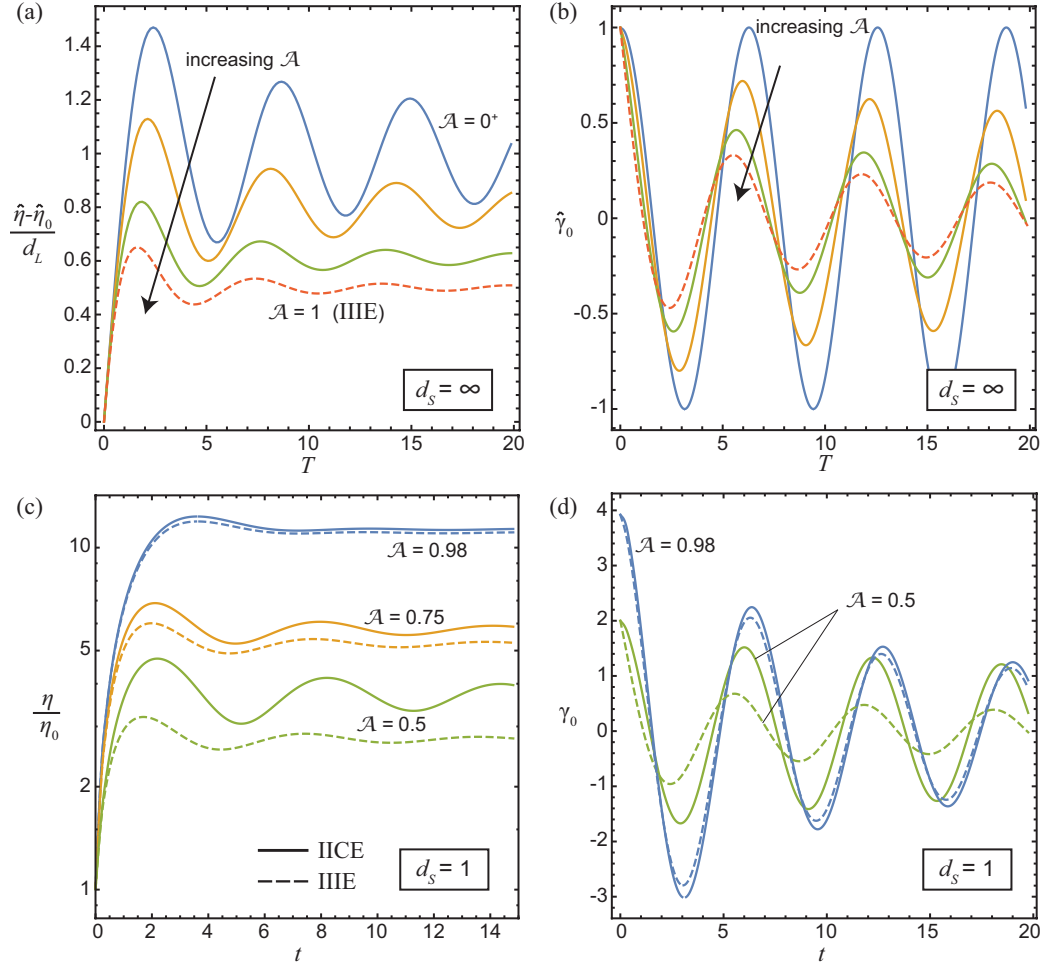


Figure 3.11: Convergence of interface statistics obtained from the IICE model (solid lines), towards those of the IIIE model (dashed lines), as $\mathcal{A} \rightarrow 1$. The $d_S = \infty$ asymptotic behavior of (a) the renormalized interface growth $\hat{\eta}$, and (b) the renormalized circulation deposition $\hat{\gamma}_0$, are plotted as functions of increasing $\mathcal{A} = 0, 0.5, 0.8, 1$. Similar comparisons are made for finite $d_S = 1$ corresponding solutions for η and γ_0 in (c) and (d), respectively. $\beta = 2$ is used throughout.

applies effectively in both cases. It is seen that the IIIE model consistently gives a smaller interface growth, through fluctuations whose amplitude dampens significantly quicker over each cycle. These differences however diminish as either d_S or β is decreased, as both models converge to the respective common limit of MHD theory, or the no-motion solution due to strong magnetic field.

In Fig. 3.11, a series of the interface characteristics obtained from both systems are shown to converge as the Atwood number \mathcal{A} approaches unity. Figures 3.11(a), (b) evidence the analysis of Sec. 3.4.3 that in the large d_S limit, the IICE and IIIE

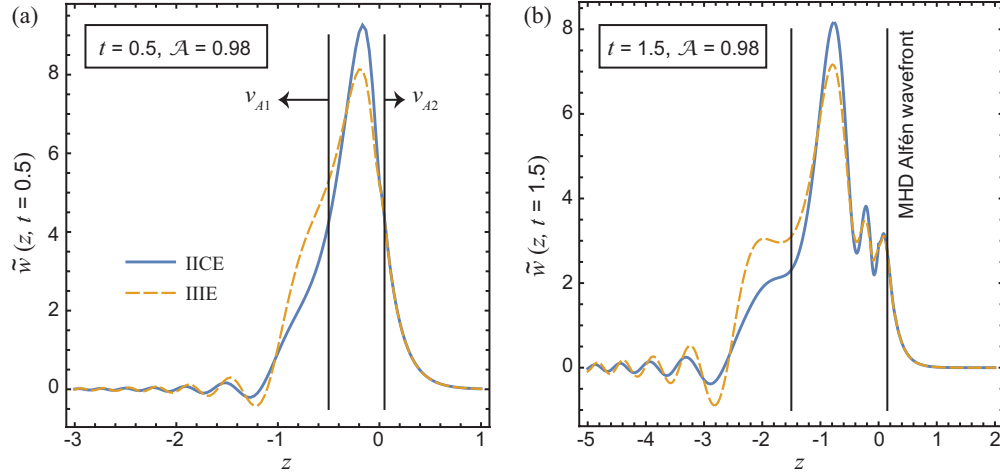


Figure 3.12: Comparison of normal velocity profile between the IICE (solid line) and IIIE (dashed line) flow models for high density ratio, $\mathcal{A} = 0.98$, at time $t = 0.5$ in (a) and $t = 1.5$ in (b). $d_S = 0.1$ and $\beta = 2$ are held fixed in all cases. The vertical lines indicate the position of Alfvén wavefronts associated with the MHD model traveling at speed v_{A_i} in the fluid region $i = 1, 2$, left or right to the interface.

models coincide when $\mathcal{A} = 1$. This property is extrapolated to hold for finite d_S as well in 3.11(c), (d), where the interface amplitude η and circulation deposition γ_0 are shown to be dependent on \mathcal{A} in both models, however with their difference diminishing as \mathcal{A} is increased. It should also be clarified that particularly η is an increasing function of \mathcal{A} , as shown in 3.11(c), which does not contradict 3.11(a) where the renormalized $\hat{\eta}$ is plotted in order to illustrate the full range of variability.

Nevertheless, the convergence of interface statistics between the IICE and IIIE models as \mathcal{A} increases do not generalize to the continuous regions of the flow, for finite d_S . This is demonstrated in Fig. 3.12 where the normal velocity profile $\tilde{w}(z)$ is computed at a high Atwood number $\mathcal{A} = 0.98$ (equivalently $\rho_2/\rho_1 = 100$) and $d_S = 1$, for both models. The vorticity transport in the light fluid side (left) is clearly different between the two models in a region close to the corresponding Alfvén wave front. The heavy fluid side however, including the neighborhood of the interface, appears insensitive to the model used for the electrons.

3.6 Summary

We have examined the behavior of an impulsively accelerated perturbed interface separating conducting fluids of different densities, in the presence of a magnetic field that is parallel to the acceleration, using the Hall-MHD equations. Assuming the ions form an incompressible fluid, two impulsive models are proposed, first

with a compressible electron flow and second with an incompressible electron flow. These models are analytically approached as linearized initial-value problems that accommodate all three components of the velocity and magnetic fields. By applying the appropriate jump conditions across contact discontinuity for each model, the resulting flow fields demonstrate that in both cases, the growth of the interface perturbation is limited by the imposed magnetic field, establishing suppression of the RMI when the ion skin depth (or the Larmor radius) is significant compared to the perturbation wavelength. In such flow regimes inaccessible to the ideal MHD theory, oscillations associated with the ion cyclotron effect are imposed onto the entire flow domain, substantially altering the vorticity dynamics displayed by the ideal MHD model that drives the suppression of the RMI. Most significantly, the jump conditions in the Hall-MHD case permit circulation deposition on the interface, which is precluded in ideal MHD when a magnetic field penetrates the interface. Together with a continuous vorticity production away from the interface due to the magnetic contribution to the vorticity equation, the total circulation in the domain is no longer a conserved quantity. Furthermore, the dispersive nature of the Hall-MHD equations also drastically affects the transport of vorticity, which is no longer confined to the Alfvén fronts propagating outwards from the interface, as in the ideal MHD case.

By varying the non-dimensional Larmor radius, the ion skin depth, the energy ratio (β), and the fluid density ratio (or the Atwood number), it is found that the hydrodynamic RM flow limit is recovered when β is large, and the MHD limit is attained when d_S (or d_L) is small. Further there exists a large d_S limit that is opposite to the MHD system, where solutions at the interface converge rapidly for d_S greater than order unity. Lastly, the two somewhat different models (IICE and IIIE) are compared to show qualitatively similar results across the entire parameter space.

Chapter 4

HALL-MHD RMI UNDER AN ARBITRARILY ORIENTED MAGNETIC FIELD

This chapter is adapted from the following journal article:

Naijian Shen, Vincent Wheatley, D. I. Pullin and Ravi Samtaney. Magneto-hydrodynamic Richtmyer-Meshkov instability under an arbitrarily oriented magnetic field. *Physics of Plasma*, 27(6):062101, 2020. doi: 10.1063/1.5142042.

The effect of an initially uniform magnetic field of arbitrary orientation on the RMI in Hall-MHD and ideal MHD is considered in this chapter. The linearized incompressible flow driven by an impulsively accelerated density interface is obtained by extending the formulation developed in Chapter 3, where a normal magnetic is applied. The accuracy and appropriateness of the incompressible model is validated by comparing its ideal MHD predictions to the results of the corresponding shock-driven nonlinear compressible simulations.

4.1 Introduction

Extending the recent work of Shen *et al.* [92] (Chapter 3) on the RMI in Hall-MHD subject to a normal magnetic field, the present chapter utilizes the IIIE Hall-MHD equations to consider the effect of a uniform initial magnetic field of completely arbitrary orientation, on the RMI flow resulting from impulsively accelerating a density interface with a single-mode sinusoidal perturbation in amplitude. The linearized incompressible impulse-driven initial value problem, which admits analytical solution in various limits, is considered to capture the leading-order features of the corresponding compressible shock-driven RM flow. The flow structure of the resulting analytical solutions is explored, with particular attention given to the dynamics of vorticity and the consequent evolution of the induced velocities at the interface. The ideal MHD theory of arbitrary field angle is naturally contained in this formulation as the limiting case of vanishing Larmor radius d_L , or equivalently, ion skin depth d_S . The adoption of the Hall-MHD model however enables access to the plasma region where $d_L, d_S > 0$. Comparisons between the ideal MHD and Hall-MHD models are made throughout. The accuracy and validity of the in-

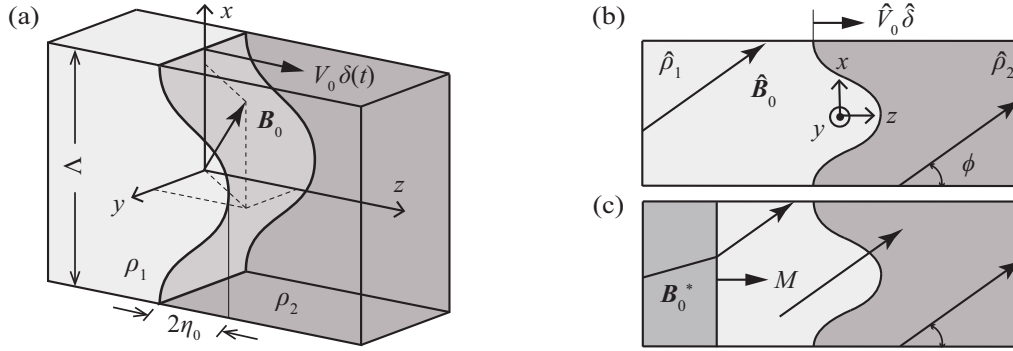


Figure 4.1: (a) Geometry and initial condition for incompressible RMI with an external magnetic field \mathbf{B}_0 of arbitrary orientation. The perturbed density interface with wavelength Λ and amplitude η_0 experiences impulsive acceleration $V_0\delta(t)$. (b) Two-dimensional incompressible RM flow representation. ϕ is the angle made by the in-plane background magnetic field with the z -axis. The hat symbol is used to denote dimensionless variables. (c) Initial conditions for the shock-driven compressible MHD RMI simulation. The asterisk symbol denotes a different non-dimensionalization scheme.

compressible formulation is assessed by a nonlinear simulation of the shock-driven compressible RM flow in the ideal MHD limit.

The rest of this chapter is structured as follows: Section 4.2 first introduces the impulsive-driven initial value problem, governed by the incompressible Hall-MHD equations. These equations, together with the corresponding Rankine-Hugoniot conditions for a contact discontinuity are linearized around the unperturbed base-flow. The general flow field solution is then obtained in Sec. 4.3 for all field angle. The resulting interface behavior, as well as vorticity transport, is examined. Section 4.4 derives limiting solutions for extreme values of a range of parameters, including the ion skin depth, the strength and direction of the initial magnetic field. The ideal MHD limit is discussed in detail. Illustrative results obtained from the linear theory and nonlinear simulation in terms of the interface perturbation growth, flow velocity, and vorticity profiles are given in Sec. 4.5, before conclusions are drawn in Sec. 4.6.

4.2 Incompressible Hall-MHD model

4.2.1 Governing equations

The initial condition for the impulse-driven RM flow under consideration is illustrated in Fig. 4.1(a). Cartesian coordinates are assigned so that the unperturbed interface lies in the x, y -plane, separating two fluids of densities ρ_1 ($z < 0$) and ρ_2

($z > 0$). The single-mode perturbation of wavelength Λ and amplitude η_0 varies its magnitude along the x -direction. The two-dimensional contact discontinuity (CD), defined by the interface, is subject to an impulsive acceleration given by $V_0\delta(t)$, where V_0 matches the imparted interface velocity from a shock-CD impact had it been traversed by an incident normal shock of Mach number M in the positive z -direction given by the unit vector \hat{z} , and $\delta(t)$ is the Dirac delta function of time t with unit of frequency. In the non-inertial reference frame moving with the interface, a body force of the form $\rho V_0\delta(t)\hat{z}$ is required for the each fluid of density $\rho \in \{\rho_1, \rho_2\}$. The shock-wave-density-interface interaction can be analyzed by the solution to a suitable Riemann-type problem. A uniform initial magnetic field \mathbf{B}_0 of arbitrary orientation is imposed.

The non-dimensional variables are obtained by choosing the following reference scales: the perturbation wave length Λ for spatial coordinates, the post-shock interface speed V_0 for velocities, the applied field strength B_0 for magnetic fields, the elementary charge e for particle charges, the ion mass m_i for particle masses, and the left region fluid density ρ_1 for mass densities. These also lead to the derived reference quantities including the time scale Λ/V_0 , the particle number density scale ρ_1/m_i , the pressure scale $\rho_1 V_0^2$, the electric field scale $V_0 B$, and the current density scale $e\rho_1 V_0/m_i$. As a result, the dimensionless Hall-MHD equations that govern the evolution of the initial accelerative impulse for incompressible ions and electrons (IIIE [92]) in the convenient non-inertial frame moving with the interface are given by

$$\nabla \cdot \mathbf{u} = 0, \quad \nabla \cdot \left(\frac{\mathbf{j}}{\rho} \right) = 0, \quad (4.1a)$$

$$\rho \left(\frac{\partial \mathbf{u}}{\partial t} + \mathbf{u} \cdot \nabla \mathbf{u} \right) = -\nabla p + \frac{1}{d_L} \mathbf{j} \times \mathbf{B} + \mathbf{f} - \rho \delta(t) \hat{z}, \quad (4.1b)$$

$$\frac{\partial \mathbf{B}}{\partial t} + \nabla \times \mathbf{E} = \mathbf{0}, \quad (4.1c)$$

$$\mathbf{E} + \mathbf{u} \times \mathbf{B} = \frac{\mathbf{j} \times \mathbf{B}}{\rho} - \frac{d_L}{\rho} \nabla p_e, \quad (4.1d)$$

$$\nabla \times \mathbf{B} = \frac{\beta}{2d_L} \mathbf{j}, \quad (4.1e)$$

$$\nabla \cdot \mathbf{B} = 0, \quad (4.1f)$$

where $\mathbf{u} = (u, v, w)$ is the flow velocity, ρ is the mass density, \mathbf{j} is the electric current density, p is the total ion and electron pressure, \mathbf{E} is the electric field, and \mathbf{B}

is the magnetic field. In the momentum equation (4.1b), the impulsive forcing that accelerates the fluids is given by

$$\mathbf{f} = [\rho_1 + H(z) (\rho_2 - \rho_1)] \delta(t) \hat{\mathbf{z}}, \quad (4.2)$$

where $H(z)$ is the Heaviside function. This body force drives the flow and differs from the fictitious force $\rho \delta(t) \hat{\mathbf{z}}$ in (4.1b) that accounts for the non-inertial reference frame. It is noted that in Eq. (4.2), $\rho_1 = 1$ and $\rho_2 = \rho_2/\rho_1$ are indeed dimensionless. However, the notation of $\rho_{i=1,2}$ is kept here and henceforth in order to conveniently indicate flow quantities of the two different fluids. Additionally, two dimensionless parameters are introduced, namely the normalized Larmor radius d_L , and the plasma parameter β , defined as

$$d_L = \frac{V_0 m_i}{e B \Lambda}, \quad \beta = \frac{2 \mu_0 \rho_1 V_0^2}{B^2}, \quad (4.3)$$

where μ_0 is the permeability of vacuum. The Larmor radius d_L is the normal radius of the helix along which an ion moves about background magnetic field lines, while the plasma parameter β measures the ratio of kinetic to magnetic energy in an incompressible flow.

A distinguishing property of the Hall-MHD model is that by approximating the motion of electrons, its generalized Ohm's law (3.2e) contains the Hall term $(\mathbf{j} \times \mathbf{B})/\rho$ and the electron pressure gradient component $d_L \nabla p_e/\rho$ [91]. The Hall term generally introduces two wave modes into the plasma system: Whistler waves and Hall-drift waves [47, 48]. Under the current IIIIE model where both ion and electron flows assume incompressibility, the Hall-drift effect is neglected. When substituted into the Faraday's law (2.24a) to give the Hall induction equation, the $\nabla p_e/\rho$ component in (3.2e) vanishes upon taking the curl in the flow regions of constant density. Shen et al. [92] showed that although p_e remains indeterminate in the IIIIE model, retaining $\nabla p_e/\rho$ in (3.2e) constrains the electron pressure jump across the interface without affecting the flow dynamics. Also, using the present non-dimensionalization scheme, the Hall-MHD system (3.2) reduces to the ideal MHD model in the continuous limit $d_L \rightarrow 0$, $\beta > 0$ [91].

4.2.2 Rankine-Hugoniot conditions

The boundary conditions for contact discontinuity of simple geometry connecting the two flows on each side of the interface are given by the Rankine-Hugoniot conditions. These are derived by writing the governing equations (4.1) in conservation

form and integrating over a shrinking volume that encloses the CD. For the present IIIE model [92], the CD jump conditions are

$$\llbracket u_n \rrbracket = 0, \quad \llbracket \frac{j_n}{\rho} \rrbracket = 0, \quad (4.4a)$$

$$\llbracket \left(p + \frac{1}{\beta} B^2 \right) \hat{\mathbf{n}} - \frac{2}{\beta} B_n \mathbf{B} \rrbracket = 0, \quad (4.4b)$$

$$\llbracket B_n \rrbracket = 0, \quad (4.4c)$$

where the square brackets denote the difference in a between the two fluid region on each side of the contact, and the subscript “ n ” indicates the vector component normal to the surface.

4.2.3 Linearized equations

The base flow solution to (4.1), denoted by the bar symbol, corresponding to the impulsive acceleration of an unperturbed interface at $z = 0$ is steady in the non-inertial frame, given by

$$\begin{aligned} \bar{\mathbf{u}} = \bar{\mathbf{j}} = \bar{\mathbf{E}} = \mathbf{0}, \quad \bar{\mathbf{B}} = \hat{\mathbf{B}}_0, \\ \bar{\rho}(z) = \rho_1 + H(z)(\rho_2 - \rho_1), \quad \bar{p}(z, t) = p_0, \end{aligned} \quad (4.5)$$

where p_0 is the constant background pressure, and the unit vector $\hat{\mathbf{B}}_0 = (B_{0x}, B_{0y}, B_{0z})$ is three-dimensional in general.

For the perturbed interface, the density profile is expressed as

$$\rho = \bar{\rho}(z - h), \quad (4.6)$$

where $h(x, t)$ is the position of the contact discontinuity and $h \ll 1$ is required to ensure a small perturbation for which linear theory applies. As a result, Eqs. (4.1) can be linearized around the base flow by perturbing all flow fields using the form

$$\xi(x, z, t) = \bar{\xi}(z) + \xi'(x, z, t), \quad (4.7)$$

where ξ generically represents the scalar pressure p , or the vector components of \mathbf{u} and \mathbf{B} ; ξ' is the corresponding perturbation of small magnitude (*i.e.*, $|\xi'| \ll |\bar{\xi}|$). In this construction the perturbation wave is aligned in the x -direction so that no y -dependency is needed.

Using (4.1e) and (4.1d), both of \mathbf{j} and \mathbf{E} are eliminated in favor of \mathbf{B} . The substitution of (4.7) then leads to the linearized equations,

$$\frac{\partial u'}{\partial x} + \frac{\partial w'}{\partial z} = 0, \quad (4.8a)$$

$$\rho \frac{\partial u'}{\partial t} + \frac{\partial p'}{\partial x} = \frac{2}{\beta} \left[B_{0z} \left(\frac{\partial B'_x}{\partial z} - \frac{\partial B'_z}{\partial x} \right) - B_{0y} \frac{\partial B'_y}{\partial x} \right], \quad (4.8b)$$

$$\rho \frac{\partial v'}{\partial t} = \frac{2}{\beta} \left(B_{0z} \frac{\partial B'_y}{\partial z} + B_{0x} \frac{\partial B'_y}{\partial x} \right), \quad (4.8c)$$

$$\begin{aligned} \rho \frac{\partial w'}{\partial t} + \frac{\partial p'}{\partial z} + \frac{2}{\beta} \left[B_{0x} \left(\frac{\partial B'_x}{\partial z} - \frac{\partial B'_z}{\partial x} \right) + B_{0y} \frac{\partial B'_y}{\partial z} \right] \\ = (\rho_2 - \rho_1) [H(z) - H(z - h)] \delta(t), \end{aligned} \quad (4.8d)$$

$$\frac{\partial B'_x}{\partial t} = B_{0z} \frac{\partial u'}{\partial z} + B_{0x} \frac{\partial u'}{\partial x} + \frac{2d_L}{\beta\rho} \left(B_{0z} \frac{\partial^2 B'_y}{\partial z^2} + B_{0x} \frac{\partial^2 B'_y}{\partial x \partial z} \right), \quad (4.8e)$$

$$\frac{\partial B'_y}{\partial t} = B_{0z} \frac{\partial v'}{\partial z} + B_{0x} \frac{\partial v'}{\partial x} - \frac{2d_L}{\beta\rho} \left[B_{0z} \frac{\partial}{\partial z} \left(\frac{\partial B'_x}{\partial z} - \frac{\partial B'_z}{\partial x} \right) + B_{0x} \frac{\partial}{\partial x} \left(\frac{\partial B'_x}{\partial z} - \frac{\partial B'_z}{\partial x} \right) \right], \quad (4.8f)$$

$$\frac{\partial B'_z}{\partial t} = B_{0z} \frac{\partial w'}{\partial z} + B_{0x} \frac{\partial w'}{\partial x} - \frac{2d_L}{\beta\rho} \left(B_{0z} \frac{\partial^2 B'_y}{\partial x \partial z} + B_{0x} \frac{\partial^2 B'_y}{\partial x^2} \right), \quad (4.8g)$$

$$\frac{\partial B'_x}{\partial x} + \frac{\partial B'_z}{\partial z} = 0, \quad (4.8h)$$

where (u', v', w') and (B'_x, B'_y, B'_z) make up the vectors \mathbf{u}' and \mathbf{B}' respectively. It is seen that the ideal MHD system is retrieved as a special case of the Hall-MHD system when $d_L = 0$ [91].

To proceed, we make the single Fourier-mode ansatz,

$$\xi'(x, z, t) = \tilde{\xi}(z, t) e^{ikx}, \quad (4.9)$$

where i is the imaginary unit and $k = 2\pi$ is the non-dimensional wavenumber since a fixed wavelength of Λ (dimensional) is used for reference length. The contact is located at

$$z = h(x, t) = \eta(t) e^{ikx}, \quad (4.10)$$

with $\eta(t)$ being the perturbation amplitude. It is required that $\eta \ll 1$ for any fixed orientation of $\hat{\mathbf{B}}_0$ so that the linear description (4.8) holds.

After the Fourier treatment, the temporal Laplace transform,

$$\mathcal{L}[\tilde{\xi}(t)] = \int_0^\infty \tilde{\xi}(t) e^{-st} dt, \quad \Re(s) > 0, \quad (4.11)$$

is further applied in the region $z < 0$ and $z > h$, where the impulsive forcing vanishes. The initial conditions are taken at $t = 0^-$, just prior to the impulse, when the velocity and magnetic field perturbations are zero. As a result, we obtain for each fluid in the region subscripted by $i = 1, 2$, a system of ordinary differential equations (ODEs) in the Laplace space given by

$$ikU_i + \partial_z W_i = 0, \quad (4.12a)$$

$$s\rho_i U_i + ikP_i = \frac{2}{\beta} [B_{0z} (\partial_z H_{x_i} - ikH_{z_i}) - ikB_{0y} H_{y_i}], \quad (4.12b)$$

$$s\rho_i V_i = \frac{2}{\beta} (B_{0z} \partial_z H_{y_i} + ikB_{0x} H_{y_i}), \quad (4.12c)$$

$$s\rho_i W_i + \partial_z P_i + \frac{2}{\beta} [B_{0x} (\partial_z H_{x_i} - ikH_{z_i}) + B_{0y} \partial_z H_{y_i}] = 0, \quad (4.12d)$$

$$sH_{x_i} = B_{0z} \partial_z U_i + ikB_{0x} U_i + \frac{2d_L}{\beta\rho_i} (B_{0z} \partial_z^2 H_{y_i} + ikB_{0x} \partial_z H_{y_i}), \quad (4.12e)$$

$$sH_{y_i} = B_{0z} \partial_z V_i + ikB_{0x} V_i - \frac{2d_L}{\beta\rho_i} [B_{0z} \partial_z (\partial_z H_{x_i} - ikH_{z_i}) + ikB_{0x} (\partial_z H_{x_i} - ikH_{z_i})], \quad (4.12f)$$

$$sH_{z_i} = B_{0z} \partial_z W_i + ikB_{0x} W_i - \frac{2d_L}{\beta\rho_i} (ikB_{0z} \partial_z H_{y_i} - k^2 B_{0x} H_{y_i}), \quad (4.12g)$$

$$ikH_{x_i} + \partial_z H_{z_i} = 0, \quad (4.12h)$$

where U, V, W, H_x, H_y, H_z and P are the Laplace transforms for $\tilde{u}, \tilde{v}, \tilde{w}, \tilde{B}_x, \tilde{B}_y, \tilde{B}_z$ and \tilde{p} , respectively.

4.3 Flow field calculation

4.3.1 Transverse magnetic field

We first consider a special case of Eqs. (4.12) where $B_{0z} = 0$, which corresponds to the background magnetic field being perpendicular to the initial impulsive acceleration, parallel to the x, y -plane.

General solution

The homogeneous system (4.12) evaluated at $B_{0z} = 0$ reduces to the following fourth-order ODE for W_i that is independent of B_{0y} :

$$\left(\frac{d^2}{dz^2} - k^2 \right) \left(\frac{d^2}{dz^2} - \mu_i^2 \right) W_i(z) = 0, \quad (4.13)$$

where

$$\mu_i = \frac{\sqrt{4k^4 \left(d_L^2 s^2 B_{0x}^2 + B_{0x}^4 \right) + 4k^2 B_{0x}^2 \beta \rho_i s^2 + \beta^2 \rho_i^2 s^4}}{2k B_{0x} d_L s}. \quad (4.14)$$

It is noted that in the ideal MHD limit $d_L \rightarrow 0$, the eigenvalue μ_i that appears in (4.13) escapes to infinity and the corresponding ODE for W_i reduces to second order.

The desired general solution for W_i to Eq. (4.13) must decay at $z = \pm\infty$, and therefore is given by

$$W_i(z) = A_i e^{-k|z|} + B_i e^{-\mu_i|z|}, \quad (4.15)$$

where A_i and B_i are coefficients to be determined from appropriate interface boundary conditions. Once W_i is known, other field variables follow directly from (4.12), including,

$$\begin{aligned} H_{y_i} &= \frac{i\beta d_L \rho_i s^2 (k^2 W_i - W_i'')}{2k^3 B_{0x}^2 + \beta k \rho_i s^2}, & H_{z_i} &= \frac{B_{0x}}{s \rho_i} \left(ik \rho_i W_i + \frac{2d_L k^2 H_{y_i}}{\beta} \right), & H_{x_i} &= \frac{-H'_{z_i}}{ik}, \\ U_i &= \frac{-W'_i}{ik}, & P_i &= -\frac{\rho_i s W'_i}{k^2} - \frac{2B_{0y} H_{y_i}}{\beta}, \end{aligned} \quad (4.16)$$

where the prime symbol here denotes derivative with respect to z .

Interface jump conditions

Linearizing Eqs. (4.4) around the baseflow given in (4.5) under the special consideration that the background magnetic field is parallel to the unperturbed CD, *i.e.*, $B_{0z} = 0$, leads to the following complete CD jump conditions in Laplace space,

$$\llbracket W \rrbracket_{z=0} = 0, \quad H_{y_i}|_{z=0} = 0, \quad (4.17a)$$

$$\left\llbracket P + \frac{2}{\beta} (B_{0x} H_x + B_{0y} H_y) \right\llbracket_{z=0} = \eta_0 (\rho_2 - \rho_1), \quad (4.17b)$$

$$\llbracket H_z \rrbracket_{z=0} = 0, \quad (4.17c)$$

where the notation $\llbracket \xi(z) \rrbracket_{z=0} = \xi_2(0) - \xi_1(0)$ is used.

In particular, Eq. (4.17a) follows from the continuity condition (4.4a); and (4.17b) is obtained by evaluating (4.4b) at the interface [$z = h(x, t)$] to give the leading order relation,

$$\begin{aligned} \tilde{p}_2(h, t) + \frac{2}{\beta} [B_{0x} \tilde{B}_{x_2}(h, t) + B_{0y} \tilde{B}_{y_2}(h, t)] \\ = \tilde{p}_1(h, t) + \frac{2}{\beta} [B_{0x} \tilde{B}_{x_1}(h, t) + B_{0y} \tilde{B}_{y_1}(h, t)], \end{aligned} \quad (4.18)$$

and integrating Eq. (4.8d) over the forcing region, $0 < z < h(x, t)$, neglecting terms of order $O(h^2)$ to yield

$$\left[\tilde{p}_1(z, t) + \frac{2}{\beta} (B_{0x} \tilde{B}_{x_1}(z, t) + B_{0y} \tilde{B}_{y_1}(z, t)) \right]_{z=0}^{z=h} = (\rho_2 - \rho_1) \delta(t) \eta(t). \quad (4.19)$$

With \tilde{p}_2 , \tilde{B}_{x_2} and \tilde{B}_{y_2} being smooth functions of z , substituting (4.18) into (4.19) and taking the temporal Laplace transform then produces (4.17b).

Oscillatory solutions

The unknown coefficients A_i and B_i can now be uniquely determined by solving the linear system obtained from substituting Eqs. (4.15)-(4.16) into (4.17).

It is also seen from (4.17) and (4.16) that the value of B_{0y} does not affect the final solution for A_i and B_i . In fact rotating the background magnetic field in the x, y -plane is equivalent to an effective change in β that matches the corresponding field strength in the x -direction, B_{0x} , while the y -component, B_{0y} , has no effect on the flow dynamics. Thus it is sufficient to set $B_{0y} = 0$ and $B_{0x} = 1$ without loss of generality. As a result, the final expression for A_i and B_i follows,

$$A_1 = A_2 = \frac{(\rho_2 - \rho_1) \beta \eta_0 k s}{4k^2 + \beta \rho_1 s^2 + \beta \rho_2 s^2}, \quad B_1 = B_2 = 0. \quad (4.20)$$

Surprisingly, the eigenvalues μ_i associated with the Hall-MHD model found in (4.14) where $d_L > 0$ does not enter the solution. Indeed taking the inverse Laplace transform of Eq. (4.15) leads to the normal flow velocity, and hence via integration the interfacial perturbation amplitude that are identical to the MHD solution given by Wheatey *et al.* [107],

$$\tilde{w}_{1,2}(z, t) = \eta_0 k \mathcal{A} \cos(\omega t) e^{-k|z|}, \quad (4.21)$$

$$\eta(t) = \eta_0 + \int_{0^+}^t \tilde{w}_{1,2}(0, \tau) d\tau = \eta_0 + \frac{\eta_0 k \mathcal{A}}{\omega} \sin(\omega t), \quad (4.22)$$

where $\mathcal{A} \equiv (\rho_2 - \rho_1)/(\rho_2 + \rho_1)$ is the Atwood number, and

$$\omega \equiv \frac{2k}{\sqrt{\beta(\rho_1 + \rho_2)}} = \frac{k}{\sqrt{\frac{1}{2}(c_{A_1}^{-2} + c_{A_2}^{-2})}} \quad (4.23)$$

is the oscillation frequency expressed in terms of the Alfvén speeds $c_{A_i} \equiv \sqrt{2/(\beta\rho_i)}$. In addition, a tangential slip velocity across the interface follows from (4.16) in this case, giving

$$\Delta \tilde{u}(t) \equiv \tilde{u}_2(0, t) - \tilde{u}_1(0, t) = -2i\eta_0 k \mathcal{A} \cos(\omega t). \quad (4.24)$$

It is concluded that in the special case where the background magnetic field is aligned with the mean interfacial location, the Hall-MHD model predicts the same flow dynamics given by the ideal MHD theory. This is because the required CD jump conditions are uniquely satisfied by the eigenmodes corresponding to the Alfvén waves alone.

4.3.2 Oblique magnetic field

Now we generalize to an arbitrary oblique orientation of the background magnetic field, particularly allowing a component that is normal to the unperturbed interface, *i.e.*, $B_{0z} > 0$.

General solution

To proceed, Eqs. (4.12) are rearranged into a system of first order homogeneous ODEs by eliminating P_i , V_i and H_{z_i} , yielding

$$\frac{d\mathbf{y}_i}{dz} = A_i \mathbf{y}_i, \quad (4.25)$$

where

$$\mathbf{y}_i = \left(H_{y_i}, \frac{dH_{y_i}}{dz}, H_{x_i}, \frac{dH_{x_i}}{dz}, U_i, W_i \right)^T, \quad (4.26)$$

and A_i is a 6×6 matrix whose elements are listed in Table 4.1.

The general solution to Eq. (4.25) is therefore given by linear combination of eigenmodes of the matrix A_i as follows,

$$\mathbf{y}_i(z) = \sum_{j=1}^6 \alpha_{i,j} \exp(\lambda_{i,j} z) \mathbf{v}_{i,j}, \quad (4.27)$$

where $\alpha_{i,j}$ are unknown coefficients to be determined from the CD jump conditions; $\lambda_{i,j}$ is the eigenvalue for fluid region i that corresponds to the j -th root of the following polynomial of λ ,

$$4(k^2 - \lambda^2) (kB_{0x} - i\lambda B_{0z})^2 [s^2 d_L^2 (k^2 - \lambda^2) + (kB_{0x} - i\lambda B_{0z})^2] + (k^2 - \lambda^2) [4\beta s^2 \rho_i (kB_{0x} - i\lambda B_{0z})^2 + \beta^2 s^4 \rho_i^2] = 0; \quad (4.28)$$

and $\mathbf{v}_{i,j}$ is the corresponding eigenvector whose components are given in Table 4.2.

Since the eigenvalues can be grouped by their signature, *i.e.*,

$$\Re(\lambda_{i,1}), \Re(\lambda_{i,2}), \Re(\lambda_{i,3}) < 0; \quad \Re(\lambda_{i,4}), \Re(\lambda_{i,5}), \Re(\lambda_{i,6}) > 0, \quad (4.29)$$

$$\begin{aligned}
a_{1,2} &= 1 \\
a_{2,1} &= \frac{2k^2 B_{0x}^2 + \beta \rho_i s^2}{2d_L^2 s^2 + 2B_{0z}^2} \\
a_{2,2} &= -\frac{ik B_{0x} (2B_{0z}^2 + s^2 d_L^2)}{s^2 B_{0z} d_L^2 + B_{0z}^3} \\
a_{2,3} &= \frac{\beta \rho_i s^3 d_L}{2(s^2 B_{0z} d_L^2 + B_{0z}^3)} \\
a_{2,5} &= -\frac{i\beta k s^2 B_{0x} d_L \rho_i}{2(s^2 B_{0z} d_L^2 + B_{0z}^3)} \\
a_{2,6} &= -\frac{i\beta k s^2 d_L \rho_i}{2(B_{0z}^2 + s^2 d_L^2)} \\
a_{3,4} &= 1 \\
a_{4,1} &= -\frac{d_L (2B_{0x}^2 (2k^4 (B_{0z}^2 + s^2 d_L^2) + \beta k^2 s^2 \rho_i) + \beta^2 s^4 \rho_i^2)}{2\beta s B_{0z} \rho_i (B_{0z}^2 + s^2 d_L^2)} \\
a_{4,2} &= \frac{ik B_{0x} d_L}{s} \left(\frac{s^2}{B_{0z}^2 + s^2 d_L^2} + \frac{2k^2}{\beta \rho_i} \right) \\
a_{4,3} &= \frac{\beta s^2 \rho_i}{2(B_{0z}^2 + s^2 d_L^2)} + k^2 \\
a_{4,4} &= -\frac{ik B_{0x}}{B_{0z}} \\
a_{4,5} &= \frac{ik B_{0x}}{2s} \left(2k^2 - \frac{\beta s^2 \rho_i}{B_{0z}^2 + s^2 d_L^2} \right) \\
a_{4,6} &= -\frac{i\beta k s B_{0z} \rho_i}{2(B_{0z}^2 + s^2 d_L^2)} - \frac{ik^3 B_{0x}^2}{s B_{0z}} \\
a_{5,1} &= -\frac{d_L (2k^2 B_{0x}^2 + \beta s^2 \rho_i)}{\beta \rho_i (B_{0z}^2 + s^2 d_L^2)} \\
a_{5,2} &= \frac{2ik B_{0x} B_{0z} d_L}{\beta B_{0z}^2 \rho_i + \beta s^2 d_L^2 \rho_i} \\
a_{5,3} &= \frac{s B_{0z}}{B_{0z}^2 + s^2 d_L^2} \\
a_{5,5} &= -\frac{ik B_{0x} B_{0z}}{B_{0z}^2 + s^2 d_L^2} \\
a_{5,6} &= \frac{iks^2 d_L^2}{B_{0z}^2 + s^2 d_L^2} \\
a_{6,5} &= -ik
\end{aligned}$$

Table 4.1: Nonzero elements of matrix A_i specified for Eq. (4.25).

$$\begin{aligned}
v_1 &= \frac{a_{2,3}(-\lambda a_{5,5} - a_{5,6} a_{6,5} + \lambda^2) + a_{5,3}(\lambda a_{2,5} + a_{2,6} a_{6,5})}{a_{6,5}(a_{2,3}(\lambda a_{5,2} + a_{5,1}) - a_{5,3}(\lambda(a_{2,2} - \lambda) + a_{2,1}))} \\
v_2 &= \lambda v_1 \\
v_3 &= \frac{-\lambda(\lambda^2 a_{2,2} + \lambda a_{2,1} + a_{2,5}(\lambda a_{5,2} + a_{5,1})) + \lambda a_{5,5}(\lambda(a_{2,2} - \lambda) + a_{2,1}) - a_{6,5}(a_{2,6}(\lambda a_{5,2} + a_{5,1}) - a_{5,6}(\lambda(a_{2,2} - \lambda) + a_{2,1})) + \lambda^4}{a_{6,5}(a_{2,3}(\lambda a_{5,2} + a_{5,1}) - a_{5,3}(\lambda(a_{2,2} - \lambda) + a_{2,1}))} \\
v_4 &= \lambda v_3 \\
v_5 &= \frac{\lambda}{c_{6,5}} \\
v_6 &= 1
\end{aligned}$$

Table 4.2: Components of the eigenvector \mathbf{v} corresponding to a given eigenvalue λ , as seen in Eq. (4.27). The matrix entries $a_{i,j}$ are specified in Table 4.1.

the boundedness of solution at $z = \pm\infty$ immediately requires that

$$\alpha_{1,1} = \alpha_{1,2} = \alpha_{1,3} = \alpha_{2,4} = \alpha_{2,5} = \alpha_{2,6} = 0. \quad (4.30)$$

Further, once y_i is determined, the remaining variables follow directly from (4.12), giving

$$H_{z_i} = \frac{B_{0z}}{s} \frac{dW_i}{dz} + \frac{ikB_{0x}}{s} W_i - \frac{2d_L}{\beta\rho_i s} \left(ikB_{0z} \frac{dH_{y_i}}{dz} - k^2 B_{0x} H_{y_i} \right), \quad (4.31a)$$

$$V_i = \frac{2}{\beta\rho_i s} \left(B_{0z} \frac{dH_{y_i}}{dz} + ikB_{0x} H_{y_i} \right), \quad (4.31b)$$

$$P_i = \frac{-i}{k} \left[\frac{2}{\beta} \left(B_{0z} \left(\frac{dH_{x_i}}{dz} - ikH_{z_i} \right) - ikB_{0y} H_{y_i} \right) - s\rho_i U_i \right]. \quad (4.31c)$$

It is worth noting that the eigenvalue system (4.25) and hence its general solution (4.27) are independent of B_{0y} , the out-of-plane component of the background field. However the total pressure derived in (4.31c) does contain the term proportional to $B_{0y}H_{y_i}$, same as in the transverse field case [see Eq. (4.16)].

Modified CD jump conditions

Because an oblique magnetic field is applied in this section, the appropriate CD jump conditions must be modified in order to determine the remaining six unknown $\alpha_{i,j}$. It follows from Eq. (4.4) that when the magnetic field is not parallel to the interface, *i.e.*, $B_n \neq 0$, both the pressure, p , and magnetic field, \mathbf{B} , must be continuous across the CD. Consequently, the linearized CD jump conditions in the Laplace space follow,

$$[[W]]_{z=0} = 0, \quad (4.32a)$$

$$[[H_z]]_{z=0} = 0, \quad (4.32b)$$

$$[[H_x]]_{z=0}, \quad (4.32c)$$

$$H_{y_1}(0) = H_{y_2}(0) = 0, \quad (4.32d)$$

$$[[P]]_{z=0} = \eta_0(\rho_2 - \rho_1), \quad (4.32e)$$

where continuity of \tilde{p} , \tilde{H}_x and \tilde{H}_y at the interface $z = h$ is used in Eq. (4.19) in order to arrive at (4.32e).

Again, as in Sec. 4.3.1, here Eqs. (4.31c), (4.32d) and (4.32e) imply that the effect of finite B_{0y} can be entirely captured by changing β . Therefore we proceed with an in-plane background field,

$$\hat{\mathbf{B}}_0 = (\sin \phi, 0, \cos \phi), \quad (4.33)$$

where $\phi \in [0, \pi/2)$ due to symmetry is the angle made by the applied field with z -axis, as shown in Fig. 4.1(b). Thereafter, substituting (4.27), (4.31) and (4.33) into (4.32) produces a set of linear equations from which the indeterminate $\alpha_{i,j}$ can be uniquely solved. The resulting expressions are cumbersome and therefore omitted for brevity.

It is important to note that forcing continuity of the tangential magnetic field as well as the pressure in (4.32c)–(4.32e) suggests that the “effective pressure” condition (4.17b) required in the transverse field case is also satisfied when an oblique field applies, making Eq. (4.32) a subset of Eq. (4.17). This means the solution space available for (4.17) is expanded since more eigenmodes are included. The significance of having a larger solution space is further discussed in Sec. 4.4.4, where the limiting flow as $\phi \rightarrow \pi/2$ is considered.

Interface response

Having obtained the flow solution in the Laplace space, the temporal behavior is determined through the inverse transform formally given by the Bromwich integral,

$$\mathcal{L}^{-1} [G(s)] = \frac{1}{2\pi i} \int_{r-i\infty}^{r+i\infty} G(s) e^{ts} ds, \quad (4.34)$$

where $r \in \mathbb{R}$ is greater than any real part of the singularities of the function $G(s)$. In particular, the interface perturbation amplitude is calculated as

$$\eta(t) = \eta_0 + \mathcal{L}^{-1} \left[\frac{W(0; s)}{s} \right]. \quad (4.35)$$

Additionally, circulation deposition at the interface due to tangential slip velocity is facilitated by the Hall-MHD description when an oblique magnetic field is present. To leading order, this circulation over a half wavelength (recalling $\Lambda = 1$, $k = 2\pi$) is given by

$$\gamma_0(t) = \mathcal{L}^{-1} \left[\Delta U \int_0^{\Lambda/2} e^{ikx} dx \right] = \mathcal{L}^{-1} \left[\frac{2i\Delta U}{k} \right], \quad (4.36)$$

where $\Delta U \equiv U_2(0) - U_1(0)$. It can be verified that the initial interface behavior is dictated by the pure hydrodynamic response, independent of the strength and orientation of the applied magnetic field, *i.e.*,

$$\left. \frac{d\eta}{dt} \right|_{t=0^+} = \eta_0 k \mathcal{A}, \quad \gamma_0(0^+) = 4\eta_0 \mathcal{A}. \quad (4.37)$$

4.3.3 Vorticity transport

The lack of a transport mechanism for vorticity, $\boldsymbol{\omega} = \nabla \times \mathbf{u}$, after its initial baroclinic generation is the essential cause of the RMI in a non-conducting gas [85]. However in a plasma described by the Hall-MHD model, vorticity is governed by

$$\frac{\partial \boldsymbol{\omega}}{\partial t} + (\mathbf{u} \cdot \nabla) \boldsymbol{\omega} = (\boldsymbol{\omega} \cdot \nabla) \mathbf{u} + \frac{\nabla \rho \times \nabla p}{\rho^2} + \frac{2}{\beta \rho} [\nabla \times (\nabla \times \mathbf{B} \times \mathbf{B})], \quad (4.38)$$

where the magnetic field clearly affects the dynamics. Linearizing (4.38) around the base-flow discussed in Sec. 4.2.3 subject to an oblique magnetic field in the x, z -plane produces,

$$\frac{\partial \tilde{\boldsymbol{\omega}}}{\partial t} = \frac{2}{\beta \rho_i} \begin{bmatrix} -\cos \phi \frac{\partial^2 \tilde{B}_y}{\partial z^2} - ik \sin \phi \frac{\partial \tilde{B}_y}{\partial z} \\ \cos \phi \left(\frac{\partial^2 \tilde{B}_x}{\partial z^2} - ik \frac{\partial \tilde{B}_z}{\partial z} \right) + \sin \phi \left(ik \frac{\partial \tilde{B}_x}{\partial z} + k^2 \tilde{B}_z \right) \\ ik \cos \phi \frac{\partial \tilde{B}_y}{\partial z} - k^2 \sin \phi \tilde{B}_y \end{bmatrix}, \quad (4.39)$$

for the linearized vorticity vector

$$\tilde{\boldsymbol{\omega}} = \left(-\frac{\partial \tilde{v}}{\partial z}, -ik \tilde{w} + \frac{\partial \tilde{u}}{\partial z}, ik \tilde{v} \right)^T. \quad (4.40)$$

Differentiating (4.39) with respect to time t once more using (4.8) then implies

$$\frac{\partial^2 \tilde{\boldsymbol{\omega}}}{\partial t^2} = \frac{2}{\beta \rho_i} \mathcal{F} [\tilde{\boldsymbol{\omega}}] + \frac{4d_L}{\beta^2 \rho_i^2} \mathcal{F} \left[\frac{\partial^2 \tilde{\mathbf{B}}}{\partial z^2} - k^2 \tilde{\mathbf{B}} \right], \quad (4.41)$$

where the operator \mathcal{F} is given by

$$\mathcal{F} = \cos^2 \phi \frac{\partial^2}{\partial z^2} + 2ik \cos \phi \sin \phi \frac{\partial}{\partial z} - k^2 \sin^2 \phi. \quad (4.42)$$

In view of $\partial/\partial x = ik$, \mathcal{F} becomes

$$\mathcal{F} = \left(\sin \phi \frac{\partial}{\partial x} + \cos \phi \frac{\partial}{\partial z} \right)^2 = \frac{\partial^2}{\partial r^2}, \quad (4.43)$$

where r is defined as the path length in the magnetic field direction:

$$x = r \sin \phi, \quad z = r \cos \phi. \quad (4.44)$$

Therefore Eq. (4.41) simplifies to a forced wave equation,

$$\frac{\partial^2 \tilde{\boldsymbol{\omega}}}{\partial t^2} = \frac{2}{\beta \rho_i} \frac{\partial^2 \tilde{\boldsymbol{\omega}}}{\partial r^2} + \frac{4d_L}{\beta^2 \rho_i^2} \frac{\partial^2 (\nabla^2 \tilde{\mathbf{B}})}{\partial r^2}, \quad (4.45)$$

where the normalized Alfvén waves propagate along the magnetic field lines at the speed of $c_{A_i} = \sqrt{2/(\beta \rho_i)}$. For an oblique field angle ϕ , a coupling between waves

traveling parallel and normal to the interface is expected, leading to a continuous change of phase at the interface.

Equation (4.45) contains a vorticity source term, produced by magnetic field perturbations, that vanishes in the MHD limit $d_L \rightarrow 0$ for all ϕ . The vorticity forcing in Hall-MHD is proportional to both the Larmor radius d_L and the square of Alfvén speed c_A^2 , suggesting that vorticity production is generated by Whistler waves available in the Hall-MHD system whose frequencies also scale as $\omega \propto c_A^2/d_L$ [42, 91]. As a result, conservation of circulation following the initial baroclinic generation, that holds for a non-conducting gas and also for regular MHD, is no longer true in Hall-MHD.

Further, the integral of (4.39) across CD at $z = h(x, t) = \eta(t)e^{ikx}$ gives the leading order evolution equation for the interface vortex strength, $\zeta(x, t) \equiv \int_{h^-}^{h^+} \tilde{\omega} e^{ikx} dz$, as follows

$$\frac{\partial \zeta}{\partial t} = \frac{2\iota \cos \phi}{\rho_1 + \rho_2} + O(\eta), \quad 0 \leq \phi < \frac{\pi}{2}, \quad (4.46)$$

where

$$\zeta = e^{ikx} \mathcal{L}^{-1} [(-\Delta V, \Delta U)^T], \quad \iota = e^{ikx} \mathcal{L}^{-1} \left[\left(-\Delta \frac{dH_y}{dz}, \Delta \frac{dH_x}{dz} \right)^T \right], \quad (4.47)$$

and $\Delta \xi \equiv \xi_2(0) - \xi_1(0)$ for $\xi \in \{U, V, dH_x/dz, dH_y/dz\}$. To see (4.46), we recall that the CD jump conditions for $\phi \in [0, 2\pi)$ demand continuity of $\{\tilde{w}, \tilde{B}_x, \tilde{B}_y, \tilde{B}_z\}$ across the interface, while allowing $\{\tilde{u}, \tilde{v}, d\tilde{B}_x/dz, d\tilde{B}_y/dz\}$ jumps discontinuously at $z = h$. Therefore by writing

$$v(z) = v(h^-) + [v(h^+) - v(h^-)] H(z - h) + O(\eta), \quad (4.48)$$

for $v \in \{U, V, W, H_x, H_y, H_z, dH_x/dz, dH_y/dz\}$ in the vicinity of $z = h$, and choosing $H(0) = 1/2$ for the Heaviside function, (4.46) follows from substituting (4.6), (4.48) into the Laplace transform of (4.39) and integrating over $z \in [h^-, h^+]$. Equations (4.46) and (4.47) thus suggest that the dynamics of interface vortex strength, ζ , understood as discontinuous jumps in perturbation vorticity $\tilde{\omega} = \nabla \times \tilde{\mathbf{u}}$, is driven by the interface current strength ι , since ι can be similarly interpreted as jumps in perturbation current density $\tilde{\mathbf{j}} = 2d_L(\nabla \times \tilde{\mathbf{B}})/\beta$.

4.4 Asymptotic analysis

In this section we explore the limiting behavior of the impulsive RM flow subject to an oblique magnetic field obtained in Sec. 4.3.2, with respect to extreme values

of the Larmor radius d_L , the plasma energy ratio β , and the field angle ϕ . It is also insightful to discuss one more related parameter, the normalized ion skin depth d_S , given by

$$d_S = d_L \sqrt{\frac{2}{\beta}}, \quad (4.49)$$

which is independent of the applied magnetic field. The plasma region beyond ideal MHD where $d_S \gg 1$ will be examined.

4.4.1 The MHD limit

Upon passing the limit $d_L \rightarrow 0$ with β held fixed, to the general Hall-MHD solution developed previously, we immediately obtain the RM flow field corresponding to the ideal MHD model. It is verified that in such limit, firstly, the out-of-plane components of the flow and magnetic fields, V_i and H_{y_i} , decouple from the system (4.12); and secondly, the MHD Rankine-Hugoniot relations, which require that u , w , B_x , B_z , and p are continuous across the contact, are uniformly satisfied by the Hall-MHD CD jump conditions (4.32). Indeed, as $d_L \rightarrow 0$, Eqs. (4.12a), (4.31a), and (4.32b) show that the tangential slip velocity vanishes, *i.e.*, $\Delta U = 0$.

Derivation for perturbation velocity

Nonetheless, physics of the limiting MHD flow is better understood by explicitly solving the corresponding boundary value problem. The solution to this problem was briefly presented by [106] and is treated in significantly more detail here. To proceed, the eigenvalue equation (4.28) factorizes as $d_L \rightarrow 0$, and (4.27) gives in particular,

$$W_i = A_i e^{kz} + B_i e^{-kz} + \left(C_i e^{s\sqrt{\beta\rho_1/2}\sec\phi} + D_i e^{-s\sqrt{\beta\rho_1/2}\sec\phi} \right) e^{-ikz \tan\phi}, \quad (4.50)$$

where $A_2 = B_1 = C_2 = D_1 = 0$ for decaying modes. The factor of $e^{ikz \tan\phi}$ that multiplies the final two terms is the only modification to the general solution found by Wheatley *et al.* [105] for the normal magnetic field case.

The CD jump conditions (4.32) in the MHD limit translate into

$$\begin{aligned} \llbracket W \rrbracket_{z=0} = \llbracket \partial_z W \rrbracket_{z=0} = \llbracket \partial_z^2 W \rrbracket_{z=0} = 0, \\ \frac{2 \cos^2 \phi}{\beta} \llbracket \partial_z^3 W \rrbracket_{z=0} - s^2 (\rho_2 \partial_z W_2|_{z=0} - \rho_1 \partial_z W_1|_{z=0}) = sk^2 (\rho_2 - \rho_1) \eta_0. \end{aligned} \quad (4.51)$$

Substituting (4.50) into (4.51) and solving simultaneously for the coefficients then produces

$$\begin{aligned}
A_1 &= k\eta_0\mathcal{A}\frac{s(s+\bar{f}_1)}{(s-f_1)(s-\theta)(s-\bar{\theta})}, \\
B_2 &= k\eta_0\mathcal{A}\frac{s(s+f_2)}{(s-\bar{f}_2)(s-\theta)(s-\bar{\theta})}, \\
C_1 &= -\frac{2\sqrt{2}\cos\phi k^2\eta_0\mathcal{A}}{\sqrt{\beta\rho_1}+\sqrt{\beta\rho_2}}\sqrt{\frac{\rho_2}{\rho_1}}\frac{s+f_2}{(s-f_1)(s-\theta)(s-\bar{\theta})}, \\
D_2 &= -\frac{2\sqrt{2}\cos\phi k^2\eta_0\mathcal{A}}{\sqrt{\beta\rho_1}+\sqrt{\beta\rho_2}}\sqrt{\frac{\rho_1}{\rho_2}}\frac{s+\bar{f}_1}{(s-\bar{f}_2)(s-\theta)(s-\bar{\theta})}.
\end{aligned} \tag{4.52}$$

Here, the poles of the above functions are defined using

$$\theta = \kappa + i\omega, \quad f_j = f_{z_j} + if_{x_j} \quad (j = 1, 2), \tag{4.53}$$

where

$$\begin{aligned}
\kappa &= -\cos\phi\sqrt{\frac{2}{\beta}}k\frac{\sqrt{\rho_1}+\sqrt{\rho_2}}{\rho_1+\rho_2}, \quad \omega = k\left[\frac{4\sin^2\phi}{\beta(\rho_1+\rho_2)} + \frac{2}{\beta}\left(\frac{\cos\phi(\sqrt{\rho_2}-\sqrt{\rho_1})}{\rho_1+\rho_2}\right)^2\right]^{1/2}, \\
f_{x_j} &= c_{A_jx}k, \quad f_{z_j} = c_{A_jz}k,
\end{aligned} \tag{4.54}$$

and $\mathbf{c}_{A_j} = (c_{A_jx}, c_{A_jz}) = \hat{\mathbf{B}}_0\sqrt{2/(\beta\rho_j)}$ is the Alfvén wave velocity in fluid j . The z -component velocity perturbations in each fluid are then obtained by taking the inverse Laplace transform of (4.50). This yields

$$w'_1(x, z, t) = \hat{a}_1(t)e^{kz+ikx} + \hat{c}_1(t+z/c_{A_1z})e^{ik(x-zc_{A_1x}/c_{A_1z})}H(t+z/c_{A_1z}), \tag{4.55a}$$

$$w'_2(x, z, t) = \hat{b}_2(t)e^{-kz+ikx} + \hat{d}_2(t-z/c_{A_2z})e^{ik(x-zc_{A_2x}/c_{A_2z})}H(t-z/c_{A_2z}), \tag{4.55b}$$

where

$$\begin{aligned}
\hat{a}_1(t) &= k\eta_0\mathcal{A} \left\{ \frac{2f_{z_1}f_1}{(f_1-\theta)(f_1-\bar{\theta})} e^{f_1 t} + \frac{e^{\kappa t}}{2i\omega} \left[\frac{\theta(\theta+\bar{f}_1)}{\theta-f_1} e^{i\omega t} - \frac{\bar{\theta}(\bar{\theta}+\bar{f}_1)}{\bar{\theta}-f_1} e^{-i\omega t} \right] \right\}, \\
\hat{b}_2(t) &= k\eta_0\mathcal{A} \left\{ \frac{2f_{z_2}\bar{f}_2}{(\bar{f}_2-\theta)(\bar{f}_2-\bar{\theta})} e^{\bar{f}_2 t} + \frac{e^{\kappa t}}{2i\omega} \left[\frac{\theta(\theta+f_2)}{\theta-f_2} e^{i\omega t} - \frac{\bar{\theta}(\bar{\theta}+f_2)}{\bar{\theta}-f_2} e^{-i\omega t} \right] \right\}, \\
\hat{c}_1(t) &= -\frac{2\sqrt{2}\cos\phi k^2\eta_0\mathcal{A}}{\sqrt{\beta\rho_1}+\sqrt{\beta\rho_2}} \sqrt{\frac{\rho_1}{\rho_2}} \\
&\quad \times \left\{ \frac{f_1+f_2}{(f_1-\theta)(f_1-\bar{\theta})} e^{f_1 t} + \frac{e^{\kappa t}}{2i\omega} \left[\frac{\theta+f_2}{\theta-f_1} e^{i\omega t} - \frac{\bar{\theta}+f_2}{\bar{\theta}-f_1} e^{-i\omega t} \right] \right\}, \\
\hat{d}_2(t) &= -\frac{2\sqrt{2}\cos\phi k^2\eta_0\mathcal{A}}{\sqrt{\beta\rho_1}+\sqrt{\beta\rho_2}} \sqrt{\frac{\rho_1}{\rho_2}} \\
&\quad \times \left\{ \frac{\bar{f}_1+\bar{f}_2}{(\bar{f}_2-\theta)(\bar{f}_2-\bar{\theta})} e^{\bar{f}_2 t} + \frac{e^{\kappa t}}{2i\omega} \left[\frac{\theta+\bar{f}_1}{\theta-\bar{f}_2} e^{i\omega t} - \frac{\bar{\theta}+\bar{f}_1}{\bar{\theta}-\bar{f}_2} e^{-i\omega t} \right] \right\}.
\end{aligned} \tag{4.56}$$

Here, the term involving $\hat{a}_1(t)$ arises from the inverse Laplace transform of $A_1(s)$ and so forth. It can be verified that substituting $\phi = \pi/2$ into (4.55) recovers Eq. (4.21), the transverse magnetic field solution discussed in Section 4.3.1.

Wave propagation

The Heaviside functions that appear in the solution (4.55) correspond to finite-amplitude, non-uniform Alfvén waves, which we refer to as Alfvén fronts. These propagate outward from the interface at the relevant Alfvén speeds. Such waves are permitted in an incompressible flow since density and normal velocity are continuous across them, as are pressure and normal magnetic field. The finite amplitude waves divide the solution into four regions: $z < -c_{A_1 z} t$, where $w' = \hat{a}_1(t)e^{kz+ikx}$; $-c_{A_1 z} t < z < 0$, where both \hat{a}_1 and \hat{c}_1 terms contribute to w' ; $0 < z < c_{A_2 z} t$, where w' is given by terms involving \hat{b}_2 and \hat{d}_2 ; and $z > c_{A_2 z} t$, where $w' = \hat{b}_2(t)e^{-kz+ikx}$. Observe that the solution below the interface is equivalent to that above, but with ρ_1 and ρ_2 interchanged and the dependence on z reversed. It is therefore sufficient to discuss the features of the solution for $z > 0$. The leading term in $\hat{b}_2(t)e^{-kz+ikx}$ has the form $K_b e^{-k(z-c_{A_2 z} t)+ik(x-c_{A_2 x} t)}$, which is wave-like in nature, propagating away from the density interface at the Alfvén speed parallel to the base magnetic field. This mode decays exponentially upstream of the upper Alfvén front and grows exponentially downstream ($0 < z < c_{A_2 z} t$). However, exponential growth in w' does not occur because in this region the leading terms arising from \hat{b}_2 and \hat{d}_2 can be shown to cancel. The remaining terms arising from \hat{b}_2 correspond to oscillations at angular frequency ω that decay exponentially in time since $\kappa < 0$. The oscillations

also decay exponentially with distance above the interface like e^{-kz} . The mode arising from $\hat{d}(t - z/c_{A2z})$ is entirely wave-like in nature and propagates parallel to the base magnetic field. This mode, which due to the Heaviside function is only present between the upper Alfvén front and the interface, introduces a gradient discontinuity in w' at the front, which from (4.12a) implies a tangential velocity discontinuity. This results in the Alfvén front, and its partner in the $z < 0$ fluid, transporting the vorticity generated by the impulsive acceleration of the interface from its location. Thus the requirement that the tangential velocity slip across the CD be zero in the MHD limit is satisfied for $t > 0$. Since the distribution of vorticity induces the interfacial velocities responsible for perturbation growth, its transport from the interface on the Alfvén fronts is the mechanism that underpins mitigation of the MHD RMI when a magnetic field is present.

4.4.2 Large skin depth limit

Shen *et al.* [91] showed that the ideal MHD equations correspond to the formal limit of small skin depth, d_S , of the Hall-MHD system. Therefore complementary to the MHD theory, the opposite limit of $d_S \rightarrow \infty$, is examined next. This limit manifests strong effect of the Hall current [42]. According to (4.49), the limit can be achieved by either taking $\beta \rightarrow 0$ with d_L held finite, or letting $d_L \rightarrow \infty$ while keeping β fixed. Both cases are shown to produce the same result in the following.

Limit approached with small β

Using quartic root formula, the eigenvalues found in (4.28) can be Taylor expanded around $\beta = 0$ to first order, giving

$$\lambda = \pm k, \pm \left[\frac{\beta \rho_i s}{2k d_L \sqrt{\sigma^2 + 1}} + \frac{k \left(\sigma \sqrt{\sigma^2 + 1} \mp i \sin \phi \cos \phi \right)}{\sigma^2 + \cos^2 \phi} \right], \pm \frac{\beta \rho_i s}{2k d_L} - ik \tan \phi, \quad (4.57)$$

where $\sigma = d_L s$.

Substituting the general solutions (4.27) and (4.31) with approximated eigenvalues and eigenvectors into (4.32) yields a system of linear equations [see Eq. (B.1), Appendix B] from which the coefficients $\alpha_{i,j}$ are solved to yield

$$\alpha_{2,2} = \alpha_{1,5} = \frac{\eta_0 k \mathcal{A} d_L}{1 + \sqrt{1 + \sigma^2}}, \quad \alpha_{2,1} = \alpha_{2,3} = \alpha_{1,4} = \alpha_{1,6} = 0. \quad (4.58)$$

Consequently, one obtains from (4.27) the transformed in-plane flow field,

$$W_{1,2}(z) = \frac{\eta_0 \mathcal{A} k d_L}{1 + \sqrt{1 + \sigma}} \exp(\chi^\pm z), \quad (4.59)$$

$$U_{1,2}(z) = \pm \frac{i \eta_0 \mathcal{A} k d_L \left(\sigma \sqrt{1 + \sigma^2} \mp i \sin \phi \cos \phi \right)}{\left(1 + \sqrt{1 + \sigma^2} \right) (\sigma^2 + \cos^2 \phi)} \exp(\chi^\pm z), \quad (4.60)$$

where

$$\chi^\pm = \pm \frac{k \left(\sigma \sqrt{\sigma^2 + 1} \mp i \sin \phi \cos \phi \right)}{\sigma^2 + \cos^2 \phi}. \quad (4.61)$$

Inspired by the definition of σ , it is convenient to renormalize time t accordingly and define the ion cyclotron time scale $T \equiv t/d_L$ [92]. Using (4.35) and (4.36), inverting the Laplace transform ($\mathcal{L}^{-1} : \sigma \rightarrow T$) thus leads to

$$\frac{\hat{\eta} - \hat{\eta}_0}{d_L} = T {}_1F_2 \left(-\frac{1}{2}; 1, \frac{3}{2}; -\frac{T^2}{4} \right) - \frac{T^2}{2}, \quad (4.62)$$

$$\hat{\gamma}_0 = \frac{(\cos^2 \phi - 1) \cos(T \cos \phi) - \cos \phi \sin(T \cos \phi) + 1}{\cos^2 \phi} - \frac{1 - \cos(T \cos \phi)}{\cos^2 \phi} * \frac{J_1(T)}{T}, \quad (4.63)$$

where $\hat{\eta} = \eta/(\mathcal{A}\eta_0 k)$, $\hat{\gamma}_0 = \gamma_0/(4\eta_0 \mathcal{A})$, ${}_1F_2$ is the generalized hypergeometric function [3], J_1 is the first order Bessel function of the first kind, and $*$ denotes the convolution integral given by

$$f(T) * g(T) = \int_0^T f(\tau) g(T - \tau) d\tau. \quad (4.64)$$

The detailed steps of Laplace transform inversion towards (4.62) and (4.63) is provided in Appendix C. Interestingly, the growth of the interface perturbation found in (4.62) is independent of the field angle ϕ , but the circulation deposition derived in (4.63) is not. In this case, the flow fields away from the CD must adjust accordingly to the varying circulation as ϕ changes, so that a common interfacial growth is maintained.

Limit approached with large d_L

The alternative route to access the large d_S region is realized in the dual Laplace space, $(s, t) \mapsto (\sigma, T)$, and applying the distinguished limit of $t \rightarrow \infty$ while holding T constant. Specifically, the eigenvalues as functions of σ are first expanded in power

series of $\epsilon \equiv 1/d_L$ around $\epsilon = 0$, giving

$$\lambda = \pm k, \pm \frac{\beta \rho_i \sigma \epsilon^2}{2k} - ik \tan \phi, \pm \frac{\sigma}{2k \sqrt{\sigma^2 + 1}} \left(\beta \rho_i \epsilon^2 + \frac{2k^2 (\sigma^2 + 1)}{\sigma^2 + \cos^2 \phi} \right) - \frac{ik \sin \phi \cos \phi}{\sigma^2 + \cos^2 \phi}. \quad (4.65)$$

Again, applying the boundary conditions to the approximated eigenmodes [see Eq. (B.3), Appendix B] leads to $\alpha_{i,j}$ in the limit,

$$\alpha_{2,2} = \alpha_{1,5} = \frac{\eta_0 k \mathcal{A}}{(1 + \sqrt{1 + \sigma^2}) \epsilon}, \quad \alpha_{2,1} = \alpha_{2,3} = \alpha_{1,4} = \alpha_{1,6} = 0, \quad (4.66)$$

which is effectively identical to the previous result (4.58). It immediately follows that the flow field in the present $d_L \rightarrow \infty$ limit, viewed in the cyclotron time scale, is the same as those given in Eqs. (4.59)–(4.63). We therefore distinctly attribute such flow field to the common large ion skin depth limit, obtained as $d_S \rightarrow \infty$.

4.4.3 Strong field limit

Here, we briefly discuss the flow region where the hydrodynamic forces are dominated by a large magnetic field. Since d_S not a function of the applied field strength, this region corresponds to the limit of $\beta \rightarrow 0$ while holding d_S fixed. In this case, all six eigenvalues take the asymptotic form of

$$\lambda \sim -ik \tan \phi + O(\beta^{1/2}), \quad (4.67)$$

leading to uniform decay of the coefficients $\alpha_{i,j}$ as

$$\alpha_{2,1} \sim \alpha_{1,6} \sim O(\beta), \quad \alpha_{2,2} \sim \alpha_{2,3} \sim \alpha_{1,4} \sim \alpha_{1,5} \sim O(\beta^{1/2}). \quad (4.68)$$

Hence, from Eq. (4.3), increasing the external magnetic field strength inhibits any perturbation to the base-flow, as all variables in (4.27) and (4.31) decay asymptotically as follows:

$$W, V \sim O(\beta^{1/2}), \quad U \sim \begin{cases} O(\beta^{1/2}), & \phi > 0 \\ O(\beta), & \phi = 0 \end{cases}, \quad H_{x,y,z} \sim O(\beta), \quad (4.69)$$

and the normal flow is always inversely proportional to the applied field strength. In the limit $\beta \rightarrow 0$, the initial impulse propagates in time with a frozen interface, due to an overwhelming background magnetic field.

4.4.4 Large angle limit

The last limit of interest occurs when the background magnetic is nearly parallel to the mean interface, namely, $\phi \rightarrow \pi/2$, while maintaining a small component in the normal direction. The flow field is approached in this case by expansions around $\varepsilon = 0$, after substituting $B_{0z} = \varepsilon$, and $B_{0x} = \sqrt{1 - \varepsilon^2}$. For the linear theory developed in Sec. 4.2.3 to be valid under this limit, it is required that the perturbation magnitude is sufficiently small, *i.e.*, $\eta \ll \varepsilon \ll 1$.

To proceed, the applicable eigenvalues are those obtained in (4.28) for an oblique magnetic field, approximated by

$$\lambda = \pm k, \pm \mu_i^* - \frac{i\varepsilon(4k^4 - \beta^2 \rho_i^2 s^4)}{4k^3 d_L^2 s^2}, \pm \frac{\beta \rho_i s}{2k d_L} + \frac{ik(\varepsilon^2 - 2)}{2\varepsilon} - \frac{i\beta^2 \rho_i^2 s^2 \varepsilon}{4k^3 d_L^2}, \quad (4.70)$$

where μ_i^* is a special value of μ_i , defined in (4.14), evaluated at $B_{0x} = 1$. It is observed that as $\varepsilon \rightarrow 0$, two of the eigenvalues diverge, in addition to recovering those associated with the transverse field case found in (4.13). As a result, all six eigenmodes are utilized in order to meet the oblique field jump conditions (4.32), generating the following coefficients from Eq. (B.5), Appendix B, at order $O(\varepsilon^0)$,

$$\begin{aligned} \alpha_{2,1} &= \frac{\beta \eta_0 k (\rho_1 - \rho_2) s (4k^4 d_L (\rho_1 - \rho_2) s - \psi)}{4\beta k^4 d_L (\rho_1 - \rho_2)^2 s^3 + 4k^2 \psi + \beta (\rho_1 + \rho_2) s^2 \psi}, \\ \alpha_{2,2} &= \frac{-8\eta_0 k^5 d_L (\rho_1 - \rho_2) (2k^2 + \beta \rho_1 s^2)}{4\beta k^4 d_L (\rho_1 - \rho_2)^2 s^3 + 4k^2 \psi + \beta (\rho_1 + \rho_2) s^2 \psi}, \\ \alpha_{1,5} &= \frac{-8\eta_0 k^5 d_L (\rho_1 - \rho_2) (2k^2 + \beta \rho_2 s^2)}{4\beta k^4 d_L (\rho_1 - \rho_2)^2 s^3 + 4k^2 \psi + \beta (\rho_1 + \rho_2) s^2 \psi}, \\ \alpha_{1,6} &= \frac{\beta \eta_0 k (\rho_1 - \rho_2) s (4k^4 d_L (\rho_2 - \rho_1) s - \psi)}{4\beta k^4 d_L (\rho_1 - \rho_2)^2 s^3 + 4k^2 \psi + \beta (\rho_1 + \rho_2) s^2 \psi}, \\ \alpha_{2,3} &= \alpha_{1,4} = 0, \end{aligned} \quad (4.71)$$

where

$$\begin{aligned} \psi &= 2k^2 \rho_2 \left(2k^2 + 2k s d_L \mu_2^* + \beta \rho_2 s^2 \right) + \beta \rho_1^2 s^2 \left(2k^2 + \beta \rho_2 s^2 \right) \\ &+ \rho_1 \left(4k^4 + 4k^3 s d_L \mu_1^* + 2k \beta \rho_2 s^2 (2k + s d_L \mu_1^* + s d_L \mu_2^*) + \beta^2 \rho_2^2 s^4 \right). \end{aligned} \quad (4.72)$$

Comparison with transverse field case

The interface growth rate is calculated using (4.27) and (4.71) as

$$W_{1,2}(0) = \frac{\eta_0 k (\rho_2 - \rho_1) (16k^6 d_L + 4\beta k^4 d_L (\rho_1 + \rho_2) s^2 + \beta s \psi)}{\beta s^2 (\rho_2 (4k^4 d_L \rho_2 s + \psi) + \rho_1 (\psi - 8k^4 d_L \rho_2 s) + 4k^4 d_L \rho_1^2 s) + 4k^2 \psi}, \quad (4.73)$$

which obviously differs from the one derived for a strictly parallel magnetic field where $\phi = \pi/2$, given in Sec. 4.3.1, rendering the latter a singular limit, as the eigenvalue equation (4.28) loses its term of highest power of λ when $\varepsilon = 0$. In addition, Eq. (4.32), the CD jump conditions associated with an oblique background field does not converge to Eq. (4.17), its parallel field counterpart. Particularly, the magnetic field may be discontinuous at the interface when a strictly parallel background is present. Indeed, substituting (4.20) into (4.16) shows when $\phi = \pi/2$,

$$\Delta H_x \equiv H_{x_2}(0) - H_{x_1}(0) = \frac{2\eta_0 k^2 \beta (\rho_2 - \rho_1)}{4k^2 + \beta (\rho_1 + \rho_2) s^2} \neq 0. \quad (4.74)$$

However, as $\phi \rightarrow \pi/2$ with $\varepsilon > 0$, using (4.27) and (4.70), it is demanded that

$$\Delta H_x = \frac{k d_L (\alpha_{2,3} + \alpha_{1,4})}{-\varepsilon^2} + \frac{k (\alpha_{2,1} + \alpha_{1,6})}{s} - \frac{\beta s (\alpha_{2,2} \rho_2 \mu_2^* + \alpha_{1,5} \rho_1 \mu_1^*)}{2k^2} + O(\varepsilon) \rightarrow 0, \quad (4.75)$$

in which the first term is essential because in fact $\alpha_{2,3} \sim \alpha_{1,4} \sim O(\varepsilon^2)$. The exact higher order expressions for $\alpha_{2,3}$ and $\alpha_{1,4}$ are not given, since the order unity approximation found in (4.71) is sufficient to determine the flow field (U, V, W) in the $\varepsilon \rightarrow 0$ limit.

Importantly, despite the difference between ΔH_x in two cases, (4.75) does not contradict (4.74), because the ‘‘effective pressure’’ condition (4.17b) for the strictly parallel field ($\varepsilon = 0$) case is otherwise satisfied in a stronger sense, that is, continuity of the tangential magnetic field, enabled by introducing extra eigenmodes in the oblique field case ($\varepsilon > 0$). Therefore Eq. (4.71) obtained for $\varepsilon = 0^+$ that lives in a larger function space, as discussed in Sec. 4.3.2, provides an alternative solution. A detailed discussion on the linearization of original CD jump conditions (4.4) that give rise to the difference between Eqs. (4.17) for $\varepsilon = 0$ and (4.32) for $\varepsilon = 0^+$, is given in Appendix D. The loss of continuity in the tangential magnetic field transitioning from $\varepsilon = 0^+$ to $\varepsilon = 0$ is the result of non-uniform convergence associated with interchanging two asymptotics: the linearization limit $\eta_0 \rightarrow 0$ and the large angle limit $\varepsilon \rightarrow 0$.

The discontinuous jump in flow fields observed between strictly and nearly parallel field cases can nonetheless be reduced by decreasing d_L . In the ideal MHD limit, substituting $d_L = 0$ into (4.71) gives

$$\alpha_{2,1} = \alpha_{1,6} = \frac{(\rho_2 - \rho_1) \beta \eta_0 k s}{4k^2 + \beta \rho_1 s^2 + \beta \rho_2 s^2}, \quad \alpha_{2,2} = \alpha_{2,3} = \alpha_{1,4} = \alpha_{1,5} = 0, \quad (4.76)$$

which are identical to those coefficients found in (4.20), exactly recovering the flow field subject to a parallel magnetic background. Therefore the difference between interface velocities W evaluated using $\varepsilon = 0$ and $\varepsilon = 0^+$ disappears as $d_L \rightarrow 0$, even though the RH conditions for the tangential magnetic field in these two cases are physically different for all $d_L \geq 0$. Particularly, it can be seen from Eqs. (4.16) and (4.24) that ΔH_x evaluated at $d_L = \varepsilon = 0$ has a nonzero sinusoidal behavior.

The key comparisons made in this section between the $\varepsilon = 0$ case and the $\eta_0 \ll \varepsilon = 0^+$ case can be summarized as follows:

$$\begin{aligned} \forall d_L > 0, \quad W_{1,2}(0)|_{\varepsilon=0^+} - W_{1,2}(0)|_{\varepsilon=0} &\neq 0, \\ \lim_{d_L \rightarrow 0} \left[W_{1,2}(0)|_{\varepsilon=0^+} - W_{1,2}(0)|_{\varepsilon=0} \right] &= 0, \\ \forall d_L \geq 0, \quad \Delta H_x|_{\varepsilon=0^+} - \Delta H_x|_{\varepsilon=0} &= -\Delta H_x|_{\varepsilon=0} \neq 0. \end{aligned} \quad (4.77)$$

We also note that the solution characteristics in the transitioning parameters region where $\eta_0 \sim \varepsilon \ll 1$ is unknown to the present linear analysis.

4.5 Numerical results

The temporal behaviour of the vector fields of interest is retrieved from the s -dependent solutions calculated in Sec. 4.3, by applying the inverse Laplace transform. For general parameter values of the Larmor radius d_L and the plasma parameter β , this is performed numerically for a given time, t , using the multi-precision Gaver-Stehfest method [2, 33, 97]. The algorithm originates from constructing a converging sequence of exponential probability density functions that naturally connects the expectation of a time-dependent function $\mathbb{E}[g(t)]$, to its Laplace transform $G(s)$. At a given time t , the temporal function value is thus approached by sampling its known transform at $2M$ different real points, namely,

$$g_M(t) \equiv \frac{\ln 2}{t} \sum_{k=1}^{2M} \psi_k G\left(\frac{k \ln 2}{t}\right) \xrightarrow{M \rightarrow \infty} g(t), \quad (4.78)$$

with ψ_k being weights given by

$$\psi_k = (-1)^{M+k} \sum_{j=\lfloor (k+1)/2 \rfloor}^{\min\{k, M\}} \frac{j^{M+1}}{M!} \binom{M}{j} \binom{2j}{j} \binom{j}{k-j}. \quad (4.79)$$

In a symbolic environment, such as mathematica[®], where the Gaver-Stehfest algorithm is implemented, the system precision is set at $5M/2$. Convergent results are obtained by gradually increasing M up to $M = 30$. Particularly, the numerical solutions for the limiting parameters match those given by the exact asymptotic expressions available in Sec. 4.4. It is also noted that since η_0 appears as a common factor of all quantities of interest, unity is assumed for its value in the subsequent numerical results, unless otherwise stated.

Additionally, a shock-driven compressible simulation for the RM flow that the present incompressible theory attempts to model is performed using the ideal MHD equations, in order to validate the analysis developed in Sec. 4.4.1. For this simulation, a shock wave of Mach number M , traveling in the positive z -direction approaches the density interface as depicted in Fig. 4.1(c). A slightly different renormalization scheme is used for the compressible simulation. Here, dimensionless variables denoted by the asterisk are defined as

$$\rho^* = \frac{\rho}{\rho_0}, \quad p^* = \frac{p}{p_0}, \quad t^* = \frac{t}{\Lambda/\sqrt{p_0/\rho_0}}, \quad \mathbf{u}^* = \frac{\mathbf{u}}{\sqrt{p_0/\rho_0}}, \quad \mathbf{B}^* = \frac{\mathbf{B}}{\sqrt{\mu_0 p_0}}, \quad (4.80)$$

where ρ_0 and p_0 are the initial equilibrium density and pressure upstream of the shock, respectively. Therefore the simulation prescribes $\rho_1^* = 1$, $\rho_2^* = 1.25$, $p_0^* = 1$, $\eta_0 = 0.01$, and $\phi = 4\pi/9$. Further, the strength of the driving shock and the applied magnetic field are characterized by $\bar{\beta} = 2\mu_0 p_0/B_0^2 = 16$ and $M = U_s/a = 1.1$, respectively, with U_s being the shock speed and a the upstream sound speed. As a result of the shock-interaction process with the interface, both fluids and consequently the interface perturbation are compressed on a timescale typically much shorter than that over which the RMI evolves. The magnetic field is also altered. Linear models such as the one described here most closely approximate the evolution of the post-shock-compression flow field [107]. Thus post-shock-compression parameter values are used as the initial conditions in the model, which are $\rho_1^* = 1.097$, $\rho_2^* = 1.372$, $B_{0x}^* = 0.381$, $B_{0z}^* = 0.061$ and $\eta_0 = 0.00874$. The velocity imparted to the interface by the shock interaction process in the compressible problem is used as the impulse magnitude in the model, which here is $V_0^* = 0.113$. The shock-driven non-linear simulation subsequently compared to the model was carried out with the compressible ideal MHD code described in [107]. It implements an eight-wave Riemann solver within an unsplit upwinding method [88]. The divergence constraint on the magnetic field is enforced at each time step using a projection method [88]. The boundary conditions of the two-dimensional simulation

periodic in the x -direction and zero gradient in the z -direction. The simulation was conducted on a uniform grid with a cell size of $\Delta x = \Delta z = \Lambda/1024$. This grid is sufficiently fine to predict the interface perturbation amplitude history to within 0.1% of the Richardson extrapolated exact value.

4.5.1 Growth of the interface perturbation

The ideal MHD growth

We first establish that under the ideal MHD description, the behavior of the interface in the oblique magnetic field case is a superposition of the oscillations of the transverse field case [107] with the exponentially decaying growth rate of the normal field case [105]. For the case shown in Fig. 4.2(a), where predictions made by the incompressible model (see Sec. 4.4.1) is compared to the η history extracted from the shock-driven compressible simulation, the incompressible model accurately predicts both the frequency and decay rate of the oscillations, while slightly overpredicting the amplitude, which also occurred for the models of the limiting cases [105, 107].

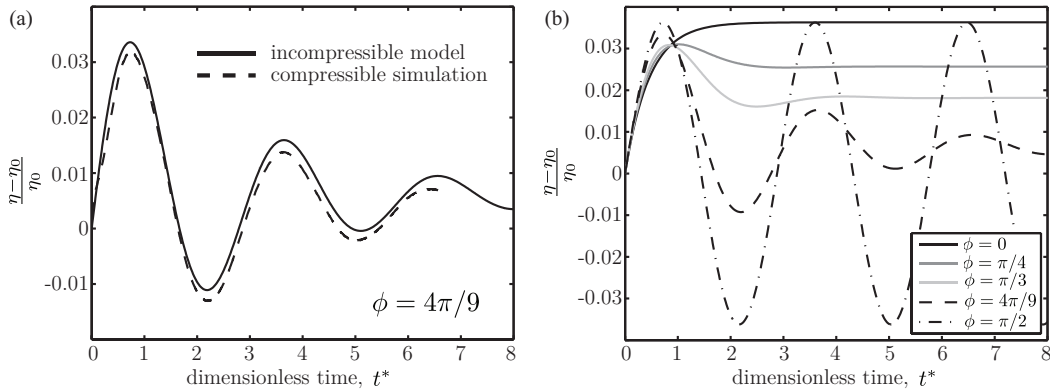


Figure 4.2: MHD interface perturbation amplitude histories. (a) Comparison of the incompressible model and the simulated η histories corresponding to the shock driven case with $\phi = 4\pi/9$. (b) Incompressible model η histories for the same parameters with varying ϕ

The interface behavior predicted by the model for a range of initial magnetic field angles (other parameters unchanged) is shown in Fig. 4.2(b). For $\phi \neq \pi/2$, the interface perturbation amplitude, as $t^* \rightarrow \infty$, tends to a limit η_∞ that is a function of ϕ . Taking the large time limit of (4.35) yields the following closed form expression,

$$\frac{\eta_\infty - \eta_0}{\eta_0} = \frac{V_0^* \sqrt{\rho_1^*}}{B_0^*} \left(\sqrt{\frac{\rho_2^*}{\rho_1^*}} - 1 \right) \cos \phi. \quad (4.81)$$

For $\phi = 0$, the limiting behaviour of the normal field case [105] is recovered. The general ϕ case exhibits the same linear dependence on V_0^* and inverse dependence on the base field magnitude B_0^* . The scaling with $\cos \phi$ demonstrates what the long term suppression of the RMI is strongest for fields that are nearly tangential to the interface. For $\phi = \pi/2$, the interface oscillates in time without decay and the limiting amplitude does not exist. The dependence of η_∞ on the problem parameters is illustrated in Fig. 4.3, where strong scaling of the asymptotic amplitude with the Atwood number is evident.

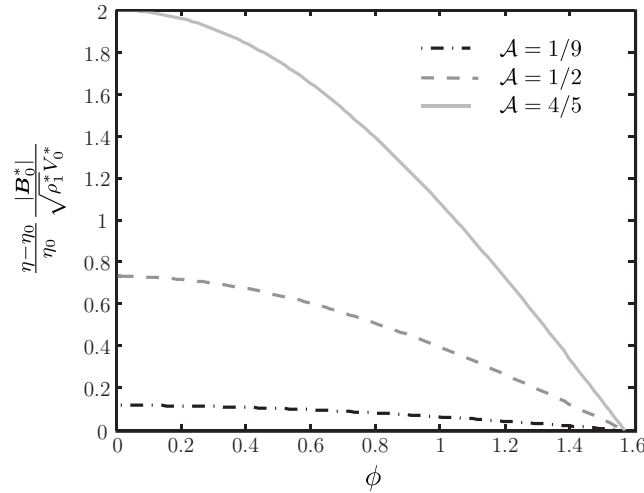


Figure 4.3: MHD normalized limiting interface perturbation amplitude for varying ϕ and Atwood number.

Hall-MHD: effect of finite Larmor radius

We next explore the effect of finite Larmor radius d_L , and ion skin depth d_S , introduced in the Hall-MHD model, on the interface behavior. Firstly, the RMI predicted by the linearized Hall-MHD equations is also inhibited in the presence of an oblique magnetic field. For instance, Fig. 4.4 shows the stabilizing evolution of the interface perturbation amplitude η when the magnetic field is applied at angle of $\phi = 70^\circ$. A wide range of the parameter space is explored in this case. In 4.4(a) the Larmor radius d_L is decreased to show convergence towards the MHD result, measured in the original time scale t , through faster decaying oscillations and smaller perturbation growth upon saturation; and in 4.4(b) a similar pattern is observed for the rescaled amplitude η/d_L in the cyclotron time scale T , when the large skin depth limit, $d_S \rightarrow \infty$, is approached with a fixed plasma energy ratio β . The fact that the interfacial oscillation frequency measured in T now varies with

different d_S fundamentally differs the normal field solution ($\phi = 0$) discussed by Shen *et al.* [92], where the interfacial oscillation synchronizes exactly with the ion cyclotron frequency. The enhanced suppression effect for the RMI in response to stronger background magnetic field strength is illustrated in 4.4(c) where β is decreased while holding d_S constant, showing that η decays inversely proportional to the external field strength, as discussed in Sec. 4.4.3.

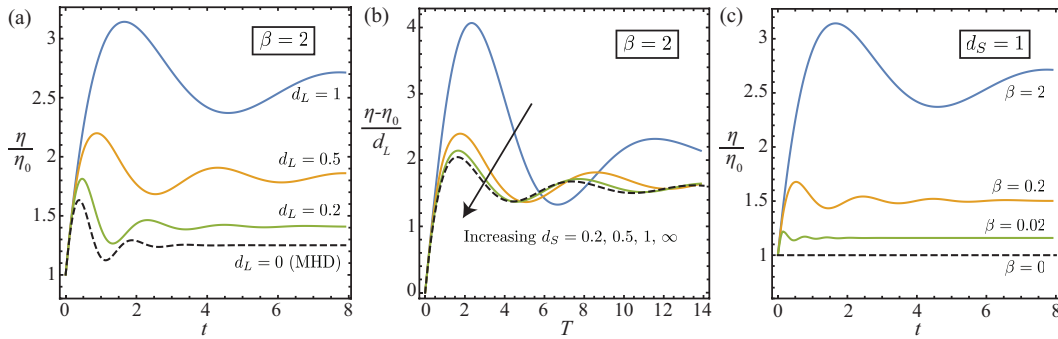


Figure 4.4: The growth of the interfacial perturbation amplitude obtained at an oblique magnetic field angle $\phi = 70^\circ$. Convergence towards (a) the MHD solution via decreasing d_L , (b) the large skin depth limit via increasing $d_L = d_S$ at a constant $\beta = 2$, and (c) the strong magnetic field limit via decreasing β at a constant $d_S = 1$ are shown. The Atwood number $\mathcal{A} = 0.5$ is held constant.

Next we investigate the effect of changing ϕ in the Hall-MHD model in Fig. 4.5, where comparisons for the interface growth are made for the entire spectrum $0 \leq \phi \leq 90^\circ$ between two cases obtained for relatively large and small values of d_L given in 4.5(a) and (b), respectively. In both cases, the singular jump between the asymptotic of $\phi \rightarrow 90^\circ$ and the exact solution of $\phi = 90^\circ$ is observed (see Sec. 4.4.4). The size of such jump continuously decreases with decreasing d_L : it is maximized in the large d_S limit where the growth of η collapses for all $\phi < 90^\circ$, and eliminated in the MHD limit when $d_L = 0$.

Further, it is clear that the interfacial oscillation becomes a strong function of the magnetic field angle for small d_L . In this region, a normal field ($\phi = 0$) excites oscillation due to the ion cyclotron motion [92], whereas a tangential field ($\phi = 90^\circ$) induces oscillating phase of the flow field immediately away from the CD due to traveling waves along the mean interface [107]. For a generally oblique field ($0 < \phi < 90^\circ$), a combination of these two mechanisms results.

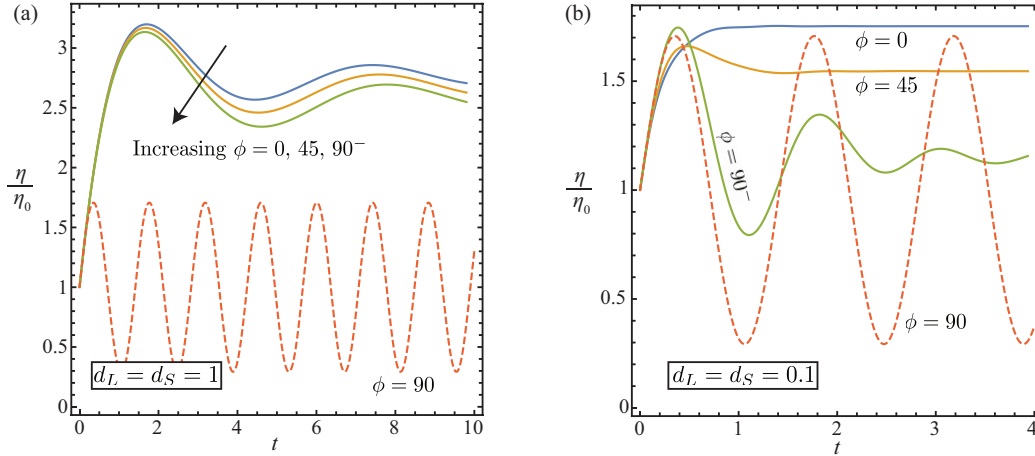


Figure 4.5: Interfacial perturbation growth as a function of the magnetic field angle ϕ . Explicit comparison between $0 \leq \phi < 90^\circ$ and $\phi = 90^\circ$ are made for $d_L = d_S = 1$ in (a) and $d_L = d_S = 0.1$ in (b). $\mathcal{A} = 0.5$ is fixed in both cases.

4.5.2 Circulation deposition

A distinct feature of the Hall-MHD model that contrasts the regular MHD theory is that its CD jump condition supports a tangential slip velocity across the interface that leads to a vortex sheet where circulation is deposited. We first demonstrate that the circulation deposition $\hat{\gamma}_0$, as a time series in T , is independent of β and hence d_L , for any given $0 \leq \phi < \pi/2$. This can be verified by substituting $\beta = 2d_L^2/d_S^2$ into the Laplace transform of (4.36) to yield an expression of the form, $\Delta U/d_L = f(d_S, \phi; \sigma)$, where the known function f does not depend on β nor d_L . For example, at $\phi = 45^\circ$, Fig. 4.6(a) shows the collapse of $\hat{\gamma}_0$ as time series in T , obtained for decreasing β while holding $d_S = 1$ constant, to a universal curve that decays as $T \rightarrow \infty$. However, in the original time frame t , decreasing β by increasing the imposed magnetic field strength in this case will rescale the collapsed curve into a smaller time window of t , giving faster oscillation and decay. This is because $T = t/d_L$ and reducing β with a fixed d_S simultaneously decreases d_L .

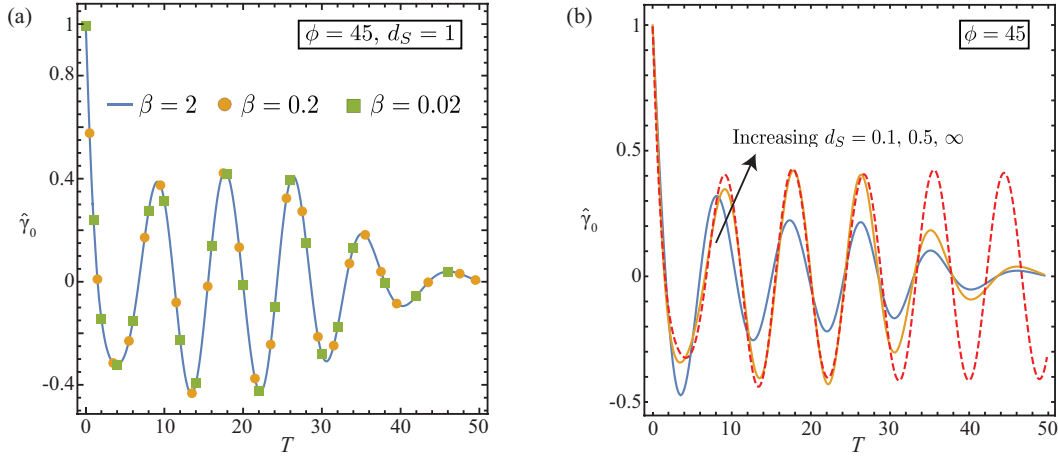


Figure 4.6: Normalized circulation deposition $\hat{\gamma}_0$ at the interface in response to (a) decreasing $\beta = 2, 0.2, 0.02$, and (b) increasing $d_S = 0.1, 0.5, \infty$. The magnetic field is imposed at an angle of $\phi = 45^\circ$ and the cyclotron time T is used for all series.

Therefore it is convenient to focus on the collapsed series and study the effect of changing d_S and ϕ . The former is examined in Fig. 4.6(b), where d_S is increased from 0.1 to 0.5 for $\phi = 45^\circ$, giving rapid convergence towards the $d_S = \infty$ limit, while a slower decay of the oscillation amplitude is observed as $d_S \rightarrow \infty$. As an aside, such behavior is in general different from results computed using the IICE model [92], where the decay rate of $\hat{\gamma}_0$ mildly rises when d_S increases, due to the compressible flow treatment for the electrons. The effect of increasing ϕ is shown in Fig. 4.7. By covering the entire range of $0 \leq \phi < 90$ in 4.7(a) for constant $d_S = 0.1$, it is established that following a transitioning period during which the behavior of $\hat{\gamma}_0$ converges to the limiting solution given by the $\phi \rightarrow 90^\circ$ asymptotic, a consistently decaying oscillation whose amplitude and period increases with ϕ is always reached. The convergence as $\phi \rightarrow 90^\circ$ is non-uniform in T and emphasized in 4.7(b) where $d_S = \infty$ is chosen to exaggerate the transitioning period. In this case, although it can be shown from Eqs. (4.36) and (4.60) that $\hat{\gamma}_0(T)|_{\phi=\pi/2} \rightarrow 1/2$ as $T \rightarrow \infty$, the actual time series corresponding to $\phi < \pi/2$ must deviate away from the limiting solution and undertake smooth oscillations around zero for sufficiently large T .

Additionally, the discontinuous jump in $\hat{\gamma}_0$ between the $\phi \rightarrow \pi/2$ solution given in Fig. 4.7, and the $\phi = \pi/2$, d_L -independent solution becomes clear after recalling

from Eqs. (4.24) and (4.36) that for all $d_L \geq 0$,

$$\hat{\gamma}_0(t)|_{\phi=\pi/2} = \cos\left(\frac{4\pi t}{\sqrt{\beta(\rho_1 + \rho_2)}}\right). \quad (4.82)$$

Indeed, the simple cosine wave given by (4.82) for $\phi = \pi/2$ differs from the limiting solution as $\phi \rightarrow \pi/2$, plotted using Eq. (4.63), again validating the analysis of Section 4.4.4.

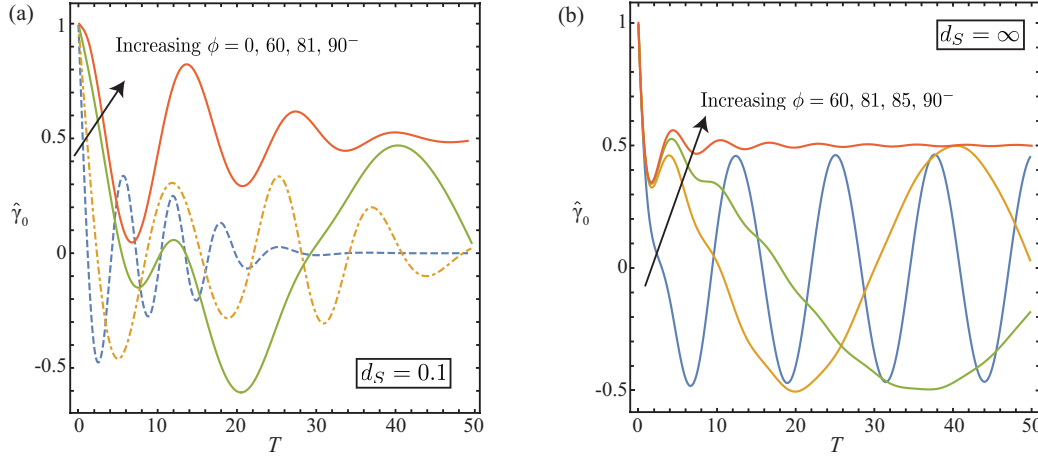


Figure 4.7: Effect of the magnetic field angle ϕ on the circulation deposition $\hat{\gamma}_0$. In (a), ϕ is increased from 0 to the left limit of 90° for finite $d_S = d_L = 0.1$. In (b), the non-uniform convergence of $\hat{\gamma}_0$ as $\phi \rightarrow 90^\circ$ is highlighted for $d_S = \infty$. $\mathcal{A} = 0.5$ is used throughout.

4.5.3 Normal velocity profile

A curious observation made in Sec. 4.4.2 concerns the cause of an universal interface growth that is independent of the magnetic field angle ϕ in the large d_S limit, even though the circulation deposition in this limit does vary with ϕ [see Fig. 4.7(b)]. To demonstrate, Fig. 4.8 depicts the evolution of the normal velocity profile w' in time T from the initial impulse, across the line $\{(x, z) \mid x = 0, z \in [0, 2]\}$, for a range of ϕ . Results are drawn for $z > 0$ since w' is an even function of z when $d_S = \infty$. It is clear that the flow profile away from the interface reduces its propagation speed in the normal direction as the field angle increases, while preserving a common velocity at the interface $z = 0$ for all time T .

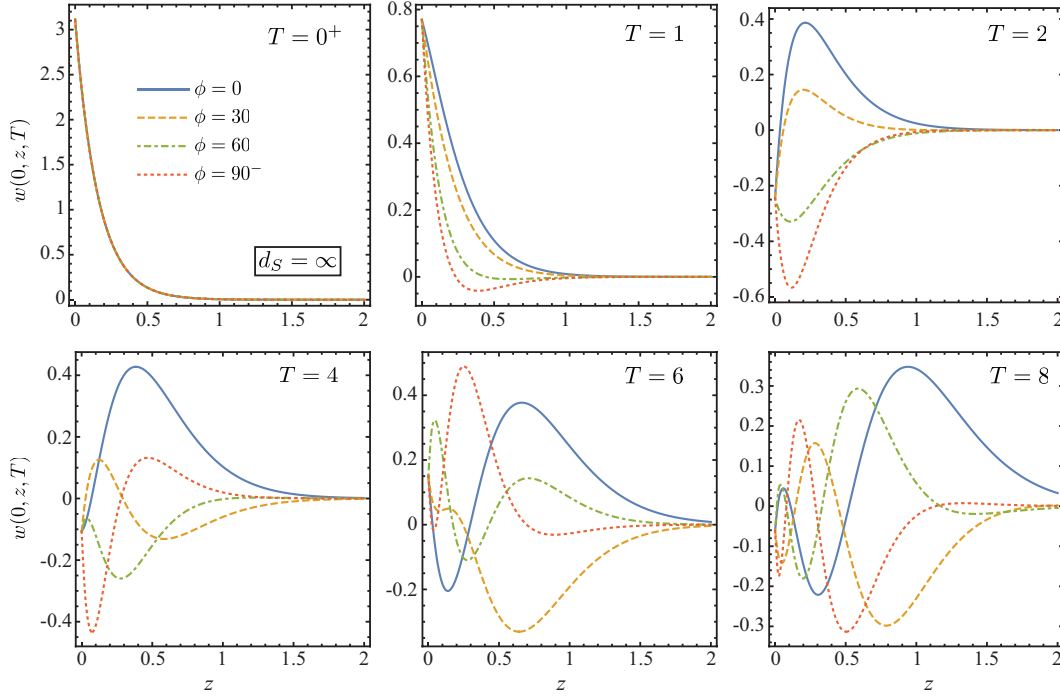


Figure 4.8: Normal velocity profile $w(x = 0, z, T)$ in the large d_S limit. Six time instances from $T = 0^+$, the initial impulse, to $T = 8$ are taken for a range of magnetic field angle: $\phi = 0$ (solid), $\phi = 30^\circ$ (dashed), $\phi = 60^\circ$ (dot-dashed) and $\phi \rightarrow 90^\circ$ (dotted). $\mathcal{A} = 0.5$ in all cases.

Figure 4.9 further explores the propagation characteristics as density plots for w' over the two-dimensional domain $\{(x, z) \mid x \in [0, 1], z \in [0, 2]\}$, noting that the flow profile is periodic in x and symmetric about the x -axis. At a particular angle $\phi = 45^\circ$, it is seen that while deforming, the velocity contours travel in a direction that is aligned with the imposed magnetic field. Flow disturbances due to vorticity generation are constantly being produced and transported away from the CD due to the interface-normal component of the wave velocity, decreasing their influence on the interface dynamics. Meanwhile, along the CD at $z = 0$, w' continuously changes its phase due to the interface-parallel component of the wave velocity and the oscillatory nature of the vorticity generation, necessarily causing oscillation of the interface. The net result of these two wave components provides the suppression mechanism for the RMI in the present Hall-MHD framework.

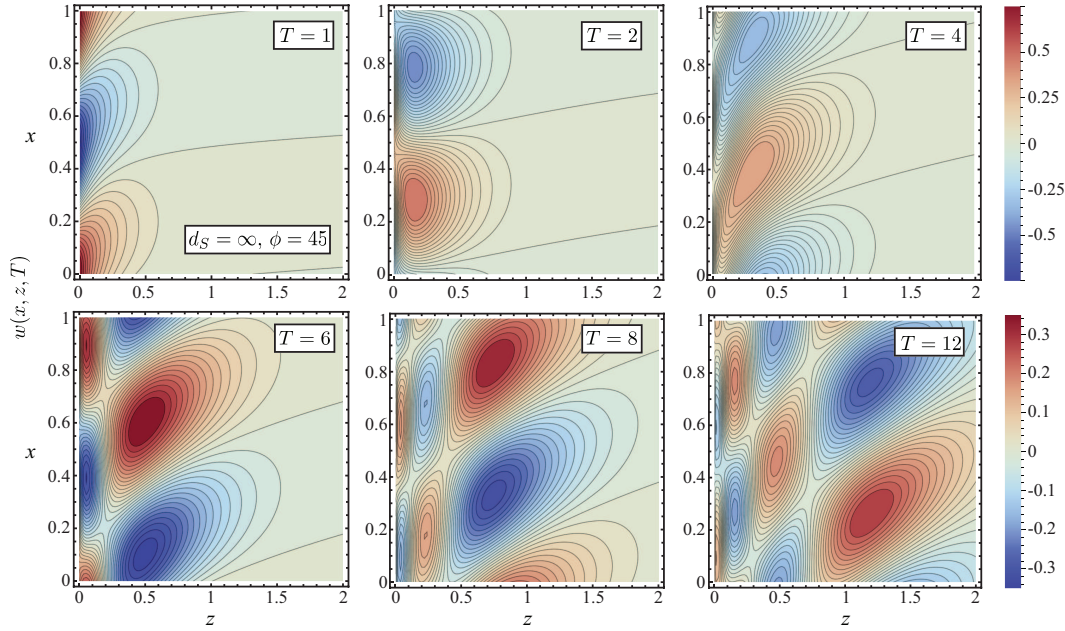


Figure 4.9: Two-dimensional contours of the normal velocity field $w(x, z, T)$ in the large d_S limit for an oblique magnetic field with $\phi = 45^\circ$, and a plasma Atwood number $\mathcal{A} = 0.5$. Two different color scales are assigned for $T = 1, 2, 4$ and $T = 6, 8, 12$, respectively.

The effect of finite ion skin depth and Larmor radius on the normal velocity distribution is examined in Fig. 4.10, where comparison is also made against the regular MHD theory. When the background magnetic field is applied at an oblique angle, e.g., $\phi = 45^\circ$, the MHD solution exhibits soliton-like behavior of the Alfvén waves in the magnetic field direction that originates from splitting the initial impulse into two fluids on each side of the interface. In contrast, a dispersive wave system available in the Hall-MHD model, including the ion cyclotron, the Alfvén and Whistler waves of finite frequencies [91], evidently complicates the flow propagation by introducing highly oscillatory patterns. This dispersive behavior in Hall-MHD develops from mild perturbation to the MHD solution immediately after the initial impulse, and gradually evolves into long time dominant feature of the flow field.

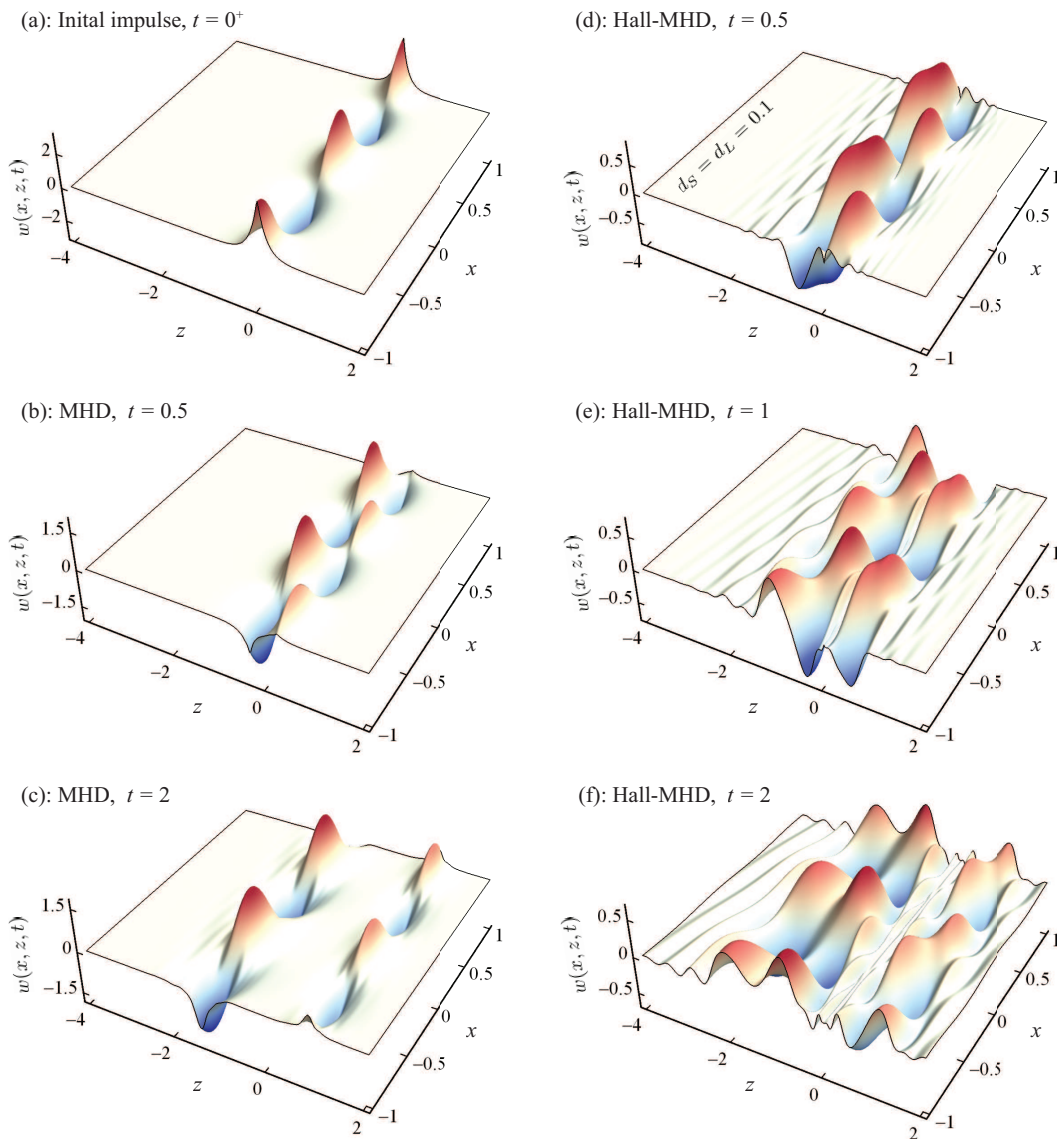


Figure 4.10: Three-dimensional surfaces of the normal velocity field $w(x, z, t)$, as a function of time t , resulted from the MHD model [(b)–(c)] where $d_L = d_S = 0$ and the Hall-MHD model [(d)–(f)] where $d_L = d_S = 0.1$. Both systems share a common initial impulse given in (a), as well as an Atwood number of $\mathcal{A} = 0.5$. Results are shown over two wavelength, $x \in [-1, 1]$, to highlight the wave propagation along the magnetic field with $\phi = 45^\circ$.

4.5.4 Vorticity dynamics

Ideal MHD

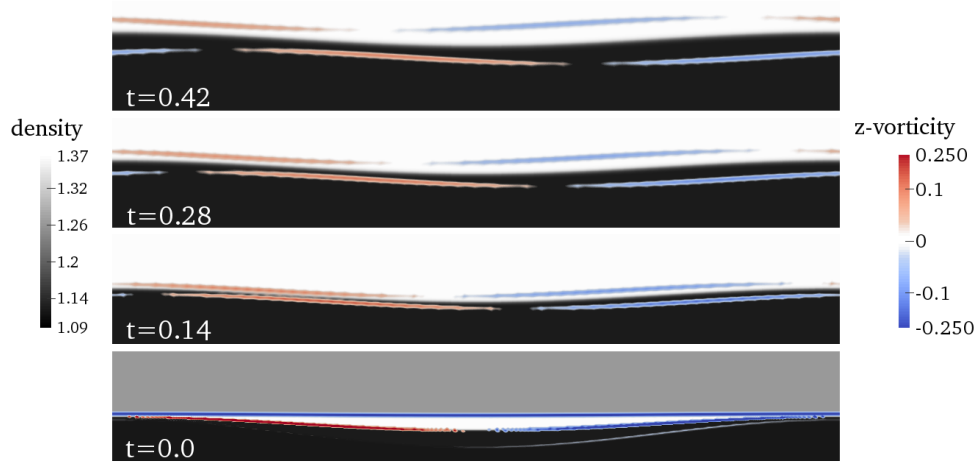


Figure 4.11: Short term evolution of the post-shock vorticity field near the interface from the compressible simulation with $\phi = 4\pi/9$. Frame timestamps are non-dimensionalized by $\Lambda\sqrt{\rho_1^*/p_0^*}$

The interface dynamics in the ideal MHD case can be explained by examining the transport of vorticity in the presence of an oblique field. This is illustrated in Fig. 4.11, which shows the vorticity field overlaid on the density field at a series of times following the shock interaction in the nonlinear simulation. After the transmitted and reflected shocks depart the vicinity of the interface, this closely matches the vorticity transport predicted by the present model. As previously noted in [106], the circulation baroclinically generated at the interface by the shock interaction process is identical to the hydrodynamic case. Thus immediately following the shock interaction, before vorticity transport has had an opportunity to occur, the vorticity distribution induces the same initial growth rate as in the hydrodynamic case. Since the oblique magnetic field penetrates the interface, however, vorticity is forbidden from remaining on the interface by the ideal MHD Rankine-Hugoniot relations. In Fig. 4.11, it can be seen that this situation is resolved by the formation of waves travelling parallel and anti-parallel to the base magnetic field that bifurcate vorticity distribution and transport it from the interface. The interface parallel component of the vorticity transport continuously alters the phase of the normal velocities induced at the interface, which causes the interface perturbation growth rate to oscillate in time. The interface normal component of vorticity transport simultaneously causes

the growth rate to decay as the vorticity distribution becomes more distant from the interface and hence the induced velocities there decrease.

The interface behavior in the $\phi \rightarrow 0$ and $\phi \rightarrow \pi/2$ limits of the oblique field case coincide with earlier results for normal [105] and tangential [107] fields. The earlier tangential field model, however, did not resolve the vorticity carrying waves and instead integrated across them. The full structure of the flow in this case is revealed by the $\phi \rightarrow \pi/2$ limit of the oblique field model.

Hall-MHD

Different from the ideal MHD prediction, the production and propagation of the out-of-plane vorticity, ω_y , in Hall-MHD model is illustrated in Fig. 4.12 for the large d_S limit, where the important features discussed in Sec. 4.3.3 are well captured. As the flow evolves, a thin layer of flow in a neighborhood of the density interface at $z = 0$ sees substantial vorticity injection due to the magnetic field perturbation, causing the growth of total circulation. This should not be confused with the circulation deposition at the interface due to shearing, which oscillates with a falling envelop, as shown in Sec. 4.5.2. The amount of vorticity production however decays rapidly away from the interface as z increases, and the transport mechanism enabled by the imposed magnetic field thereby manifests. That is, the Alfvén waves traveling along the magnetic field are responsible for carrying away the vorticity at an oblique angle.

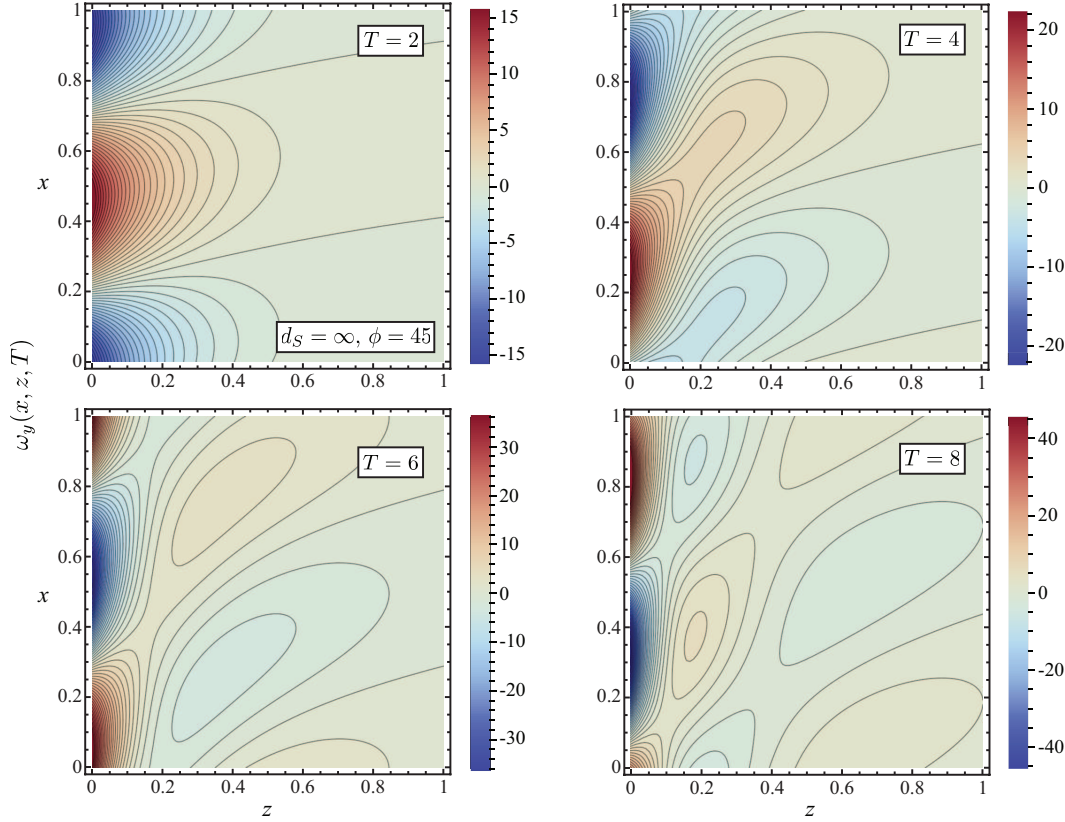


Figure 4.12: Two-dimensional contours of the out-of-plane vorticity $\omega_y(x, z, T)$ in the $d_S = \infty$ limit for an oblique magnetic field with $\phi = 45^\circ$, and a plasma Atwood number $\mathcal{A} = 0.5$. The color scale is reset for each time instant ($T = 2, 4, 6, 8$) to show vorticity production as the flow evolves.

Lastly, the in-plane interface vortex strength $\zeta(x, t)$ and its time derivative $\iota(x, t)$ at $x = \pi/4$ computed using Eq. (4.47) are shown in Fig. 4.13. A normal background magnetic field with $\phi = 0$ is applied to a plasma given by $\mathcal{A} = 0.5$ and $d_S = d_L = 1$ in this case. The out-of-phase evolution of its two components shown in 4.13(a) suggests in-plane rotation of the ζ vector, demonstrated clearly in 4.13(b). From Eq. (4.46), this rotational behavior, absent in ideal MHD, is entirely driven by the current density jump across the interface, namely, ι , resulted from the Hall effect that modifies the magnetic term $\mathbf{j} \times \mathbf{B}$ in the vorticity equation (4.38). Here, the interface serves simultaneously as a vortex and current sheet whose strength diminishes over time, allowing a coupled circling dynamics enabled by an external magnetic field that explains the oscillatory interface perturbation growth and the suppression of RMI in Hall-MHD. This mechanism is exactly analogous to the role played by the Lorentz force on the interfacial vorticity observed in the magnetized two-fluid

plasma simulation by Bond *et al.* [13] (see Figure 1.8).

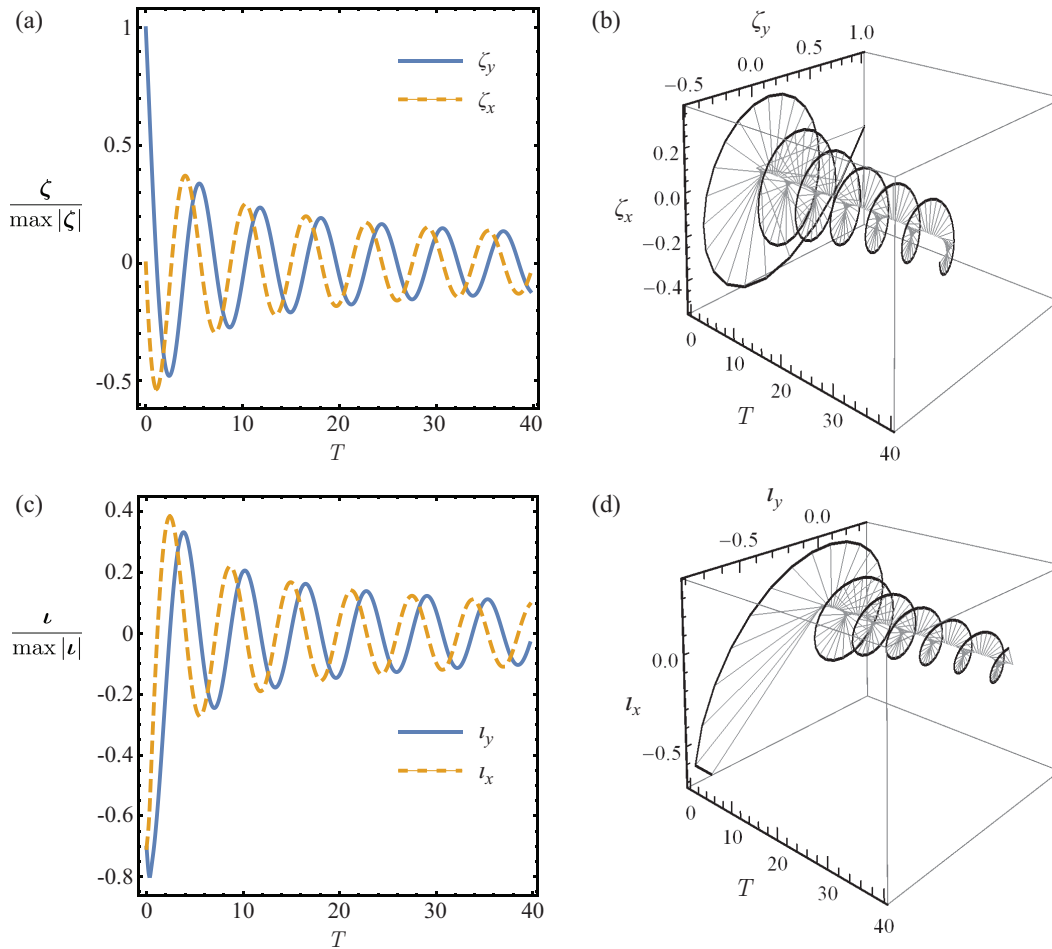


Figure 4.13: Evolution of the interface vortex strength ζ in (a) components and (b) vector form. Its time derivative ι is similarly given in (c)-(d). Results are obtained at $x = \pi/4$ using a magnetic field angle $\phi = 0$ and plasma parameters $\mathcal{A} = 0.5$, $d_S = d_L = 1$.

4.6 Summary

An incompressible model for the two-dimensional Hall-MHD RMI has been developed for an arbitrary initial magnetic field angle. The reduced growth of the instability is established for all field orientations other than strictly out-of-plane. However, the suppression is most effective for near tangential fields but becomes less effective with increasing plasma length scales, namely the Larmor radius d_L and ion skin depth d_S .

The behavior of the interface was shown to be governed by the production and transport of vorticity via waves traveling along the magnetic field. In the ideal

MHD limit, obtained by taking the ion skin depth to zero, the component of vorticity transport normal to the interface causes the perturbation growth rate to decay, while the component of transport parallel to the perturbation direction causes a continuous change in the phase of the induced velocities at the interface, resulting in growth rate oscillation. The interface behavior predicted in this case compares well with the results of nonlinear MHD simulations. For Hall-MHD flow of finite d_L and d_S , oscillations associated with the ion cyclotron effect are imposed when the initial magnetic field is not strictly parallel to the interface. The normal component of the field in Hall-MHD allows vorticity production across the flow domain and introduces a dispersive wave system transporting the vorticity.

Other than the ideal MHD theory, asymptotic behavior of the general incompressible Hall-MHD RM flow is also studied for limiting values of the ion skin depth, the plasma kinetic-to-magnetic energy ratio and the initial magnetic field angle. Analytical results are derived in each limit. When the appropriate limits for the initial field angle are taken, the present analysis replicates the predictions made by existing models for the normal and parallel field cases in both Hall-MHD and ideal MHD.

Chapter 5

CONCLUSIONS

The perturbation growth of a shock-driven, impulsively accelerated, perturbed density interface, or contact discontinuity (CD), separating two fluids is known as the Richtmyer-Meshkov instability (RMI). Typically characterized in a neutral gas, the RMI has found importance in a wide range of science and engineering applications [16]. Particularly, in inertial confinement fusion (ICF), controlling the RMI is critical for fusion reaction sustainability [58, 94]. This is because mixing occurs between the target capsule material and the fuel within, as a result of hydrodynamic instabilities, including RMI, compromising the chance of achieving energy break-even or production [59].

The extreme temperatures required for ICF implosion inevitably causes rapid ionization of the involved materials, which then leads to interaction between the conducting fluids and magnetic fields. Suitable continuum plasma models are therefore needed in order to describe the coupled evolution of the involved plasmas and electromagnetic fields. One popular framework is the single-fluid ideal magnetohydrodynamic (MHD) system, explored in the context of RMI by many [5, 17, 75, 76, 87, 88, 104, 105, 107]. However, the applicability of the ideal MHD model is limited to low frequency, macroscopic processes, where microscopic plasma length scales are negligible. Recent numerical simulations of RMI type of flows in the two-fluid plasma paradigm by Bond *et al.* [12] suggest significant deviations in the flow characteristics from the MHD results, when the plasma Debye length and Larmor radius are resolved.

To rigorously understand the various simplifying assumptions required for the single-fluid MHD reduction from a two-fluid perspective, we perform in Chapter 2 a sequence of formal expansions for the dimensionless ideal two-fluid plasma equations with respect to limiting values of the speed-of-light c , ion-to-electron mass ratio M , and the plasma skin depth d_S . Several different closed systems of equations result, including separate systems for each limit applied in isolation, and those resulting from limits applied in combination, which correspond to the well-known Hall-MHD and single-fluid ideal MHD equations. In particular it is shown that while the zeroth-order description corresponding to the $c \rightarrow \infty$ limit, with M, d_S

fixed, is strictly charge neutral, it nonetheless uniquely determines the perturbation charge non-neutrality at first order. Furthermore, the additional $M \rightarrow \infty$ limit is found to be not required to obtain the single-fluid MHD equations, despite being essential for the Hall-MHD system. The associated homogeneous dispersion relation for each derived limiting system is also calculated analytically. Physical insight into the appropriate wave-propagation properties is gained via asymptotic analysis of the dispersion relations for extreme values of the frequency and wave number. The hierarchy of systems presented in this chapter demonstrate how plasmas can be appropriately modeled in situations where only one of the limits apply, which lie in the parameter space in-between where the two-fluid plasma and ideal MHD models are appropriate.

We then devote Chapter 3 into modeling the impulse-driven RMI for conducting fluids subject to a magnetic field that is normal to the mean interface, using the Hall-MHD equations. Two versions of the Hall-MHD equations are explored. In the first, the ions are treated as an incompressible fluid but the electron gas retains its compressibility, while for the second version, the incompressible limit for both species is invoked. The linearized equations of motion are first formulated for a sinusoidal interface perturbation and then solved as an initial-value problem using a Laplace transform method with general numerical inversion but with analytical inversion for some limiting parameter cases. While the field equations are identical for both Hall-MHD models, the CD-jump conditions differ leading to qualitatively similar but quantitatively different CD dynamics. For both models, the presence of the magnetic field is found to suppress the incipient interfacial growth associated with neutral-gas, RMI. When the ion skin depth and Larmor radius are nonzero, oscillations associated with the ion cyclotron effect are imposed onto the entire flow domain, substantially altering the vorticity dynamics displayed by the ideal MHD model that drives the suppression of the RMI. Most significantly, on the interface, the Hall-MHD description allows the presence of a tangential slip velocity which leads to finite circulation deposition. Away from the interface, vorticity is produced by the perturbed magnetic fields and transported to infinity by a dispersive wave system. This leads to decay of the velocity slip at the interface with the effect that interface growth remains bounded but distorted by damped oscillations that resemble the properties of a two-fluid plasma.

In Chapter 4, the incompressible ion incompressible electron (IIIE) Hall-MHD model developed in Chapter 3 is extended for the RM flow to accommodate an

initially uniform magnetic field of arbitrary orientation. The ideal MHD theory is naturally obtained by taking the limit of vanishing ion skin depth. The limiting flow of large ion skin depth is also explored. It is shown that the out-of-plane magnetic field component normal to both the impulse and the interface perturbation does not affect the evolution of the flow. For all field orientations other than strictly out-of-plane, the growth of interface perturbations is suppressed. However the suppression is most effective for near tangential fields but becomes less effective with increasing ion skin depth and Larmor radius. The modeled suppression mechanism is transport of vorticity along magnetic field lines via Alfvén fronts in ideal MHD, and via a dispersive wave system in Hall-MHD. Oscillation of the interface growth rate is caused by a continuous phase change of the induced velocities at the interface due to vorticity transporting parallel to the perturbation direction in ideal MHD; while it can also result from interfacial vorticity production associated with the ion cyclotron effect in Hall-MHD with finite Larmor radius. Particularly, the interface vortex strength in Hall-MHD is found to be rotating in the vortex plane, driven by the Hall-drift due to current density jump across the interface, recovering another feature of the magnetized two-fluid plasma theory [13].

In the future, a numerical study of the nonlinear compressible RM flow in Hall-MHD is desired, so that direct comparisons against the linear incompressible theory presented in this thesis, and the two-fluid plasma simulations of Bond *et al.* [12, 13] can be made. Further, in principle, the impulsive RMI model is also applicable to the 2FMHD system derived in Chapter 2, where the electron flow is treated separately. Similar linear analysis for the initial value problems discussed in Chapters 3 and 4 can be employed for the 2FMHD equations to investigate the effect of electron cyclotron resonance.

Part II

**Evolution of Perturbed Planar
Shockwaves**

OVERVIEW

The second part of this thesis extends on the following journal article:

N. Shen, D. I. Pullin, R. Samtaney and V. Wheatley. Evolution of a shock generated by an impulsively accelerated, sinusoidal piston. *Journal of Fluid Mechanics*, 2020. (accepted).

We consider here the evolution of slightly perturbed two-dimensional shock-waves of two origins: one generated by an impulsively accelerated piston with a sinusoidally corrugated surface, and another due to a planar shock traversing a density perturbation field. We develop a complex-variable formulation for a nonlinear theory of generalized geometrical shock dynamics (GGSD) [10, 11] as a hierarchical expansion of the Euler equations that can be closed at any order. The zeroth-order truncation of GGSD is related to the equations of Whitham's geometrical shock dynamics (GSD) [108] while higher-order corrections incorporate non-uniformity of the flow immediately behind the perturbed shocks. Numerical solutions to GGSD systems up to second order are coupled to an edge-detection algorithm in order to investigate the hypothesized development of a shock-shape curvature singularity as the rippled shocks evolve. This singular behavior, together with the simultaneous development of a Mach-number discontinuity, is found at all orders of the GGSD hierarchy for both weak and strong shocks. The critical time at which a curvature singularity occurs converges as the order of the GGSD system increases at fixed perturbation size ϵ , and follows a scaling inversely proportional to ϵ at sufficiently small values. This result agrees with the weakly nonlinear GSD analysis of Mostert *et al.* [78] for a general Mach number perturbation on a planar shock, and suggests that this represents the universal behavior of a slightly perturbed, planar shock.

Chapter 6

INTRODUCTION

The stability of a two-dimensional rippled shock has been a classical hydrodynamic problem, dynamically relevant to a diversity of science and engineering applications, including astrophysical phenomena [25, 70], inertial confinement fusion [58, 69], Bose-Einstein condensates and nonlinear optics [43]. It has long been known that planar gaseous shock waves are linearly stable, that is, small perturbations along the shock surface decay over time following a power law [31, 32, 56, 57, 102, 112]. The predictions of linear analysis are supported by the pioneering experiments of Lapworth [54] and Briscoe & Kovtiz [15]. But the experiments do display noticeable singular flow behaviour associated with the formation of a triple point, or Mach stem on the shock front that cannot be explained by linear theory.

The dynamics of a triple point on a strongly perturbed shock was modeled by Whitham [108], using his non-linear theory of geometrical shock dynamics (GSD), as a shock on a shock, or a “shock-shock” that propagates transversely along the shock profile. The cellular structure of Mach stems ubiquitously observed in detonation waves [23, 98] have motivated a number of theoretical investigations of the spontaneous formation of triple points [22, 30, 66]. Shock instabilities are also reported in non-reacting flows associated with perturbations of various origin. The nonlinear analysis of Clavin [21] shows the formation of a singularity in the slope of a wrinkled shock produced by a shock-vortex interaction, under the distinguished limit where the shock Mach number becomes infinite while the specific heat ratio of the gas approaches unity. A two-stage description of the shock evolution and an order-of-magnitude estimate for the Mach stem formation time was provided. Later, the shock tube experiment of Denet *et al.* [24], and the direct numerical simulations of Lodato *et al.* [60, 61] confirmed the triple point formation of shock reflected off a wavy wall, but did not relate the formation time to the initial perturbation size of the wall. Wan *et al.* [103] investigated numerically and experimentally the triple point trajectory due to shock interaction with a water wedge. Mostert *et al.* [78, 79] hypothesised a sinusoidal perturbation in the Mach number distribution for both initially flat and cylindrical shock geometry, finding that a shock curvature singularity, as a prelude to the formation of a triple point, occurs at a critical time τ_c that is inversely proportional to the initial perturbation amplitude, ϵ . This result is

obtained analytically via weakly nonlinear Fourier analysis using Whitham's GSD approximation. A short review of the GSD theory is given in Section 6.1.

The strict GSD framework of Mostert *et al.* [78] has limitations. First, the GSD formulation neglects the non-uniform effects of flow behind the shock carried by the C^+ characteristics, and second, the physical origin of the shock perturbation is not well defined owing to the restriction posed by the $A-M$ relation on the initial conditions of the shock shape and Mach number profiles. In the present study, we address these issues by applying the generalized geometrical shock dynamics (GGSD) formulation, developed by Best [10] as a hierarchical expansion of the Euler equations that can be closed at any order. The GGSD systems relaxes the $A-M$ relation while specifically incorporating the non-uniformity of the flow immediately behind the shock into its dynamical description in terms of evolution equations for higher order derivatives of the primitive flow variables. Katko *et al.* [51] showed that, owing to the inclusion of flow non-uniformity, the GGSD model successfully captures the analytical solution for the expansion of a blast wave in comparison with the GSD result.

The GGSD theory enables analysis of two specific problems in this thesis using complex coordinates. First, the evolution of a shock generated by a two-dimensional impulsive piston with a sinusoidally corrugated surface is considered. This is a classical problem spanning over sixty years from the original work of Freeman [31] to the more recent analysis of Bates [8]. While Freeman showed the piston-generated shock is linearly stable, Bates [7, 8] found an unstable region of the D'yakov parameter [26] for gases of arbitrary equation-of-state, where a small perturbation on the shock front grows in time. The second problem concerns a planar shock traversing a density perturbation field, where a GSD based theory was first given by Caherasoo & Sturtevant [18]. In both cases, we focus on an ideal gas equation-of-state and propose a perturbation ansatz where unstable modes are controlled by the intrinsic shock nonlinearity that ultimately leads to the spontaneous formation of a curvature singularity, detected numerically as a discontinuity of the Mach number distribution along the shock. The critical time at which singularity occurs converges as the order of the GGSD system increases from zero to two, and the inverse power law, $\tau_c \propto 1/\epsilon$, established by Mostert *et al.* [78] holds universally true with the present inclusion of the non-uniform effects of the shocked flow.

6.1 Geometrical shock dynamics

As a prerequisite, we briefly review Whitham's development of geometrical shock dynamics (GSD) [109].

6.1.1 The A - M relation

The propagation of a shock wave down a tube of non-uniform cross-section into a homogeneous gas is considered. If the cross-sectional area $A(x)$ of the tube as a function of the tube length is slowly varying compared to a mean value A_0 , that is, $|A(x) - A_0|/A_0 \ll 1$, then the incompressible inviscid flow of density ρ , velocity u , pressure p and speed-of-sound a can be described by the following quasi-one-dimensional (1D) Euler equations,

$$\begin{aligned} \frac{\partial \rho}{\partial t} + u \frac{\partial \rho}{\partial x} + \rho \frac{\partial u}{\partial x} + \frac{\rho u}{A} \frac{dA}{dx} &= 0, \\ \frac{\partial u}{\partial t} + u \frac{\partial u}{\partial x} + \frac{1}{\rho} \frac{\partial p}{\partial x} &= 0, \\ \frac{\partial p}{\partial t} + u \frac{\partial p}{\partial x} - a^2 \left(\frac{\partial \rho}{\partial t} + u \frac{\partial \rho}{\partial x} \right) &= 0, \end{aligned} \quad (6.1)$$

where t is time and $a = \sqrt{\gamma p / \rho}$ with γ being the specific heat ratio. With the designation ρ_1, u_1, p_1, a_1 for flow quantities behind the shock, satisfying (6.1), one has along the C^+ characteristic lines defined by

$$\frac{dx}{dt} = u_1 + a_1, \quad (6.2)$$

the following C^+ characteristic equation:

$$\frac{d}{dx} (p + \rho_1 a_1 u) + \frac{\rho_1 a_1^2 u_1}{u_1 + a_1} \frac{1}{A} \frac{dA}{dx} = 0. \quad (6.3)$$

Taking $u_0 = 0, p = p_0, \rho = \rho_0, a = a_0$ in the undisturbed state ahead of the shock, the shock-processed variables are given by the shock-jump conditions,

$$\begin{aligned} u_1 &= \frac{2a_0}{\gamma + 1} \left(M - \frac{1}{M} \right), \\ \rho_1 &= \frac{\rho_0 (\gamma + 1) M^2}{(\gamma - 1) M^2 + 2}, \\ p_1 &= \frac{\rho_0 a_0^2}{\gamma (\gamma + 1)} \left(2\gamma M^2 - \gamma + 1 \right), \end{aligned} \quad (6.4)$$

where $M = M(x) = U/a_0$ is the Mach number determined by the shock speed U .

Next, Whitham's characteristic rule is applied, namely, setting $\rho = \rho_1$, $u = u_1$, $p = p_1$ and substituting (6.4) into (6.3). This gives

$$\frac{M}{M^2 - 1} \lambda(M) \frac{dM}{dx} + \frac{1}{A} \frac{dA}{dx} = 0, \quad (6.5)$$

where

$$\lambda(M) = \left(1 + \frac{2}{\gamma + 1} \frac{1 - \mu^2}{\mu} \right) \left(1 + 2\mu + \frac{1}{M^2} \right), \quad (6.6)$$

and

$$\mu^2 = \frac{(\gamma - 1)M^2 + 2}{2\gamma M^2 - (\gamma - 1)}. \quad (6.7)$$

Integrating (6.8) leads to the A - M relation,

$$\frac{A}{A_0} = \frac{f(M)}{f(M_0)}, \quad f(M) = \exp \left(- \int \frac{M \lambda(M)}{M^2 - 1} dM \right). \quad (6.8)$$

6.1.2 Two-dimension shock propagation

To generalize the quasi-1D flow into the two-dimensional (2D) GSD theory, an (α, β) -curvilinear orthogonal coordinates system, as shown in Figure 6.1, is introduced. Here, family of curves defined by constant α and β represents successive 2D shock shape profiles and propagation rays, respectively.

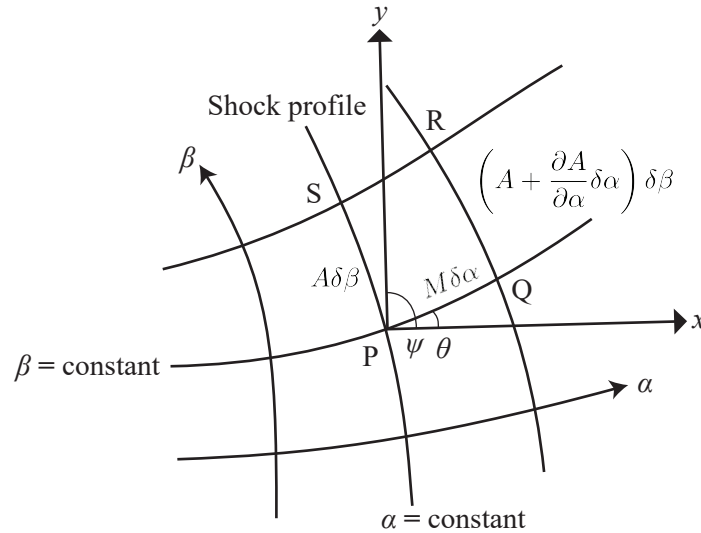


Figure 6.1: (α, β) -curvilinear orthogonal coordinates system for geometrical shock dynamics.

For the quadrilateral PQRS in Figure 6.1, an increment $\delta\alpha$ corresponds to a change of position in rescaled time $\delta t = \delta\alpha/a_0$, such that the shock locally advances in the

normal direction by distance

$$PQ = M(\alpha, \beta)\delta\alpha, \quad (6.9)$$

and an increment $\delta\beta$ is related to the arclength along the shock through

$$PS = A(\alpha, \beta)\delta\beta, \quad (6.10)$$

where $A(\alpha, \beta)$ is a function proportional to the width of the ray channel between rays β and $\beta + \delta\beta$, analogous to the quasi-1D flow. It follows from geometry that the neighboring distances SR and QR are given by

$$SR = \left(M + \frac{\partial M}{\partial \beta} \delta\beta \right) \delta\alpha, \quad QR = \left(A + \frac{\partial A}{\partial \alpha} \delta\beta \right) \delta\alpha. \quad (6.11)$$

Further, a local Cartesian coordinates system with its origin at P is overlaid, and let $\psi(\alpha, \beta)$ be the angle between the shock and the x -axis. The change in shock inclination from P to Q is then $\delta\psi = -(SR - PQ)/PS$, giving

$$\frac{\partial\psi}{\partial\alpha} = -\frac{1}{A} \frac{\partial M}{\partial\beta}. \quad (6.12)$$

Similarly, let $\theta(\alpha, \beta)$ be the angle between the ray and the x -axis, and then the change in ray inclination from P to S is $\delta\theta = (QR - PS)/PR$, giving

$$\frac{\partial\theta}{\partial\beta} = \frac{1}{M} \frac{\partial A}{\partial\alpha}. \quad (6.13)$$

Since $\psi = \pi/2 + \theta$, eliminating θ in (6.12) and (6.13) produces

$$\frac{\partial}{\partial\alpha} \left(\frac{1}{M} \frac{\partial A}{\partial\alpha} \right) + \frac{\partial}{\partial\beta} \left(\frac{1}{A} \frac{\partial M}{\partial\beta} \right) = 0. \quad (6.14)$$

Equation (6.14) and the previously derived A - M relation (6.8) form a closed set of partial differential equations to determine $A(\alpha, \beta)$ and $M(\alpha, \beta)$. This completes Whitham's formulation of GSD.

6.2 Part II outline

The remainder of thesis Part II is organized as follows. We first discuss in Chapter 7 the approximation error of GSD compared to the two-dimensional Euler equations, and introduce the GGSD expansion that improves the GSD theory. Evolution of a periodically perturbed planar shock is formulated using complex variables. The zeroth, first, and second order truncated GGSD models are derived explicitly in the strong and weak shock limits as closed systems of partial differential equations that

can be solved numerically using a simple technique such as method-of-lines. A linear stability analysis is also given. We then consider two specialized shocks using the GGSD framework in Chapter 8. First, section 8.1 studies the motion of a shock generated by a corrugated piston of sinusoidal surface being impulsively accelerated to a steady velocity. The necessary initial conditions required to integrate the GGSD systems for this shock are derived. Numerical results that characterise the shock shape curvature singularity formation, and demonstrate the inverse power law that predicts the onset of triple points are presented. In section 8.2, the interaction of a planar shock with a density perturbation field of compact domain is investigated. It is shown that after the shock exits the perturbation field, its two-dimensional shape and Mach number distributions again evolve into the development of curvature singularities. Finally, conclusions are drawn in Chapter 9.

Chapter 7

GENERALIZED GEOMETRICAL SHOCK DYNAMICS

We begin by giving an alternative derivation of the A – M relation in GSD. Its limitations are identified in a direct comparison against the 2D Euler equations. We then introduce GGSD developed by Best [10, 11], in order to improve the approximation error. The evolution equations for a periodically perturbed planar shock are formulated using the GGSD systems up to second order in complex coordinates.

7.1 Quasi-one-dimensional Euler equations

The foundation for constructing the evolution equations for shocks in two-dimensional unsteady flow is the quasi-one-dimensional (1D) Euler equations that describe flow of a polytropic gas down a tube of slowly varying cross-sectional area $A = A(x)$, along the propagation direction denoted by the spatial variable x . By averaging the inviscid compressible flow equations across the tube, one obtains the following approximation [108]

$$\begin{aligned} \rho_t + u\rho_x + \rho u_x + \rho u \frac{A'(x)}{A(x)} &= 0, \\ \rho(u_t + uu_x) + p_x &= 0, \\ p_t + up_x - a^2(\rho_t + u\rho_x) &= 0, \end{aligned} \tag{7.1}$$

where ρ , u , p are fluid density, velocity and pressure, respectively; $a = \sqrt{\gamma p/\rho}$ is the local sound speed for a perfect-gas equation of state, γ is the constant specific heat ratio; x , t are distance and time; the prime symbol denotes full derivative with respect to x , and the subscript t and x are used to signal their respective partial derivatives. Equations (7.1) can be written in characteristic form as

$$p_t + (u + a)p_x + \rho a(u_t + (u + a)u_x) + \rho a^2 u A'/A = 0, \quad \text{on } C^+ : \frac{dx}{dt} = u + a, \tag{7.2a}$$

$$p_t + (u - a)p_x - \rho a(u_t + (u - a)u_x) + \rho a^2 u A'/A = 0, \quad \text{on } C^- : \frac{dx}{dt} = u - a, \tag{7.2b}$$

$$p_t + up_x - a^2(\rho_t + u\rho_x) = 0, \quad \text{on } S : \frac{dx}{dt} = u. \tag{7.2c}$$

Denoting the trajectory of a shock propagating down the tube of uniform medium at rest by $x_s = x_s(t)$, its velocity is given by

$$\frac{dx_s}{dt} = a_0 M(t), \quad (7.3)$$

where a_0 is the upstream speed-of-sound, M is the shock Mach number. We define total time derivatives of ρ , u and p immediately behind the shock as their rate-of-change observed by a marker traveling with the shock, given by

$$\frac{D\rho}{Dt} = \rho_t + a_0 M \rho_x, \quad \frac{Du}{Dt} = u_t + a_0 M u_x, \quad \frac{Dp}{Dt} = p_t + a_0 M p_x, \quad (7.4)$$

The following Rankine-Hugoniet (RH) conditions connect flow variables behind the shock to their upstream values via Mach number,

$$\begin{aligned} u &= F^u(M) \equiv \frac{2a_0}{\gamma+1} \left(M - \frac{1}{M} \right), \\ \rho &= F^\rho(M) \equiv \frac{\rho_0(\gamma+1)M^2}{(\gamma-1)M^2+2}, \\ p &= F^p(M) \equiv \frac{\rho_0 a_0^2}{\gamma(\gamma+1)} (2\gamma M^2 - \gamma + 1), \\ a &= F^a(M) \equiv \frac{a_0 \mu (2\gamma M^2 - \gamma + 1)}{(\gamma+1)M}, \end{aligned} \quad (7.5)$$

where ρ_0 is the upstream fluid density, and

$$\mu = \sqrt{\frac{(\gamma-1)M^2+2}{2\gamma M^2-\gamma+1}}. \quad (7.6)$$

7.1.1 A-M relation revisited

By applying the RH conditions along the C^+ characteristics instead of the shock, namely, substituting Eqs. (7.5) into Eq. (7.2a), Whitham [108, 109] obtained an expression for $M(A)$ that relates the shock Mach number, M , to the tube's local cross-sectional area, A . This so-called A - M relation gives the basis of the GSD theory. Here we attempt to recover the A - M relation using a different method. With (7.1) and (7.4) combined, all six partial derivatives, p_t , p_x , u_t , u_x , ρ_t , ρ_x , can be solved from the resulting six linear equations. In particular, we have

$$\begin{aligned} p_t &= \frac{a_0 M \rho u a^2 (a_0 M - u) A' + A \left[a^2 (a_0 M \rho \frac{D\rho}{Dt} + \frac{Dp}{Dt}) + u \frac{Dp}{Dt} (a_0 M - u) \right]}{A [a^2 - (u - a_0 M)^2]}, \\ u_t &= \frac{a_0 M \rho u a^2 A' + A \left[\rho \frac{Du}{Dt} (a^2 + u(a_0 M - u)) + a_0 M \frac{Dp}{Dt} \right]}{A \rho [a^2 - (u - a_0 M)^2]}. \end{aligned} \quad (7.7)$$

Substituting (7.7) into the expression $(p_t + \rho au_t)$ and using the identity $D/Dt = (dM/dt)(d/dM)$ then gives an equation from which dM/dt can be solved, producing

$$\left(\frac{dp}{dM} + \rho a \frac{du}{dM} \right) \frac{dM}{dt} = - \left[\frac{a_0 M \rho a^2 u A'}{(a+u)A} + \left(\frac{a_0 M}{a+u} - 1 \right) (p_t + \rho au_t) \right], \quad (7.8)$$

where dp/dM , du/dM , ρ , a and u are known as functions of M , from Eqs. (7.5).

In Whitham's [108] original development of the A - M relation, it is argued that $|p_t + \rho au_t|$ must be small to justify the use "characteristic rule". In the current formulation, this is equivalent to neglecting the last term in (7.8), noting that the component $|a_0 M / (a + u) - 1|$ is uniformly bounded for all $M \in (1, \infty)$. As a result, using $dA/dx = (dA/dt)/(a_0 M)$, the A - M relation follows,

$$\frac{1}{A} \frac{dA}{dM} = \frac{-M}{M^2 - 1} \left(1 + \frac{2(1 - \mu^2)}{(\gamma + 1)\mu} \right) \left(1 + 2\mu + \frac{1}{M^2} \right), \quad (7.9)$$

which can then be integrated to give $M = M(A)$, up to a multiplying constant.

One useful feature of the present derivation of (7.9) is that, compared to Whitham's original "characteristic rule" [108, 109], which essentially assumes that the non-uniform flow effect behind the shock carried by the C^+ characteristics does not modify the shock motion, the error associated with this assumption can be exactly quantified. Here, the neglected term is the product of two terms, where $|a_0 M / (a + u) - 1|$, as a function of M only, measures the geometrical closeness between the C^+ characteristics and the shock, while $|p_t + \rho au_t|$ captures the non-uniformity of the flow immediately behind the shock.

7.2 Two-dimensional Euler equations

We can extend the Quasi-1D theory to two-dimensional (2D) flows. A 2D shock-shape profile must be specified in terms of an intrinsic coordinate that labels points along the shock. Following Whitham's [108, 109] GSD theory, we spatially parameterize points on the shock with the parameter β . This is defined as a continuous, monotonically increasing variable along the shock such that a point with fixed β is instantaneously moving with velocity (in the laboratory frame) that is normal to the shock. This can be taken as the present definition of the "shock velocity". Conceptually it is related to the quasi-one-dimensional concept that the shock moves along "ray tubes" that are locally normal to the shock front.

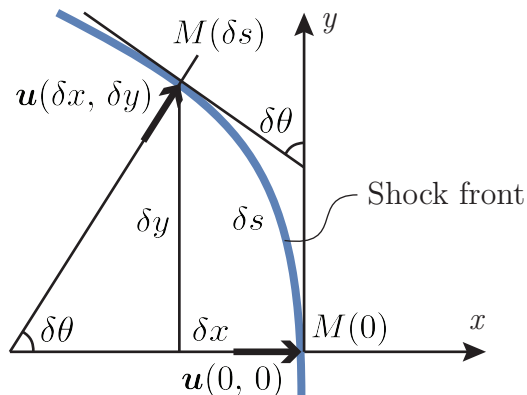


Figure 7.1: (a) Local Cartesian coordinates fixed at a point on shock normal (x -direction) and tangential (y -direction) to the curve. Downstream velocity vectors and Mach numbers are shown at the origin and a differential nearby point at $(\delta x, \delta y)$, whose arclength is δs .

For a given β at time t , we set up a laboratory-fixed, local Cartesian coordinate system shown in figure 7.1, whose origin sits on the shock point defined by β . The positive x -direction aligns with the instantaneous shock velocity at the origin and the positive y -direction corresponds to an increase of β along the shock. The Mach number profile along the shock may be parameterized as a function of arclength, s , measured from the origin in the positive y -direction. In GSD, s and β are related by defining the normalized ray tube area A as,

$$A = \frac{ds}{d\beta}. \quad (7.10)$$

The flow that defines the shock is governed by the 2D Euler equations,

$$\rho_t + u\rho_x + v\rho_y + \rho(u_x + v_y) = 0, \quad (7.11a)$$

$$\rho(u_t + uu_x + vu_y) + p_x = 0, \quad (7.11b)$$

$$\rho(v_t + uv_x + vv_y) + p_y = 0, \quad (7.11c)$$

$$p_t + up_x + vp_y + \gamma p(u_x + v_y) = 0. \quad (7.11d)$$

7.2.1 Tangential derivatives

In order to obtain an evolution equation analogous to (7.8) that governs the shock motion in 2D, all partial derivatives of the flow variables present in (7.11) must be evaluated immediately behind the shock. In particular, this can be done explicitly

for the tangential derivatives, *i.e.*, those with respect to y . At the origin, we have just downstream the shock, x and y components of flow velocity (in the laboratory frame), density and pressure given by

$$\begin{aligned} u(0, 0) &= F^u(M(0)), & v(0, 0) &= 0, \\ \rho(0, 0) &= F^\rho(M(0)), & p(0, 0) &= F^p(M(0)). \end{aligned} \quad (7.12)$$

At a nearby point on the shock $(\delta x, \delta y)$ with arclength $\delta s = \sqrt{\delta x^2 + \delta y^2}$, making a tangent angle of $\delta\theta$ with the y -axis (figure 7.1(a)), these flow quantities become

$$\begin{aligned} u(\delta x, \delta y) &= F^u(M(\delta s)) \cos(\delta\theta), & v(\delta x, \delta y) &= F^u(M(\delta s)) \sin(\delta\theta), \\ \rho(\delta x, \delta y) &= F^\rho(M(\delta s)), & p(\delta x, \delta y) &= F^p(M(\delta s)), \end{aligned} \quad (7.13)$$

where the Mach number has the Taylor expansion

$$M(\delta s) = M(0) + \left. \frac{dM}{ds} \right|_{(0,0)} \delta s + o(\delta s). \quad (7.14)$$

To proceed we make use of the following three limits:

$$\lim_{\delta y \rightarrow 0} \delta x / \delta y = 0, \quad \lim_{\delta y \rightarrow 0} \delta s / \delta y = 1, \quad \lim_{\delta y \rightarrow 0} \delta\theta / \delta y = \kappa, \quad (7.15)$$

where κ is the signed curvature of the shock at the origin. As a result, Eqs. (7.13) are further Taylor expanded as

$$\begin{aligned} u(0, 0) + \left. \frac{\partial u}{\partial y} \right|_{(0,0)} \delta y &= F^u(M(0)) + \left[\frac{dF^u}{dM} \frac{dM}{ds} \right]_{(0,0)} \delta y + o(\delta y), \\ v(0, 0) + \left. \frac{\partial v}{\partial y} \right|_{(0,0)} \delta y &= F^u(M(0)) \delta\theta + o(\delta y), \\ \rho(0, 0) + \left. \frac{\partial \rho}{\partial y} \right|_{(0,0)} \delta y &= F^\rho(M(0)) + \left[\frac{dF^\rho}{dM} \frac{dM}{ds} \right]_{(0,0)} \delta y + o(\delta y), \\ p(0, 0) + \left. \frac{\partial p}{\partial y} \right|_{(0,0)} \delta y &= F^p(M(0)) + \left[\frac{dF^p}{dM} \frac{dM}{ds} \right]_{(0,0)} \delta y + o(\delta y). \end{aligned} \quad (7.16)$$

Substituting (7.12) into (7.16) and applying the $\delta y \rightarrow 0$ limit then gives the desired tangential derivatives at the origin,

$$\begin{aligned} \frac{\partial u}{\partial y} &= \frac{dF^u}{dM} \frac{dM}{ds}, & \frac{\partial v}{\partial y} &= F^u(M) \kappa, \\ \frac{\partial \rho}{\partial y} &= \frac{dF^\rho}{dM} \frac{dM}{ds}, & \frac{\partial p}{\partial y} &= \frac{dF^p}{dM} \frac{dM}{ds}, \end{aligned} \quad (7.17)$$

where we may write

$$\frac{dM}{ds} = \frac{dM}{d\beta} \frac{d\beta}{ds} = \frac{1}{A} \frac{dM}{d\beta}. \quad (7.18)$$

Using (7.10) and (7.18), the derivatives in (7.17) can be calculated at time t provided both the shock shape and Mach number profiles are known functions of β .

7.2.2 Time and normal derivatives

Since the shock marker located at the origin at time t has velocity normal to itself, the time and normal derivatives of flow variables immediately behind the shock are related through the total derivatives,

$$\frac{Du}{Dt} = \frac{dF^u}{dM} \left(\frac{\partial M}{\partial t} \right)_\beta = \frac{\partial u}{\partial t} + a_0 M \frac{\partial u}{\partial x}, \quad (7.19a)$$

$$\frac{Dv}{Dt} = 0 = \frac{\partial v}{\partial t} + a_0 M \frac{\partial v}{\partial x}, \quad (7.19b)$$

$$\frac{D\rho}{Dt} = \frac{dF^\rho}{dM} \left(\frac{\partial M}{\partial t} \right)_\beta = \frac{\partial \rho}{\partial t} + a_0 M \frac{\partial \rho}{\partial x}, \quad (7.19c)$$

$$\frac{Dp}{Dt} = \frac{dF^p}{dM} \left(\frac{\partial M}{\partial t} \right)_\beta = \frac{\partial p}{\partial t} + a_0 M \frac{\partial p}{\partial x}. \quad (7.19d)$$

In addition, all the partial derivatives discussed so far satisfy the 2D Euler equations (7.11). Therefore, substituting (7.12) and (7.17) into (7.11), together with (7.19) gives eight linear equations for eight unknowns, *i.e.*, the x and t partial derivatives of u , v , ρ and p . This process is analogous to the derivation of Eqs. (7.7) for the quasi-1D problem. In particular, the solution yields

$$\begin{aligned} \frac{\partial u}{\partial t} &= \frac{\rho(a^2 - u^2) \left(\frac{\partial M}{\partial t} \right)_\beta \frac{du}{dM} + a_0 M \left[\left(\frac{\partial M}{\partial t} \right)_\beta \left(\rho u \frac{du}{dM} + \frac{dp}{dM} \right) + \kappa \rho a^2 u \right]}{\rho [a^2 - (u - a_0 M)^2]}, \\ \frac{\partial p}{\partial t} &= \frac{u(a_0 M - u) \left(\frac{\partial M}{\partial t} \right)_\beta \frac{dp}{dM} + a^2 \left[\left(\frac{\partial M}{\partial t} \right)_\beta \left(\frac{dp}{dM} + a_0 \rho M \frac{du}{dM} \right) + a_0 \kappa \rho u M (a_0 M - u) \right]}{a^2 - (u - a_0 M)^2}. \end{aligned} \quad (7.20)$$

7.3 Geometrical equivalence

Using (7.20) to expand the expression $(p_t + \rho a u_t)$ then gives at any β and t ,

$$\left(\frac{\partial M}{\partial t} \right)_\beta = - \frac{\frac{\kappa a_0 M \rho a^2 u}{(a+u)} + \left(\frac{a_0 M}{a+u} - 1 \right) \left(\frac{\partial p}{\partial t} + \rho a \frac{\partial u}{\partial t} \right)}{\frac{dp}{dM} + \rho a \frac{du}{dM}}. \quad (7.21)$$

An expedited route to arrive at (7.21) is to observe that because $v = 0$, the momentum equation (7.11c) for v decouples from the rest of Eqs. (7.11). Also comparing (7.11) to (7.1), and (7.4) to (7.19), the only difference is that A'/A in (7.1) is replaced by κ in (7.11). As a result, (7.21) is directly analogous to (7.8).

We can conclude that GSD in its complete form given by (7.8) with the $(p_t + \rho au_t)$ term retained, is equivalent to 2D Euler if and only if

$$\kappa = A'/A = \frac{1}{a_0 M A} \left(\frac{\partial A}{\partial t} \right)_\beta. \quad (7.22)$$

By defining A in 2D flow as the normalized ray-tube area given in (7.10), Whitham [109] (Eq. (8.59)) showed, using the standard α - β curvilinear coordinates in GSD, that

$$\frac{\partial \theta}{\partial \beta} = \frac{1}{M} \frac{\partial A}{\partial \alpha}, \quad (7.23)$$

where $\alpha \equiv a_0 t$ is defined as a time-like label for the position of a shock along a ray corresponding to constant β . Equation (7.23) can be shown equivalent to (7.22) by noting $ds = Ad\beta$. For example, the geometrical equivalence for a converging/diverging cylindrical shock of radius r is trivially verified by identifying $A = A(r) = 2\pi r$, and thus $A'/A = 1/r = \kappa$.

Notably, the geometrical equivalence between the evolution of shocks in quasi-1D and genuine 2D flows is invariant with respect to the Cartesian coordinates used in Sec. 7.2. Best [11] observed this equivalence and derived an alternative to the original GGSD theory [10] resulting from defining the shock velocity to include the local flow velocity component that is tangential to the shock at a time instant. In contrast, in Sec. 7.2, we spatially parameterize the shock using β that labels shock points that propagate locally normal to the shock front. This difference illustrates the somewhat arbitrary definition of the shock velocity. The formulations are physically equivalent. An immediate implication of the geometrical equivalence is that it suffices to consider the quasi-1D formulation alone in order to construct the shock dynamics in 2D, by effectively stacking ray tubes of normalized area A . We can thus proceed in the following analysis without invoking the 2D Euler equations.

7.4 A hierarchical expansion of the Euler equations

As shown in Sections. 7.1.1 and 7.3, compared to the true Euler equations, the non-uniform details of the flow behind the shock that is missing in the GSD approximation is entirely encapsulated in the quantity $(p_t + \rho au_t)$. Therefore a suitable evolutionary model for such quantity is desired to provide corrections to the GSD description. In the present study, we adapt the GGSD model proposed by Best [10], which expands the Euler equations as a hierarchical system that can be closed at any order. A summary of Best's formulation is outlined here.

The construction begins with assuming sufficient smoothness of quasi-1D flow and defining

$$Q_n \equiv \frac{\partial^{n-1}}{\partial t^{n-1}} \left(\frac{\partial p}{\partial t} + \rho a \frac{\partial u}{\partial t} \right), \quad n = 1, 2, \dots, \quad (7.24)$$

evaluated immediately downstream of the shock. It is noted that Q_1 gives the non-uniformity measure, the quantity of interest. Computing the expansion of Q_n involves the following convenient differential operator,

$$\mathcal{F}^{i,j} \equiv \frac{\partial^{i+j}}{\partial x^i \partial t^j}, \quad i, j \in \{0, 1, 2, \dots\}, \quad (7.25)$$

acting on the flow variables p , u , ρ and a . Let $\xi \in \{p, u, \rho\}$: then along the trajectory of the shock, the total derivative of ξ is given by

$$\frac{D}{Dt} (\mathcal{F}^{i,j}[\xi]) = \mathcal{F}^{i,j+1}[\xi] + a_0 M \mathcal{F}^{i+1,j}[\xi], \quad (7.26)$$

Further, the following identity for continuously differentiable functions A and B ,

$$\mathcal{F}^{i,j}[AB] = \sum_{n=0}^i \sum_{m=0}^j \binom{i}{n} \binom{j}{m} \mathcal{F}^{n,m}[A] \mathcal{F}^{i-n,j-m}[B], \quad (7.27)$$

where $\binom{i}{n}$ and $\binom{j}{m}$ are the binomial operators, allows the Euler equations (7.2) to be differentiated by the operator $\mathcal{F}^{i,j}$. This, together with (7.26), forms six linear equations for six unknowns:

$$\left(\mathcal{F}^{i+1,j}[p], \mathcal{F}^{i+1,j}[u], \mathcal{F}^{i+1,j}[\rho], \mathcal{F}^{i,j+1}[p], \mathcal{F}^{i,j+1}[u], \mathcal{F}^{i,j+1}[\rho] \right)^T, \quad (7.28)$$

which can be solved analogously to the derivation of (7.7). The explicit solutions due to Best [10] are reported in Appendix F. Best's result can be viewed as extensions of the RH condition to the jump in partial derivatives of flow variables across a curved shock, which is a topic that has also been studied in references [28, 29, 45, 50, 73, 82, 101].

With (7.28) determined, it is then possible to prove by induction the following dependency relation for the partial derivatives,

$$\mathcal{F}^{0,0}[\xi] = \xi(M), \quad (7.29a)$$

$$\mathcal{F}^{i,j}[\xi] = \mathcal{F}^{i,j}[\xi] \left(M, Q_1, \dots, Q_k, A'/A, \dots, \frac{d^{k-1}(A'/A)}{dx^{k-1}} \right), \quad (7.29b)$$

for $k = i + j$, and $i, j \in \{0, 1, \dots\}$. With some manipulations, (7.29) leads to

$$\frac{DM}{Dt} = \frac{DM}{Dt} (M, Q_1, A'/A), \quad (7.30a)$$

$$\frac{DQ_{k+1}}{Dt} = \frac{DQ_{k+1}}{Dt} \left(M, Q_1, \dots, Q_{k+2}, A'/A, \dots, \frac{d^k(A'/A)}{dx^k} \right). \quad (7.30b)$$

The explicit expansion of (7.30a) was earlier derived in (7.8) where only first-order partial derivatives of the flow variables were used. In general, higher order partial derivatives are required to expand (7.30b) and give

$$\begin{aligned} \frac{DQ_{k+1}}{Dt} = & - \left[a_0 M \frac{\partial^{k+1}}{\partial t^{k+1}} \left(\frac{\rho a^2 u}{a+u} \right) A'/A + a_0 M \sum_{i=1}^{k+1} \binom{k+1}{i} \frac{\partial^i}{\partial t^i} \left(\frac{1}{a+u} \right) Q_{k-i+2} \right. \\ & \left. + a_0 M \frac{\partial^k}{\partial t^k} \left(\frac{\partial(\rho a)}{\partial t} \frac{\partial u}{\partial x} - \frac{\partial(\rho a)}{\partial x} \frac{\partial u}{\partial t} \right) + \left(\frac{a_0 M}{a+u} - 1 \right) Q_{k+2} \right]. \quad (7.31) \end{aligned}$$

Importantly, (7.29b) and (7.30b) show that the dependence of DQ_{k+1}/Dt upon derivatives of ξ of order $\leq k+1$ is fully specified by knowing M and Q_i of order $i \leq k+1$. Therefore, for a sequence of coupled nonlinear evolution equations described by (7.30) for $k = 1, \dots, N$, closure can be achieved by truncating the term $[a_0 M/(a+u) - 1]Q_{N+2}$ in (7.31). This results in a closed system of $N+2$ nonlinear differential equations for the variables M, Q_1, \dots, Q_{N+1} , that can be integrated in time provided the initial conditions for M, Q_1, \dots, Q_{N+1} are known.

For instance, it has been shown in Sec. 7.1.1 that truncation at Q_1 in (7.30a) leads to the A - M relation in GSD. And by sampling Q_1 and its higher derivatives $Q_{i \geq 1}$, at time $t = 0$, the non-uniformity of the initial flow behind the shock is described, which then evolves in time according to the expansion of the Euler equations. Similar to applying the ‘‘characteristic rule’’ in GSD, where the C^+ characteristic is applied at the shock, the truncation error associated with the present higher order approach is due to forcing the DQ_N/Dt equation along the C^+ characteristic at the shock.

A solution to any truncated GGSD system of order $N \geq 1$ gives an approximated 2D Euler flow field at time t when $\kappa (= A'/A)$, M , and Q_1 are known. The flow variables, u, v, ρ and p , as well as their partial derivatives with respect to x, y and t , that appear in Eq. (7.11) can be consequently evaluated using (7.12), (7.17), and the full set of (7.20). In particular, the x and t derivatives seen in (7.20) depend explicitly on Q_1 through the term $\partial M/\partial t$ given by (7.21). The conditions for convergence of the Mach number M to the solution obtained from the full 2D Euler equations as a function of t , when the truncation number N increases remains an open problem that is addressed incompletely in Best [10, 11]. We hypothesize that conditions for convergence may be problem dependent. It is noted that Best’s formulation certainly breaks down when the smooth flow assumption is violated, especially if additional discontinuous disturbances that originated downstream and carried by the C^+ characteristics overtake the shock. Such flow conditions are excluded in the present study.

7.5 Evolution of a periodic, perturbed planar shock

7.5.1 A complex-variable formulation

With the truncated GGSD equations established in Sec. 7.4, we can now describe the motion of a slightly perturbed planar shock, parameterized periodically using ray tube marker $\beta \in [0, 2\pi)$ [see Sec. 7.2], by correctly replacing $A(x)$ in the quasi-1D case with the normalized ray tube area given in (7.10) for a 2D shock. The 2π -periodic formulation is convenient for our application to a shock generated by a periodically corrugated piston in Section 8.1. Following Mostert *et al.* [78], we describe the shock shape in a complex $z = x + iy$ plane by $z = Z(\beta, t) = X(\beta, t) + iY(\beta, t)$.

By defining ray tube markers along the shock whose velocity is locally normal to the shock curve, the kinematic equation for the shock profile reads as

$$\left(\frac{\partial Z}{\partial t}\right)_{\beta} = a_0 M(\beta, t) \hat{n}(\beta, t), \quad (7.32)$$

where $Z \in \mathbb{C}$ is the complex variable that describes the shock curve, a_0 is the upstream constant sound speed, M is the local Mach number and $\hat{n} \in \mathbb{C}$ is the unit normal vector aligned with the local shock velocity. Non-dimensional variables are used according to a reference length scale \bar{L}_0 , where $2\pi\bar{L}_0$ is the initial perturbation wavelength; a reference velocity \bar{a}_0 and density $\bar{\rho}_0$. The time and pressure scales are thus derived as \bar{L}_0/\bar{a}_0 and $\bar{\rho}_0\bar{a}_0^2$, respectively.

The complex shock profile Z is now decomposed into a steady flat shock of constant Mach number M_0 moving in the positive imaginary direction, and its perturbation,

$$Z = Z_0 + z(\beta, t), \quad Z_0 = \beta + ia_0 M_0 t. \quad (7.33)$$

It is noted that the unperturbed shock at $t = 0$ here lies on the real axis in the complex plane, and moves in the positive y -direction. This notation conventionally differs from the discussion in Sec. 7.2.

Further, the unit normal vector, $\hat{n} = i\hat{s}$, is obtained through a rotation of the unit tangent \hat{s} , given by

$$\hat{s} = \frac{1}{A(\beta, t)} \frac{\partial Z}{\partial \beta}, \quad (7.34)$$

where

$$A(\beta, t) = \left| \frac{\partial Z}{\partial \beta} \right| = \sqrt{\frac{\partial Z}{\partial \beta} \frac{\partial Z^*}{\partial \beta}}, \quad (7.35)$$

is the normalized ray tube area in the complex-variable formulation, following (7.10), and * denotes complex conjugate. The kinematic equation for the shock profile perturbation then becomes

$$\frac{\partial z}{\partial t} = ia_0 M_0 \left[\frac{M}{M_0} \left(1 + \frac{\partial z}{\partial \beta} \right) \left| 1 + \frac{\partial z}{\partial \beta} \right|^{-1} - 1 \right]. \quad (7.36)$$

7.5.2 Zeroth-order GGSD system: GGSD-0

In order to determine the evolution of the shock shape z , it remains to specify the dynamics of the Mach number profile M , which can also be written in the perturbation form

$$M = M_0 + m. \quad (7.37)$$

Conveniently, using Eq. (7.21) with the help of (7.22) and (3.23), we have shown that the Euler equations dictates

$$\frac{\partial m}{\partial t} = - \frac{\frac{\rho a^2 u \Phi a_0 M}{(a+u)} + \left(\frac{a_0 M}{a+u} - 1 \right) Q_1}{dp/dM + \rho a (du/dM)}, \quad (7.38)$$

where $\Phi \equiv (\partial A / \partial t) / (a_0 M A)$ and can be obtained by differentiating (7.35) using (7.32) as

$$\Phi = \Phi(Z) = - \left| \frac{\partial Z}{\partial \beta} \right|^{-3} \Im \left(\frac{\partial^2 Z}{\partial \beta^2} \frac{\partial Z^*}{\partial \beta} \right). \quad (7.39)$$

Now, by setting $Q_1 = 0$, Eqs. (7.36) and (7.38) form a set of coupled non-linear differential equations that describes the shock motion. Such system corresponds to the zeroth-order truncation of the hierarchical GGSD equations introduced in Sec. 7.4, which gives rise to the A - M relation seen in the GSD model.

There is a subtle difference between GSD and the zeroth-order GGSD system, henceforth referred to as GGSD-0. In GSD, the A - M relation, once determined with a unique integration constant, serves as a global constraint over the entire shock profile. For example, Mostert *et al.* [78] derived an expression for the Mach number profile M for a planar shock that is completely determined by the local shock shape Z , namely, $M = M(Z)$. Consequently, Eqs. (7.36) and (7.38) reduce and combine into a single equation for Z that governs the shock shape [see Eq. (2.9) of [78]]. In contrast, by separating (7.36) and (7.38) as two independent evolution equations in GGSD-0, the A - M relation applies locally at a given β , allowing the integration constant to differ along the shock. The obvious benefit of such separation is that GGSD-0 is able to handle more general initial value problems that are forbidden in GSD, where the initial shock shape and Mach number profile do not satisfy a global

A - M relation everywhere on the shock. Nevertheless if the initial conditions are compatible with a global A - M relation, then GGSD-0 is identical to GSD.

Strong and weak shock limits

Here, we simplify Eq. (7.38) in the strong and weak shock limits, as $M \rightarrow \infty$ and $M \rightarrow 1$, respectively. This is achieved by utilising the limiting forms of the RH conditions (7.5) given by

$$u \sim \alpha_1 a_0 M, \quad p \sim \alpha_1 \rho_0 a_0^2 M^2, \quad \rho \sim \alpha_2 \rho_0, \quad a \sim \alpha_3 a_0 M, \quad (7.40)$$

as $M \rightarrow \infty$, where $\alpha_{1,2,3}$ are constant functions of γ , given in Table E.1, Appendix E; and similarly,

$$u \sim 2\alpha_1 a_0 \varepsilon, \quad p \sim \rho_0 a_0^2 \left(\frac{1}{\gamma} + 2\alpha_1 \varepsilon \right), \quad \rho \sim \rho_0 (1 + 2\alpha_1 \varepsilon), \quad a \sim a_0 \left(1 + \frac{2\varepsilon}{\alpha_2} \right), \quad (7.41)$$

where $\varepsilon \equiv M - 1$ and $\varepsilon \rightarrow 0$ defines the weak-shock limit. We note that Appendix E contains lists of parameters that we use throughout the present study.

Evaluating (7.38) using Eqs. (7.40) and (7.41), respectively, then yields

$$\left(\frac{\partial M}{\partial t} \right)_\beta = \begin{cases} -\zeta_1 a_0 \Phi M^2 + \frac{\zeta_2 Q_1}{\rho_0 a_0^2 M} + O\left(\frac{1}{M^2}\right), & M \rightarrow \infty, \\ -\frac{a_0 \Phi \varepsilon}{2} + \frac{Q_1 \varepsilon}{4\alpha_1 \rho_0 a_0^2} + O(\varepsilon^2), & \varepsilon \rightarrow 0, \end{cases} \quad (7.42)$$

where $\zeta_{1,2}$ are again constants listed in Table E.1, Appendix E. In this asymptotic form, it is assumed that Q_1 is at least of order $O(M^3)$ in the strong shock limit, and of order $O(\varepsilon^0)$ in the weak shock limit, for the correction term to be comparable in the respective leading order expression. Although not necessary for the zeroth-order GGSD model, where the correction is neglected by letting $Q_1 = 0$, such assumptions about the magnitude of Q_1 will be shown essential for deriving the limiting expressions for higher order GGSD models in the following sections.

For completeness, the zeroth-order GGSD systems in the strong and weak shock limits are given by the following closed system,

$$\frac{\partial Z}{\partial t} = i a_0 M \frac{\partial Z}{\partial \beta} \left| \frac{\partial Z}{\partial \beta} \right|^{-1}, \quad \left(\frac{\partial M}{\partial t} \right)_\beta = \begin{cases} -\zeta_1 a_0 \Phi M^2, & M \rightarrow \infty, \\ -\frac{a_0 \Phi}{2} (M - 1), & M \rightarrow 1. \end{cases} \quad (7.43)$$

7.5.3 First order GGSD system: GGSD-1

As discussed in Sec. 7.4, corrections to GGSD-0 can be made by including higher order equations that capture the evolution of Q_1 . In this section, we obtain the GGSD-1 model explicitly in the weak and strong shock limits.

The evolution of Q_1 following the shock trajectory in the Quasi-1D flow is governed by Eq. (7.31) with $k = 0$. Using the present complex-variable formulation, the total time derivative, DQ_1/Dt , described by Eq. (7.31) directly equates to the partial time derivative tracing a fixed ray tube marker β , namely, $(\partial Q_1/\partial t)_\beta$. Similarly, the full differential dx that appears in A' is now understood as the differential distance traveled by the shock in the ray tube direction, *i.e.*,

$$dx = a_0 M(\beta, t) dt, \quad \frac{A'}{A} = \frac{1}{a_0 M A} \left(\frac{\partial A}{\partial t} \right)_\beta = \Phi, \quad (7.44)$$

where Φ is given in (7.39). Now substituting (7.44) into (7.31) yields

$$\begin{aligned} \left(\frac{\partial Q_1}{\partial t} \right)_\beta = & -a_0 M \left[\frac{\partial}{\partial t} \left(\frac{\rho a^2 u}{a+u} \right) \Phi + \frac{\partial(\rho a)}{\partial t} \frac{\partial u}{\partial x} - \frac{\partial(\rho a)}{\partial x} \frac{\partial u}{\partial t} \right. \\ & \left. + \frac{\partial}{\partial t} \left(\frac{1}{a+u} \right) Q_1 + \left(\frac{1}{a+u} - \frac{1}{a_0 M} \right) Q_2 \right]. \end{aligned} \quad (7.45)$$

Expanding (7.45) and noting $a = \sqrt{\gamma p/\rho}$ produces first order partial derivatives of ρ , u and p with respect to t and x , which are found as a subset of solution (7.28), where $i = j = 0$. Therefore in view of (7.29b), Eq.(7.45) is fully specified knowing M , Q_1 and Φ , except for the last term that contains Q_2 . Hence truncation at $Q_2 = 0$ provides closure. GGSD-1 then comprises (7.36), (7.38) and (7.45) with $Q_2 = 0$.

The weak shock limit

The full expansion of $\mathcal{F}^{0,1}[\xi^*]$ and $\mathcal{F}^{1,0}[\xi^*]$, where $\xi^* \in \{\rho, u, p, a\}$, can be obtained as a subset from the solution process to the arrival of (7.28). Using the asymptotic forms (7.41) and (7.42), these first order partial derivatives, listed in Eqs. (F.11)–(F.14) of Appendix F, simplify in the weak shock limit as $\varepsilon = M-1 \rightarrow 0$. It is noted that the leading order behaviour of all eight partial derivatives in this limit relies on the assumption that $Q_1 \sim O(\varepsilon^0) \sim O(1)$, which is consistent with the observation made with Eq. (7.42) when $Q_1 \neq 0$ is allowed.

Substituting Eqs. (7.41) and (F.11)–(F.14) into (7.45) then gives the leading order evolution of Q_1 in the weak shock limit,

$$\left(\frac{\partial Q_1}{\partial t}\right)_\beta = \frac{Q_1}{2} \left(\frac{Q_1}{\alpha_1 \rho_0 a_0^2} - a_0 \Phi \right) + Q_2 \varepsilon + O(\varepsilon), \quad (7.46)$$

where the correction term $Q_2 \varepsilon$ enters only if $Q_2 \sim O(1/\varepsilon)$ at least. However, closure of the GGSD system at first order demands $Q_2 = 0$; and therefore combining Eqs. (7.36), (7.42), and (7.46) completes the weak shock limiting GGSD-1 equations as follows:

$$\begin{aligned} \frac{\partial Z}{\partial t} &= i a_0 M \frac{\partial Z}{\partial \beta} \left| \frac{\partial Z}{\partial \beta} \right|^{-1}, \\ \frac{\partial M}{\partial t} &= \left(-\frac{a_0 \Phi}{2} + \frac{Q_1}{4 \alpha_1 \rho_0 a_0^2} \right) (M - 1), \\ \frac{\partial Q_1}{\partial t} &= \frac{Q_1}{2} \left(\frac{Q_1}{\alpha_1 \rho_0 a_0^2} - a_0 \Phi \right). \end{aligned} \quad (7.47)$$

The strong shock limit

Analogous analysis can be carried out for the strong shock limit. Substituting (7.40) into the general solution of the first order partial derivatives leads to the strong shock limits of Eqs. (F.11)–(F.14) in Appendix F, where M' is understood similarly as in (7.44), such that upon using (7.42), one has

$$M' = \frac{dM}{dx} = \frac{1}{a_0 M} \left(\frac{\partial M}{\partial t} \right)_\beta \sim -\zeta_1 \Phi M + \frac{\zeta_2 Q_1}{\rho_0 a_0^3 M^2}, \quad (7.48)$$

It is thus observed that $M' \sim O(M)$, so the M' notation is preferably kept in (F.11)–(F.14) and henceforth for convenient identification of the leading order behaviour.

Again, substituting (7.40), (F.11)–(F.14) and (7.48) into (7.45) yields the limiting Q_1 equation,

$$\left(\frac{\partial Q_1}{\partial t}\right)_\beta = \gamma_1 \rho_0 a_0^4 \Phi^2 M^4 + \gamma_2 a_0 M \Phi Q_1 + \frac{\gamma_3 Q_1^2}{\rho_0 a_0^2 M^2} + \gamma_4 Q_2 + O(M^3), \quad (7.49)$$

where $\gamma_{1,2,3,4}$ are coefficients listed in Table E.1, Appendix E. Setting $Q_2 = 0$, which otherwise is assumed as $Q_2 \sim O(M^4)$, Eq. (7.49) is joined with (7.36) and

(7.42) to form the GGSD-1 equations in the strong shock limit,

$$\begin{aligned}\frac{\partial Z}{\partial t} &= ia_0M \frac{\partial Z}{\partial \beta} \left| \frac{\partial Z}{\partial \beta} \right|^{-1}, \\ \frac{\partial M}{\partial t} &= -\zeta_1 a_0 \Phi M^2 + \frac{\zeta_2 Q_1}{\rho_0 a_0^2 M}, \\ \frac{\partial Q_1}{\partial t} &= \gamma_1 \rho_0 a_0^4 \Phi^2 M^4 + \gamma_2 a_0 \Phi M Q_1 + \frac{\gamma_3 Q_1^2}{\rho_0 a_0^2 M^2}.\end{aligned}\quad (7.50)$$

7.5.4 Second order GGSD system: GGSD-2

The second order GGSD system can be similarly established by incorporating the evolution of Q_2 , governed by Eq. (7.31) where $k = 1$ and $Q_3 = 0$,

$$\begin{aligned}\left(\frac{\partial Q_2}{\partial t} \right)_\beta &= -a_0 M \Phi \frac{\partial^2}{\partial t^2} \left(\frac{\rho a^2 u}{a+u} \right) - a_0 M \left[\frac{\partial^2}{\partial t^2} \left(\frac{1}{a+u} \right) Q_1 + 2 \frac{\partial}{\partial t} \left(\frac{1}{a+u} \right) Q_2 \right] \\ &\quad - a_0 M \frac{\partial}{\partial t} \left(\frac{\partial(\rho a)}{\partial t} \frac{\partial u}{\partial x} - \frac{\partial(\rho a)}{\partial x} \frac{\partial u}{\partial t} \right) - \left(\frac{a_0 M}{a+u} - 1 \right) Q_3.\end{aligned}\quad (7.51)$$

Again, without the Q_3 correction, the rest of (7.51) is fully determined because the second order partial derivatives, $\{\mathcal{F}^{n,m}[\xi^*] : \xi^* \in \{\rho, u, p, a\}, n+m=2\}$, only depends on M , Q_1 , Q_2 and ultimately Z . To see this, the apparent dependency of $(A'/A)'$ in (7.29b) for quasi-1D flow here becomes

$$\frac{d}{dx} \left(\frac{A'}{A} \right) = \frac{1}{a_0 M} \left(\frac{\partial \Phi}{\partial t} \right)_\beta, \quad (7.52)$$

which can be evaluated according to the definition of Φ (7.39), after obtaining the partial derivatives, $Z_{\beta t}$ and $Z_{\beta \beta t}$, from differentiating (7.32) and its complex conjugate with respect to β , once and twice, respectively. As a result, one defines $\Psi \equiv (A'/A)'$ and arrives at

$$\Psi = \Psi(Z, M) = -\Phi^2 - \frac{1}{A^4 M} \left[A^2 \frac{\partial^2 M}{\partial \beta^2} - \Re \left(\frac{\partial^2 Z}{\partial \beta^2} \frac{\partial Z^*}{\partial \beta} \right) \frac{\partial M}{\partial \beta} \right], \quad (7.53)$$

where $A = |\partial Z / \partial \beta|$. The explicit expansion of (7.51) is determined next in the weak and strong shock limits.

The weak shock limit

In order to obtain the various second order partial derivatives involved in (7.51), the shock local acceleration is also required. This is computed by differentiating (7.42)

(recall $\epsilon = M - 1$). as follows,

$$\frac{\partial^2 \epsilon}{\partial t^2} = \frac{1}{4\alpha_1 \rho_0^2 a_0^2} \left\{ \epsilon \frac{\partial Q_1}{\partial t} + Q_1 \frac{\partial \epsilon}{\partial t} - 2\alpha_1 \rho_0^2 a_0^3 \left[\Phi \frac{\partial \epsilon}{\partial t} + a_0 \epsilon (1 + \epsilon) \Psi \right] \right\} \sim O(\epsilon), \quad (7.54)$$

where $\partial Q_1/\partial t$, $\partial \epsilon/\partial t$, Φ and Ψ are known due to Eqs. (7.46), (7.42), (7.39) and (7.53).

With (7.41), (F.11)–(F.14), (7.53), and (7.54) available, expressions for the required second-order partials of flow variables are Taylor expanded around $\epsilon = 0$, yielding the leading order behaviour given in Eqs. (F.15)–(F.18) of Appendix F. We note that $Q_2 \sim O(1/\epsilon)$ and recall (7.46). Finally, substituting (7.41) and (F.15)–(F.18) into (7.51) while letting $Q_3 = 0$ produces the evolution equation for Q_2 as $\epsilon \rightarrow 0$, which is then joined to (7.36), (7.42) and (7.46) to form the following GGSD-2 system in the weak shock limit,

$$\begin{aligned} \frac{\partial Z}{\partial t} &= i a_0 M \frac{\partial Z}{\partial \beta} \left| \frac{\partial Z}{\partial \beta} \right|^{-1}, \\ \frac{\partial M}{\partial t} &= (M - 1) \left(-\frac{a_0 \Phi}{2} + \frac{Q_1}{4\alpha_1 \rho_0 a_0^2} \right), \\ \frac{\partial Q_1}{\partial t} &= \frac{Q_1}{2} \left(\frac{Q_1}{\alpha_1 \rho_0 a_0^2} - a_0 \Phi \right) + (M - 1) Q_2, \\ \frac{\partial Q_2}{\partial t} &= \frac{[(\gamma + 1)Q_1 - 2\rho_0 a_0^3 \Phi] Q_2}{4\rho_0 a_0^2}. \end{aligned} \quad (7.55)$$

The strong shock limit

As an analogy to (7.54), the second time derivative $\partial^2 M/\partial t^2$ is prepared first

$$\frac{\partial^2 M}{\partial t^2} = -\zeta_1 a_0 M \left(a_0 \Psi M^2 + 2\Phi \frac{\partial M}{\partial t} \right) + \frac{\zeta_2}{\rho_0 a_0^2 M^2} \left(M \frac{\partial Q_1}{\partial t} - Q_1 \frac{\partial M}{\partial t} \right), \quad (7.56)$$

where $\partial Q_1/\partial t$, $\partial M/\partial t$, Φ and Ψ are found in (7.49), (7.42), (7.39) and (7.53), respectively. However here in the strong shock limit, it is more convenient to further attain $M'' \equiv d(M')/dx$, fully expanded using (7.44), (7.42), (7.49), and (7.56) as

$$M'' = \left[(\zeta_1^2 + \gamma_1 \zeta_2) \Phi^2 - \zeta_1 \Psi \right] M + \frac{(\zeta_1 + \gamma_2) \zeta_2 \Phi Q_1}{\rho_0 a_0^3 M^2} + \frac{\zeta_2 (\gamma_3 - 2\zeta_2) Q_1^2}{\rho_0^2 a_0^6 M^5} + \frac{\zeta_2 \gamma_4 Q_2}{\rho_0 a_0^4 M^3}. \quad (7.57)$$

Consequently, $M'' \sim M' \sim O(M)$ is established.

Next, the second order partial derivatives contributing to the expansion of $\partial Q_2/\partial t$ can be expressed in terms of M'' , for the same reason that M' is preferred in Eqs. (F.11)–(F.14). The explicit asymptotic formulas are reported in Eqs. (F.15)–(F.18), Appendix F. After evaluating (7.51) using Eqs. (F.15)–(F.18) in the strong shock limit, the GGSD-2 equations follows:

$$\begin{aligned}
\frac{\partial Z}{\partial t} &= ia_0 M \frac{\partial Z}{\partial \beta} \left| \frac{\partial Z}{\partial \beta} \right|^{-1}, \\
\frac{\partial M}{\partial t} &= -\zeta_1 a_0 \Phi M^2 + \frac{\zeta_2 Q_1}{\rho_0 a_0^2 M}, \\
\frac{\partial Q_1}{\partial t} &= \gamma_1 \rho_0 a_0^4 \Phi^2 M^4 + \gamma_2 a_0 \Phi M Q_1 + \frac{\gamma_3 Q_1^2}{\rho_0 a_0^2 M^2} + \gamma_4 Q_2, \\
\frac{\partial Q_2}{\partial t} &= \rho_0 a_0^5 M^5 \left(\chi_1 \Phi \Psi + \chi_2 \Phi^3 \right) - a_0^2 M^2 \left(\chi_3 \Psi + \chi_4 \Phi^2 \right) Q_1 - \frac{\chi_5 \Phi Q_1^2}{\rho_0 a_0 M} \\
&\quad + \frac{\chi_6 Q_1^3}{\rho_0^2 a_0^4 M^4} + \frac{\chi_7 Q_1 Q_2}{\rho_0 a_0^2 M^2} + \chi_8 a_0 \Phi M Q_2,
\end{aligned} \tag{7.58}$$

where $\chi_{1,2,\dots,8}$ are again constant functions of γ listed in Table E.1, Appendix E. This completes the derivation of shock-evolution equations used presently.

7.5.5 Unbounded linear growth

We now demonstrate that the zeroth-order GGSD system is linearly stable, whilst including the Q_1 correction in the first order GGSD equations leads to linearised solutions that exhibit unbounded growth in time. Equations (7.47) and (7.50) are expanded around a plane shock of constant Mach number M_0 , and consequently a steady downstream flow with $Q_1 = Q_{10}$. The plane shock motion is described by $Z_0 = \beta + ia_0 M_0 t$, and the following rescaled perturbation fields are considered,

$$Z = Z_0 + z_1(\beta, t)\delta + \dots, \quad M = M_0 + m_1(\beta, t)\delta + \dots, \quad Q_1 = Q_{10} + q_1(\beta, t)\delta + \dots, \tag{7.59}$$

where $\delta \ll 1$ is the dimensionless perturbation size, and the subscript “1” is used to distinguish from unscaled variables used in (7.33) and (7.37). The $\delta \rightarrow 0$ asymptotic behaviour is explored next for the limiting equations (7.47) and (7.50), corresponding to weak and strong shocks where the respective $M_0 \rightarrow 1$ and $M_0 \rightarrow \infty$ limits have been applied. Substituting (7.59) into Eqs. (7.47) and (7.50) respectively yields, at order $O(\delta^0)$, that for both weak and strong shocks,

$$Q_{10} = 0, \tag{7.60}$$

implying that the linear behaviour of the shock is entirely explained by the zeroth-order GGSD system. Further, at order $O(\delta)$, one has

$$\frac{\partial z_1}{\partial t} = \frac{ia_0 M_0}{2} \left(\frac{\partial z}{\partial \beta} - \frac{\partial z^*}{\partial \beta} \right) + ia_0 m_1, \quad (7.61a)$$

$$\frac{\partial m_1}{\partial t} = \begin{cases} \frac{\zeta_2 q_1}{\rho_0 a_0^2 M_0} - \frac{i\zeta_1 a_0 M_0^2}{2} \left(\frac{\partial^2 z_1}{\partial \beta^2} - \frac{\partial^2 z_1^*}{\partial \beta^2} \right), & M_0 \rightarrow \infty, \\ \frac{(M_0-1)q_1}{4\alpha_1 \rho_0 a_0^2} - \frac{ia_0(M_0-1)}{4} \left(\frac{\partial^2 z_1}{\partial \beta^2} - \frac{\partial^2 z_1^*}{\partial \beta^2} \right), & M_0 \rightarrow 1, \end{cases} \quad (7.61b)$$

$$\frac{\partial q_1}{\partial t} = 0. \quad (7.61c)$$

As a result of (7.61c), q_1 is a constant function of β to be determined from the initial conditions of the flow immediately behind the shock, namely,

$$q_1(\beta, t) = q_1(\beta, 0), \quad \forall t > 0. \quad (7.62)$$

By differentiating (7.61a) with respect to β , (7.61b) can be cast into

$$\frac{\partial m_1}{\partial t} = \begin{cases} -\frac{\zeta_1 M_0}{2} \frac{\partial}{\partial t} \left(\frac{\partial z_1}{\partial \beta} + \frac{\partial z_1^*}{\partial \beta} \right) + \frac{\zeta_2 q_1}{\rho_0 a_0^2 M_0}, & M_0 \rightarrow \infty, \\ -\frac{(M_0-1)}{4M_0} \frac{\partial}{\partial t} \left(\frac{\partial z_1}{\partial \beta} + \frac{\partial z_1^*}{\partial \beta} \right) + \frac{(M_0-1)q_1}{4\alpha_1 \rho_0 a_0^2}, & M_0 \rightarrow 1, \end{cases} \quad (7.63)$$

which can be integrated with respect to t because of (7.62) to give

$$m_1 = \begin{cases} -\frac{\zeta_1 M_0}{2} \left(\frac{\partial z_1}{\partial \beta} + \frac{\partial z_1^*}{\partial \beta} \right) + \frac{\zeta_2 q_1}{\rho_0 a_0^2 M_0} t + f(\beta), & M_0 \rightarrow \infty, \\ -\frac{M_0-1}{4} \left(\frac{\partial z_1}{\partial \beta} + \frac{\partial z_1^*}{\partial \beta} \right) + \frac{(M_0-1)q_1}{4\alpha_1 \rho_0 a_0^2} t + f(\beta), & M_0 \rightarrow 1, \end{cases} \quad (7.64)$$

where $f(\beta)$ is prescribed from the initial Mach number profile $m_1(\beta, 0)$. Further, (7.64) is substituted into (7.61a), to show

$$\frac{\partial z_1}{\partial \tau} = \begin{cases} i \left(\frac{1-\zeta_1}{2} \frac{\partial z}{\partial \beta} - \frac{1+\zeta_1}{2} \frac{\partial z^*}{\partial \beta} + \frac{\zeta_2 q_1 \tau}{\rho_0 a_0^3 M_0^3} + \frac{f}{M_0} \right), & M_0 \rightarrow \infty, \\ i \left(\frac{3-M_0}{4} \frac{\partial z_1}{\partial \beta} - \frac{1+M_0}{4} \frac{\partial z_1^*}{\partial \beta} + \frac{(M_0-1)q_1 \tau}{4\alpha_1 \rho_0 a_0^3} + f \right), & M_0 \rightarrow 1, \end{cases} \quad (7.65)$$

where $\tau = a_0 M_0 t$ is a time-like length unit defined for convenience. The solution for z_1 can be obtained using a Fourier expansion in β ,

$$z_1(\beta, \tau) = \sum_{n=-\infty}^{\infty} \hat{z}_n(\tau) e^{in\beta}, \quad q_1(\beta) = \sum_{n=-\infty}^{\infty} \hat{q}_n e^{in\beta}, \quad f(\beta) = \sum_{n=-\infty}^{\infty} \hat{f}_n e^{in\beta}, \quad (7.66)$$

in both (7.65) and its complex conjugate. This yields the following second order ordinary differential equations for the Fourier coefficients \hat{z}_n ,

$$\frac{d^2 \hat{z}_n}{d\tau^2} = \begin{cases} -\zeta_1 n^2 \hat{z}_n + i \left[\frac{\zeta_2 (1-n\tau) \hat{q}_n}{\rho_0 a_0^3 M_0^3} - \frac{n \hat{f}_n}{M_0} \right], & M_0 \rightarrow \infty, \\ -\frac{M_0-1}{2} n^2 \hat{z}_n + i \left[\frac{(M_0-1)(1-n\tau) \hat{q}_n}{4\alpha_1 \rho_0 a_0^3} - n \hat{f}_n \right], & M_0 \rightarrow 1, \end{cases} \quad (7.67)$$

whose solutions are given by

$$\hat{z}_n = \begin{cases} A_n \cos(\sqrt{\zeta_1} n \tau) + B_n \sin(\sqrt{\zeta_1} n \tau) + i(C_n \tau + D_n), & M_0 \rightarrow \infty, \\ A_n \cos\left(\sqrt{\frac{M_0-1}{2}} n \tau\right) + B_n \sin\left(\sqrt{\frac{M_0-1}{2}} n \tau\right) + i(C_n \tau + D_n), & M_0 \rightarrow 1, \end{cases} \quad (7.68)$$

where A_n and B_n are constants to be determined from the initial shock shape $z_1(\beta, 0)$; and from the particular linear source term,

$$C_n = \begin{cases} \frac{-\zeta_2 \hat{q}_n}{\zeta_1 \rho_0 a_0^3 M_0 n^2}, \\ \frac{-\hat{q}_n}{2 \alpha_1 \rho_0 a_0^3 n}, \end{cases} \quad D_n = \begin{cases} \frac{\zeta_2 \hat{q}_n - \rho_0 a_0^3 M_0^2 n \hat{f}_n}{\zeta_1 \rho_0 a_0^3 M_0^3 n^2}, & M_0 \rightarrow \infty, \\ \frac{1}{2n^2} \left(\frac{\hat{q}_n}{\alpha_1 \rho_1 a_0^3} - \frac{4n \hat{f}_n}{M_0 - 1} \right), & M_0 \rightarrow 1. \end{cases} \quad (7.69)$$

Finally substituting (7.69) into (7.66) and subsequently (7.64) completes the general solutions for z_1 and m_1 .

It is now clear from Eqs. (7.69) and (7.64) that in the case of $q_1 = 0$, which corresponds to the zeroth-order GGSD model, initial shock perturbations undertake stable oscillations with fixed amplitude and frequency. Such linear analysis therefore does not capture the wave-reinforcing behaviour that could lead to the possible formation of a curvature singularity or shock-shocks found by Whitham [109] and Mostert *et al.* [78]. In contrast, incorporating first order correction, *i.e.*, $q_1 \neq 0$, in the GGSD system produces, in addition to the stable oscillations, a growth term that is linear in time for both the shock shape and Mach number perturbations. Hence the GGSD model suggests unbounded shock acceleration in the linear region, driven by the downstream non-uniformities. Since such growth is not physical, it is expected to be controlled by the non-linear effects of the model.

Chapter 8

**APPLICATIONS: FORMATION OF SHOCK CURVATURE
SINGULARITY**

In this chapter, we apply the GGSD models to investigate the stability of plane shocks with initial perturbations of two different origins: one due to an impulsively started corrugated piston, and another caused by shock traversing a density gradient. The evolution of shock perturbations in both cases are formulated as initial value problems (IVP) to be solved numerically. As the shocks evolve, curvature singularities evidenced by discontinuities in Mach number distributions are observed universally.

The GGSD approach is chosen over numerical solutions of the full Euler equations. Shock-capturing Euler methods contain their own shock modeling in the form of highly nonlinear artificial dissipation focused on the shock profile, making them a questionable choice for investigating the long-time evolution of tiny disturbances to a plane shock. A shock-fitting method would seem ideal but is difficult to implement at order sufficiently high to accurately capture spontaneous singularity formation.

8.1 Shock generated by a corrugated piston

We first consider the evolution and stability of a shock generated by an impulsively started piston of sinusoidal shape.

8.1.1 Base motion

The second shock considered in this study is produced by the impulsive motion of a piston from rest, whose velocity as a complex variable in the Y -direction is given by

$$U_p(t) = UH(t)e^{i\pi/2}, \quad (8.1)$$

where $U > 0$ is the constant speed that the piston gains and $H(t)$ is the Heaviside function. For a piston with flat surface located at $Y = 0$ moving into a uniform stationary medium, such impulse in the limit of $U \rightarrow \infty$ or $U \rightarrow 0$ generates a normal plane shock of constant Mach number,

$$M_0 = \begin{cases} \frac{U}{\alpha_1 a_0}, & M \rightarrow \infty, \\ 1 + \frac{U}{2a_0\alpha_1}, & M \rightarrow 1, \end{cases} \quad (8.2)$$

after applying the strong and weak shock limits of the RH conditions [equations (7.40) and (7.41)]. The base motion of the shock in the form of (7.33) is

thus established, namely,

$$Z_0 = \beta + ia_0M_0t. \quad (8.3)$$

It is noted that for $t > 0$, the shock-processed flow between the piston and shock front is uniform with velocity also given by (8.1). Additionally, it is safe to write dimensionless variables $a_0 = \rho_0 = 1$ if the constant upstream density and sound speed are chosen as references.

8.1.2 Initial values for Z and M

Next, a cosine perturbation of small amplitude $\epsilon \ll 1$ is imposed to the piston surface. Freeman [31] showed that the corresponding shock generated by such corrugated piston must have the same initial shape profile as the piston surface. Therefore, at $t = 0^+$, the shock shape is prescribed as

$$Z(\beta, 0^+) = Z_0(\beta, 0^+) + z(\beta, 0^+) = \beta + i\epsilon \cos(\beta). \quad (8.4)$$

In order to obtain the initial Mach number distribution of this curved shock produced by the same piston impulse (8.1), it is noted that along the infinitely thin layer of fluid sandwiched between the piston and shock at $t = 0^+$, only the piston velocity component locally normal to the boundary is transferred into the fluid, whereas the tangential component slips through the fluid under the present Euler description. Therefore in the laboratory frame where the piston velocity (8.1) is measured, the initial boundary fluid velocity distribution follows as the projection of piston velocity onto the unit normal vector given in (7.34), leading to

$$u_0 \equiv u(\beta, 0^+) = \begin{cases} \frac{\alpha_1 M_0}{\sqrt{\epsilon^2 \sin^2(\beta)+1}}, & M_0 \rightarrow \infty, \\ \frac{2\alpha_1(M_0-1)}{\sqrt{\epsilon^2 \sin^2(\beta)+1}}, & M_0 \rightarrow 1, \end{cases} \quad (8.5)$$

where the base motion Mach number M_0 found in (8.2) is used as the input parameter. Because the shock curve coincides with the piston surface at $t = 0^+$, the normal RH conditions can be applied again to convert (8.5) into the required initial values of Mach number,

$$M(\beta, 0^+) = \begin{cases} \frac{M_0}{\sqrt{\epsilon^2 \sin^2(\beta)+1}}, & M_0 \rightarrow \infty, \\ 1 + \frac{M_0-1}{\sqrt{\epsilon^2 \sin^2(\beta)+1}}, & M_0 \rightarrow 1. \end{cases} \quad (8.6)$$

A schematic comparison between shocks generated by flat and corrugated pistons is shown in figure 8.1, where the infinitesimal layer of shock-processed flow attached to the piston boundary at $t = 0^+$ is illustrated with kinematic quantities including acceleration and jerk that are discussed in the next section.

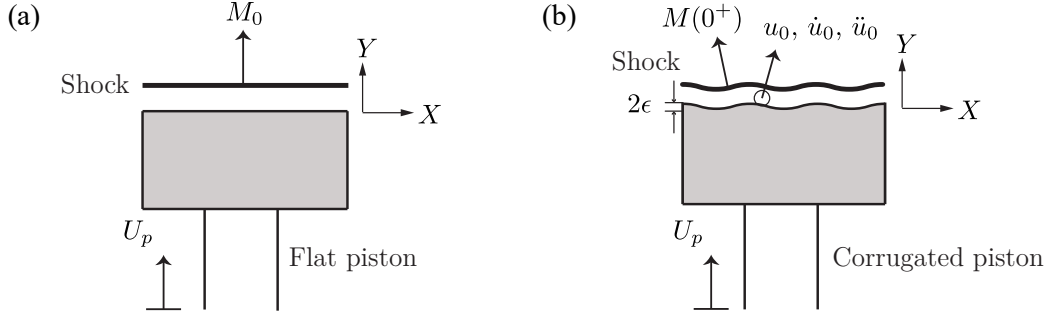


Figure 8.1: Shock generated by a flat piston shown in (a), and a corrugated piston of perturbation amplitude ϵ shown in (b), at time $t = 0^+$. Both pistons share the same velocity U_p , giving a constant Mach number M_0 when the piston is flat. In (b) the Mach number profile is $M(\beta, 0^+)$. The flow between the piston and the shock is uniform in (a), but non-uniform with initial velocity u_0 , acceleration \dot{u}_0 , and jerk \ddot{u}_0 in (b).

8.1.3 Initial values for Q_1 and Q_2

To complete the GGSD initial value problem formulation for the piston-generated shock, it remains to determine Q_1 and Q_2 at $t = 0^+$. This is achieved by utilising two kinematic conditions of the boundary flow, about its initial acceleration \dot{u}_0 and jerk \ddot{u}_0 in the shock normal direction. For each β , these quantities take the form of a full derivative moving with the piston,

$$\dot{u}_0(\beta) = u_t(\beta, 0^+) + u_0 u_x(\beta, 0^+), \quad (8.7a)$$

$$\ddot{u}_0(\beta) = \left. \frac{\partial(u_t + uu_x)}{\partial t} \right|_{t=0^+} + u_0 \left. \frac{\partial(u_t + uu_x)}{\partial x} \right|_{t=0^+}, \quad (8.7b)$$

where u_0 is derived in (8.5), and the first and second order derivatives of u are given in Eqs. (F.11)–(F.14) and (F.15)–(F.18), respectively, in Appendix F.

Expanding (8.7a) using (F.12a) and (F.12b), while in the strong shock case expressing M' in terms of Q_1 via (7.48) leads to the initial values for Q_1 ,

$$Q_1(\beta, 0^+) = \begin{cases} \frac{M(\beta, 0^+)^2}{\zeta_2} \left[\zeta_1 \Phi M + \frac{4\gamma M(u_0 - 1)\Phi + (\gamma + 1)^2 \dot{u}_0}{2(\gamma + 1)(4M - 3u_0)} \right]_{t=0^+}, & M_0 \rightarrow \infty, \\ \frac{4(M - 1)\Phi(-2\gamma + (3\gamma - 1)u_0 + 2) + 2(\gamma + 1)^2 \dot{u}_0}{(\gamma + 1)^2(2M - u_0 - 1)} \Big|_{t=0^+}, & M_0 \rightarrow 1, \end{cases} \quad (8.8)$$

where in both limits, $\Phi|_{t=0^+}$ can be evaluated from its definition (7.39) using the initial shock profile (8.4) as

$$\Phi(\beta, 0^+) = \frac{\epsilon \cos(\beta)}{(\epsilon^2 \sin^2(\beta) + 1)^{3/2}}. \quad (8.9)$$

Substituting (8.5), (8.6) and (8.9) into (8.8) completes the expression. Specifically, evaluating $Q_1(\beta, 0^+)$ at $\epsilon = 0$ shows

$$Q_1(\beta, 0^+) |_{\epsilon=0} = \begin{cases} \frac{(\gamma+1)M_0\dot{u}_0(\beta)}{(8-6\alpha_1)\zeta_2}, & M_0 \rightarrow \infty, \\ \frac{2\dot{u}_0(\beta)}{1-2(\alpha_1-1)(M_0-1)}, & M_0 \rightarrow 1. \end{cases} \quad (8.10)$$

As discussed in Sec. 8.1.1, the unperturbed flow between the piston and shock is uniform, implying that $Q_1(\beta, 0^+) |_{\epsilon=0} = 0$ for all β . Therefore it is concluded that $\dot{u}_0(\beta) = 0$, that is, the initial boundary flow is acceleration free. Hence $Q_1(\beta, 0^+)$ simplifies to yield the following leading order behaviour as $\epsilon \rightarrow 0$,

$$Q_1(\beta, 0^+) \sim \begin{cases} \frac{M_0^3 \epsilon \cos(\beta) [\alpha_1(3(\gamma+1)\zeta_1 - 2\gamma) - 4(\gamma+1)\zeta_1]}{(3\alpha_1 - 4)(\gamma+1)\zeta_2}, & M_0 \rightarrow \infty, \\ \frac{8(M_0-1)\epsilon(1-\gamma)\cos(\beta)}{(\gamma+1)^2}, & M_0 \rightarrow 1. \end{cases} \quad (8.11)$$

We note that our conclusion that the initial boundary flow along the piston surface has zero acceleration, with consequence (8.11), does not involve truncation error associated with the GGSD systems. Instead the presence of the Q_1 correction in the evolution equation of M allows its initial condition to be inferred without knowledge of higher order corrections $Q_{i \geq 2}$.

Next, from the kinematic condition of Eq. (8.7b), the initial jerk of flow between the piston surface and the shock is related to the initial values of partial derivatives u_t , u_x , u_{tt} , u_{tx} and u_{xx} given in Eqs. (F.11)–(F.14) and (F.15)–(F.18). Particularly in the strong shock limit, the M' and M'' dependency of these derivatives can be expanded using (7.48) and (7.57) to give expressions in terms of M , Q_1 , Q_2 , Φ and Ψ . As a result, solving Eq. (8.7b) for Q_2 and evaluating at $t = 0^+$ gives for $M \rightarrow \infty$,

$$Q_2(\beta, 0^+) = \left\{ -\zeta_2 \left[\Phi \left(\iota_1 M^2 + \iota_2 u_0^2 + \iota_3 u_0 M \right) M^3 Q_1 - \left(\iota_4 u_0^2 - \iota_5 M^2 + \iota_6 u_0 M \right) Q_1^2 \right] \right. \\ \left. - M^6 \left[\left(\iota_7 \Phi^2 + 2\iota_8 \Psi \right) u_0 M + \left(\iota_9 \Phi^2 + \iota_{10} \Psi \right) M^2 + \left(\iota_{11} \Phi + \iota_{12} \Psi \right) u_0^2 \right] \right. \\ \left. + M^5 \ddot{u}_0 \right\} \Big|_{t=0^+} / \left[\zeta_2 \gamma_4 M^2 \left(\omega_{11} M^2 + 2\omega_{16} u_0 M + \omega_{41} u_0^2 \right) \right] \Big|_{t=0^+}, \quad (8.12)$$

where $\iota_{1,2,\dots,12}$ and $\omega_{11,16,41}$ are coefficients given in Table E.2, Appendix E. Here the initial value of Ψ remains to be determined. This is achieved by substituting the perturbed shock profile (8.4), together with $\Phi(\beta, 0^+)$ found in (8.9), into its definition (7.53), implying

$$\Psi(\beta, 0^+) = -\frac{\epsilon^2 \sin^2(\beta) (\epsilon^2 \cos(2\beta) + 2\epsilon^2 + 1)}{(\epsilon^2 \sin^2(\beta) + 1)^3}. \quad (8.13)$$

Similarly for the weak shock limit, expanding (8.7b) and solving for Q_2 directly gives for $M \rightarrow 1$,

$$Q_2(\beta, 0^+) = \frac{2\ddot{u}_0}{(u_0 - 1)^2} + \frac{4(3\gamma - 1)\Phi(M - 1) + (\gamma + 1)^2 Q_1}{2(\gamma + 1)^4 (u_0 - 1)^2} \Big|_{t=0^+} \left\{ (\gamma + 1)^2 Q_1 \right. \\ \left. \times (2(M - 1) - u_0 + 1) + 4\Phi(M - 1) [2(\gamma - 1) - (3\gamma - 1)u_0] \right\}_{t=0^+}. \quad (8.14)$$

Now substituting (8.6), (8.8), (8.9) and (8.13) into both of (8.12) and (8.14) prepares the full expression of $Q_2(\beta, 0^+)$ in terms of the parameters M_0 , ϵ and $\ddot{u}_0(\beta)$. Setting $\epsilon = 0$ then produces

$$Q_2(\beta, 0^+) |_{\epsilon=0} = \begin{cases} \frac{M_0 \ddot{u}_0}{\gamma_4 \xi_2 (\omega_{11} + 2\alpha_1 \omega_{16} + \alpha_1^2 \gamma_4)}, & M_0 \rightarrow \infty, \\ \frac{2(\gamma+1)^2 \ddot{u}_0}{(5+\gamma-4M_0)^2}, & M_0 \rightarrow 1, \end{cases} \quad (8.15)$$

which must vanish as required by the unperturbed uniform flow condition. Therefore one demands $\ddot{u}_0 = 0$, suggesting that the initial flow attached to the piston has zero acceleration and jerk. Finally, for small ϵ , Eqs. (8.12) and (8.14) are Taylor expanded to give the following asymptotic form of $Q_2(\beta, 0^+)$,

$$Q_2(\beta, 0^+) \sim \begin{cases} (\xi_1 \cos^2(\beta) + \xi_2 \sin^2(\beta)) M_0^4 \epsilon^2, & M_0 \rightarrow \infty, \\ -\frac{32\gamma \cos^2(\beta)(M_0-1)^3 \epsilon^2}{(\gamma+1)^3}, & M_0 \rightarrow 1, \end{cases} \quad (8.16)$$

where ξ_1 and ξ_2 are coefficient functions of γ tabulated in Table E.2, Appendix E.

With initial conditions served by Eqs. (8.4), (8.6), (8.11) and (8.16), evolution of the shock generated by the perturbed piston can be tracked by the GGSD systems up to second order, by integrating in time the system of equations (7.55) and (7.58) for weak and strong shocks, respectively. While at $t = 0$, the initial values for M , Q_1 , and Q_2 can be obtained faithfully from the full 2D Euler equations, the GGSD construction does not directly propagate additional flow disturbances due to the piston motion, and carried by the C^+ characteristics when $t > 0$. Our adoption of the GGSD theory therefore assumes that perturbations caused by the corrugated piston after the initial impulse are small and smooth, while sufficiently far from the piston wall, the shock dynamics is mainly controlled by the intrinsic nonlinearity of its free propagation. The question of whether shock motion predicted by the GGSD systems as a function of time converge to the true solution for the Euler equations when the GGSD system order increases remains open until a direct comparison can be made.

8.1.4 Numerical results

We describe numerical simulations of the initial-value problem formulated in Sec. 8.1 for the specific heat ratio fixed at $\gamma = 5/3$. Spatial derivatives with respect to β in the GGSD systems are discretised using a fourth-order compact finite difference scheme [55], for its ability to capture traveling waves and pseudo-spectral convergence, on a uniform grid in β of size $N = 2048$. The spectral method is not used owing to large aliasing errors produced to the high order nonlinearities in the systems. Time integration is performed with a variable time-stepping fourth-order Runge-Kutta method (RK4). All results are presented using the length unit $\tau = a_0 M_0 t$ for time measurement, as τ corresponds to the distance traveled by an unperturbed shock at any given time t .

If the shock profile remains smooth we expect that $M(\beta, t)$, $z(\beta, t)$ will remain a single-valued functions with bounded derivatives. We consider that a singularity has appeared at a time when an unbounded derivative in any quantity, of any order has developed. As the systems evolve an edge-detection algorithm [36] that searches for discontinuities on discrete data is applied on the data set representing $M(\beta, t)$. A brief outline of the algorithm is given in Appendix G. Detection of an “edge” in the discrete $M(\beta, t)$ at some $t = t_c$ is interpreted to indicate the presence of an infinite $\partial M/\partial\beta$ corresponding to “overturning”, and hence a singularity in the GGSD solution. This will generally also indicate the occurrence of curvature singularities in the shock shape Z [77, 78]. For each set of given initial values, varying the choices of the two required tuning parameters q and J_{crit} [see Eqs. (G.7) and (G.8) in Appendix G] leads to less than 2% variations in estimating t_c compared to the reported t_c values obtained using $q = 1.1$ and $J_{\text{crit}} = 1$.

For $t > t_c$, the numerical solution for $M(\beta, t)$ quickly develops rapid oscillations around the jump location. The spatial derivatives, $\partial M/\partial\beta$ and $\partial^2 M/\partial\beta^2$, can no longer be accurately captured by the compact finite-difference method. Proper continuation of the shock evolution for $t > t_c$ would require the insertion of a shock-shock into the GGSD shock-evolution description, much as in done following shock formation for the Euler equations [27]. Our present interest is evolution up to $t = t_c$ only and so this is not done presently. It is demonstrated in the sequel that all three GGSD systems, the zeroth, first and second order, predict spontaneous development of curvature singularities on the shock shape at a finite time that is inversely proportional to the small initial perturbation size ϵ . The critical time at which singularity occurs converges within the GGSD hierarchy as the order of

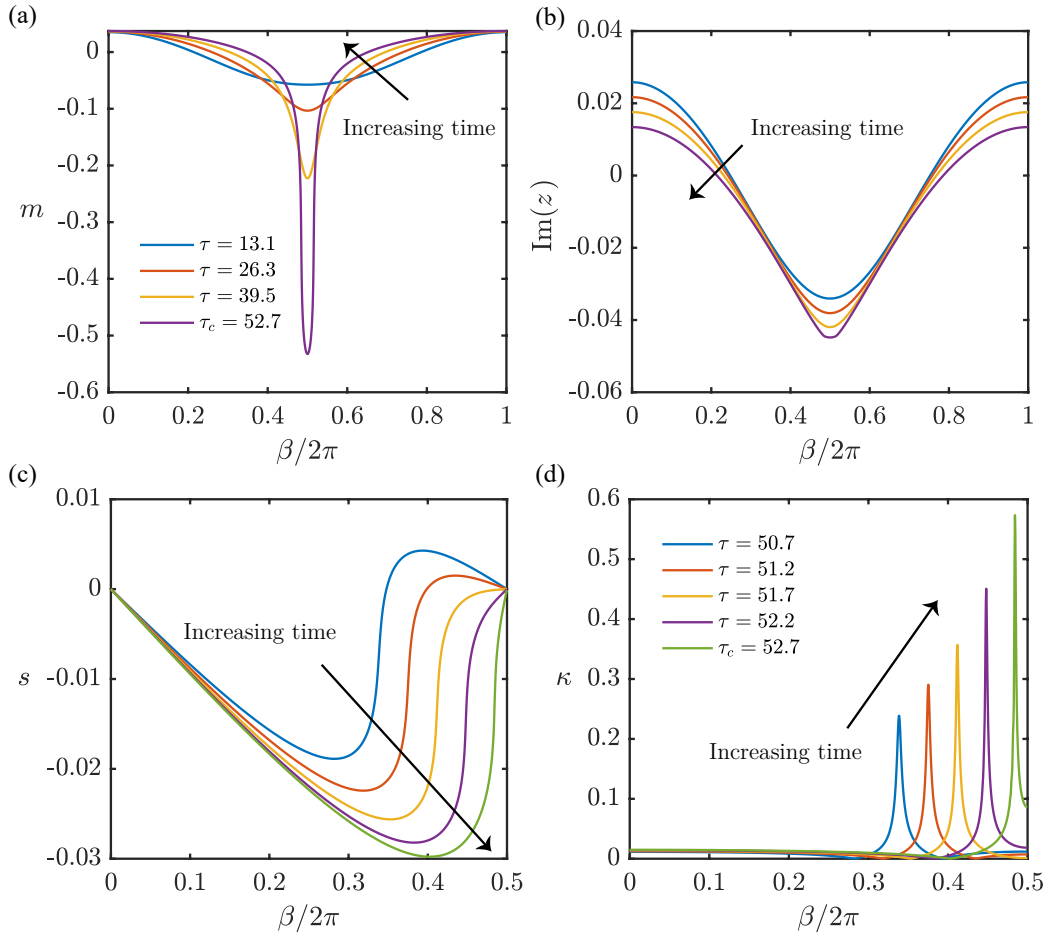


Figure 8.2: Spontaneous development of curvature singularities illustrated using GGSD-0 with initial conditions $M_0 = 50$ and $\epsilon = 0.03$. The Mach number and shock shape perturbation profiles are given over four oscillation periods up to the critical time in (a) and (b), respectively. The shock slope and curvature distributions are shown as the critical time is approached with time increments of $\Delta\tau = 0.5$, in (c) and (d), respectively.

systems increases.

Spontaneous singularity formation

We first show the perturbation profiles of mach number m , and shock shape z as a function of the ray-tube marker β in figure 8.2(a) and (b), respectively, for successive times obtained using GGSD-0 with initial piston Mach number $M_0 = 50$ and perturbation amplitude $\epsilon = 0.03$. Here, curves of different times are separated by the period of the fundamental linear mode in Eq. (7.68), *i.e.*, $\Delta\tau = 1/\sqrt{\zeta_1} = 13.2$, up to the critical time, $t_c = 52.7$, when discontinuities in m are detected by the

edge-detection algorithm. As time increases, it is seen in figure 8.2(a) that the symmetric m distribution steepens in each oscillation cycle, and correspondingly in figure 8.2(b), the normal shock displacement given by $\mathfrak{I}(z)$ evolves towards the formation of two kinks. Because the lateral displacement $\mathfrak{R}(z)$ is a continuous function of β , the observed loss of continuity in m and smoothness in z also occur spatially in terms of shock positions Z . In a closer look, figure 8.2(c) and (d) employ a smaller time interval $\Delta\tau = 0.5$ within one period for the same parameters $M_0 = 50$, $\epsilon = 0.03$ to show leading up to the critical time, the evolution of shock slope s , calculated as $s = \mathfrak{I}(\partial Z/\partial\beta)/\mathfrak{R}(\partial Z/\partial\beta)$; and curvature κ , identified as $\kappa = \Phi$ thanks to Eqs. (7.22) and (7.44). We see that near the critical time, s is everywhere finite but approaching a discontinuity at the point where κ appears to form a singularity. These results are consistent with the findings of Mostert *et al.* [78], where the Whitham's original GSD equations are applied to a hypothetical initial value problem for a plane shock with a single Mach number perturbation.

Although the example given here is obtained using GGSD-0, the character of the spontaneous curvature singularity development is similarly found for GGSD-1 and GGSD-2. It is thus suggested that the “shock-shock” mechanism described by Whitham [109], where nonlinear compression waves propagating along the shock, reinforcing each other to the formation of discontinuities, also holds in the present study where a global A – M relation breaks down and non-uniform effects of the flow immediately behind the shock are accommodated.

Next, typical weak and strong shocks' evolving trajectories for $0 \leq \tau \leq \tau_c$, predicated by the three GGSD systems are presented in figure 8.3 for both a weak shock with $M_0 = 1.1$, $\epsilon = 0.05$ [8.3(a)–(c)] and a strong shock with $M_0 = 10$, $\epsilon = 0.05$ [8.3(d)–(f)]. A transition of the amplified shock shape from its smooth initial value to a non-differentiable profile with two cusps at critical time is observed in all cases shown. The oscillatory shock shape patterns given by GGSD-0 are evident in both limits, with oscillation frequencies that match the linear analysis of fundamental mode in Eq. (7.68), *i.e.*, $\omega = \sqrt{\zeta_1}$ in the strong shock limit ($M_0 = 10$) and $\omega = \sqrt{(M_0 - 1)/2}$ in the weak shock limit ($M_0 = 1.1$). Comparing the GGSD models of different orders, differences in the detailed trajectories are small for $M_0 = 1.1$, noting that the values for τ_c are also close to each other. This suggests that in the weak shock limit, the non-uniform effect behind the shock is small and that GGSD-0 provides a good approximation.

In contrast, with $M_0 = 10$, the first and second order systems predict very similar

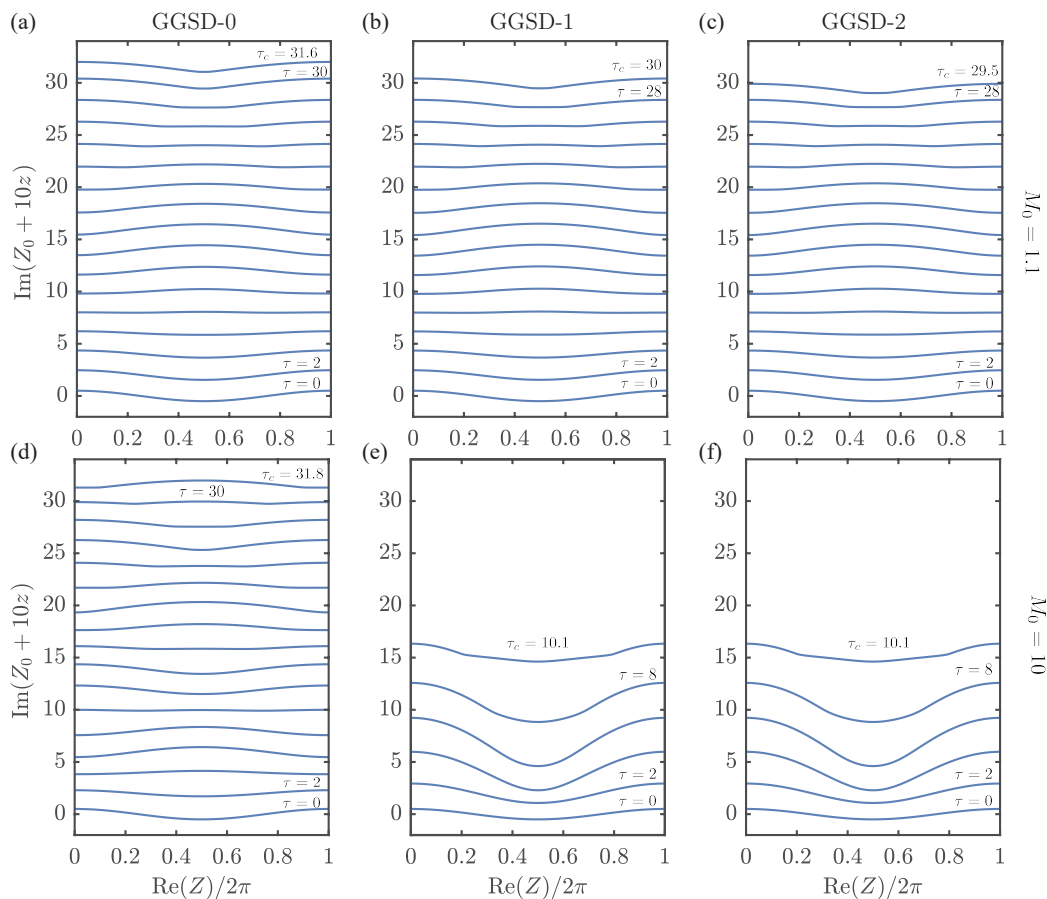


Figure 8.3: Shock trajectories with perturbation in the Y -direction amplified ten times for piston perturbation size $\epsilon = 0.05$. The initial piston Mach number is $M_0 = 1.1$ in (a)–(c) and $M_0 = 10$ in (d)–(f), corresponding to results obtained from the zeroth, first, and second order GGSD systems, respectively. In each panel, successive trajectories are shown in increments of $\Delta\tau = 2$, up to the final curve given at the critical time τ_c .

trajectories with almost the same τ_c that is significantly shorter than the zeroth-order value. In this case, evolution of the Mach number perturbation m is further investigated in figure 8.4 using the same parameters $M_0 = 10$ and $\epsilon = 0.05$, where the profiles of m along the shock are shown for the entire history of the shock trajectories. The nonlinear solution of GGSD-0 seen in figure 8.4(a) again shows the oscillatory pattern that is consistent with the corresponding linear theory, noting that stable oscillation in time is here terminated by the onset of discontinuities in m owing to reinforcing waves on the shock. In contrast, for GGSD-1 and GGSD-2 where linear analysis predicts a growth that is linear in time, the Mach number profiles in figure 8.4(b) and (c) demonstrate that the underlying oscillations are dominated

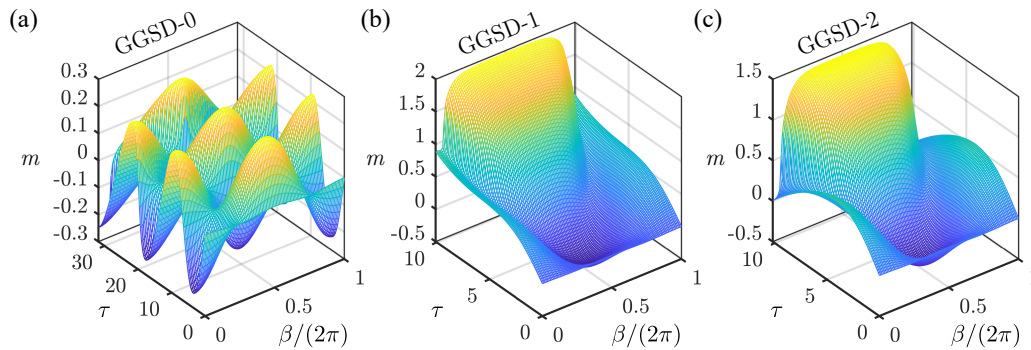


Figure 8.4: History of Mach number perturbation profile m along the evolving shock, for $\epsilon = 0.05$ and $M_0 = 10$. Results obtained using three different orders of GGSD models are shown in (a)–(c).

by approximately linear growth, until nonlinear effects accumulate, leading to m -discontinuities at the critical time. This result shows that the initial and subsequent downstream non-uniformity plays a crucial role in determining the shock motion.

Critical time

Figure 8.5 shows τ_c given by the three GGSD systems as a function of the piston perturbation ϵ , in both strong [figure 8.5(a,b)] and weak [figure 8.5(c,d)] shock limits. First, in agreement with the observation made from figure 8.3, the strong shock limit sees a dramatic reduction in τ_c comparing GGSD-0 to the other two higher order models, while GGSD-1 and GGSD-2 appear to have converged within the GGSD framework in terms of their τ_c predictions. The weak-shock limit shows much smaller differences between the three models. When at least the Q_1 correction is considered in the equations, for the cases shown here with initial Mach number $M_0 = 10$ and $M_0 = 50$, the decrease in τ_c is found to be over 50% across all simulations with varying ϵ . For $M_0 = 1.1$ and $M_0 = 1.02$ a decrease in τ_c is still consistently present, although the magnitude falls within the uncertainties of the edge-detection algorithm. On the other hand, the difference made by further including the Q_2 correction in GGSD-2 is insignificant for all M_0 simulated. These results provide convincing evidence for the convergence of the GGSD hierarchy and showcase the power of higher-order methods in handling shocks that lead to a strongly non-uniform flow, whose effect seems to increase with Mach number.

An intuitive explanation of the GGSD hierarchy convergence in this application can be offered by comparing the order of magnitude estimates made for Q_1 and Q_2 when

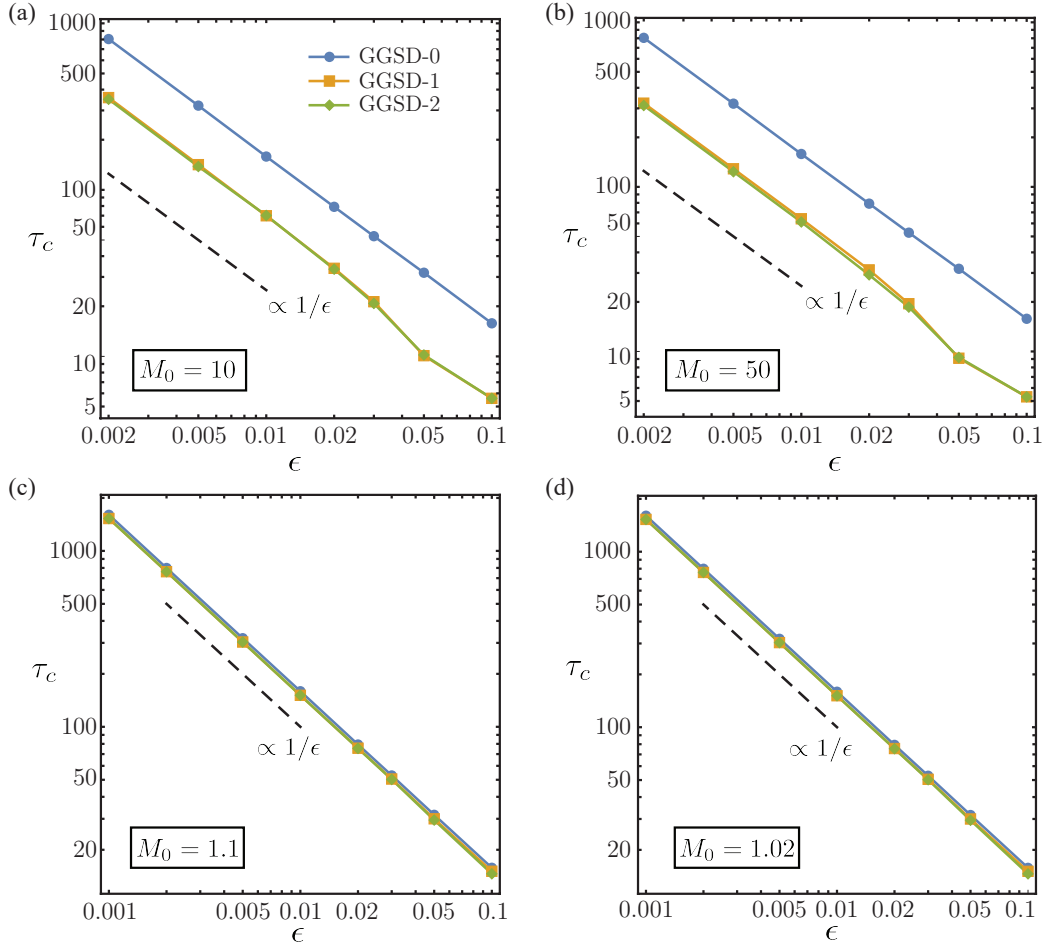


Figure 8.5: Critical times in strong and weak shock limits given for (a) $M_0 = 10$, (b) $M_0 = 50$, (c) $M_0 = 1.1$ and (d) $M_0 = 1.02$. In all four cases, results obtained using GGSD-0 are shown as disks, GGSD-1 as squares and GGSD-2 as diamonds. In each panel, the dashed line without markers displays a reference function that has inverse power law of degree one.

deriving the GGSD equations, to the independently calculated initial values of Q_1 and Q_2 . In Sections 7.5.2 and 7.5.3, it was shown that $Q_1 \gtrsim O(\epsilon^0)$, $Q_2 \gtrsim O(1/\epsilon)$ as $\epsilon = M - 1 \rightarrow 0$, and $Q_1 \gtrsim O(M^3)$, $Q_2 \gtrsim O(M^4)$ as $M \rightarrow \infty$, in order to retain the corresponding Q_1 and Q_2 corrections in the leading order dominant balance. Meanwhile, as $\epsilon \rightarrow 0$, the initial conditions for Q_1 and Q_2 , obtained in Sec. 8.1.3 without the GGSD truncation error, are $Q_1 \sim \epsilon(M_0 - 1)$, $Q_2 \sim \epsilon^2(M_0 - 1)^3$ as $M_0 \rightarrow 1$ and $Q_1 \sim \epsilon M_0^3$, $Q_2 \sim \epsilon^2 M_0^4$, as $M_0 \rightarrow \infty$. As a result, the initial condition that best matches its minimum order of magnitude required by the asymptotic GGSD equations is that of Q_1 in the strong shock limit, where indeed the effect of Q_1 on τ_c is shown the largest.

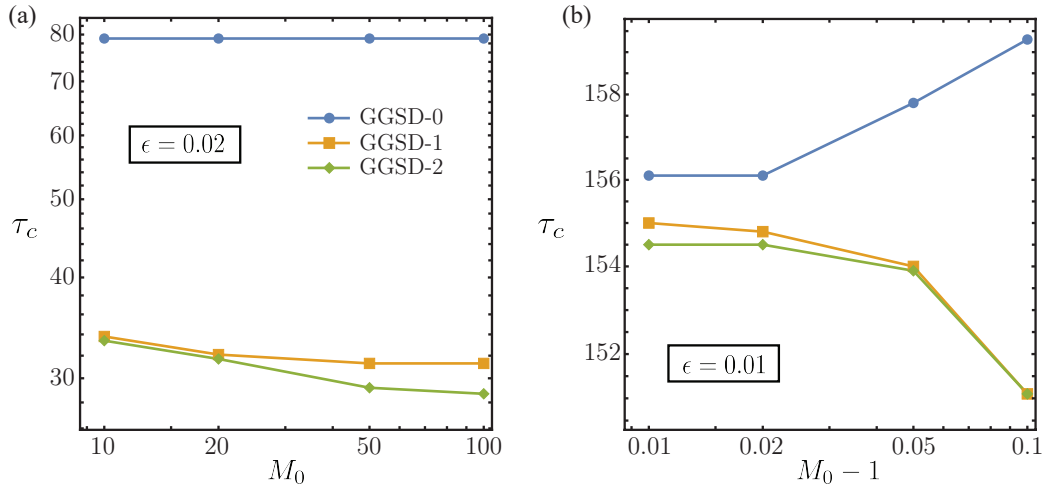


Figure 8.6: Convergence of critical time as M_0 increases in the strong shock limit for $\epsilon = 0.02$ in (a), and as M_0 decreases in the weak shock limit for $\epsilon = 0.01$ in (b). Disks, squares, and diamonds correspond to GGSD-0, GGSD-1, and GGSD-2 data.

Another finding of interest from figure 8.5 is that all three GGSD methods show a critical time $\tau(\epsilon)$ as inversely proportional to the initial perturbation size ϵ for sufficiently small ϵ , for all Mach numbers M_0 . A suggested form is

$$\tau_c = \tau_c(\epsilon, M_0; d) = \frac{K_1(M_0; d)}{\epsilon}, \quad (8.17)$$

where K_1 is a proportionality constant that depends on M_0 and the order of the GGSD models, $d \in \{0, 1, 2\}$. Together with the similar analytic form obtained by Mostert *et al.* [78], the present results, including the established connection between the GGSD hierarchy and the Euler equations, provides compelling evidence that (8.17) is a universal form for perturbed planar shock waves.

From a computational perspective we note that in figure 8.5, the smallest ϵ achieved in the strong shock limit is $\epsilon = 0.002$, doubling $\epsilon = 0.001$ in the weak shock limit. This is because an explicit time integration method such as RK4 appears to be unstable and costly for further reduction in ϵ . An implicit method might be preferred should results for $\epsilon < 0.002$ and $M \gg 1$ be desired. This is not done presently owing to the associated high cost of iteratively solving order N nonlinear equations at each time step.

To illustrate that the choice of M_0 in figure 8.5 adequately represent the strong and weak shock limits, figure 8.6 plots τ_c for two sequences of extreme values of M_0 , obtained for $\epsilon = 0.02$ when $M_0 \gg 1$ and $\epsilon = 0.01$ when $M_0 - 1 \ll 1$, in all three

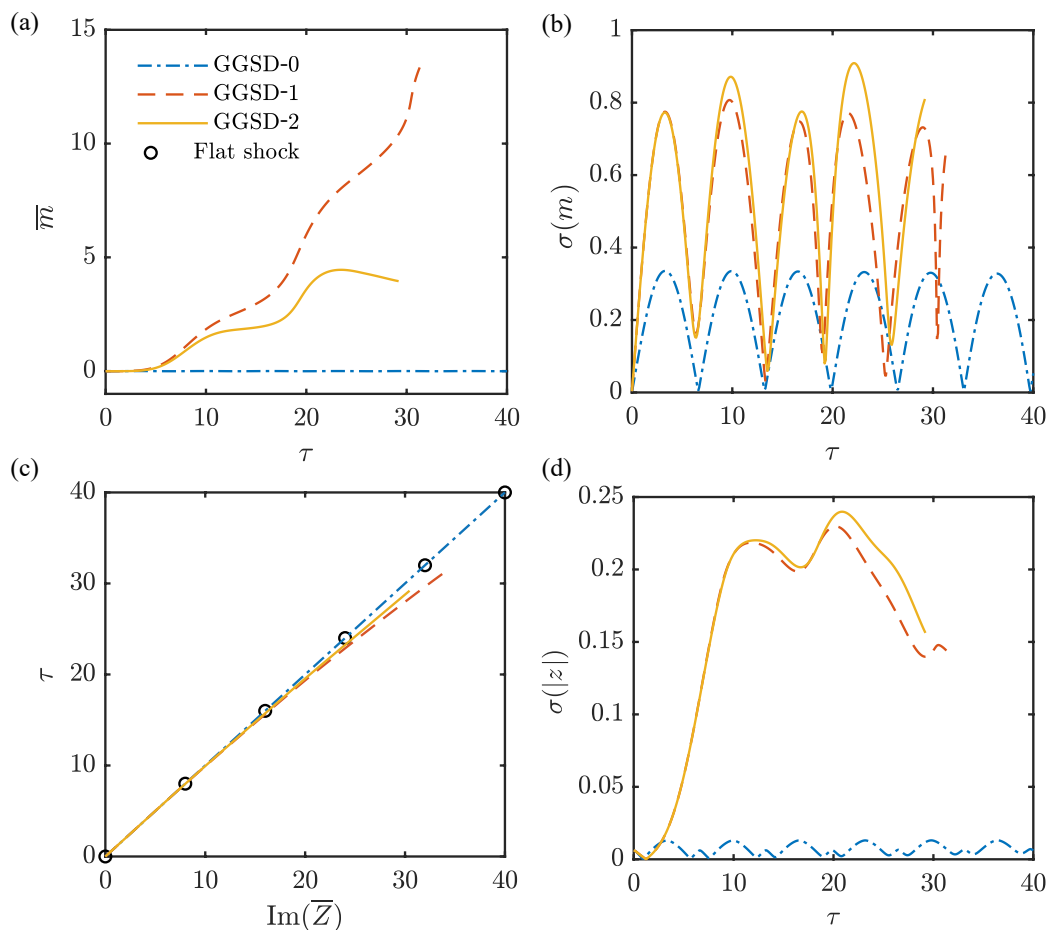


Figure 8.7: Temporal shock profile statistics comparison between the flat (hollow circles) and perturbed shock due to three GGSD systems (lines of different dashing), made for $M_0 = 50$ and $\epsilon = 0.02$. (a,b) Mean and standard deviation of the Mach number perturbation profile. (c) Average shock advancement in the unperturbed shock normal direction. (d) Standard deviation of the shock shape perturbation.

GGSD systems. Convergence in τ_c is clear as $M_0 > 50$ and $M_0 - 1 < 0.02$ for strong and weak shocks, respectively.

Diagnostic statistics

We have seen in figure 8.3 that the GGSD-1 and GGSD-2 in the strong shock limit produce distinctly interesting shock trajectories before curvature singularities form. Figure 8.7 therefore presents the key statistics that characterises the evolution given by these higher order methods up to their critical times using $M_0 = 50$ and $\epsilon = 0.02$. The mean and standard deviation of Mach number perturbation over the shock,

defined as

$$\bar{m} = \frac{1}{2\pi} \int_0^{2\pi} m d\beta, \quad \sigma(m) = \left(\frac{1}{2\pi} \int_0^{2\pi} (m - \bar{m}) d\beta \right)^{1/2}, \quad (8.18)$$

are shown in figure 8.7 (a) and (b), respectively. It is observed that GGSD-0 gives an oscillating Mach number perturbation profile around the mean, that is zero, across the profile, for all time until a discontinuity develops (critical time not shown for the dotted dash lines in the figures). GGSD-1 and GGSD-2 both produce on average an upward drift for m over time, where the increase is smaller with GGSD-2. This is consistent with the linear analysis in Sec. 7.5.5, where Eqs. (7.64) and (7.69) clearly states the linear growth. Whether this mean drift will further reduce with increasing order of the GGSD systems, or if it faithfully represents the Euler equations, remains to be confirmed by direct comparisons against direct numerical simulations of the full Euler equations with high-order accurate shock tracking. Nevertheless, despite the mean rise, the standard deviation of m obtained from GGSD-1 and GGSD-2 shows qualitatively similar periodic fluctuations that do not grow in times, as seen in GGSD-0.

Further, as a consequence of the positive Mach number perturbation increasing, the shock trajectories given by the higher order methods must be accelerating at an increasingly faster rate compared to either the unperturbed flat shock, or the GGSD-0 prediction. Indeed, this is reflected in the figure 8.7(c) where the mean shock advancement, $\mathfrak{I}(\bar{Z})$, is plotted as a function of τ . As expected from $\bar{m} = 0$, the zeroth order GGSD system yields a history of mean shock positions that is exactly the same as the unperturbed shock; whereas with an increasing positive \bar{m} , the mean shock position given by GGSD-1 and GGSD-2 accelerate and outrun the flat shock. Particularly, the Q_2 correction made by GGSD-2 to GGSD-1 partially negates the Q_1 correction applied by GGSD-1 to GGSD-0. Additionally, figure 8.7(d) shows that although the standard deviation $\sigma(|z|)$, defined analogously to Eq. (8.18), is significantly larger in GGSD-1 and GGSD-2 compared to GGSD-0, the shock shape perturbations remain bounded.

The negation effect of GGSD-2 is related to the measure of immediate non-uniformity Q_1 shown in figure 8.8, as a function of the evolving shock position in the complex plane for the same parameters $M_0 = 50$ and $\epsilon = 0.02$. Identically zero in GGSD-0, the evolution of non-zero Q_1 in the higher-order models has been demonstrated to provide a considerable Mach number correction. Specifically, comparing figure 8.8(a) and (b), the overall larger increase of Q_1 given by GGSD-1

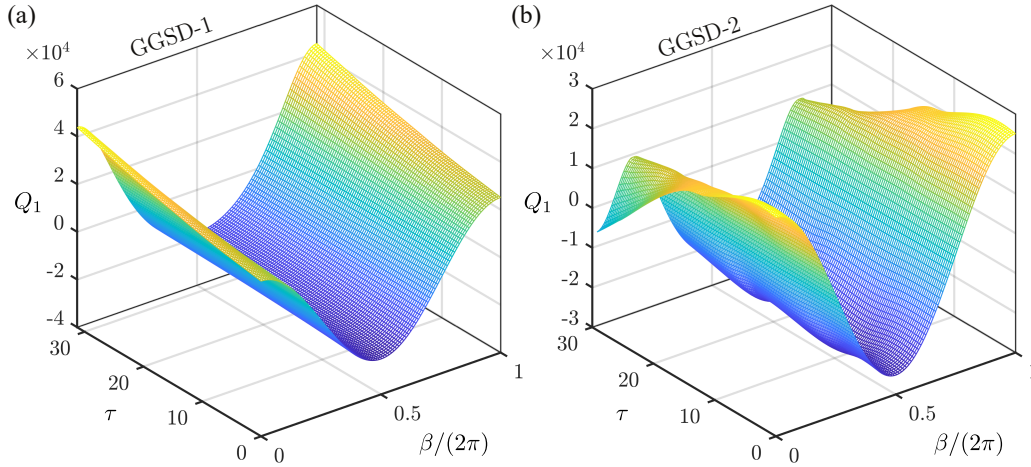


Figure 8.8: History of the non-uniformity measure Q_1 behind the evolving shock as a function of shock positions in two-dimensions. (a) and (b) compare results obtained for $M_0 = 50$ and $\epsilon = 0.02$, using GGSD-1 and GGSD-2, respectively.

than GGSD-2, especially the fact that when the critical time is approached Q_1 actually decreases in GGSD-2, matches the different growth rates of \bar{m} observed in figure 8.7(a).

Curiously, referencing figure 8.7(b), the distance gap between mean shock position predicted by GGSD-1 and GGSD-2 is further examined in figure 8.9. Denoting ΔY as the lead distance, its maximum obviously occurs at the critical time of each model. The percentage of $\max(\Delta Y)$ over the advancement of the reference flat shock, which also equals τ_c by definition, is shown in figure 8.9(a) as a function of ϵ . A converging result of approximately 9.5% for GGSD-1 and 4.5% for GGSD-2 is found, noting that $\max(\Delta Y)/\tau_c$ is overall weakly dependent on the simulated range of ϵ . More interestingly, examining ΔY at a given time τ that is at most the earliest critical time among different models, *i.e.*, $\tau < \min_{d \in \{0,1,2\}}(\tau_c(M_0; d))$, for instance choosing $\tau = \tau_c(0.03, 50; 2) = 18.6$ as shown in figure 8.9(b), reveals a quadratic scaling law with respect to ϵ which holds for both GGSD-1 and GGSD-2, that is,

$$\Delta Y|_{\tau} = K_2(M_0; d)\epsilon^2, \quad (8.19)$$

where again K_2 is the constant multiplier that depends on M_0 and order number $d \in \{1, 2\}$.

In order to enable such distance lead obtained using higher order methods over a flat shock, the flow behind the shock must gain more kinetic energy from the corrugated piston advancing, than for the flat piston whose motion is

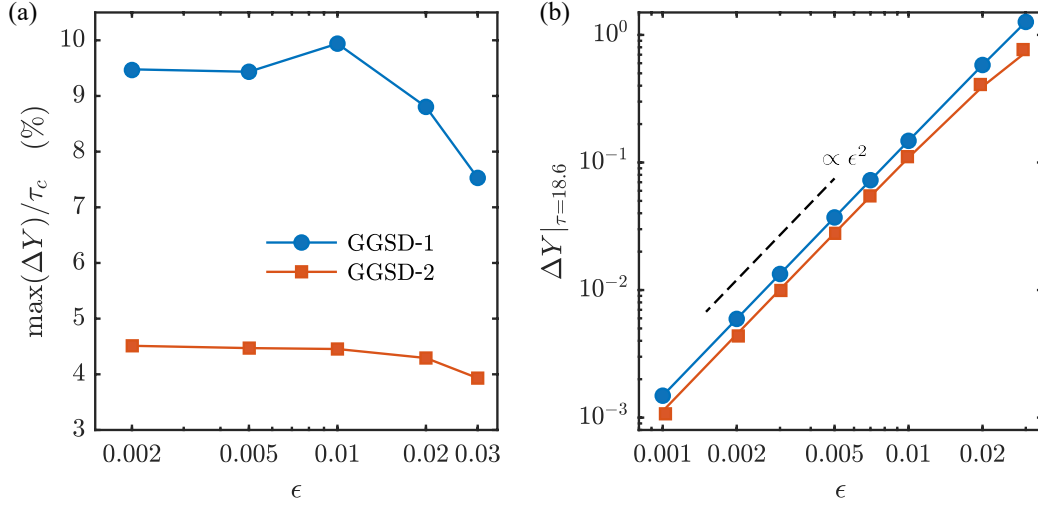


Figure 8.9: (a) Percentage maximum distance lead of average shock position given by GGSD-1 (disks) and GGSD-2 (squares) over the reference flat shock. (b) Distance lead of average shock position at a fixed time that is the critical time for the second order method. In both cases, $M_0 = 50$, $\epsilon = 0.03$, and the dashed line represents the first order, while the solid line gives the second order method. The dashed line without markers in (b) shows an explicit function of quadratic power law.

given by the Heaviside function [see Eq. (8.1)], which advances at the same speed with the flow behind the shock for all $t > 0$, a corrugated piston of the same velocity continues to accelerate fluid in the local normal direction, possibly generating more kinetic energy into the flow for $t > 0$.

8.2 Shock traversing a density gradient

Here we consider the evolution of shape and Mach number perturbations developed in an initially flat shock from it passing through a quiescent upstream fluid with a compact field of varying densities.

8.2.1 Compact perturbation field

The density field is constructed in the complex plane using a Gaussian profile along the initial shock normal direction, which is spatially distributed as a cosine wave in the initial shock span direction. As a function of $Z = X + iY$, the upstream fluid density prior to shock-processing reads,

$$\rho_0(Z) = \bar{\rho}_0 \left[1 + \epsilon_\rho \exp \left(\frac{-(Y - Y_p(X))^2}{2\sigma^2} \right) \right], \quad (8.20)$$

where $\bar{\rho}_0$ is the unperturbed far-field density, ϵ_ρ is the maximum perturbation magnitude relative to $\bar{\rho}_0$, σ is the Gaussian standard deviation measuring the width

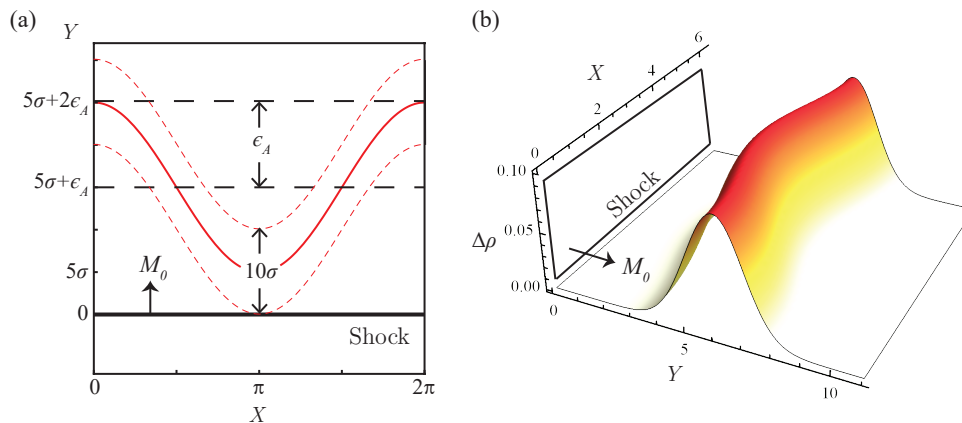


Figure 8.10: Plane shock of constant Mach number M_0 traversing a density gradient of compact domain. (a) The peak perturbation line Y_p of amplitude ϵ_A is given by the solid line; and width of the perturbation field, 10σ , is bounded by the dashed lines. (b) 3D visualisation of the shock initial conditions drawn for $\epsilon_\rho = 0.1$, $\sigma = 1$ and $\epsilon_A = 0.5$. Here $\Delta\rho = \rho_0 - \bar{\rho}_0$ is colour coded.

of the perturbed domain, and

$$Y_p(X) = \epsilon_A(\cos(X) + 1) + 5\sigma \quad (8.21)$$

gives the peak perturbation locations as a function of span-wise coordinates X , where ϵ_A is the wave amplitude. Here an offset distance of $(\epsilon_A + 5\sigma)$ is chosen such that for a shock initially given by $\{X = \beta \in [0, 2\pi), Y = 0\}$ at time $t = 0$, the perturbation field is sufficiently far away, and consequently $\rho_0 = \bar{\rho}_0$ holds everywhere on the shock. Similarly, the upstream density in the region $Y > Y_p + 5\sigma$ is also considered uniform. Visualisation for a typical density perturbation field is illustrated in figure 8.10.

Correspondingly, a perturbation field for the upstream sound speed is also assigned for the domain $Y > 0$ by assuming constant upstream pressure, implying

$$a_0(Z) = \bar{a}_0 \sqrt{\frac{\bar{\rho}_0}{\rho_0(Z)}}, \quad (8.22)$$

where \bar{a}_0 is the unperturbed far-field speed-of-sound. Since $\bar{\rho}_0$ and \bar{a}_0 coincide with their respective reference scales used for nondimensionalization, it is convenient to proceed with $\bar{\rho}_0 = \bar{a}_0 = 1$.

8.2.2 Leading order IVP

Here we argue that the GGSD models developed previously can be adapted to tackle the present problem of shock traversing a non-uniform medium. Although derived

under the assumption that ρ_0 and a_0 are constants, the GGSD equations of all orders are built with extended RH relations [see Eqs. (7.29)] that apply locally to the flow immediately ahead and behind the shock, and therefore hold if ρ_0 and a_0 vary in space. One caveat is that the second (and higher) order GGSD system also contains the gradient of the sound speed. Specifically, the arrival of Eqs. (7.54) and (7.56) in the weak and strong shock limits now involve differentiating a_0 , giving additional terms of the form

$$g(\beta, t) \frac{da_0}{dt} = g a_0 M \frac{da_0}{dx} = g a_0 M \left(\frac{\partial a_0}{\partial X}, \frac{\partial a_0}{\partial Y} \right) \cdot (\mathfrak{K}(\hat{n}), \mathfrak{J}(\hat{n})), \quad (8.23)$$

where g is a function of order unity, d/dx is understood as normal derivative, and $\hat{n} = i\hat{s}$ is the normal vector defined in (7.34). However, as the perturbation size $\epsilon_\rho \rightarrow 0$, these additional terms vanish since $da_0/dt \sim O(\epsilon_\rho)$; and therefore the limiting second order GGSD equations, (7.55) and (7.58), with ρ_0 and a_0 relaxed to be functions of Z , still capture the leading order behaviour of a shock traversing a non-uniform medium of small density perturbations.

The initial value for the GGSD systems of all orders in this case is straightforward, if flow downstream of the flat shock is uniform, before the density gradient is encountered. By positioning the shock initially at $Y = 0$, which as mentioned above is considered the beginning of the perturbation field, one has

$$Z(\beta, 0) = \beta, \quad M(\beta, 0) = M_0, \quad Q_1(\beta, 0) = Q_2(\beta, 0) = 0. \quad (8.24)$$

With initial values prescribed, the zeroth (7.43), first [(7.47), (7.50)], and second order [(7.55), (7.58)] GGSD systems are solved numerically in the next section.

8.2.3 Numerical results

The same numerical method described in Sec. 3.5 is used here to evolve the GGSD systems for a shock passing through the density gradient. The critical time τ_c at which discontinuities occur along the shock Mach number profile is again determined by the edge detection algorithm of Gelb & Tadmor [36]. It is noted that τ_c in this case is measured from the initial shock position at $\tau = 0$, just prior to the shock-density-gradient interaction. This choice is justified if τ_c measures significantly larger than the duration of the density gradient domain.

Shock trajectories due to all three GGSD systems using $M_0 = 50$ are shown in figure 8.11, where the density perturbation field with $\epsilon_\rho = 0.1$, $\sigma = \epsilon_A = 0.5$ is overlaid. It is observed that the shock shape perturbation developed from the density

gradient oscillates while a symmetric pair of high curvature points moving along the shock front. At the common critical time $\tau_c = 49.6$ of all three GGSD models, the kinks on the shock are identified by the edge detector. The difference between GGSD models of increasing order is small even in this strong shock case. This is because as the shock exits the density gradient, Q_1 is not sufficiently large to affect the shock dynamics, thus the uniform downstream flow assumption made by GGSD-0 provides a good approximation.

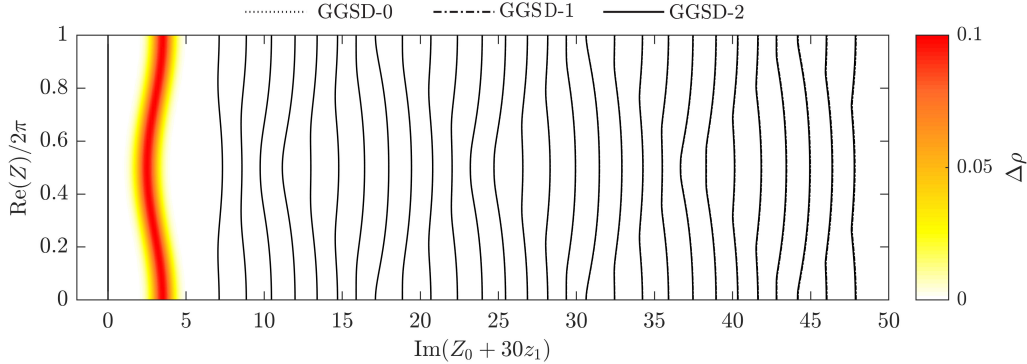


Figure 8.11: Trajectories of an initially flat shock of $M_0 = 50$ traversing a color coded density gradient with $\epsilon_\rho = 0.1$, $\sigma = \epsilon_A = 0.5$. The shock shape perturbation z_1 is amplified 30 times in the Y -direction. A sequence of instances at $\tau = 0, 9, 10.5, 13, \dots, 48, 49.6$ is given. The dotted, dash-dotted, and solid lines correspond to GGSD-0, GGSD-1, and GGSD-2, respectively.

Next we show that the inverse scaling law of critical time established for the piston-generated shock also holds here for all three density perturbation parameters, ϵ_ρ , σ and ϵ_A , that is,

$$\tau_c = \frac{K_3}{\sigma \epsilon_\rho \epsilon_A}, \quad \sigma, \epsilon_\rho, \epsilon_A \ll 1, \quad (8.25)$$

where K_3 is a constant. In all the simulations presented in the following, the critical times for each case differ within the edge detection uncertainty between all three GGSD models. Therefore it is argued that K_3 in (8.25) is model independent. For strong shock of $M_0 = 50$, τ_c is given for a wide range of perturbation parameters in figure 8.12.

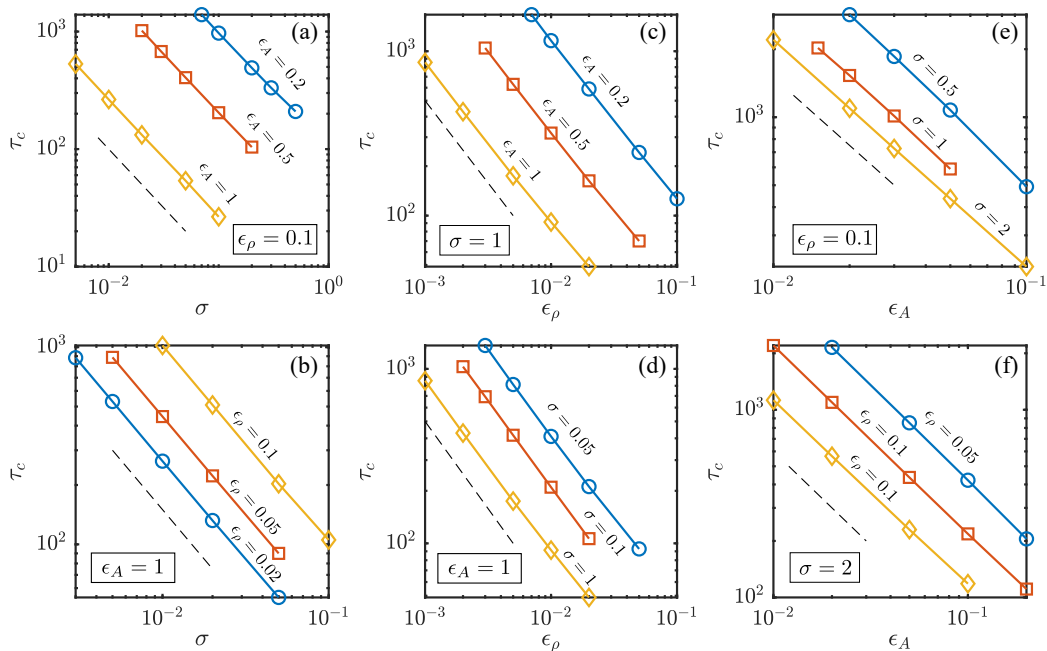


Figure 8.12: Critical time τ_c as a function of σ [in (a,b)], ϵ_ρ [in (c,d)] and ϵ_A [in (e,f)], for a strong shock of $M_0 = 50$. In each panel, the dashed line indicates a slope of negative one in log-log scale.

Specifically, 8.12(a) shows that $\tau_c = \tau_c(\epsilon_\rho) \propto 1/\sigma$ for $\sigma \ll 1$ across a range of ϵ_A when ϵ_ρ is fixed; 8.12(b) alone leads to $\tau_c = \tau_c(\epsilon_A) \propto 1/\sigma$ for a range of ϵ_ρ with ϵ_A fixed. Together, $\tau_c \propto \sigma$ independent of ϵ_A and ϵ_ρ is established. Similarly, 8.12(c,d) gives $\tau_c \propto 1/\epsilon_\rho$ for $\epsilon_\rho \ll 1$ for all σ and ϵ_A , while 8.12(e,f) gives $\tau_c \propto 1/\epsilon_A$ for $\epsilon_A \ll 1$, for all σ and ϵ_ρ .

The same inverse scaling behaviour is also found for a weak shock of $M_0 = 1.1$, as shown in figure 8.13. In (a)–(c), τ_c is given as a function of σ , ϵ_ρ and ϵ_A , respectively; and in each case the inverse scaling is independent of the other two parameters. Therefore we conclude that (8.25), with K_3 being a function of M_0 , holds universally true. This result is consistent with the previous finding (8.17) for the piston-driven shock.

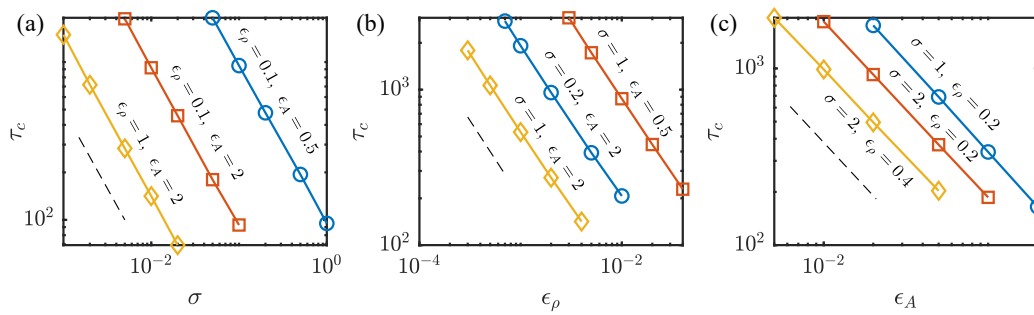


Figure 8.13: Critical time τ_c as a function of σ [in (a)], ϵ_ρ [in (b)] and ϵ_A [in (c)], for a weak shock of $M_0 = 1.1$. In each panel, the dashed line indicates a slope of negative one in log-log scale.

Chapter 9

CONCLUSIONS

We have reported numerical simulations of the evolution of a shock produced by an impulsively accelerated, two-dimensional piston with a sinusoidal surface corrugation of amplitude ϵ , and shock traversing a density perturbation field. First a complex-variable formulation of generalised geometrical shock dynamics, referred to as GGSD, is derived up to second order for both strong- and weak- shock limits. In these limits, the simplified expressions for derivative jump conditions across the shock required by the GGSD systems are given explicitly. However for general Mach number, this task becomes algebraically intractable. The resulting closed systems of partial differential equations are then solved numerically to give the evolution of the shock shape and Mach number distributions. An edge-detection algorithm is applied to test for the appearance of a singularity in the shock evolution profile at some critical time τ_c . These simulations provide strong evidence supporting the hypothesis that a spontaneous curvature singularity develops in the shock shape as a prelude to the formation of triple points or Mach stems in τ_c inversely proportional to the original perturbation magnitude. For the piston-driven shock, the original perturbation size is the amplitude of the piston corrugation ϵ , and for the shock-density-gradient interaction, the perturbations refer to all three of the wavelength ϵ_A , magnitude ϵ_ρ and width σ of the sinusoidally distributed Gaussian distribution for the density gradient.

The adoption of the GGSD hierarchy overcomes the limitations of previously used theories of geometrical shock dynamics by first accommodating well-defined shock initial conditions for the shock generation process, and second, by incorporating a quantitative description of non-uniform flow effects immediately behind the shock in terms of higher-order derivatives of velocity and pressure. For both flow applications, it is shown that the initial conditions for the retained, higher-order corrections are calculated exactly with respect to the Euler equations. Specifically, for the piston-driven shock, this is achieved by considering the kinematic relations between velocity, acceleration and jerk. By forcing continuous convergence to the unperturbed impulsive flow generated by a flat piston as $\epsilon \rightarrow 0$, the initial values of flow acceleration and jerk behind the perturbed shock are determined to be zero.

For the piston-generated shock, the behaviour of weak shocks with Mach number close to unity are found to witness small changes when increasing the system order, while maintaining oscillations around the unperturbed shock up to the critical time of curvature singularity formation. For strong shocks with large Mach number, the inclusion of non-uniform flow correction $Q_1 \neq 0$ behind the shock in GGSD-1 and GGSD-2 predicts an overall shock acceleration compared to GGSD-0 where $Q_1 = 0$. The corresponding Mach number perturbation growth is eventually terminated by the onset of the curvature singularity, which occurs in GGSD-1 and GGSD-2 at τ_c that converges with the GGSD order converging, and that scales as $\tau_c \propto 1/\epsilon$ as in GGSD-0 albeit with a significantly smaller proportionality constant. Between the higher-order methods, GGSD-2 gives a smaller Q_1 correction effect than GGSD-1, manifested particularly in the smaller average shock acceleration relative to the unperturbed shock. This leaves uncertainty in the convergence of shock trajectories given by the GGSD expansion hierarchy, and remains to be resolved by direct numerical simulations for the Euler equations with accurate shock tracking.

However when the nonuniform downstream flow effect is weak, as found for both strong and weak shocks passing through a small density gradient, the GGSD systems converge convincingly, and the lowest order GGSD-0 model provides a good approximation for the shock trajectories. In particular, $\tau_c \propto 1/(\sigma \epsilon_\rho \epsilon_A)$ is established, consistent with the result of the piston-driven shock.

Appendix A

ZERO PLASMA BETA LIMIT OF 2FP

Here we make a brief comment on the alternative route to achieve the small Larmor radius assumption, *i.e.*, the $\beta \rightarrow 0$ limit, discussed in Sec. 2.5. A similar perturbation procedure used throughout this paper could be attempted where series in powers of $\beta^{1/2}$ is used to expand the field variables. However, such an expansion necessarily leads to a trivial solution for all variables at zeroth order, for all sets of equations discussed in this paper. That is, a magnetized background with no motion. Physically this agrees with the definition of plasma beta when magnetic energy dominates. However, if perturbed variables at higher order were to be extracted, equations are not closed at any truncated order.

Closure may be mathematically enforced if the zeroth order magnetic field vanishes, that is, $\mathbf{B} = \mathbf{B}_1\beta^{1/2} + O(\beta)$. Such an artificial construction performs no more than rescaling the original governing equations. For example, applying the aforementioned expansion to the 2FMHD system produces the following set of equations that is identical to the rescaled 2FMHD system discussed as a remark in Section 2.3.1,

$$\frac{\partial \rho}{\partial t} + \nabla \cdot (\rho \mathbf{u}) = 0, \quad (\text{A.1})$$

$$\rho \left(\frac{\partial \mathbf{u}}{\partial t} + \mathbf{u} \cdot \nabla \mathbf{u} \right) = -\nabla p - \nabla \cdot \left(\frac{m_i^2}{e^2} \frac{\mathbf{j}\mathbf{j}}{M\rho} \right) + \frac{\sqrt{2}}{d_S} \mathbf{j} \times \mathbf{B}_1, \quad (\text{A.2})$$

$$\begin{aligned} \frac{\partial \mathbf{j}}{\partial t} + \nabla \cdot \left(\mathbf{u}\mathbf{j} + \mathbf{j}\mathbf{u} - \frac{m_i(1-M)}{e\rho M} \mathbf{j}\mathbf{j} + \frac{e(p - (M+1)p_e)}{m_i} \mathbf{I} \right) \\ = \frac{\sqrt{2}e}{d_S m_i} \left(\frac{eM\rho}{m_i} (\mathbf{E}_1 + \mathbf{u} \times \mathbf{B}_1) + (1-M)\mathbf{j} \times \mathbf{B}_1 \right), \end{aligned} \quad (\text{A.3})$$

$$\frac{\partial}{\partial t} \left(\mathcal{E} + \frac{m_i^2}{e^2} \frac{j^2}{2M\rho} \right) + \nabla \cdot ((\mathcal{E}_h + p)\mathbf{u} + 2\mathbf{E}_1 \times \mathbf{B}_1) + \nabla \cdot \mathbf{f}_{erg} = 0, \quad (\text{A.4})$$

$$\frac{\partial p_e}{\partial t} + (\mathbf{u} - \frac{m_i}{e\rho} \mathbf{j}) \cdot \nabla p_e + \gamma p_e \nabla \cdot (\mathbf{u} - \frac{m_i}{e\rho} \mathbf{j}) = 0, \quad (\text{A.5})$$

$$\frac{\partial \mathbf{B}_1}{\partial t} + \nabla \times \mathbf{E}_1 = \mathbf{0}, \quad (\text{A.6})$$

$$\nabla \times \mathbf{B}_1 = \frac{1}{\sqrt{2}d_S} \mathbf{j}, \quad (\text{A.7})$$

$$\nabla \cdot \mathbf{B}_1 = 0, \quad (\text{A.8})$$

where

$$\begin{aligned}\mathcal{E}_h &= \frac{p}{\gamma - 1} + \frac{1}{2}\rho u^2, \quad \mathcal{E} = \mathcal{E}_h + B_1^2 \\ \mathbf{f}_{erg} &= \frac{j^2 m_i^2}{2e^2 M \rho} \mathbf{u} - \frac{\gamma m_i (e(M+1)p_e \rho - e p \rho)}{(\gamma - 1)e^2 M \rho^2} \mathbf{j} - \frac{j m_i^2 (e j (M - 1) m_i - 2e^2 M \rho u)}{2e^4 M^2 \rho^2} \mathbf{j} \\ \mathbf{B}_1 &= \mathbf{B} \beta^{-1/2}, \quad \mathbf{E}_1 = \mathbf{E} \beta^{-1/2}.\end{aligned}\tag{A.9}$$

Appendix B

LIMITING LINEAR EQUATIONS FOR COEFFICIENTS α

Here we provide the linear systems derived in Sec. 4.4 that are used to determine the coefficients $\alpha_{i,j}$ under various limits.

Large skin depth ($\beta \rightarrow 0, d_L < \infty$)

In Sec. 4.4.2, the linear equations that lead to solution (4.58) have the following matrix representation:

$$\begin{bmatrix} -1 & -1 & -1 & 1 & 1 & 1 \\ \frac{k \exp(-i\phi)}{s} & 0 & \frac{kd_L}{\cos\phi} & \frac{kd_L}{\cos\phi} & 0 & \frac{k \exp(i\phi)}{s} \\ k(\sin\phi + i \cos\phi) & 0 & \frac{kd_L \sin\phi}{\cos^2\phi} & \frac{kd_L \sin\phi}{\cos^2\phi} & 0 & \frac{ik \exp(i\phi)}{s} \\ -s & 0 & 0 & 0 & -\frac{i\beta\rho_1}{2kd_L} & 0 \\ 0 & 0 & 0 & C_{44} & 0 & 0 \\ 0 & -\frac{i\beta\rho_2}{2kd_L} & C_{53} & 0 & 0 & 0 \\ \frac{\rho_2 s}{k} & \frac{\rho_2 \sqrt{\sigma^2+1}}{kd_L} & C_{63} & C_{64} & \frac{\rho_1 \sqrt{\sigma^2+1}}{kd_L} & \frac{\rho_1 s}{k} \end{bmatrix} \begin{bmatrix} \alpha_{2,1} \\ \alpha_{2,2} \\ \alpha_{2,3} \\ \alpha_{1,4} \\ \alpha_{1,5} \\ \alpha_{1,6} \end{bmatrix} = \begin{bmatrix} 0 \\ 0 \\ 0 \\ 0 \\ 0 \\ b \end{bmatrix}, \quad (\text{B.1})$$

where

$$\begin{aligned} C_{44} &= \frac{\beta\rho_1(-2sd_L \tan\phi + i)}{2kd_L} + ikd_L \sec^2\phi, \quad C_{53} = \frac{\beta\rho_2(2sd_L \tan\phi + i)}{2kd_L} + ikd_L \sec^2\phi, \\ C_{63} &= \frac{2kd_L \sec^2\phi}{\beta} + \frac{\rho_2(2-3isd_L \tan\phi)}{kd_L}, \quad C_{64} = \frac{2kd_L \sec^2\phi}{\beta} + \frac{\rho_1(2+3isd_L \tan\phi)}{kd_L}, \\ b &= \eta_0(\rho_2 - \rho_1). \end{aligned} \quad (\text{B.2})$$

In order to obtain the correct limiting solution for $\alpha_{i,j}$, it is sufficient to truncate the matrix entries at $O(\beta^0)$ in their Taylor expansions, except for those in the fourth and fifth row, where truncation is made at $O(\beta)$.

Large skin depth ($d_L \rightarrow \infty, \beta > 0$)

Similarly, the following limiting linear system gives rise to solution (4.66) in Sec. 4.4.2,

$$\begin{bmatrix} -1 & -1 & -1 & 1 & 1 & 1 \\ \frac{k \exp(-i\phi)}{\sigma\epsilon} & 0 & \frac{k \sec\phi}{\epsilon} & \frac{k \sec\phi}{\epsilon} & 0 & \frac{k \exp(i\phi)}{\sigma\epsilon} \\ k(\sin\phi + i \cos\phi) & 0 & \frac{k \tan\phi \sec\phi}{\epsilon} & \frac{k \tan\phi \sec\phi}{\epsilon} & 0 & \frac{ik \exp(i\phi)}{\sigma\epsilon} \\ -\sigma\epsilon & 0 & 0 & 0 & -\frac{i\beta\rho_1\epsilon}{2k} & 0 \\ 0 & 0 & 0 & C_{44} & 0 & 0 \\ 0 & -\frac{i\beta\rho_2\epsilon}{2k} & C_{53} & 0 & 0 & 0 \\ \frac{\rho_2\sigma\epsilon}{k} & \frac{\rho_2 \sqrt{\sigma^2+1}\epsilon}{k} & C_{63} & C_{64} & \frac{\rho_1 \sqrt{\sigma^2+1}\epsilon}{k} & \frac{\rho_1\sigma\epsilon}{k} \end{bmatrix} \begin{bmatrix} \alpha_{2,1} \\ \alpha_{2,2} \\ \alpha_{2,3} \\ \alpha_{1,4} \\ \alpha_{1,5} \\ \alpha_{1,6} \end{bmatrix} = \begin{bmatrix} 0 \\ 0 \\ 0 \\ 0 \\ 0 \\ b \end{bmatrix}, \quad (\text{B.3})$$

where

$$\begin{aligned} C_{44} &= \frac{\beta\rho_1\epsilon(-2\sigma \tan\phi + i)}{2k} + \frac{ik \sec^2\phi}{\epsilon}, \quad C_{53} = \frac{\beta\rho_2\epsilon(2\sigma \tan\phi + i)}{2k} + \frac{ik \sec^2\phi}{\epsilon}, \\ C_{63} &= \frac{2k \sec^2\phi}{\beta\epsilon} + \frac{\rho_2\epsilon(2-3i\sigma \tan\phi)}{k}, \quad C_{64} = \frac{2k \sec^2\phi}{\beta\epsilon} + \frac{\rho_1\epsilon(2+3i\sigma \tan\phi)}{k}. \end{aligned} \quad (\text{B.4})$$

Here the entries are truncated at $O(\epsilon^0)$ for the first three rows and at $O(\epsilon)$ for the last three rows.

Large angle limit

Again, in the limiting case of $\phi \rightarrow \pi/2$, or equivalently, $\varepsilon \rightarrow 0$ studied in Sec. 4.4.4, the flow coefficients are determined from

$$\begin{bmatrix} -1 & -1 & -1 & 1 & 1 & 1 \\ -\frac{ik}{s} & \frac{is\beta\rho_2}{2k} & \frac{kd_L}{\varepsilon} - \frac{is\beta\rho_2}{2k} & \frac{kd_L}{\varepsilon} + \frac{is\beta\rho_1}{2k} & -\frac{is\beta\rho_1}{2k} & \frac{ik}{s} \\ -\frac{k}{s} & \frac{s\beta\mu_2^*\rho_2}{2k^2} & C_{33} & C_{34} & \frac{s\beta\mu_1^*\rho_1}{2k^2} & -\frac{k}{s} \\ 0 & 0 & 0 & C_{44} & -\frac{i\beta\rho_1(2k^2+s^2\beta\rho_1)}{4k^3d_L} & 0 \\ 0 & -\frac{i\beta\rho_2(2k^2+s^2\beta\rho_2)}{4k^3d_L} & C_{53} & 0 & 0 & 0 \\ \frac{s\rho_2}{k} & \frac{s\mu_2^*\rho_2}{k^2} & C_{63} & C_{64} & \frac{s\mu_1^*\rho_1}{k^2} & \frac{s\rho_1}{k} \end{bmatrix} \begin{bmatrix} \alpha_{2,1} \\ \alpha_{2,2} \\ \alpha_{2,3} \\ \alpha_{1,4} \\ \alpha_{1,5} \\ \alpha_{1,6} \end{bmatrix} = \begin{bmatrix} 0 \\ 0 \\ 0 \\ 0 \\ 0 \\ b \end{bmatrix}, \quad (\text{B.5})$$

where

$$\begin{aligned} C_{33} &= \frac{\beta\varepsilon\rho_2(4(\varepsilon - isd_L)k^2 + 3s^2\beta\varepsilon\rho_2) - 2k^4(\varepsilon^2 - 2)d_L^2}{4k^3\varepsilon^2d_L}, \\ C_{34} &= \frac{\beta\varepsilon\rho_1(4(\varepsilon + isd_L)k^2 + 3s^2\beta\varepsilon\rho_1) - 2k^4(\varepsilon^2 - 2)d_L^2}{4k^3\varepsilon^2d_L}, \\ C_{44} &= \frac{i(4d_L^2k^4 + \beta\varepsilon\rho_1(2(\varepsilon + 2isd_L)k^2 + s^2\beta\varepsilon\rho_1))}{4k^3\varepsilon^2d_L}, \\ C_{53} &= \frac{ikd_L}{\varepsilon^2} + \frac{s\beta\rho_2}{k\varepsilon} + \frac{i\beta\rho_2(2k^2 + s^2\beta\rho_2)}{4k^3d_L}, \\ C_{63} &= \frac{2kd_L}{\beta\varepsilon^2} + \frac{\rho_2(4(\varepsilon - isd_L)k^2 + 3s^2\beta\varepsilon\rho_2)}{2k^3\varepsilon d_L}, \\ C_{64} &= \frac{2kd_L}{\beta\varepsilon^2} + \frac{\rho_1(4(\varepsilon + isd_L)k^2 + 3s^2\beta\varepsilon\rho_1)}{2k^3\varepsilon d_L}, \end{aligned} \quad (\text{B.6})$$

and all entries are approximated up to $O(\varepsilon^0)$.

Appendix C

ANALYTICAL LAPLACE TRANSFORM INVERSION

In this section, we document the derivation of Eqs. (4.62) and (4.63). First, from Eqs. (4.35) and (4.59), the limiting interfacial growth is given by

$$\frac{\eta(t) - \eta_0}{\mathcal{A}\eta_0 k} = \mathcal{L}^{-1} \left[\frac{d_L}{s \left(1 + \sqrt{1 + \sigma(s)}\right)}; s \mapsto t \right], \quad (\text{C.1})$$

where $\sigma(s) = d_L s$ and the operator ($\mathcal{L}^{-1} : s \rightarrow t$) is understood as the Bromwich integral given in Eq. (4.34). Using the cyclotron time scale, $T = t/d_L$, Eq. (C.1) is equivalent to

$$\frac{\hat{\eta}(T) - \hat{\eta}_0}{d_L} = \mathcal{L}^{-1} \left[\frac{1}{\sigma \left(1 + \sqrt{1 + \sigma}\right)}; \sigma \mapsto T \right], \quad (\text{C.2})$$

where $\hat{\eta} = \eta/(\mathcal{A}\eta_0 k)$, $\hat{\eta}_0 = 1/(\mathcal{A}k)$, and the inversion operator now maps σ in the Laplace space to T in time space. To proceed, we commit to the ($\mathcal{L}^{-1} : \sigma \rightarrow T$) mapping and write

$$\begin{aligned} \frac{\hat{\eta} - \hat{\eta}_0}{d_L} &= \mathcal{L}^{-1} \left[\frac{1}{\sigma^2} \sqrt{1 + \frac{1}{\sigma^2}} - \frac{1}{\sigma^3} \right] \\ &= \mathcal{L}^{-1} \left[\sum_{k=0}^{\infty} \binom{1/2}{k} \sigma^{-2k-2} - \frac{1}{\sigma^3} \right], \end{aligned} \quad (\text{C.3})$$

where the binomial expansion is used. Now for each polynomial of σ , the Laplace inversion is standard, giving the desired result of Eq. (4.62), namely,

$$\begin{aligned} \frac{\hat{\eta} - \hat{\eta}_0}{d_L} &= \sum_{k=0}^{\infty} \binom{1/2}{k} \frac{T^{2k+1}}{(2k+1)!} - \frac{T^2}{2} \\ &= T {}_1F_2 \left(-\frac{1}{2}; 1, \frac{3}{2}; -\frac{T^2}{4} \right) - \frac{T^2}{2}. \end{aligned} \quad (\text{C.4})$$

Similarly, the limiting interfacial circulation, $\hat{\gamma}_0(T) = \gamma_0(t)/(4\eta_0\mathcal{A})$, follows from

Eqs. (4.36) and (4.60) as

$$\begin{aligned}\hat{\gamma}_0(T) &= \mathcal{L}^{-1} \left[\frac{\sigma \sqrt{\sigma^2 + 1}}{(\sqrt{\sigma^2 + 1} + 1) (\cos^2 \phi + \sigma^2)} \right] \\ &= \mathcal{L}^{-1} \left[\frac{\sigma^2 - \sigma + 1}{\sigma \cos^2 \phi + \sigma^3} - \frac{\sqrt{\sigma^2 + 1} - \sigma}{\sigma \cos^2 \phi + \sigma^3} \right].\end{aligned}\quad (\text{C.5})$$

While the first term in (C.5) can be inverted easily, inversion for the second term is achieved by the convolution of two standard integrals

$$\begin{aligned}\mathcal{L} \left[\frac{J_1(T)}{T} \right] &= \sqrt{\sigma^2 + 1} - \sigma, \\ \mathcal{L} \left[\frac{1 - \cos(T \cos \phi)}{\cos^2 \phi} \right] &= \frac{1}{\sigma \cos^2 \phi + \sigma^3}.\end{aligned}\quad (\text{C.6})$$

As a result, Eq. (4.63) in closed form follows:

$$\hat{\gamma}_0 = \frac{(\cos^2 \phi - 1) \cos(T \cos \phi) - \cos \phi \sin(T \cos \phi) + 1}{\cos^2 \phi} - \frac{1 - \cos(T \cos \phi)}{\cos^2 \phi} * \frac{J_1(T)}{T}.\quad (\text{C.7})$$

Appendix D

LINEARIZED RANKINE-HUGONIOT CONDITIONS

For the purpose of this discussion, we consider a real valued interfacial perturbation profile, $h(x, t) = \eta(t) \cos(kx)$ where $1 \gg \eta(t) \in \mathbb{R}$. The corresponding unit tangent and normal vectors along the interface in the x, z -plane are thus,

$$\hat{\mathbf{t}} = \frac{1}{1 + \eta^2 k^2 \sin^2(kx)} (1, 0, -\eta k \sin(kx)) = (1, 0, -K\eta) + O(\eta^2), \quad (\text{D.1})$$

$$\hat{\mathbf{n}} = \frac{1}{1 + \eta^2 k^2 \sin^2(kx)} (\eta k \sin(kx), 0, -1) = (K\eta, 0, 1) + O(\eta^2), \quad (\text{D.2})$$

where $K = k \sin(kx)$ is a constant.

The background magnetic field can be expressed as

$$\mathbf{B}_0 = (\sqrt{1 - \epsilon^2}, 0, \epsilon), \quad 0 \leq \epsilon \leq 1. \quad (\text{D.3})$$

However in the following we specialize to the case where $\epsilon \ll 1$. For sufficiently small η , the perturbed magnetic field that results from the initial density interface distortion of magnitude $\eta_0 [= O(\eta)]$ can be expanded in a perturbation series

$$\mathbf{B} = \mathbf{B}_0 + \mathbf{B}_1 \eta_0 + O(\eta_0^2) = \left(1 + O(\epsilon^2) + B_{1x} \eta_0, B_{1y} \eta_0, \epsilon + B_{1z} \eta_0 \right) + O(\eta_0^2), \quad (\text{D.4})$$

where $\mathbf{B}_1 = \mathbf{B}_1(x, z, t)$ is of order unity. Extracting normal and tangential components of the field to first order gives,

$$B_n = \mathbf{B} \cdot \hat{\mathbf{n}} = K\eta + \epsilon + B_{1z} \eta_0, \quad (\text{D.5})$$

$$B_t = \mathbf{B} \cdot \hat{\mathbf{t}} = 1 + B_{1x} \eta_0. \quad (\text{D.6})$$

As a reminder, the nonlinear Rankine-Hugoniot CD jump conditions listed in (4.4) include

$$\left[\left(p + \frac{1}{\beta} B^2 \right) \hat{\mathbf{n}} - \frac{2}{\beta} B_n \mathbf{B} \right] = 0, \quad (\text{D.7})$$

$$\llbracket B_n \rrbracket = 0, \quad (\text{D.8})$$

which apply to both regular MHD and Hall-MHD systems. In particular, using (D.5) and (D.6), the tangential component of (D.7) requires

$$\llbracket B_n B_t \rrbracket = \llbracket B_{1z} \eta_0 + B_{1x} \eta_0 \epsilon + O(\eta_0^2) \rrbracket = 0. \quad (\text{D.9})$$

To be consistent with the linearization of the governing equations discussed in Sec. 4.2.3, the CD jump conditions must be imposed at order $O(\eta_0)$. It follows that the first term in (D.9) automatically drops due to (D.8), and (D.9) is non-trivial only if $\eta_0 \ll \epsilon$, in which case, continuity of B_{1x} is strictly required. Otherwise, (D.9) is equivalent to (D.8) to leading order, and even though the unperturbed magnetic field lines still cut through the CD, continuity of B_{1x} should not be demanded in the linear region.

This analysis therefore justifies the use of correct boundary conditions given in Eqs. (4.17) where $\epsilon = 0$, and (4.32) where $\eta_0 \ll \epsilon \ll 1$.

Appendix E

TABLES OF COEFFICIENTS

This section lists all the coefficient functions used throughout this study in Table E.1 and E.2, as constant functions of the specific heat ratio γ .

$$\begin{aligned}
\bar{\mu} &= \sqrt{\frac{\gamma-1}{2\gamma}} \\
\alpha_1 &= \frac{2}{\gamma+1} \\
\alpha_2 &= \frac{\gamma+1}{\gamma-1} \\
\alpha_3 &= \frac{2\gamma\bar{\mu}}{\gamma+1} \\
\sigma_1 &= \frac{4\gamma(\gamma(2(5\gamma-7)+3\gamma(4\gamma-5)\bar{\mu}+\bar{\mu})+4)}{(\gamma-1)^2(\gamma+1)(\gamma\bar{\mu}+1)^2} - \frac{4\sqrt{2\gamma}(\gamma^2+\gamma+2)}{(\gamma-1)^{3/2}(\gamma+1)^2} \\
\sigma_2 &= \frac{\gamma^2(\gamma(\gamma(3\gamma-10)-4)-2)+2(\gamma((\gamma-17)\gamma-9)+5)\bar{\mu}-3}{(\gamma-1)(\gamma+1)^3(\gamma\bar{\mu}+1)^3} \\
\sigma_3 &= \frac{4\gamma^2(4\gamma+(\gamma(5\gamma-2)-1)\bar{\mu}-2)}{(\gamma-1)(\gamma+1)^2(\gamma\bar{\mu}+1)^2} \\
\sigma_4 &= \frac{2\sqrt{2\gamma}}{(\gamma-1)^{3/2}(\gamma+1)^3} \left(\gamma(-\gamma^2+\gamma-15) + \frac{\gamma(\gamma+1)(\gamma(\gamma(7\gamma-18)+(\gamma(\gamma+1)(7\gamma-15)+10)\bar{\mu}-11)+24)}{(\gamma\bar{\mu}+1)^3} + 3 \right) \\
\sigma_5 &= \frac{8(\gamma(2\gamma-11)+10)}{(\gamma^2-1)^2\bar{\mu}} - \frac{\sqrt{2}\gamma^{3/2}(3\gamma^4\bar{\mu}+\gamma^3(9-33\bar{\mu})+17\gamma^2(5\bar{\mu}-3)+\gamma(91-103\bar{\mu})-73)}{(\gamma-1)^{5/2}(\gamma+1)(\gamma\bar{\mu}+1)^3} \\
\sigma_6 &= -\frac{(1+\gamma)^2}{4(1+\bar{\mu}\gamma)^2} \left(\frac{4(7\gamma-6)}{\gamma^2-1} + \frac{2\sqrt{2}(\gamma(5\gamma-12)+9)\sqrt{\gamma}}{(\gamma-1)^{3/2}(\gamma+1)} \right) \\
\sigma_7 &= \frac{\gamma(9(\gamma-1)\gamma+(3\gamma((\gamma-1)\gamma+3)+11)\bar{\mu}-9)+5}{4\bar{\mu}(\gamma+1)(\gamma\bar{\mu}+1)^3} \\
\sigma_8 &= -\frac{\gamma((2\gamma-1)\bar{\mu}+3)}{(\gamma\bar{\mu}+1)^2} \\
\sigma_9 &= \frac{\sqrt{\gamma}(\gamma(23\gamma-54)+13)+2(\gamma(\gamma(4\gamma-11)+17)-5)-2)\bar{\mu}+20}{\sqrt{2}(\gamma-1)^{3/2}(\gamma\bar{\mu}+1)^3} \\
\sigma_{10} &= \frac{\sqrt{\gamma}(\gamma+1)(\gamma(\gamma(75\gamma-253)+233)+(\gamma(\gamma(29\gamma-111)+191)-173)+88)\bar{\mu}-31}{2\sqrt{2}(\gamma-1)^{5/2}(\gamma\bar{\mu}+1)^3} \\
\sigma_{11} &= -\frac{4\sqrt{2\gamma}(\gamma(2\gamma-11)+11)}{(\gamma-1)^{5/2}(\gamma+1)} \\
\sigma_{12} &= \frac{8\gamma(5\gamma+1)\bar{\mu}}{(\gamma^2-1)^2} \\
\sigma_{13} &= \frac{2\sqrt{2\gamma}(5\gamma((\gamma-3)\gamma-1)+39)}{(\gamma-1)^{7/2}(\gamma+1)} \\
\sigma_{14} &= \frac{(\gamma+1)(6\gamma^2\bar{\mu}+\gamma(8-10\bar{\mu})-8)}{(\gamma-1)(2\gamma\bar{\mu}+2)^2} \\
\sigma_{15} &= \frac{\gamma(2(\gamma-1)\bar{\mu}+4)}{(2\gamma\bar{\mu}+2)^2} \\
\zeta_1 &= \frac{(\gamma-1)\gamma}{\gamma+\gamma^2(2\bar{\mu}+1)-2} \\
\zeta_2 &= \frac{(\gamma-1)(\gamma+1)(\gamma(2\bar{\mu}-1)+1)}{4(\gamma+\gamma^2(2\bar{\mu}+1)-2)} \\
\gamma_1 &= -\frac{4(\gamma-2)\gamma^2((\gamma-1)^2+(\gamma^3-\gamma^2-2)\bar{\mu})}{(\gamma+1)(\gamma\bar{\mu}+1)^2(\gamma+\gamma^2(2\bar{\mu}+1)-2)^2} \\
\gamma_2 &= -\frac{\gamma(\gamma^4+\gamma^3(54\bar{\mu}-47)+8\gamma^2(3\bar{\mu}+4)-4\gamma(2\bar{\mu}+7)+32)}{(\gamma-2)^4(\gamma+1)} \\
\gamma_3 &= \frac{(\gamma+1)(4\gamma+\gamma^4(13\bar{\mu}-9)+\gamma^3(51-68\bar{\mu})+\gamma^2(52\bar{\mu}-54)+8)}{2(\gamma-2)^4} \\
\gamma_4 &= \frac{\gamma-\gamma\bar{\mu}-1}{\gamma-2} \\
\chi_1 &= \zeta_1(\sigma_1 + \sigma_{12} - \sigma_{11}\zeta_1) - \sigma_3 \\
\chi_2 &= \zeta_1(\sigma_4 + \sigma_{11}\gamma_1\zeta_2) - \sigma_1\gamma_1\zeta_2 - (\sigma_1 + \sigma_5)\zeta_1^2 + (\sigma_{11} + \sigma_{13})\zeta_1^3 - \sigma_2 \\
\chi_3 &= -\zeta_1(\sigma_6 + \sigma_{11}\zeta_2) + \sigma_{12}\zeta_2 + \sigma_8 \\
\chi_4 &= \sigma_7 - \sigma_9\zeta_1 + (\sigma_1 - 2\sigma_5 - \sigma_{11}\gamma_2)\zeta_1\zeta_2 + (\sigma_6 + \sigma_{10} + 3\sigma_{13}\zeta_2)\zeta_1^2 + (\sigma_4 + \sigma_6\gamma_1 + \sigma_1\gamma_2 + \sigma_{11}\gamma_1\zeta_2)\zeta_2 \\
\chi_5 &= \zeta_2(\sigma_9 + \sigma_1\gamma_3 - 2\sigma_{10}\zeta_1 - \sigma_{11}\gamma_3\zeta_1 + \sigma_6(\gamma_2 + \zeta_1) + \zeta_2(-2\sigma_1 + \sigma_5 + \sigma_{11}\gamma_2 + 3\sigma_{11}\zeta_1 - 3\sigma_{13}\zeta_1)) \\
\chi_6 &= \zeta_2(-\sigma_6\gamma_3 - (\sigma_{10} - 2\sigma_6 + \sigma_{11}\gamma_3)\zeta_2 + (2\sigma_{11} - \sigma_{13})\zeta_2^2) \\
\chi_7 &= \zeta_2(-\sigma_6\gamma_4 + 2\sigma_{14} - \sigma_{11}\gamma_4\zeta_2) \\
\chi_8 &= 2(\sigma_{15} - \sigma_{14}\zeta_1) + \gamma_4\zeta_2(\sigma_{11}\zeta_1 - \sigma_1)
\end{aligned}$$

Table E.1: Constant coefficient functions in the GGSD systems, up to second order, in terms of the specific heat ratio γ .

$$\begin{aligned}
\omega_1 &= \frac{8(5\gamma-2)}{\gamma^2-1}, & \omega_2 &= -\frac{8\gamma(2\gamma^2+3\gamma-1)}{(\gamma-1)(\gamma+1)^3}, & \omega_3 &= \frac{8\gamma(2\gamma-1)}{(\gamma-1)(\gamma+1)^2}, & \omega_4 &= \frac{8(\gamma-3)\gamma}{(\gamma-1)(\gamma+1)^2} \\
\omega_5 &= -\frac{8(\gamma-4)\gamma}{(\gamma-1)^2(\gamma+1)}, & \omega_6 &= \frac{8-28\gamma}{\gamma^2-1}, & \omega_7 &= \frac{4\gamma(3\gamma^2+6\gamma-1)}{(\gamma-1)(\gamma+1)^3}, & \omega_8 &= \frac{4(1-3\gamma)\gamma}{(\gamma-1)(\gamma+1)^2} \\
\omega_9 &= \frac{4\gamma(\gamma+3)}{(\gamma-1)(\gamma+1)^2}, & \omega_{10} &= \frac{8(4\gamma^2-9\gamma+2)}{(\gamma-1)^2(\gamma+1)}, & \omega_{11} &= \frac{4(7\gamma-6)}{\gamma^2-1}, & \omega_{12} &= -\frac{4\gamma(3\gamma+5)}{(\gamma+1)^3} \\
\omega_{13} &= \frac{12\gamma}{(\gamma+1)^2}, & \omega_{14} &= -\frac{4(\gamma^2+3\gamma-2)}{(\gamma-1)(\gamma+1)^2}, & \omega_{15} &= -\frac{8(4\gamma-3)}{\gamma^2-1}, & \omega_{16} &= -\frac{4(5\gamma-4)}{\gamma^2-1} \\
\omega_{17} &= \frac{8\gamma(\gamma+2)}{(\gamma+1)^3}, & \omega_{18} &= -\frac{8\gamma}{(\gamma+1)^2}, & \omega_{19} &= \frac{4(3\gamma-2)}{\gamma^2-1}, & \omega_{20} &= \frac{8(5\gamma-4)}{\gamma^2-1} \\
\omega_{21} &= \frac{4(\gamma+1)(5\gamma-7)}{(\gamma-1)^3}, & \omega_{22} &= -\frac{4(3\gamma^2+5\gamma-2)}{(\gamma-1)^2(\gamma+1)}, & \omega_{23} &= \frac{8\gamma-4}{(\gamma-1)^2}, & \omega_{24} &= -\frac{4(5\gamma^2+8\gamma-15)}{(\gamma-1)^3} \\
\omega_{25} &= -\frac{4(10\gamma^3+\gamma^2-22\gamma-13)}{(\gamma-1)^4}, & \omega_{26} &= -\frac{2(\gamma+1)(7\gamma-11)}{(\gamma-1)^3}, & \omega_{27} &= \frac{2(5\gamma^2+10\gamma-3)}{(\gamma-1)^2(\gamma+1)}, & \omega_{28} &= \frac{2-6\gamma}{(\gamma-1)^2} \\
\omega_{29} &= \frac{22\gamma^2+28\gamma-58}{(\gamma-1)^3}, & \omega_{30} &= \frac{4(10\gamma^3+\gamma^2-22\gamma-13)}{(\gamma-1)^4}, & \omega_{31} &= -\frac{2\sqrt{2}(5\gamma^2-12\gamma+9)}{\left(\frac{\gamma-1}{\gamma}\right)^{3/2}\gamma(\gamma+1)} \\
\omega_{32} &= \frac{\sqrt{2}(5\gamma^3+\gamma^2-17\gamma+7)}{\sqrt{\frac{\gamma-1}{\gamma}}(\gamma+1)^3}, & \omega_{33} &= -\frac{2\sqrt{2-\frac{2}{\gamma}}\gamma(2\gamma-1)}{(\gamma+1)^2}, & \omega_{34} &= \frac{4\sqrt{2}(\gamma^3-13\gamma+13)}{\left(\frac{\gamma-1}{\gamma}\right)^{3/2}\gamma(\gamma+1)^2} \\
\omega_{35} &= \frac{\sqrt{2}(11\gamma^3-33\gamma^2-15\gamma+61)}{\left(\frac{\gamma-1}{\gamma}\right)^{5/2}\gamma^2(\gamma+1)}, & \omega_{36} &= \frac{\sqrt{2}(-7\gamma^2+16\gamma-13)}{\left(\frac{\gamma-1}{\gamma}\right)^{3/2}\gamma(\gamma+1)}, & \omega_{37} &= \frac{2\sqrt{2}(2\gamma^3+\gamma^2-8\gamma+3)}{\sqrt{\frac{\gamma-1}{\gamma}}(\gamma+1)^3} \\
\omega_{38} &= -\frac{\sqrt{2-\frac{2}{\gamma}}\gamma(3\gamma-1)}{(\gamma+1)^2}, & \omega_{39} &= \frac{2\sqrt{2}(3\gamma^3-3\gamma^2-23\gamma+25)}{\left(\frac{\gamma-1}{\gamma}\right)^{3/2}\gamma(\gamma+1)^2}, & \omega_{40} &= \frac{2\sqrt{2}(7\gamma^2-29\gamma+28)}{\left(\frac{\gamma-1}{\gamma}\right)^{5/2}\gamma^2} \\
\omega_{41} &= \frac{2(7\gamma-5)}{\gamma^2-1}, & \omega_{42} &= -\frac{4\gamma(\gamma+3)}{(\gamma+1)^3}, & \omega_{43} &= \frac{4\gamma}{(\gamma+1)^2}, & \omega_{44} &= \frac{8-16\gamma^2}{(\gamma-1)(\gamma+1)^2}, & \omega_{45} &= -\frac{8(5\gamma-4)}{\gamma^2-1} \\
v_1 &= \frac{8}{\gamma+1} \\
v_2 &= \frac{4\gamma}{(\gamma+1)^2} \\
v_3 &= \frac{6}{\gamma+1} \\
\iota_1 &= \omega_{14} - v_1 v_2 - 2\omega_{15}\zeta_1 + 2v_1 v_3 \zeta_1 + \omega_{11}(\gamma_2 + \zeta_1) \\
\iota_2 &= \omega_{44} - 2\omega_{45}\zeta_1 + \omega_{41}(\gamma_2 + \zeta_1) \\
\iota_3 &= 2(\omega_{19} + v_2 v_3 - (2\omega_{20} + v_3^2)\zeta_1 + \omega_{16}(\gamma_2 + \zeta_1)) \\
\iota_4 &= \omega_{41}(\gamma_3 - 2\zeta_2) + \omega_{45}\zeta_2 \\
\iota_5 &= -\omega_{11}\gamma_3 + 2\omega_{11}\zeta_2 - \omega_{15}\zeta_2 + v_1 v_3 \zeta_2 \\
\iota_6 &= 2\omega_{16}(\gamma_3 - 2\zeta_2) + (2\omega_{20} + v_3^2)\zeta_2 \\
\iota_7 &= 2(\omega_{16}\gamma_1 \zeta_2 + \omega_{17} + \omega_{18} - \omega_{19}\zeta_1 - v_2 v_3 \zeta_1) + v_2^2 + (2(\omega_{16} + \omega_{20}) + v_3^2)\zeta_1^2 \\
\iota_8 &= \omega_{18} - \omega_{16}\zeta_1 \\
\iota_9 &= \omega_{12} + \omega_{13} + \zeta_1(v_1 v_2 - \omega_{14} + (\omega_{11} + \omega_{15} - v_1 v_3)\zeta_1) + \omega_{11}\gamma_1 \zeta_2 \\
\iota_{10} &= \omega_{13} - \omega_{11}\zeta_1 \\
\iota_{11} &= \omega_{42} + \omega_{43} - \omega_{44}\zeta_1 + (\omega_{41} + \omega_{45})\zeta_1^2 + \omega_{41}\gamma_1 \zeta_2 \\
\iota_{12} &= \omega_{43} - \omega_{41}\zeta_1 \\
\lambda_1 &= \alpha_1(\alpha_1 \iota_{11} + \iota_7) \\
\lambda_2 &= \frac{v_1 \zeta_1 + \alpha_1(v_2 - v_3 \zeta_1)}{(v_1 - \alpha_1 v_3)^2 \zeta_2} \\
\lambda_3 &= (\alpha_1(\alpha_1 \iota_4 + \iota_6) - \iota_5)(v_1 \zeta_1 + \alpha_1(v_2 - v_3 \zeta_1)) \\
\lambda_4 &= (\alpha_1(\alpha_1 \iota_2 + \iota_3) + \iota_1)(v_1 - \alpha_1 v_3)\zeta_2 \\
\xi_1 &= -\frac{\lambda_1 + \iota_9 + \lambda_2(\lambda_3 + \lambda_4)}{(\omega_{11} + \alpha_1(2\omega_{16} + \omega_{41}\alpha_1))\gamma_4 \zeta_2} \\
\xi_2 &= \frac{2\alpha_1 \iota_8 + \iota_{10} + \alpha_1^2 \iota_{12}}{\gamma_4 \zeta_2(\omega_{11} + 2\alpha_1 \omega_{16} + \alpha_1^2 \omega_{41})}
\end{aligned}$$

Table E.2: Constant coefficients for the second order partial derivatives of flow variables in the strong shock limit, found in Eqs. (F.15)–(F.18); and those for the initial value of Q_2 , found in Eq. (8.12), associated with shock driven by a corrugated piston. These coefficients are expressed in terms of other constant functions of γ listed in Table E.1.

Appendix F

PARTIAL DERIVATIVES OF FLOW VARIABLES

The partial derivatives used in the expansions of GGSD systems are given in this section.

F.1 General solutions

The general solutions to Eq. (7.28) are

$$\begin{aligned} \mathcal{F}^{i,j+1}[p] = & \left\{ [a^2 + u(a_0M - u)] \frac{d\mathcal{F}^{i,j}[p]}{dt} + a_0M\rho a^2 \frac{d\mathcal{F}^{i,j}[u]}{dt} \right. \\ & \left. + \frac{a_0M}{2}(a + a_0M - u)f_1^{i,j} - \frac{a_0M}{2}(a - a_0M + u)f_2^{i,j} \right\} / [a^2 - (a_0 - u)^2], \quad (\text{F.1}) \end{aligned}$$

$$\begin{aligned} \mathcal{F}^{i+1,j}[p] = & \left\{ -(a_0M - u) \frac{d\mathcal{F}^{i,j}[p]}{dt} - a_0M\rho a^2 \frac{d\mathcal{F}^{i,j}[u]}{dt} \right. \\ & \left. - \frac{a_0M}{2}(a + a_0M - u)f_1^{i,j} + \frac{a_0M}{2}(a - a_0M + u)f_2^{i,j} \right\} / [a^2 - (a_0 - u)^2], \quad (\text{F.2}) \end{aligned}$$

$$\begin{aligned} \mathcal{F}^{i,j+1}[u] = & \left\{ \frac{a_0M}{\rho} \frac{d\mathcal{F}^{i,j}[p]}{dt} + [a^2 + u(a_0M - u)] \frac{d\mathcal{F}^{i,j}[u]}{dt} \right. \\ & \left. + \frac{a_0M}{2\rho a}(a + a_0M - u)f_1^{i,j} + \frac{a_0M}{2\rho a}(a - a_0M + u)f_2^{i,j} \right\} / [a^2 - (a_0 - u)^2], \quad (\text{F.3}) \end{aligned}$$

$$\begin{aligned} \mathcal{F}^{i+1,j}[u] = & \left\{ -\frac{1}{\rho} \frac{d\mathcal{F}^{i,j}[p]}{dt} - (a_0M - u) \frac{d\mathcal{F}^{i,j}[u]}{dt} \right. \\ & \left. - \frac{1}{2\rho a}(a + a_0M - u)f_1^{i,j} - \frac{1}{2\rho a}(a - a_0M + u)f_2^{i,j} \right\} / [a^2 - (a_0 - u)^2], \quad (\text{F.4}) \end{aligned}$$

$$\begin{aligned} \mathcal{F}^{i+1,j}[u] = & \left\{ -\frac{1}{\rho} \frac{d\mathcal{F}^{i,j}[p]}{dt} - (a_0M - u) \frac{d\mathcal{F}^{i,j}[u]}{dt} \right. \\ & \left. - \frac{1}{2\rho a}(a + a_0M - u)f_1^{i,j} - \frac{1}{2\rho a}(a - a_0M + u)f_2^{i,j} \right\} / [a^2 - (a_0 - u)^2], \quad (\text{F.5}) \end{aligned}$$

$$\begin{aligned} \mathcal{F}^{i,j+1}[\rho] = & \left\{ a_0 M a^2 \frac{d\mathcal{F}^{i,j}[p]}{dt} + a_0 M \rho a^2 (a_0 M - u) \frac{d\mathcal{F}^{i,j}[u]}{dt} \right. \\ & - a^2 u [a^2 - (a_0 M - u)^2] \frac{d\mathcal{F}^{i,j}[\rho]}{dt} + \frac{a_0 M}{2} (a_0 M - u) (a + a_0 M - u) f_1^{i,j} \\ & \left. - \frac{a_0 M}{2} (a_0 M - u) (a - a_0 M + u) f_2^{i,j} + a_0 M [a^2 - (a_0 M - u)^2] f_3^{i,j} \right\} \\ & \Big/ [a^2 - (a_0 M - u)^2], \quad (\text{F.6}) \end{aligned}$$

$$\begin{aligned} \mathcal{F}^{i+1,j}[\rho] = & \left\{ -a^2 \frac{d\mathcal{F}^{i,j}[p]}{dt} - \rho a^2 (a_0 M - u) \frac{d\mathcal{F}^{i,j}[u]}{dt} \right. \\ & + a^2 [a^2 - (a_0 M - u)^2] \frac{d\mathcal{F}^{i,j}[\rho]}{dt} - \frac{1}{2} (a_0 M - u) (a + a_0 M - u) f_1^{i,j} \\ & \left. + \frac{1}{2} (a_0 M - u) (a - a_0 M + u) f_2^{i,j} - [a^2 - (a_0 M - u)^2] f_3^{i,j} \right\} \\ & \Big/ [a^2 - (a_0 M - u)^2], \quad (\text{F.7}) \end{aligned}$$

where

$$\begin{aligned} f_1^{i,j} = & \sum_{\substack{n=0, m=0 \\ (n,m) \neq (0,0)}}^{i,j} \binom{i}{n} \binom{j}{m} \left\{ \mathcal{F}^{n,m}[u+a] \mathcal{F}^{i-n+1, j-m}[p] + \mathcal{F}^{n,m}[\rho a] \mathcal{F}^{i-n, j-m+1}[u] \right. \\ & \left. + \mathcal{F}^{n,m}[\rho a(u+a)] \mathcal{F}^{i-n+1, j-m}[u] \right\} + \mathcal{F}^{i,j} \left[\frac{\rho a^2 u A'}{A} \right], \quad (\text{F.8}) \end{aligned}$$

$$\begin{aligned} f_2^{i,j} = & \sum_{\substack{n=0, m=0 \\ (n,m) \neq (0,0)}}^{i,j} \binom{i}{n} \binom{j}{m} \left\{ \mathcal{F}^{n,m}[u-a] \mathcal{F}^{i-n+1, j-m}[p] - \mathcal{F}^{n,m}[\rho a] \mathcal{F}^{i-n, j-m+1}[u] \right. \\ & \left. - \mathcal{F}^{n,m}[\rho a(u-a)] \mathcal{F}^{i-n+1, j-m}[u] \right\} + \mathcal{F}^{i,j} \left[\frac{\rho a^2 u A'}{A} \right], \quad (\text{F.9}) \end{aligned}$$

$$\begin{aligned} f_3^{i,j} = & \sum_{\substack{n=0, m=0 \\ (n,m) \neq (0,0)}}^{i,j} \binom{i}{n} \binom{j}{m} \left\{ \mathcal{F}^{n,m}[u] \mathcal{F}^{i-n+1, j-m}[p] - \mathcal{F}^{n,m}[a^2] \mathcal{F}^{i-n, j-m+1}[\rho] \right. \\ & \left. - \mathcal{F}^{n,m}[a^2 u] \mathcal{F}^{i-n+1, j-m}[\rho] \right\}. \quad (\text{F.10}) \end{aligned}$$

F.2 Asymptotic solutions

Asymptotic expressions are obtained for both the weak and strong shock limits up to second order. In the weak shock limit where $\varepsilon = M - 1 \rightarrow 0$, and the strong shock limit where $M \sim M' \rightarrow \infty$, the first order partial derivatives are given by

$$\rho_t = \begin{cases} \frac{Q_1}{2a_0^2} + 2 \left[\frac{2Q_1}{(1+\gamma)a_0^2} + \frac{(\gamma-3)\rho_0 a_0 \Phi}{(1+\gamma)^2} \right] \varepsilon + O(\varepsilon^2), & \varepsilon \rightarrow 0, \\ \rho_0 a_0 \left[\frac{6(\gamma+1)}{(\gamma-1)^2} M' + \frac{2}{\gamma-1} \Phi M \right] + O(M^0), & M \rightarrow \infty, \end{cases} \quad (\text{F.11a})$$

$$\rho_x = \begin{cases} \frac{-Q_1}{2a_0^3} + \left[\frac{(\gamma-3)Q_1}{(1+\gamma)a_0^3} - \frac{4(\gamma-1)\rho_0 \Phi}{(1+\gamma)^2} \right] \varepsilon + O(\varepsilon^2), & \varepsilon \rightarrow 0, \\ -\rho_0 \left[\frac{6(\gamma+1)}{(\gamma-1)^2} \frac{M'}{M} + \frac{2}{\gamma-1} \Phi \right] + O(M^{-1}), & M \rightarrow \infty, \end{cases} \quad (\text{F.11b})$$

$$u_t = \begin{cases} \frac{Q_1}{2\rho_0 a_0} + \left[\frac{Q_1}{\rho_0 a_0} + \frac{4(\gamma-1)a_0^2 \Phi}{(1+\gamma)^2} \right] \varepsilon + O(\varepsilon^2), & \varepsilon \rightarrow 0, \\ a_0^2 M \left[\frac{8}{\gamma+1} M' + \frac{4\gamma}{(\gamma+1)^2} \Phi M \right] + O(M^1), & M \rightarrow \infty, \end{cases} \quad (\text{F.12a})$$

$$u_x = \begin{cases} \frac{-Q_1}{2\rho_0 a_0^2} + \left[\frac{(2-6\gamma)a_0 \Phi}{(1+\gamma)^2} \right] \varepsilon + O(\varepsilon^2), & \varepsilon \rightarrow 0, \\ -a_0 \left[\frac{6}{\gamma+1} M' + \frac{4\gamma}{(\gamma+1)^2} \Phi M \right] + O(M^0), & M \rightarrow \infty, \end{cases} \quad (\text{F.12b})$$

$$p_t = \begin{cases} \frac{Q_1}{2} + 2 \left[Q_1 + \frac{(\gamma-3)\rho_0 a_0^3 \Phi}{(1+\gamma)^2} \right] \varepsilon + O(\varepsilon^2), & \varepsilon \rightarrow 0, \\ \rho_0 a_0^3 M^2 \left[\frac{4(3\gamma-2)}{\gamma^2-1} M' + \frac{4\gamma}{(\gamma+1)^2} \Phi M \right] + O(M^2), & M \rightarrow \infty, \end{cases} \quad (\text{F.13a})$$

$$p_x = \begin{cases} \frac{-Q_1}{2a_0} - \left[\frac{Q_1}{a_0} + \frac{4(\gamma-1)\rho_0 a_0^2 \Phi}{(1+\gamma)^2} \right] \varepsilon + O(\varepsilon^2), & \varepsilon \rightarrow 0, \\ -4\rho_0 a_0^2 M \left[\frac{2\gamma-1}{\gamma^2-1} M' + \frac{\gamma}{(\gamma+1)^2} \Phi M \right] + O(M^1), & M \rightarrow \infty, \end{cases} \quad (\text{F.13b})$$

$$a_t = \begin{cases} \frac{(\gamma-1)Q_1}{4\rho_0 a_0} + \left[\frac{(\gamma-1)Q_1}{2\rho_0 a_0} + \frac{(\gamma-1)(\gamma-3)a_0^2 \Phi}{(1+\gamma)^2} \right] \varepsilon + O(\varepsilon^2), & \varepsilon \rightarrow 0, \\ 2a_0^2 M \sqrt{\frac{\gamma-1}{2\gamma}} \left[\frac{\gamma(3\gamma-5)}{\gamma^2-1} M' + \frac{\gamma(\gamma-1)}{(\gamma+1)^2} \Phi M \right] + O(M^1), & M \rightarrow \infty, \end{cases} \quad (\text{F.14a})$$

$$a_x = \begin{cases} \frac{-(\gamma-1)Q_1}{4\rho_0 a_0^2} - \left[\frac{2(\gamma-1)^2 a_0 \Phi}{(1+\gamma)^2} \right] \varepsilon + O(\varepsilon^2), & \varepsilon \rightarrow 0, \\ -a_0 \sqrt{\frac{\gamma-1}{2\gamma}} \left[\frac{4\gamma(\gamma-2)}{\gamma^2-1} M' + \frac{2\gamma(\gamma-1)}{(\gamma+1)^2} \Phi M \right] + O(M^0), & M \rightarrow \infty. \end{cases} \quad (\text{F.14b})$$

Similarly the leading order behavior of the second order partial derivatives as $\varepsilon \rightarrow 0$

and $M \sim M' \sim M'' \rightarrow \infty$ are as follows:

$$p_{tt} = \begin{cases} \frac{Q_2}{2}, \\ \rho_0 a_0^4 M^2 (M (\omega_1 M'' + (\omega_2 + \omega_3) \Phi^2 M + \omega_3 \Psi M) + \omega_4 \Phi M M' + \omega_5 M'^2), \end{cases} \quad (\text{F.15a})$$

$$p_{tx} = \begin{cases} -\frac{Q_2}{2a_0}, \\ \rho_0 a_0^3 M (M (\omega_6 M'' + (\omega_7 + \omega_8) \Phi^2 M + \omega_8 \Psi M) + \omega_9 \Phi M M' + \omega_{10} M'^2), \end{cases} \quad (\text{F.15b})$$

$$u_{tt} = \begin{cases} \frac{Q_2}{2\rho_0 a_0}, \\ a_0^3 M (\omega_{11} M M'' + M^2 ((\omega_{12} + \omega_{13}) \Phi^2 + \omega_{13} \Psi) + \omega_{14} \Phi M M' + \omega_{15} M'^2), \end{cases} \quad (\text{F.16a})$$

$$u_{tx} = \begin{cases} -\frac{Q_2}{2\rho_0 a_0^2}, \\ a_0^2 (\omega_{16} M M'' + M^2 ((\omega_{17} + \omega_{18}) \Phi^2 + \omega_{18} \Psi) + \omega_{19} \Phi M M' + \omega_{20} M'^2), \end{cases} \quad (\text{F.16b})$$

$$u_{xx} = \begin{cases} \frac{Q_2}{2\rho_0 a_0^3}, \\ \frac{a_0}{M} (\omega_{41} M M'' + M^2 ((\omega_{42} + \omega_{43}) \Phi^2 + \omega_{43} \Psi) + \omega_{44} \Phi M M' + \omega_{45} M'^2), \end{cases} \quad (\text{F.16c})$$

$$\rho_{tt} = \begin{cases} \frac{Q_2}{2a_0^2}, \\ \rho_0 a_0^2 (\omega_{21} M M'' + M^2 ((\omega_{22} + \omega_{23}) \Phi^2 + \omega_{23} \Psi) + \omega_{24} \Phi M M' + \omega_{25} M'^2), \end{cases} \quad (\text{F.17a})$$

$$\rho_{tx} = \begin{cases} -\frac{Q_2}{2a_0^3}, \\ \frac{\rho_0 a_0}{M} (\omega_{26} M M'' + M^2 ((\omega_{27} + \omega_{28}) \Phi^2 + \omega_{28} \Psi) + \omega_{29} \Phi M M' + \omega_{30} M'^2), \end{cases} \quad (\text{F.17b})$$

$$a_{tt} = \begin{cases} \frac{(\gamma-1)Q_2}{4\rho_0 a_0}, \\ -a_0^3 M (\omega_{31} M M'' + M^2 ((\omega_{32} + \omega_{33}) \Phi^2 + \omega_{33} \Psi) + \omega_{34} \Phi M M' + \omega_{35} M'^2), \end{cases} \quad (\text{F.18a})$$

$$a_{tx} = \begin{cases} -\frac{(\gamma-1)Q_2}{4\rho_0 a_0^2}, \\ a_0^2 (\omega_{36} M M'' + M^2 ((\omega_{37} + \omega_{38}) \Phi^2 + \omega_{38} \Psi) + \omega_{39} \Phi M M' + \omega_{40} M'^2), \end{cases} \quad (\text{F.18b})$$

where $\omega_{1,2,\dots,45}$ are constant functions of γ given in Table E.2, Appendix E.

Appendix G

AN EDGE-DETECTION ALGORITHM

The specific edge-detection algorithm used in Sec. 8.1.4 that searches for the onset of a discontinuity on discrete values of the periodic function $M(\beta, t)$ is briefly outlined in this section. The algorithm is taken from a family of spectral methods developed by Gelb & Tadmor [35, 36].

At each time step, discrete data for the Mach number profile, \bar{M}_j , subject to the rescaling $\min_j(\bar{M}_j) = 0$ and $\max_j(\bar{M}_j) = 1$, is obtained first on the size $2N$ uniform grid $\beta_j = 2\pi j/(2N+1)$, where $j = 0, 1, \dots, 2N$. The discrete concentration detector is defined as

$$\tilde{T}_N^c[\bar{M}](\beta) = \pi i \sum_{k=-N}^N \text{sgn}(k) c\left(\frac{|k|\Delta\beta}{\pi}\right) \tilde{M}_k \exp(ik\beta), \quad (\text{G.1})$$

where \tilde{M}_k are the Fourier coefficients,

$$\tilde{M}_k = \frac{1}{2N+1} \sum_{j=0}^{2N} \bar{M}_j \exp(-ik\beta_j), \quad (\text{G.2})$$

and $c(s_k)$ with $s_k = |k|\Delta\beta/\pi$ is the concentration factor. The following two admissible concentration factors are considered next: the first order polynomial factor,

$$c^{\text{pol}}(s_k) = \sin\left(\frac{\pi s_k}{2}\right); \quad (\text{G.3})$$

and the exponential factor,

$$c^{\text{exp}}(s_k) = \sin\left(\frac{\pi s_k}{2}\right) \exp\left(\frac{1}{\alpha s_k(s_k - 1)}\right) \left(\int_0^1 \exp\left(\frac{1}{\alpha s(s - 1)}\right) ds\right)^{-1}, \quad (\text{G.4})$$

where $\alpha = 6$ is chosen [34]. By invoking the minmod operator,

$$\text{minmod}(f_1, f_2) = \begin{cases} \min(f_1, f_2), & \text{if } f_1, f_2 > 0, \\ \max(f_1, f_2), & \text{if } f_1, f_2 < 0, \\ 0, & \text{otherwise} \end{cases} \quad (\text{G.5})$$

the two concentration factors can be combined to give

$$\tilde{T}_N^{\text{minmod}}[\bar{M}](\beta) = \text{minmod}\left(\tilde{T}_N^{\text{pol}}[\bar{M}](\beta), \tilde{T}_N^{\text{exp}}[\bar{M}](\beta)\right). \quad (\text{G.6})$$

The concentration factors c are chosen such that all three aforementioned discrete detectors \tilde{T}_N^c converge to the desired limit that selects jump discontinuities, i.e., $\lim_{\delta \rightarrow 0} [\tilde{M}(\beta + \delta) - \tilde{M}(\beta - \delta)]$, for all $\beta \in [0, 2\pi)$ as $N \rightarrow \infty$. The separation of scales achieved by these discrete detectors is further enhanced by the nonlinear function,

$$E_{q,N} = N^{q/2} \left(\tilde{T}_N^{\text{minmod}} [\tilde{M}] (\beta) \right)^q, \quad (\text{G.7})$$

for some $q > 1$. And this leads to the enhanced concentration method

$$E_N^{\text{minmod}} [\tilde{M}] (\beta) = \begin{cases} \tilde{T}_N^{\text{minmod}} [\tilde{M}] (\beta), & \text{if } |E_{q,N}| > J_{\text{crit}}, \\ 0, & \text{if } |E_{q,N}| \leq J_{\text{crit}}, \end{cases} \quad (\text{G.8})$$

where $J_{\text{crit}} \sim O(1)$ is a global threshold below which jump discontinuities are neglected. The minmod detector is chosen here for its better performance locating discrete jumps to the nearest grid point while removing spurious oscillations.

BIBLIOGRAPHY

- [1] J. Abate and P. P. Valkó. Multi-precision Laplace transform inversion. *International Journal for Numerical Methods in Engineering*, 60(5):979–993, 2004. doi: 10.1002/nme.995.
- [2] J. Abate and W. Whitt. A unified framework for numerically inverting laplace transforms. *INFORMS Journal on Computing*, 18(4):408–421, 2006.
- [3] M. Abramowitz and I. A. Stegun. *Handbook of mathematical functions: with formulas, graphs, and mathematical tables*, volume 55. Courier Corporation, 1965.
- [4] D. Arnett. The role of mixing in astrophysics. *The Astrophysical Journal Supplement Series*, 127(2):213, 2000.
- [5] A. Bakhsh and R. Samtaney. Incompressible models of magnetohydrodynamic richtmyer-meshkov instability in cylindrical geometry. *Physical Review Fluids*, 4(6):063906, 2019.
- [6] R. Balescu. *Transport Processes in Plasmas: Classical transport*. Transport Processes in Plasmas. North-Holland, 1988.
- [7] J. W. Bates. On the theory of a shock wave driven by a corrugated piston in a non-ideal fluid. *Journal of fluid mechanics*, 691:146–164, 2012.
- [8] J. W. Bates. Theory of the corrugation instability of a piston-driven shock wave. *Physical Review E*, 91(1):1–6, 2015. ISSN 15502376. doi: 10.1103/PhysRevE.91.013014.
- [9] P. M. Bellan. *Fundamentals of plasma physics*. Cambridge University Press, 2008.
- [10] J. P. Best. A generalisation of the theory of geometrical shock dynamics. *Shock Waves*, 1(4):251–273, 1991.
- [11] J. P. Best. Accounting for transverse flow in the theory of geometrical shock dynamics. *Proceedings of the Royal Society of London. Series A: Mathematical and Physical Sciences*, 442(1916):585–598, 1993.
- [12] D. Bond, V. Wheatley, R. Samtaney, and D. I. Pullin. Richtmyer-Meshkov instability of a thermal interface in a two-fluid plasma. *Journal of Fluid Mechanics*, 833:332–363, 2017. doi: 10.1017/jfm.2017.693.
- [13] D. Bond, V. Wheatley, Y. Li, R. Samtaney, and D. I. Pullin. The magnetised richtmyer-meshkov instability in two-fluid plasmas. *Journal of Fluid Mechanics*, 903:A41, 2020.

- [14] S. I. Braginskii. Transport processes in a plasma. *Reviews of plasma physics*, 1, 1965.
- [15] M. G. Briscoe and A. A. Kovitz. Experimental and theoretical study of the stability of plane shock waves reflected normally from perturbed flat walls. *Journal of Fluid Mechanics*, 31(3):529–546, 1968.
- [16] M. Brouillette. The richtmyer-meshkov instability. *Annual Review of Fluid Mechanics*, 34(1):445–468, 2002.
- [17] J. Cao, Z. Wu, H. Ren, and D. Li. Effects of shear flow and transverse magnetic field on richtmyer–meshkov instability. *Physics of Plasmas*, 15(4): 042102, 2008.
- [18] C. Jeyaparan Catherasoo and B. Sturtevant. Shock dynamics in non-uniform media. *Journal of Fluid Mechanics*, 127:539–561, 1983.
- [19] S. Chapman, T. G. Cowling, and D. Burnett. *The mathematical theory of non-uniform gases: an account of the kinetic theory of viscosity, thermal conduction and diffusion in gases*. Cambridge university press, 1970.
- [20] D. S. Clark, C. R. Weber, J. L. Milovich, J. D. Salmonson, A. L. Kritcher, S. W. Haan, B. A. Hammel, D. E. Hinkel, O. A. Hurricane, O. S. Jones, et al. Three-dimensional simulations of low foot and high foot implosion experiments on the national ignition facility. *Physics of Plasmas*, 23(5): 056302, 2016.
- [21] P. Clavin. Nonlinear analysis of shock–vortex interaction: Mach stem formation. *Journal of Fluid Mechanics*, 721:324–339, 2013.
- [22] P. Clavin and B. Denet. Diamond patterns in the cellular front of an overdriven detonation. *Physical review letters*, 88(4):044502, 2002.
- [23] R. Courant and K. O. Friedrichs. *Supersonic flow and shock waves*, volume 21. Springer Science & Business Media, 1999.
- [24] B. Denet, L. Biamino, G. Lodato, L. Vervisch, and P. Clavin. Model equation for the dynamics of wrinkled shockwaves: comparison with dns and experiments. *Combustion Science and Technology*, 187(1-2):296–323, 2015.
- [25] R. P. Drake, S. G. Glendinning, Kent Estabrook, B. A. Remington, Richard McCray, R. J. Wallace, L. J. Suter, T. B. Smith, J. J. Carroll, R. A. London, and E. Liang. Observation of forward shocks and stagnated ejecta driven by high-energy-density plasma flow. *Physical Review Letters*, 1998. ISSN 10797114. doi: 10.1103/PhysRevLett.81.2068.
- [26] S. P. D’yakov. Shock wave stability. *Zh. Eksp. Teor. Fiz*, 27(3):288–295, 1954.

- [27] J. Eggers, T. Grava, M. A. Herrada, and G. Pitton. Spatial structure of shock formation. *Journal of Fluid Mechanics*, 820:208–231, 2017.
- [28] G. Emanuel. *Analytic fluid dynamics*. CRC Press, 3rd edition, 2016.
- [29] G. Emanuel. Derivatives on the downstream side of a moving, curved shock. *Journal of Engineering Mathematics*, 117(1):79–105, 2019. doi: 10.1007/s10665-019-10010-0.
- [30] L. M. Faria, A. R. Kasimov, and R. R. Rosales. Theory of weakly non-linear self-sustained detonations. *Journal of Fluid Mechanics*, 2015. ISSN 14697645. doi: 10.1017/jfm.2015.577.
- [31] N. C. Freeman. A theory of the stability of plane shock waves. *Proceedings of the Royal Society of London. Series A. Mathematical and Physical Sciences*, 228(1174):341–362, 1955.
- [32] N. C. Freeman. On the stability of plane shock waves. *Journal of Fluid Mechanics*, 1957. ISSN 14697645. doi: 10.1017/S0022112057000208.
- [33] Donald P. Gaver Jr. Observing stochastic processes, and approximate transform inversion. *Operations Research*, 14(3):444–459, 1966.
- [34] A. Gelb and D. Cates. Detection of edges in spectral data iii—refinement of the concentration method. *Journal of Scientific Computing*, 36(1):1–43, 2008.
- [35] A. Gelb and E. Tadmor. Detection of edges in spectral data ii. nonlinear enhancement. *SIAM Journal on Numerical Analysis*, 38(4):1389–1408, 2000.
- [36] A. Gelb and E. Tadmor. Adaptive edge detectors for piecewise smooth data based on the minmod limiter. *Journal of Scientific Computing*, 28(2-3):279–306, 2006.
- [37] S. H. Glenzer, B. J. MacGowan, P. Michel, N. B. Meezan, L. J. Suter, S. N. Dixit, J. L. Kline, G. A. Kyrala, D. K. Bradley, D. A. Callahan, E. L. Dewald, L. Divol, E. Dzenitis, M. J. Edwards, A. V. Hamza, C. A. Haynam, D. E. Hinkel, D. H. Kalantar, J. D.ilkenny, O. L. Landen, J. D. Lindl, S. LePape, J. D. Moody, A. Nikroo, T. Parham, M. B. Schneider, R. P. J. Town, P. Wegner, K. Widmann, P. Whitman, B. K. F. Young, B. Van Woutherghem, L. J. Atherton, and E. I. Moses. Symmetric inertial confinement fusion implosions at ultra-high laser energies. *Science*, 327:1228, 2010.
- [38] J. P. Goedbloed and S. Poedts. *Principles of magnetohydrodynamics: with applications to laboratory and astrophysical plasmas*. Cambridge university press, 2004.
- [39] P. J. Goldston and P. H. Rutherford. *Introduction to plasma physics*. CRC Press, 1995.

- [40] G. I. Hagstrom and E. Hameiri. Traveling waves in hall-magnetohydrodynamics and the ion-acoustic shock structure. *Physics of Plasmas*, 21(2):022109, 2014.
- [41] E. Hameiri. Generalized shock conditions and the contact discontinuity in the Hall-magnetohydrodynamics model. *Physics of Plasmas*, 20(2), 2013. doi: 10.1063/1.4792258.
- [42] E. Hameiri, A. Ishizawa, and A. Ishida. Waves in the hall-magnetohydrodynamics model. *Physics of plasmas*, 12(7):072109, 2005.
- [43] M. A. Hoefler, M. J. Ablowitz, and P. Engels. Piston dispersive shock wave problem. *Physical Review Letters*, 2008. doi: 10.1103/PhysRevLett.100.084504.
- [44] M. Hohenberger, P.-Y. Chang, G. Fiskel, J. P. Knauer, R. Betti, F. J. Marshall, D. D. Meyerhofer, F. H. Séguin, and R. D. Petrasso. Inertial confinement fusion implosions with imposed magnetic field compression using the OMEGA Laser. *Physics of Plasmas*, 19:056306, 2012.
- [45] H. G. Hornung. Deriving features of reacting hypersonic flow from gradients at a curved shock. *AIAA Journal*, 2010. doi: 10.2514/1.39993.
- [46] S. H. R. Hosseini and K. Takayama. Experimental study of Richtmyer-Meshkov instability induced by cylindrical shock waves. *Physics of Fluids*, 17:084101, 2005.
- [47] J. D. Huba. Theory and simulation of a high-frequency magnetic drift wave. *Physics of Fluids B: Plasma Physics*, 3(12):3217–3225, 1991.
- [48] Joseph D Huba. Hall magnetohydrodynamics-a tutorial. In *Space Plasma Simulation*, pages 166–192. Springer, 2003.
- [49] I. V. Igumenshchev, A. B. Zylstra, C. K. Li, P. M. Nilson, V. N. Goncharov, and R. D. Petrasso. Self-generated magnetic fields in direct-drive implosion experiments. *Physics of Plasmas*, 21(6):062707, 2014.
- [50] R. P. Kanwal. Determination of the vorticity and the gradients of flow parameters behind a three-dimensional unsteady curved shock wave. *Archive for Rational Mechanics and Analysis*, 1(1):225–232, 1957.
- [51] B. J. Katko, R. Chavez, H. Liu, B. Lawlor, C. McGuire, L. Zheng, J. Zanteson, and V. Eliasson. Experimental and numerical study of blast-structure interaction. In *Structures Congress 2020*, pages 105–118. American Society of Civil Engineers Reston, VA, 2020.
- [52] A. M. Khokhlov, E. S. Oran, and G. O. Thomas. Numerical simulation of deflagration-to-detonation transition: the role of shock–flame interactions in turbulent flames. *Combustion and Flame*, 117(1-2):323–339, 1999.

- [53] N. E. Lanier, C. W. Barnes, S. H. Batha, R. D. Day, G. R. Magelssen, J. M. Scott, A. M. Dunne, K. W. Parker, and S. D. Rothman. Multimode seeded Richtmyer-Meshkov mixing in a convergent, compressible, miscible plasma system. *Physics of Plasmas*, 10:1816, 2003.
- [54] K. C. Lapworth. An experimental investigation of the stability of plane shock waves. *Journal of Fluid Mechanics*, 1959. doi: 10.1017/S0022112059000763.
- [55] S. K. Lele. Compact finite difference schemes with spectral-like resolution. *Journal of computational physics*, 103(1):16–42, 1992.
- [56] M. J. Lighthill. The diffraction of blast. i. *Proceedings of the Royal Society of London. Series A. Mathematical and Physical Sciences*, 198(1055):454–470, 1949.
- [57] M. J. Lighthill. The diffraction of blast. ii. *Proceedings of the Royal Society of London. Series A. Mathematical and Physical Sciences*, 200(1063):554–565, 1950.
- [58] J. Lindl, O. Landen, J. Edwards, Ed Moses, and NIC team. Review of the national ignition campaign 2009-2012. *Physics of Plasmas*, 21(2):020501, 2014.
- [59] J. D. Lindl, R. L. McCrory, and E. M. Campbell. Progress toward ignition and burn propagation in inertial confinement fusion. *Physics Today*, 45(9): 32–40, 1992.
- [60] G. Lodato, L. Vervisch, and P. Clavin. Direct numerical simulation of shock wavy-wall interaction: analysis of cellular shock structures and flow patterns. *Journal of Fluid Mechanics*, 789:221–258, 2016.
- [61] G. Lodato, L. Vervisch, and P. Clavin. Numerical study of smoothly perturbed shocks in the newtonian limit. *Flow, Turbulence and Combustion*, 99(3-4): 887–908, 2017.
- [62] M. Lombardini, D. I. Pullin, and D. I. Meiron. Turbulent mixing driven by spherical implosions. part 2. turbulence statistics. *Journal of Fluid Mechanics*, 748:113–142, 2014. doi: 10.1017/jfm.2014.163.
- [63] M. Lombardini, D. I. Pullin, and D. I. Meiron. Turbulent mixing driven by spherical implosions. part 1. flow description and mixing-layer growth. *Journal of Fluid Mechanics*, 748:85–112, 2014. doi: 10.1017/jfm.2014.161.
- [64] A. López Ortega, M. Lombardini, D. I. Pullin, and D. I. Meiron. Numerical simulations of the Richtmyer-Meshkov instability in solid-vacuum interfaces using calibrated plasticity laws. *Physical Review E*, 89(3), 2014.

- [65] A. López Ortega, M. Lombardini, P. T. Barton, D. I. Pullin, and D. I. Meiron. Richtmyer-Meshkov instability for elastic-plastic solids in converging geometries. *Journal of the Mechanics and Physics of Solids*, 76:291–324, 2015.
- [66] A. Majda and R. Rosales. A theory for spontaneous mach stem formation in reacting shock fronts, i. the basic perturbation analysis. *SIAM Journal on Applied Mathematics*, 43(6):1310–1334, 1983.
- [67] MJ-E Manuel, C. K. Li, F. H. Séguin, J. Frenje, D. T. Casey, R. D. Petrasso, S. X. Hu, R Betti, J. D. Hager, D. D. Meyerhofer, et al. First measurements of rayleigh-taylor-induced magnetic fields in laser-produced plasmas. *Physical review letters*, 108(25):255006, 2012.
- [68] G. H. Markstein. Flow disturbances induced near a slightly wavy contact surface, or flame front, traversed by a shock wave. *Journal of the Aeronautical Sciences*, 24:238–239, 1957.
- [69] N. Matsui, K. Mima, M. Honda, and A. Nishiguchi. Analysis of rippled shock-wave propagation and ablation-front stability by theory and hydrodynamic simulation. *Journal of Plasma Physics*, 1999. doi: 10.1017/S0022377898007260.
- [70] A. Maxwell, M. Dryer, and P. McIntosh. A piston-driven shock in the solar corona. *Solar physics*, 97(2):401–413, 1985.
- [71] E. E. Meshkov. Instability of the interface of two gases accelerated by a shock wave. *Fluid Dynamics*, 4(5):101–104, 1969.
- [72] K. O. Mikaelian. Rayleigh-Taylor and Richtmyer-Meshkov instabilities and mixing in stratified cylindrical shells. *Physic of Fluids*, 17:094105, 2005.
- [73] S. Mölder. Curved shock theory. *Shock Waves*, 2016. ISSN 09381287. doi: 10.1007/s00193-015-0589-9.
- [74] E. I. Moses, R. N. Boyd, B. A. Remington, C. J. Keane, and R. Al-Ayat. The national ignition facility: Ushering in a new age for high energy density science. *Physics of Plasmas*, 16(4):041006, 2009.
- [75] W. Mostert, V. Wheatley, R. Samtaney, and D. I. Pullin. Effects of seed magnetic fields on magnetohydrodynamic implosion structure and dynamics. *Physics of Fluids*, 26(12):126102, 2014.
- [76] W. Mostert, V. Wheatley, R. Samtaney, and D. I. Pullin. Effects of magnetic fields on magnetohydrodynamic cylindrical and spherical Richtmyer-Meshkov instability. *Physics of Fluids*, 27(10):104102, 2015.
- [77] W Mostert, D. I. Pullin, R. Samtaney, and V. Wheatley. Geometrical shock dynamics for magnetohydrodynamic fast shocks. *Journal of Fluid Mechanics*, 811, 2017.

- [78] W. Mostert, D. I. Pullin, R. Samtaney, and V. Wheatley. Singularity formation on perturbed planar shock waves. *Journal of Fluid Mechanics*, 846:536–562, 2018.
- [79] W. Mostert, D. I. Pullin, R. Samtaney, and V. Wheatley. Spontaneous singularity formation in converging cylindrical shock waves. *Physical Review Fluids*, 3(7):071401, 2018.
- [80] S. Ohsaki and S. M. Mahajan. Hall current and alfvén wave. *Physics of Plasmas*, 11(3):898–902, 2004.
- [81] A. L. Ortega, D. J. Hill, D. I. Pullin, and D. I. Meiron. Linearized richtmyer-meshkov flow analysis for impulsively accelerated incompressible solids. *Physical Review E*, 81(6):066305, 2010.
- [82] J. C. Pant. Some aspects of unsteady curved shock waves. *International Journal of Engineering Science*, 1969. doi: 10.1016/0020-7225(69)90059-7.
- [83] L. J. Perkins, B. G. Logan, G. B. Zimmerman, and C. J. Werner. Two-dimensional simulations of thermonuclear burn in ignition-scale inertial confinement fusion targets under compressed axial magnetic fields. *Physics of Plasmas*, 20(7), 2013.
- [84] B. A. Remington, H. Park, D. T. Casey, R. M. Cavallo, D. S. Clark, C. M. Huntington, C. C. Kuranz, A. R. Miles, S. R. Nagel, K. S. Raman, et al. Rayleigh–taylor instabilities in high-energy density settings on the national ignition facility. *Proceedings of the National Academy of Sciences*, 116(37):18233–18238, 2019.
- [85] R. D. Richtmyer. Taylor instability in shock acceleration of compressible fluids. *Communications on Pure and Applied Mathematics*, 13(2):297–319, 1960.
- [86] P. Rosenau, J. A. Tataronis, and G. Conn. Elements of magnetohydrodynamics with the Hall current. Part 1. Nonlinear phenomena. *Journal of Plasma Physics*, 21(3):385–399, 1979. doi: 10.1017/S0022377800021966.
- [87] R. Samtaney. Suppression of the richtmyer–meshkov instability in the presence of a magnetic field. *Physics of Fluids*, 15(8):L53–L56, 2003.
- [88] R. Samtaney, P. Colella, T. J. Ligocki, D. F. Martin, and S. C. Jardin. An adaptive mesh semi-implicit conservative unsplit method for resistive MHD. *Journal of Physics: Conference Series*, 16:40, 2005.
- [89] D. D. Schnack. *Lectures in magnetohydrodynamics: with an appendix on extended MHD*, volume 780. Springer, 2009.

- [90] F. H. Séguin, C. K. Li, MJ-E Manuel, H. G. Rinderknecht, N. Sinenian, J. A. Frenje, J. R. Rygg, D. G. Hicks, R. D. Petrasso, J. Delettrez, et al. Time evolution of filamentation and self-generated fields in the coronae of directly driven inertial-confinement fusion capsules. *Physics of Plasmas*, 19(1):012701, 2012.
- [91] N. Shen, Y. Li, D. I. Pullin, R. Samtaney, and V. Wheatley. On the magnetohydrodynamic limits of the ideal two-fluid plasma equations. *Physics of Plasmas*, 25(12):122113, 2018.
- [92] N. Shen, D. I. Pullin, V. Wheatley, and R. Samtaney. Impulse-driven richtmyer-meshkov instability in hall-magnetohydrodynamics. *Phys. Rev. Fluids*, 4:103902, Oct 2019. doi: 10.1103/PhysRevFluids.4.103902.
- [93] N. Shen, V. Wheatley, D. I. Pullin, and R. Samtaney. Magnetohydrodynamic richtmyer-meshkov instability under an arbitrarily oriented magnetic field. *Physics of Plasmas*, 27(6):062101, 2020. doi: 10.1063/1.5142042.
- [94] V. A. Smalyuk, C. R. Weber, O. L. Landen, S. Ali, B. Bachmann, P. M. Celliers, E. L. Dewald, A. Fernandez, B. A. Hammel, G. Hall, et al. Review of hydrodynamic instability experiments in inertially confined fusion implosions on national ignition facility. *Plasma Physics and Controlled Fusion*, 62(1):014007, 2019.
- [95] B. Srinivasan and U. Shumlak. Analytical and computational study of the ideal full two-fluid plasma model and asymptotic approximations for Hall-magnetohydrodynamics. *Physics of Plasmas*, 18(9), 2011. doi: 10.1063/1.3640811.
- [96] B. Srinivasan and X. Tang. Mechanism for magnetic field generation and growth in rayleigh-taylor unstable inertial confinement fusion plasmas. *Physics of Plasmas*, 19(8):082703, 2012.
- [97] H. Stehfest. Algorithm 368: Numerical inversion of laplace transforms [d5]. *Communications of the ACM*, 13(1):47–49, 1970.
- [98] R. A. Strehlow and F. D. Fernandes. Transverse waves in detonations. *Combustion and Flame*, 1965. ISSN 00102180. doi: 10.1016/0010-2180(65)90057-X.
- [99] D. G. Swanson. *Plasma waves*. Elsevier, 2012.
- [100] A. Talbot. The accurate numerical inversion of laplace transforms. *IMA Journal of Applied Mathematics*, 23(1):97–120, 1979.
- [101] T. Y. Thomas. On Curved Shock Waves. *Journal of Mathematics and Physics*, 1947. doi: 10.1002/sapm194726162.

- [102] W. K. Van Moorhem and A. R. George. On the stability of plane shocks. *Journal of Fluid Mechanics*, 68(1):97–108, 1975.
- [103] Q. Wan, H. Jeon, R. Deiterding, and V. Eliasson. Numerical and experimental investigation of oblique shock wave reflection off a water wedge. *Journal of Fluid Mechanics*, 826:732–758, 2017.
- [104] V. Wheatley, D. I. Pullin, and R. Samtaney. Stability of an impulsively accelerated density interface in magnetohydrodynamics. *Physical Review Letters*, 95(12):1–4, 2005. doi: 10.1103/PhysRevLett.95.125002.
- [105] V. Wheatley, R. Samtaney, and D. I. Pullin. The Richtmyer-Meshkov instability in magnetohydrodynamics. *Physics of Fluids*, 21(8):1–13, 2009. doi: 10.1063/1.3194303.
- [106] V. Wheatley, R. M. Gehre, R. Samtaney, and D. I. Pullin. The magnetohydrodynamic richtmyer-meshkov instability: the oblique field case. In R. Bonazza and D. Randan, editors, *29th International Symposium on Shock Waves*, pages 1107–1112. Springer, 2013.
- [107] V. Wheatley, R. Samtaney, D. I. Pullin, and R. M. Gehre. The transverse field Richtmyer-Meshkov instability in magnetohydrodynamics. *Physics of Fluids*, 26(1):0–17, 2014. doi: 10.1063/1.4851255.
- [108] G. B. Whitham. A new approach to problems of shock dynamics part i two-dimensional problems. *Journal of Fluid Mechanics*, 2(2):145–171, 1957.
- [109] G. B. Whitham. *Linear and nonlinear waves*, volume 42. John Wiley & Sons, 2011.
- [110] J. Yang, T. Kubota, and Edward E. Zukoski. Applications of shock-induced mixing to supersonic combustion. *AIAA journal*, 31(5):854–862, 1993.
- [111] Y. D. Yoon and P. M. Bellan. A generalized two-fluid picture of non-driven collisionless reconnection and its relation to whistler waves. *Physics of Plasmas*, 24(5):052114, 2017.
- [112] R. M. Zaidel. Development of perturbations in plane shock waves. *Journal of Applied Mechanics and Technical Physics*, 1967. doi: 10.1007/BF00913564.